Exploring the Generative Architecture of Intramembranous Ossification

Kate Weymouth-Crocker Jordan

Thesis submitted in fulfilment of the requirements for the degree of Doctor of Philosophy

University of Warwick, Systems Biology Centre

April 2011

PAGE NUMBERS ARE CLOSE TO THE EDGE OF THE PAGE.

SOME ARE CUT OFF

TABLE OF CONTENTS

i. LIST OF FIGURES & TABLES

Technical Appendices

Table 11.2.5: Properties of samples from microarray analyses

Table 11.2.6: Expression of genes characteristic of certain lineages within the final experimental cohort of 12 samples

ii. ACKNOWLEDGEMENTS

I am immeasurably grateful to my supervisor, Professor Georgy Koentges, for his unwavering support, guidance and insight without which my work would never have been possible. In the words of another great teacher: ὁ δὲ ἀνεξέταστος βίος οὐ βιωτὸς ἀνθρώπῳ.

I would also like to thank the members of the Koentges group, past and present, for being such wonderful colleagues, teachers and –most importantly- friends who made my PhD an absolute joy.

I would be remiss not to thank the members of my advisory committee, Dr Sascha Ott, Dr Keith Vance and Dr Sach Mukherjee; especially Sascha and Keith for their infinite advice.

I am extremely appreciative of the help I was given by the members of Warwick University's Genomics Facility and Biological Services Unit, especially Dr Helen Brown and Sue Davis for their assistance with the Chiari project; and Sam Dixon and Ian Bagley, for enabling all my projects to succeed by their perseverance in attempting to get shy mice to behave themselves!

Many thanks to the excellent collaborators I have been privileged to work with during my PhD.

I remain extremely grateful to Dr Leo Cheng and Dr Paul Greenwood, for their continual mentorship.

I am exceedingly fortunate to have amazing family and friends for which I am very thankful and to whom I owe so much!

Above all I am grateful to my parents for their unconditional love and their unique inputs: to my father for his tenacity and laughter, to Lorna for her strength of character, to Bob for reminding me to be of good cheer and his sage advice, and to my mother for *everything* which is beyond words.

Finally, for Tom, for his patience, love and for our life together.

iii. DECLARATION

I, Kate Weymouth-Crocker Jordan, confirm that the work presented in this thesis is my own and is submitted in its entirety in fulfilment of the degree of Doctor of Philosophy in Systems Biology at the University of Warwick. No material included herein has been submitted for any other degree. I further confirm that information included in this thesis that derives from other sources is clearly indicated and the extent of collaborative work is detailed below.

INCLUSION OF COLLABORATIVE WORK

I declare that work presented in my thesis is my own; where conjoint work is being described it is clearly indicated in both the relevant results section and the Materials and Methods chapter. Specific work undertaken collaboratively includes:

The use of the following transgenic strains of mice, generously donated for this work as indicated: *Hand2*-Cre x ROSA26LacZ, specimen and live mice provided by D. Clouthier (University of Colorado); *Hand2*$^{fl/fl}$ x *Wnt1*-Cre-R26LacZ mice, bred and maintained by H. Yanigasawa (University of Texas), specimen and slides provided by H. Yanigasawa and D. Clouthier; *BAenh-/-* mice, specimen provided by D. Clouthier; XZ-DR reporter mice, generated and maintained by X. Zhang (University of Warwick), specimen provided by X. Zhang; SMO-/- mice, generated by T. Matsuoka, unanalysed phenotypic data provided by G. Koentges.

Bioinformatic work, including analyses of microarray data detailed in Chapter 8 (AffyBatch quality controls, principle component analyses, RNA degradation analysis and differential gene analyses) were conducting using algorithms generated by Dr Sascha Ott (University of Warwick).

Comparisons made between murine dermal bones and phylogenetically distant species was made on the basis of data shared between the Koentges group and Prof P Donoghue (including images in Figure 5.1).

iv. ABSTRACT

Dermal bone is the oldest of vertebrate hard tissues; despite its evolutionary and developmental significance, its histogenesis is poorly understood. The present thesis investigates aspects of frontal bone and clavicle formation including layer morphogenesis, vasculogenesis, biomineralization and muscle:bone connectivity. I apply an array of molecular markers in a 3D time-course at single-cell resolution to genetically tracked and mutated mouse cell lineages. I uncover a growth mode not commensurate with traditional models of intramembranous ossification, whereby two molecularly distinct generative layers (external and internal) intercalate cells into the intervening cancellous/spongious layer, which elaborates with time. Cells in the external layer organize into rosette formations that act as archetypal units of cellular introgression, bearing the hallmarks of a tangential convergence-extension movement. Both osteoblasts and endothelia enter into the spongious bone from the generative layers, forming an osteoblast-endothelial interface in the cancellous layer and *de novo* vasculature in the maturing bone. Ablation of Hand2 in the neural crest lineage abrogates this internal sheet formation, substantiating the notion of ingression from the outer and inner (Hand2+) layers; Hand2 mediates this process *in vivo* by regulating the nuclear import of Runx2 protein, at the post-transcriptional level. The highly dynamic processes of layer formation and vascularization are related to bone mineralization using a time-course of matrix labeling, examined *ex vivo* and *in vivo*; this reveals extensive remodeling of existing mineral by osteoblasts and endothelial cells, which modulate the collagen scaffolds along which hydroxyapatite crystals are assembled in the absence of osteoclasts. This sheds light on possible mechanisms of skeletogenesis in acellular bone among jawed vertebrate ancestors. I finally investigate endochondral ossification of classically mesodermal occipital regions and find an additional neural crest-based invasion in those tissues. This sheds light onto the etiology of neurocristopathies and prompts a modification of present fate maps.

v. ABBREVIATIONS

AFM	atomic force microscopy
AMV	avian myeloblastosis virus
BA	branchial arch
BSA	bovine serum albumin
BSP II	Bone sialoprotein II
CD31	PECAM1, platelet endothelial cell adhesion molecule 1
cDNA	complementary DNA
CNS	central nervous system
Coll I	Collagen Type I
Coll II	Collagen Type II
CRABP1	Cellular retinoic acid binding protein 1
Cre	cre recombinase
Cy5	Cyanine 5
Cy3	Cyanine 3
DABCO	1,4-diazobicyclo-[2.2.2]-octane
DAPI	4',6-diamidino-2-phenylindole
ddATP	dideoxyadenosine triphosphate
dH2O	double distilled water
DIG	digoxigenin
DMSO	dimethyl sulfoxide
DNA	deoxyribonucleic acid
DNP	2,4-dinitrophenol
dNTP	deoxyribonucleotide
EDTA	ethylenediaminetetraacetate
EtOH	ethanol
FBS	fetal bovine serum
FGFR1	Fibroblastic growth factor receptor 1
FGFR2	Fibroblastic growth factor receptor 2
FITC	fluorescein isothiocyanate
FN	Fibronectin
GAPDH	glyceraldehyde 3-phosphate dehydrogenase
gDNA	genomic DNA
GFP	green fluorescent protein
H&E	standard hematoxylin and eosin histological stain
H2O2	hydrogen peroxide
HAP	hydroxyapatite
HCl	hydrochloric acid
hUbC	human Ubiquitin C
ICP	intracranial pressure
IHC	immuno-histochemistry
ISH	*in situ* hybridisation

LB/Amp	lysogeny broth (LB) containing the antibiotic ampicillin
LCM	laser capture microdissection
LoxP	locus of X-over P1
LTBP	Latent trasforming growth factor-β
MgCL2	magnesiumchloride
MMLV	moloney murine leukemia Virus
MMP	matrix metalloproteinase
MRI	magnetic resonance imaging
MSX2	Msh homeobox 2
NaCl	sodiumchloride
NaOH	sodiumhydroxide
NC	neural crest
OCN	Osteocalcin
OCT	optimal cutting temperature media
OPN	Osteopontin
PBS	phosphate buffered saline
PCA	principle component analysis
PCF	posterior cranial fossa
PCP	planar cell polarity
PCR	polymerase chain reaction
PE	pectoralis muscle
PFA	paraformaldehyde
POD	peroxidase
polyA	poly-adenylation
PONC	post-otic neural crest
POSTN	Periostin, osteoblast specific factor 2 (OSF-2)
QC	quality control
qPCR	quantitative polymerase chain reaction
qRT-PCR	qualitative real time polymerase chain reaction
RA	retinoic acid
RNA	ribonucleic acid
RPh	Rhodamine phalloidin
Runx2	Runt related transcription factor 2, CBFA1
SCM	sternocleidomastoid muscle
SHH	Sonic hedgehog
SMA	α-Smooth muscle actin
Smo	Smoothened SHH ligand
SOC	super optimal broth with catabolite repression
SOS	spheno-occipital synchondrosis
SSC	saline sodium citrate buffer
TAE	400 mM tris-acetate and 10 mM EDTA
TdT	terminal deoxynucleotidyl transferase
TGFβ1	tranforming growth factor beta-1
TRIS	tris-hydroxymethyl-aminomethane

vWF	von Willibrand factor
X-Gal	bromo-chloro-indolyl-galactopyranoside
β-Cat	β-Catenin
β-Gal	Beta-Galactosidase

v. OVERVIEW- GENERAL INTRODUCTION TO THESIS CONTENTS

Dermal bone is the oldest form of ossification in evolutionary history, and one of the key novelties of jawed vertebrates, displaying a three-layered (diploë) organisation in the earliest known taxa. Two layers, one external (underneath the dermis, herein termed Layer 1) and one internal (adjacent to the brain, termed Layer 3 in this study) sandwich an intervening spongious/cancellar area, denoted Layer 2. During early paleontological studies the spongious layer was considered a passive 'bystander' of other biomineralisation processes, therefore, the underlying developmental processes responsible for bone layering, and the resulting three-dimensional bone architecture, has remained poorly understood. Although a large corpus of literature -genetic and developmental- exists, these studies rarely examined co-expression of relevant genes nor were they examined in 3D at high resolution (Abzhanov *et al.* 2007; Bandyopadhyay *et al* 2008; Franz-Odendaal *et al.* 2006; Buckwalter *et al.* 1995; Hall 2005; Paic *et al. 2009*). Therefore, molecular identities, fates and lineage origins of cells participating in dermal bone formation have not been studied in a comprehensive fashion and the gamut of literature describing intramembranous ossification is highly contradictory.

While many studies have focused on sutures as places of lateral dermal bone expansion, the mechanism of how dermal bones grow in thickness has remained almost entirely obscure (Johnson *et al.* 2000; Lana-Elola *et al.* 2007; Opperman *et al.* 2000; Ting *et al.* 2009). Instead, endochondral bone formation is often used as a proxy for understanding the ontogeny of dermal bones; patterns observed in studies of intramembranous bones are usually reconciled with the formation of the endochondral skeleton (Lieberman & Friedlaender 2005; Buckwalter 1995; Hall 2005). For example, the process of appositional addition of osteoblasts and matrix to the bone front in dermal bone was originally modelled based on what is known about mesodermal long bone formation. This co-opting of endochondral formation to resolve dermal bone formation means that the exact mechanism of intramembranous ossification is unresolved.

Work for this thesis aims to explore the entire process of dermal bone formation, from the condensed mesenchyme stage in murine embryonic development, through early post-natal maturation. In order to fully explore bone development an array of molecular markers was employed, chosen to encompass those traditionally associated with the four key processes in bone formation: Chapter 1. the establishment of layer morphogenesis as dictated by the osteoblastic cells within the bone; Chapter 2. the process of angiogenesis in bone growth – thus the emergence of an osteoblastic/endothelial interface; Chapter 3. the mechanism by which the osteoid is calcified and the mineral phase is formed; and finally, Chapter 4. the generation of the bone:skeletal muscle interface. These features of bone maturation were concurrently 'explored utilising 3D reconstructions to visualise marker expression at the single-cell level in wild-type and genetically labelled and/or mutated murine tissues.

The establishment of layer morphogenesis in dermal bone is explored in Chapter 1. There I will examine the number and location of generative (growth) surfaces in the frontal and clavicle bones in a time-course of development (sections 1.1-1.2). I discover that, in contrast to the traditional model of intramembranous ossification, the bone anlagen comprise two generative layers each of which remain contiguous from mid-way through murine gestation (E13) though postnatal development (P8) (section 1.1). I will describe how new cells, osteoblasts and endothelial cells, become part of growing layers and I provide molecular markers and genetic (ablation) evidence pointing towards an unusual process of cells percolating into the inner (previously called 'spongious' or cancellar') layer of the dermal bone from both sides and (re)forming osteoblastic-endothelial sheets inside that inner layer, which generates the increasingly complex cancellous bone (sections 1.2-1.4). The process by which this occurs is similar to what is known in embryology as a convergence-extension/sheet migration process (section 1.5).

The incorporation of new cells into the growing middle layer appears to take place at specific privileged places where cells organize in a rosette-type fashion in the external layer (L1) (section 1.3). I will describe the molecular

and cellular nature of these rosettes, as well as evidence that rosettes are archetypal units of dermal thickness growth. Surprisingly, a (hitherto unrecognized) key process for regulated cell invasion appears to be the post-transcriptional modification of transcription factors inside rosette cells. In section 1.4 I describe a new process of tethering by which the transcription factor Hand2 regulates the Runx2 protein's nuclear localization. I show how genetic ablation of Hand2 abrogates this process, which has fundamental implications for sheet formation, layer morphogenesis and ensuing biomineralisation.

In Chapter 2 I test the validity of the traditionally held notion that dermal bones are pre-patterned by existing vasculature in the overlying dermis, which becomes encompassed by the growing bone (section 2.1). Contrasting this, I find the generative layers introducing osteoblasts to the nascent bone also provide the bone vasculature (section 2.2). There is *de novo* vessel formation in the bone and a unique relationship whereby osteoblasts and vasculature develop concurrently in direct juxtaposition to one another, preventing precocious ossification impinging on vascular formation (section 2.2.2). Furthermore, the rosettes discovered during experiments of Chapter 1 are shown to act as the mammalian counterpart to the pore canal system of basal vertebrates (section 2.2.3).

The formation of the mineral phase of dermal bones is analysed in Chapter 3 with specific regard to how layer morphogenesis affects the process of mineralisation. I examine how the spongious Layer 2 grows as a mineral entity using a time-course of both *ex vivo* (section 3.2) and *in vivo* (section 3.3) labelling of the biomineralising zone. Traditionally (and to date) only matrix apposition from the outside (by osteoblasts) was considered, as mineral decay is believed to be established by osteoclasts. In contrast to this, results in Chapter 3 indicate younger matrix is found on the inside of older matrix, thus matrix is continually remodelled by reshaping the collagenous scaffolds upon which hydroxyapatite crystals are built (section 3.4); surprisingly this is achieved by osteoblasts that etch themselves into previously mineralised areas, cleave the collagen scaffolds on which mineral is laid, and expand mineralised areas from within (section 3.5). This

remodelling by cells from both generative layers leads to an amorphous core of mineral that is only later surrounded by late appositional matrix after birth (section 3.3). This sheds new light on the temporal sequence and directionality of mineralization.

Having established the layer morphogenesis, vascularisation and biomineralisation in Chapters 1, 2 and 3, respectively, in Chapter 4 I examine the means by which musculoskeletal attachments can form, without impinging on the thickness growth of the bone. I find a unique subdivision of the most external periost-like tissue forms the enthesis (section 4.2.1) and I establish molecular marker signatures for the cells within the attachment region responsible for muscle connectivity (section 4.2.2), a finding that explains how the muscle scaffold can remain stable over long evolutionary periods while the process of ossification of attachment points might change.

Results from Chapters 1 to 4 lead to the formation of a new model of dermal bone formation, the synopsis of which is found in Chapter 5. The coordination of layer morphogenesis, vasculogenesis, biomineralisation and enthesis formation are all dependent on the behaviours of highly invasive neural crest cells that form an osteoblastic-endothelial interface through sheet neogenesis. The continual expansion of the bone relies on perpetual integration of new cellular material; in the frontal bone both the osteoblastic and endothelial cells are found to derive from the neural crest and mesoderm.

The discovery of a new contribution of neural crest to endothelia led to the final work of my PhD, where I re-examine the potential contribution of the neural crest to endochondral ossification in the cranial base. The development of this anatomical region holds significance for understanding the process of indirect ossification and has direct relevance to human diseases such as the Chiari malformation, as recent studies have indicated areas of the cranial base that are primarily affected in Chiari malformations are neural crest in origin. I map the previous evidence that the neural crest contributes cells to regions of the cranial base affected in Chiari I/II in Chapter 6, where the etiological origins of affected areas is shown to be the

first unifying feature for the multitude of incongruent symptoms of the condition.

In Chapter 7 I continue to explore the possibility that Chiari is a neurocristopathy and map the contributions of the neural crest to the late development of the posterior cranial fossa, the chief anatomical region affected in Chiari malformations. I find that cartilages that have previously been mapped as mesodermal (somitic) – namely the occipitals – become later invaded by an osteoblastic-endothelial front of neural crest origin. The surprising contribution of neural crest-derived endothelia to regions including the occipital protuberance, suprocciput, atlas and clivus, at late stages of murine pre-natal development, as well as the arachnoids, pericytes, and endothelia of the cortex indicate previously established fate maps may need to be amended as aspects of a wider time time-course (section 7.2).

Finally, results from single cell transcriptome analyses of several neural crest-derived regions in the cranial base are presented in Chapter 8, supporting Chiari as a potential vasculogenic neurocristopathy and/or a connective tissue disorder (section 8.2).

The work conducted in this thesis aimed to explore the generative architecture of intramembranous ossification and the role of the neural crest in the development of the cranial base. Each chapter includes the relevant introduction, results and an independent discussion, and each part (I and II) concludes with a summarising discussion pertaining to dermal bone formation (Chapter 5) and establishing Chiari as a neurocristopathy (Chapter 9), respectively.

PART I:

THE GENERATIVE ARCHITECTURE OF DERMAL BONE DEVELOPMENT

1. Cell biological foundations of dermal bone development

1.1 The generative architecture of dermal bone formation

1.1.1 Introduction

The vertebrate skeleton comprises two types of bone, dermal and endochondral: dermal bone is the oldest form of ossification in evolutionary history, with the craniofacial region being the most primitive skeleton (Donoghue *et al.* 2006). Despite its ancient origins, the process of dermal bone development remains poorly understood (Hall and Miyake 2000; Donoghue and Sansom 2002; Janvier 2008). Dermal bone arises directly from mesenchymal cells in direct or intramembranous ossification; a process that differs dramatically from the extensively studied mechanism by which indirect/endochondral bones are formed.

In the traditional model of intramembranous ossification, dermal bone formation is preceded by an increase in vascularisation at the site of future skeletogenesis, after which mesenchymal cells migrate to the area and are subjected to epithelial-mesenchymal interactions (Hall and Miyake 2000). These interactions lead to the condensation of the mesenchyme into trabeculae (Hall and Miyake 1992). Proper osteogenesis intitates when a sheet of mesenchymal cells in the trabecle differentiate into the osteoblastic lineage, as indicated by the expression of genes associated with a pre-osteoblastic condition, namely Runx2 and Collagen I (Abzhanov *et al.* 2007). Next, a single layer of osteoblastic precursors further differentiate from pre-osteoblasts into osteoblasts (a transition reportedly indicated by the expression of Osteopontin, and BSP II) and these cells start producing osteoid (Figure 1.1), which mineralises to form the hardened calcified tissue (Lieberman and Friedlaender 2005; Abzhanov *et al.* 2007). Some osteoblasts become engulfed by the matrix they secrete and further differentiate into osteocytes capable of small amounts of rapid osteolysis (Boukhechba *et al.* 2009); at this stage the next layer of pre-osteoblasts

differentiates into osteoblasts and a second layer of osteoid is deposited (Figure 1.1). The osteogenic front thus continues to move through the mesenchyme, with successive layers of cells depositing new osteoid on top of the existing mineralized surface, growing the bone by apposition (Buckwalter *et al.* 1995). This arrangement results in the most mature mineralisation found at the deepest margin, with the superficial aspects of the bone being the most recently mineralised. Bone formation is completed by the addition of the inner and outer compacta, establishing the periosteum (Birnbaum *et al.* 2001; Hall 2005). Any further remodelling to the bone (to accommodate additional vasculature, bone resorption, etc.) is accomplished via osteoclasts arising from the bone marrow from monocyte and megakaryocyte precursors (Cohen 2006). Unlike endochondral bone formation, dermal bone develops from the mesenchyme without any cartilage precursor as a template. The architecture of the intramembranous anlagen is, therefore, dictated by two features: the pre-existing vasculature, around which the bone must form, and the generative layer of osteoblasts secreting the osteoid and mineralising the matrix (Figure 1.1).

Dermal bone gives rise to the majority of the craniofacial skeleton (Gans and Northcutt 1983; Noden 1983; Couly *et al.* 1993; Le Douarin *et al.* 1993) and the histogenetic mechanism by which the bones form while accommodating the simultaneous expansion of the brain is poorly understood. Specifically of interest in the current study was elucidating the mechanism by which the dermal bones of the cranial vault expand in thickness without compromising cerebro-cortical development.

The current study aimed to examine the validity of the traditional model of intramembranous ossification (described above), and explore the generative architecture and molecular characteristics of the cells involved in direct ossification. The study employed a wide-array of molecular markers to probe bone maturation and resolve the widely conflicting expression domains of these markers as reported in dermal bone development literature (Abzhanov *et al.* 2003; Hall 2005; Franz-Odendaal *et al.* 2006; Abzhanov *et al.* 2007; Bandyopadhyay *et al.* 2008). Markers were chosen such that they would assess the progression of overall bone formation and also the development

of cells through various stages of osteoblastic lineages (expected to advance from pre-osteoblast to osteoblast to osteocyte) (Table 1.1).

The formation of the mesenchymal anlagen would be monitored using Fibronectin, a cell adhesion molecule and marker of sheet migration downstream of TGFβ1 required for mesenchymal condensation formation, secreted by cells depositing a basal membrane (Bilezikian *et al.* 2008) and expressed by early pre-osteoblasts (Franz-Odendaal *et al.* 2006). Traditional pre-osteoblastic markers also included Runx2 (widely expressed in fibroblasts), as well as Collagen I and Collagen II (Franz-Odendaal *et al.* 2006). The previously identified transition to osteoblasts would be marked by Osteopontin and Osteocalcin expression (Franz-Odendaal *et al.* 2006). Finally, the end stage of bone development, when bone is encased by a periosteum, would be indicated by the presence of CRABP1 and Undulin (Collagen XIV) (Bandyopadhyay *et al.* 2008). Periostin (POSTN), or Osteoblast Specific Factor-2, is an additional marker of the periosteum which may also be expressed by pre-osteoblasts and has been found to regulate sheet migration of cells, a phenomenon well described for neural crest cells migrating into branchial arches or into the developing heart outflow tracts (Horiuchi *et al.* 1999; Franz-Odendaal *et al.* 2006; Zhu *et al.* 2008).

The current study mapped murine intramembranous ossification using high resolution imaging, which enables the structures to be recapitulated in 3D at single cell resolution. This approach would allow the bone maturation process to be examined *in situ* as any alternative approach (such as explant studies and *in vitro* bone growth) may have unknown consequences on the normal progression of dermal bone development. Double and triple immunohistochemistry (IHC) was favoured over RNA *in situ* hybridisation in order to monitor changes in protein localization (ex: nuclear versus cytoplasmic); the ramifications of using this methodology could not be predicted as high resolution imaging combined with IHC has not been previously utilised for *in vivo* analysis of dermal bone formation.

1.1.2 Results

The traditional model of dermal bone formation describes differentiation progressing through the condensed mesenchyme, organising the anlage into layers of pre-osteoblasts (Runx2-positive, no osteoid secretion) and fully functioning osteoblasts that deposit osteoid and then calcify the matrix. In this model, at a given time-point there is only a single generative layer of fully differentiated osteoblasts, which abuts the pre-osteoblastic layer (Figure1.1). In addition to the expression of several characteristic markers, the progression through the osteoblastic lineages is accompanied by morphological changes (Table 1.1); mesenchymal cells of the dermis have the flattened morphology of fibroblasts, pre-osteoblasts have a relatively more rounded shape, and osteoblasts are expected to be round or cuboidal during their growth phase and pyramidal with extensive cellular processes thereafter (Lieberman and Friedlaender 2005; Lerner 2006; Schiavi 2006). In the traditional model of intramembranous ossification, cells percolate at random from the single osteoblastic front into the matrix.

My initial analysis focused on a time-point midway through murine gestation when the characteristic architecture of the frontal bone would be established but bone development is incomplete, such that territories of the different cell lineages (pre-osteoblasts vs. osteoblasts) should be easily defined. In contrast to the expectation of a single generative (outer) surface, I find a tri-layered architecture of the immature frontal bone where two laminae of thin, flattened cells sandwich an intervening space populated by larger, more rounded cells (Figure 1.2). Progressing from the dermis side, the external lamina is hitherto referred to as Layer 1 (L1), the internal space as Layer 2 (L2), and the internal lamina as Layer 3 (L3) (Figure 1.2A). Although containing morphogenically similar cells, Layers 1 and 3 are molecularly distinct.

L1, the external layer of flattened cells at the dermis-bone interface, expresses markers associated with the pre-osteoblastic condition, namely Runx2 and Collagen II (Figure 1.2). Notably, Runx2 expression is largely localised to the cytoplasm. In contrast, L3, the internal layer of flattened cells at the dura-bone interface, expresses markers associated with mature osteoblasts, namely Osteopontin and Collagen I (Figure 1.2), but is negative

for Runx2 and Collagen II proteins. Despite the flattened cell morphology, this finding may imply L3 contains the most mature (osteoblast) cells, while L1 comprises the pre-osteoblasts; this formation would be consistent with a traditional model where the oldest layers are considered to be at the bottom of the bone and the youngest areas as the most superficial.

However, contradicting this model of spatial segregation of pre-osteoblasts and osteoblasts, both layers 1 and 3 are populated by cells expressing proteins associated with the various stages of osteoblast maturation. The external layer, L1, and the dermis display a wide expression of Osteocalcin, a marker traditionally associated with late osteoblasts in intramembranous ossification and osteocytes in endochondral ossification (Figure 1.3A) (Franz-Odendaal *et al.* 2006). Cells of both L1 and L3 express the osteoblast/osteocyte marker β-Catenin required for proper osteogenesis (Figure 1.3B) (Chen *et al.* 2007; Kramer *et al.* 2010). Conversely, Hand2, a gene associated with both heart and limb formation whose abrogation leads to craniofacial abnormalities (Yanagisawa *et al.* 2003), is more widely expressed by cells of L3, although focal expression of Hand2 in L1 is noted (Figure 1.3C).

Further complicating the characterisation of the laminar layers, both L1 and L3 carry markers of the periosteum and/or perichondrium, which would not be expected to be present until the final stages of bone maturation. L1 strongly expresses CRABP1 and Undulin, with weaker expression of both found in L3; contrarily, L3 expression of POSTN is more marked than POSTN expression in L1 (Figure 1.4). The perichondrium and periosteum are fundamental to endochondral bone development; they act as a cambial growth zone and a source of osteoblasts, they regulate differentiation of adjacent tissues and are critical for the growth and maintenance of the bones they encapsulate (Colnot *et al.* 2004; Bandyopadhyay *et al.* 2008). The current results may indicate periosteal-like tissues are critical for early dermal bone formation.

In addition to being periosteum-like, L1 and L3 contain cells with high lateral mobility potential as they express Fibronectin, as well as F-Actin, a

component of lamellipodia and filopodia and a marker of cellular motility (Figure 1.5) (Fujii *et al.* 2010). The potential motility of cells within L1 and L3 is consistent with recent DiI labelling experiments exhibiting extensive lateral spreading from areas corresponding to the location of the laminar layers of the frontal bone (Figure 1.5 C-D) (Morriss-Kay 2001).

The complexity of markers expressed in Layers 1 and 3 means neither can easily be ruled the single generative osteoblast layer, and there is a complete incongruence with traditional classification as both express pre-osteoblastic, osteoblastic, osteocytic and non-osteoblastic markers; this raises the possibility that both layers could act as generative surfaces. To explore the roles of Layers 1 and 3 in bone development, the spatial and ontogenetic development of the diploë architecture of intramembranous bones was closely examined.

1.1.2.1 Spatial maturation of the frontal bone

Dermal bone maturation progresses in a vectorial manner: along the dorso-ventral axis the youngest bone lies closest to the coronal suture (separating the frontal and parietal bones) while at the nasal end the mature bone has acquired a characteristic trabeculated appearance (within L2) (Figure 1.6). This growth pattern ensures that in sagittal cross-section, a snapshot of the various stages of bone development is available at a single time-point of analysis (Yoshida *et al.* 2008).

At a semi-mature stage of frontal bone development, at a late period of murine gestation between E17-18, the bone has a tripartite structure; in a sagittal cross-section through the bone the cancellous core is sandwiched between two laminar layers (L1 and L3) of thin, flattened cells that fully line the length of the bone (Figure 1.6). The two border layers of cells are contiguous sheets across the expanding length of the bone. Molecular analysis confirms the two laminar layers are L1 and L3, and there is a continuity of gene expressing along the dorso-ventral axis within the layers: L1 contains Runx2(+)/Osteocalcin(+)/β-Catenin(+) cells, while L3 contains

Osteopontin(+)/Hand2(+)/β-Catenin(+) cells and both layers are positive for periosteal/perichondrial markers and markers of sheet mobility (Figure 1.7).

Despite the morphological and molecular continuity of Layers 1 and 3, the intervening Layer 2 becomes more elaborate with time and along the dorso-venral axis. Near the coronal suture, L2 is a nascent layer only a single to a few cells thick and sparsely populated. Progressing toward the nasal end, L2 increases in complexity and carries the matrix and cancellous bone structure. Within L2 the distinctive layered appearance of the developing bone, as predicted by the traditional model of dermal bone development, was not evident. Instead Layer 2 was a patchwork of cells that carried the hallmarks of either Layer 1 or Layer 3 (Figures 1.3, 1.4, 1.5, 1.7). This could suggest that L1 and L3 are indeed both generative layers and cells from them that are in Layer 2 have maintained the unique combination of gene expression from the layer with which that cell is associated. This single time-point analysis cannot, however, rule out the possibility that transitory gene expression may mean cells alternate marker expression within L2, and a time-course analysis necessary to confirm the uninterrupted expression of the marker combinations throughout dermal bone formation.

1.1.2.2 Ontogeny of frontal bone development

The time-course analysis of layer formation in dermal bone focused on the development of the frontal bone from a stage mid-way through foetal development (at the condensed mesenchyme stage) through embryonic maturation and birth. Frontal bone formation is initiated at embryonic day E12-13 when the primordia to the frontal bone consists of a loose mesenchyme encasing the developing telencephalon (Yoshida *et al.* 2008) (Figure 1.8). The mesenchyme, which is in the process of condensing, lies beneath a thin layer of dermis and above the forebrain. At this stage, the dermis expresses the markers associated with Layer 1, namely Runx2, Osteocalcin, F-Actin, β-Catenin and Fibronectin (Figure 1.9). Conversely, the forebrain expresses Hand2, and POSTN, akin to Layer 3 (Figure 1.10). The brain also expresses an activated form of Notch (nuclear) and β-Catenin

(Figure 1.10). The margin of the forebrain is delineated by a border of cells expressing the endothelial marker CD31, indicating the boundary of the developing meninges and the medial margin of the condensed mesenchyme (Figure 1.10G).

Utilising the same molecular markers as in the single time-point study, I find the condensed sheet of mesenchyme, while morphological indistinct, is already a bi-layered system carrying the hallmarks of L1 and L3 (Figure_). Cells adjacent to the dermis express cytoplasmic β-Catenin and Runx2; while cells abutting the meninges express POSTN and Hand2 (Figure 1.11). Within the next day of embryological development (through late day E13 in gestation), the mesenchymal condensation rapidly expands. The population of cells within L1 is extremely dense and cells have a variety of morphologies with the majority having acquired a slightly flattened shape (Figure 1.12). The expression of Runx2 is ubiquitous within L1 (Figure 1.12). Conversely, L3 and the forebrain express Osteopontin, with expression in the brain being markedly more pronounced than that in L3 (Figure 1.12). At this young stage the two layers, L1 and L3, are directly juxtaposed to one another without the intervening physical space, L2.

At the next time-point examined, E16, near the coronal suture, the bone has acquires the same architecture as displayed at E18, whereby L1 and L3 remain continuous layers lining the bone; their characteristic composition includes their molecular signatures, as well as the thin-flattened morphology of the cells within them. The morphological and gene-expression signatures of Layer 1 and 3 continue to be unbroken in the final stages of analysis, at the first day of postnatal development.

1.1.3 Conclusion

Results from the time-course study of frontal bone ontogeny reveal Layer 1 and Layer 3 are incipient layers of bone formation between the dermis and brain, respectively. These layers are a continual presence within the frontal bone, lining it on either side. The molecular expression patterns of Layers 1

and 3 are unchanged from E13 through birth, and morphologically by E16 the cells within them have achieved a thin-flattened appearance that is constant through all prenatal development. Contrasting this, L2 expands with time to become the spongious bone and it is the continually increasing complexity of this layer (and the subsequently increasing separation of L1 and L3) that is responsible for expanding the thickness of the frontal bone. The mechanism by which L2 becomes populated was further explored in the next study, utilising genetic lineage labelling in transgenic strains of mice.

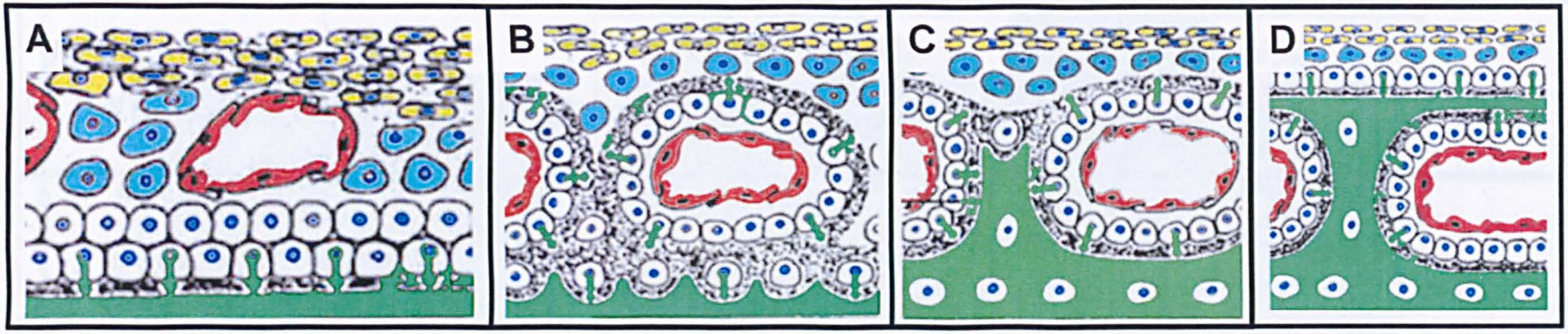

Figure 1.1: Diagrammatic representation of the traditional model of dermal ossification

The process of intramembranous ossification occurs when a condensed mesenchyme forms a bone, without a cartilage template, in a process termed direct ossification. Condensed mesenchymal cells (yellow) differentiate into pre-osteoblasts (teal) which further differentiate into fully functioning osteoblasts (white), which secrete osteoid (grey) and subsequently mineralise the matrix (green). In this model the area where the dermal bone will form is highly vascularised and the bone is pre-pattered by the existing blood vessels (red), which the bone must engulf and accommodate.

A. A single layer of osteoblasts acts as the generative front, depositing matrix appositionally; the wave of differentiation continues through the mesenchyme, so the next layer of pre-osteoblasts differentiates into osteoblasts (**B**) and cells are oriented around the blood vessels as the osteoid is continually mineralised (**C**). In the next stage, a second layer of mineral will be deposited as the process repeats (**D**) and the bone will grow by apposition and layering of the mineral on top of the previously laid calcifications. In the resulting architecture the oldest bone will be at the bottom and the most immature regions are the most superficial.

A-D Modified from Bruder & Scaduto in *Bone Regeneration and Repair,* 2005, Human Press Inc. Lieberman & Friedlaender, eds.

Table 1.1: Marker expression as mapped in dermal bone development in published studies and the expected morphology of each type of cell in the osteoblastic lineage (see text for details & references)

	Expected Expression Patterns			
	Periosteum/ Perichondrium	Pre-Osteoblast	Osteoblast	Osteocyte
Fibronectin		X	X	X
Runx2		X		
Collagen II		X		
Periostin	X	X	X	
Collagen I		X	X	
Osteopontin			X	X
Osteocalcin			X	X
β-Catenin			X	X
Undulin	X			
CRABP-I	X			
EXPECTED MORPHOLOGY		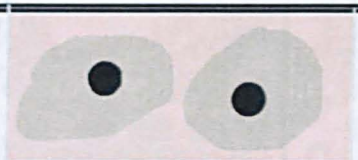	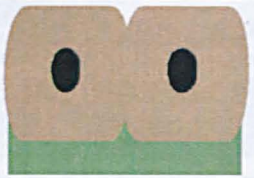	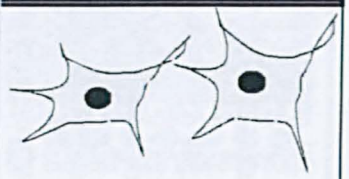

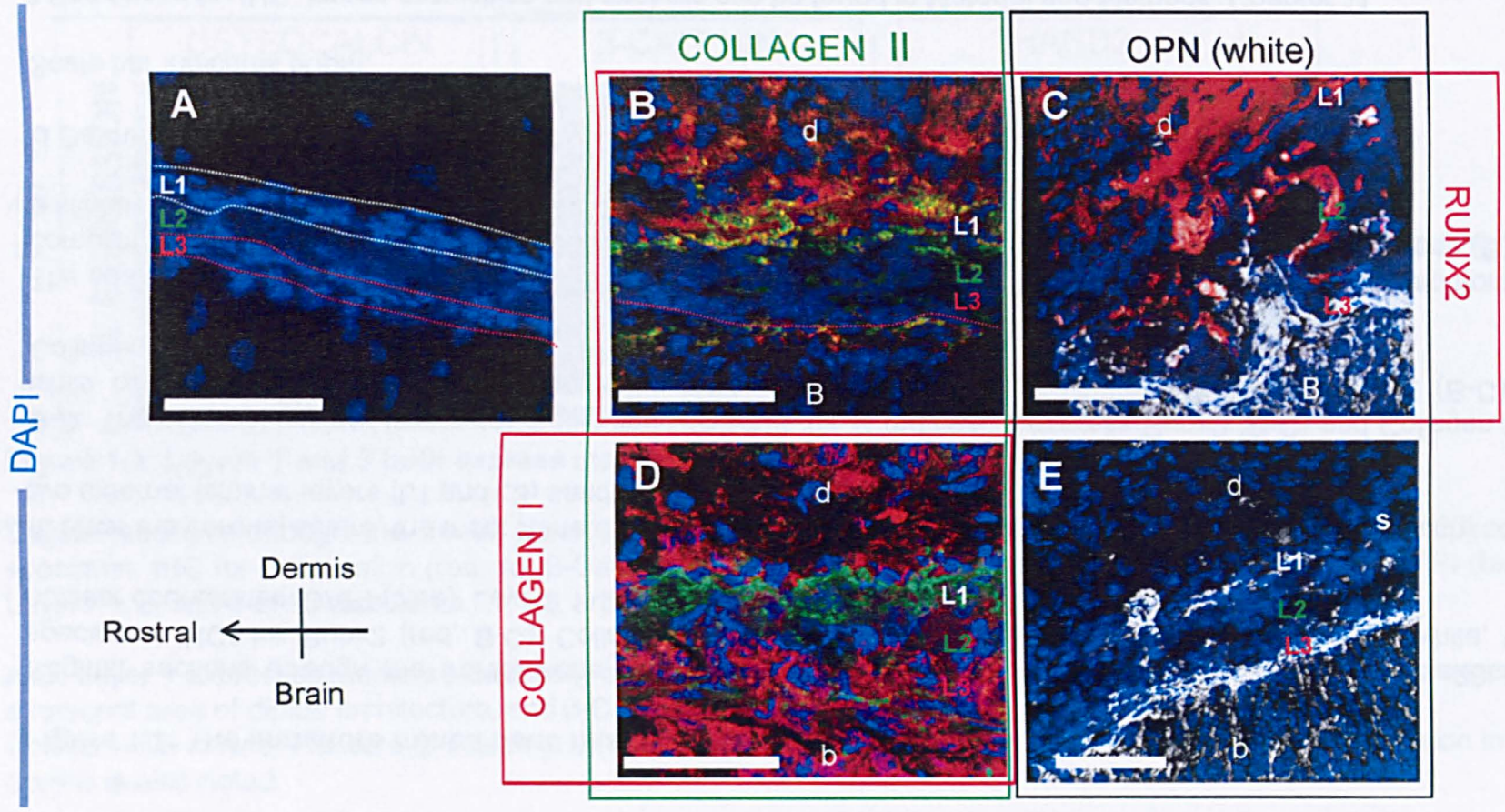
DAPI
A
L1
L2
L3
COLLAGEN II
B
d
L1
L2
L3
B
OPN (white)
C
d
L1
L2
L3
B
RUNX2
COLLAGEN I
D
d
L1
L2
L3
b
E
d
s
L1
L2
L3
b
Dermis
Rostral
Brain

Figure 1.2: The immature frontal bone has a diploë architecture

Sagittal sections through the frontal bone at embryonic day E18 after conception; *Wnt*1-Cre$^{+/-}$ x Rosa26LacZ$^{+/-}$ specimen. IHC* for Runx2 (red, **B-C**), Collagen II (green, **C**), Collagen I (red, **D**), and Osteopontin (white, **C,E**); nuclear counterstain DAPI (blue). Layers 1, 2, and 3 are indicated as **L1**, **L2**, and **L3**, respectively.

A. Near the coronal suture, the most immature area of the bone, the frontal bone has a tri-partite (diploë) architecture; two external laminar layers (L1 and L3) sandwich an intervening space that is cell sparse (L2).

B-D. The external laminar layers are molecularly different. Cells of Layer 1 express Runx2 (**B-C**) and Collagen II (**B**) while cells of Layer 3 express Collagen I (**D**) and Osteopontin (**C, E**). The dermis expresses Runx2 (**B-C**) and Collagen I (**D**), while cells of the forebrain express Collagen I (**D**) and Osteopontin (**E**).

The spatial expression of the traditional pre-osteoblast markers (Runx2 and Collagen II) are notably defined from and complimentary to the expression area of the osteoblast markers (OPN and Collagen I) in the immature bone (**B**) and a slightly more mature region from the same section (**C**) .

d Dermis, **b** Brain

Scale bar indicates 50μm.

* Conditions for IHC, image acquisition and analysis can be found in Material and Methods, Chapter 11.

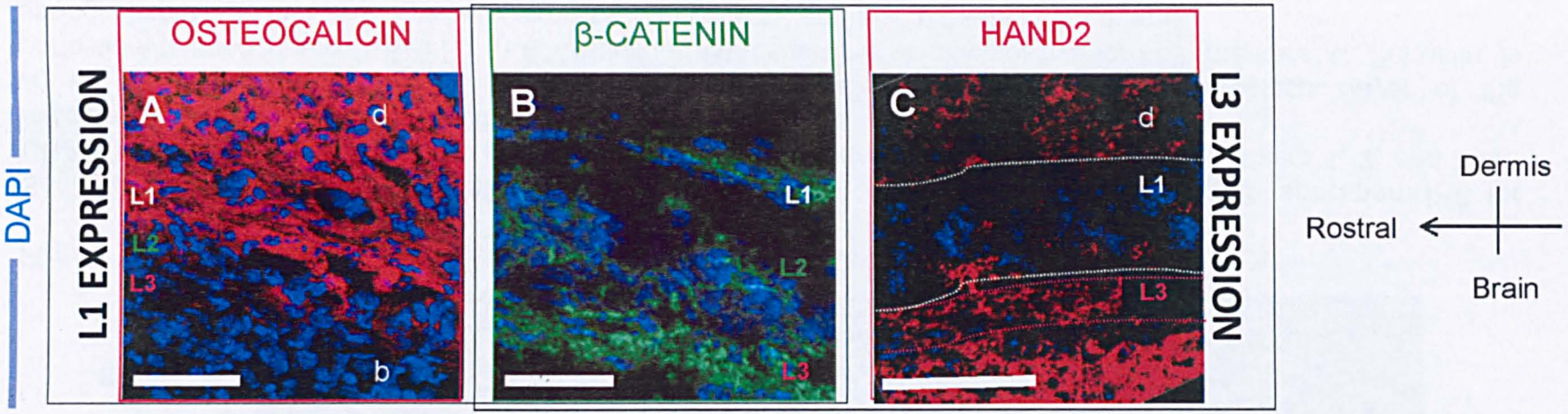

Figure 1.3: Layers 1 and 3 both express markers of osteoblasts

Sagittal sections through the frontal bone at embryonic day E18 after conception; *Wnt*1-Cre$^{+/-}$ x Rosa26LacZ$^{-/-}$ specimen. IHC for Osteocalcin (red, **A**), β-Catenin (green, **B**) and Hand2 (red, **C**); nuclear counterstain DAPI (blue). Layers 1, 2, and 3 are indicated as **L1**, **L2**, and **L3**, respectively.

A-B. Layer 1 expresses markers traditionally associated with fully mature osteoblasts: Osteocalcin (**A**) is expressed in a nascent area of diploe architecture, and β-Cantenin (**B**) expression is in Layer 1 and in Layers 2-3.
C. Bird's-eye view of Hand2 expression in an immature region of the frontal bone (L2 is not visible); expression in the dermis is also noted.

d Dermis, **b** Brain

Scale bar indicates 50μm.

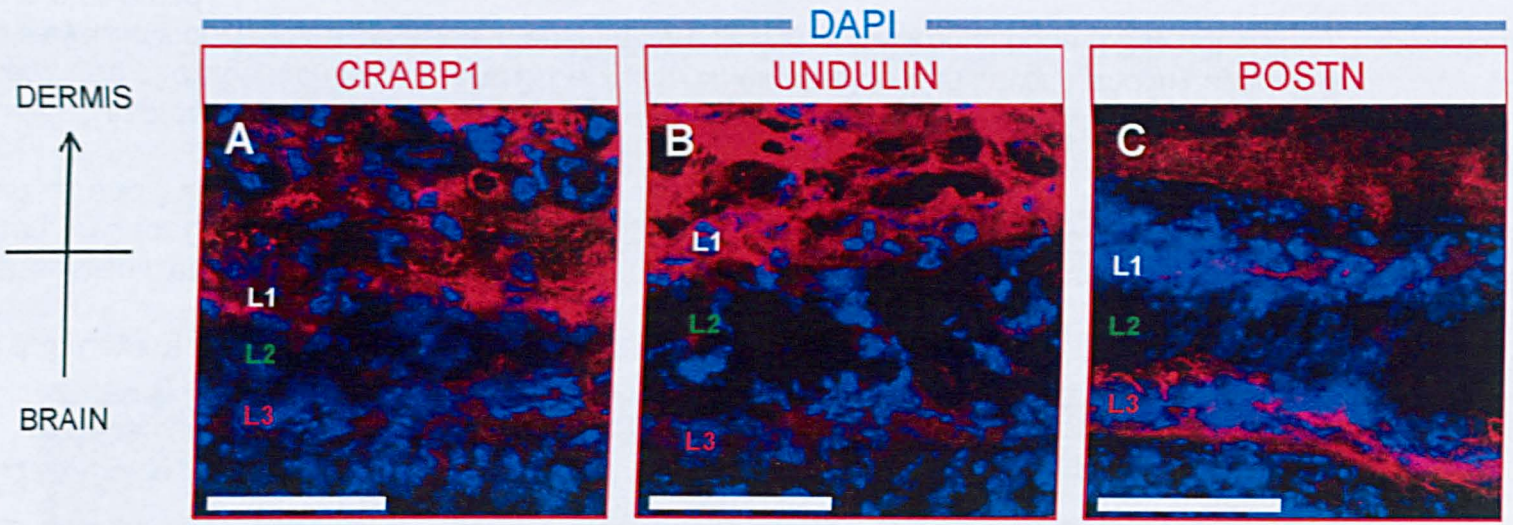

Figure 1.4: Layers 1 and 3 are periosteum/perichondrium-like tissues

Sagittal sections through the frontal bone at embryonic day E18; *Wnt*1-Cre$^{+/-}$ x Rosa26LacZ$^{-/-}$ specimen. IHC for CRABP1 (red, **A**), Undulin (red, **B**) and Periostin (red, **C**); nuclear counterstain DAPI (blue). Layers 1, 2, and 3 are indicated as **L1**, **L2**, and **L3**, respectively.

A, B. Layer 1 and the dermis strongly expresses markers associated with the fibroblastic layer of the periostium/perichondrium (CRABP1 in **A**; Undulin in **B**). Layer 3 is weakly positive for both markers. **C.** Periostin, is strongly expressed by Layer 3, weakly expressed in Layer 1, and also present in the dermis.

Scale bar indicates 50μm.

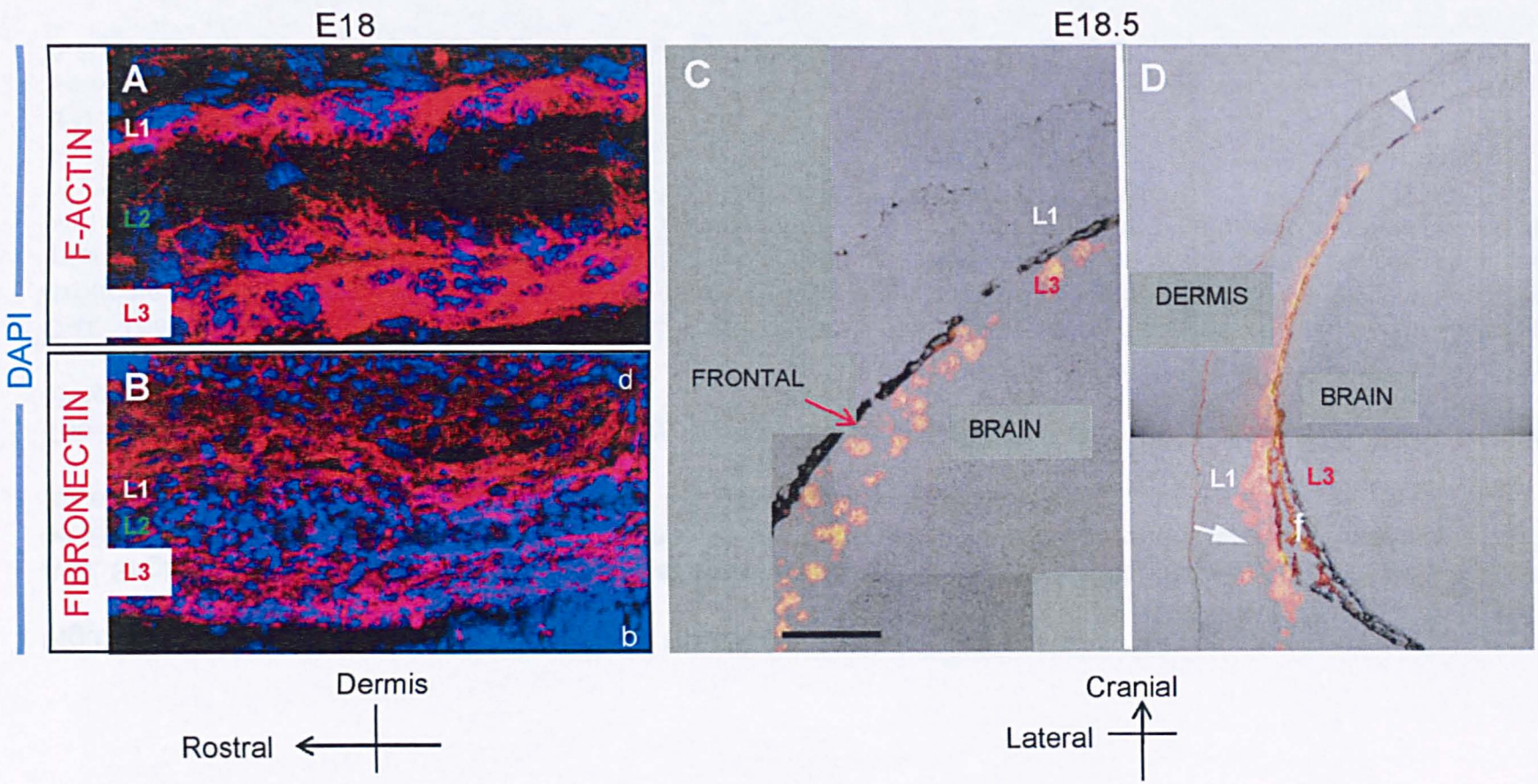
Wild-Type
E18
E18.5
DAPI
F-ACTIN
FIBRONECTIN
A
B
C
D
L1
L2
L3
d
b
FRONTAL
BRAIN
DERMIS
Dermis
Rostral
Cranial
Lateral

Figure 1.5: Cells of Layers 1 and 3 have high mobility potential

A-B. Sagittal sections through the frontal bone at embryonic day E18 after conception (positive vaginal plug is taken as E0); wild-type specimen. IHC for F-Actin (red, **A**) and Fibronectin (red, **B**) specimen; nuclear counterstain DAPI (blue) (**A-B**). Layers 1, 2, and 3 are indicated as **L1**, **L2**, and **L3**, respectively.

The cells of Layers 1 and 3 both ubiquitously express markers associated with sheet mobility, F-Actin (**A**) and Fibronectin (**B**).

C-D. The possibility that cells from L1 and L3 are capable of lateral motility supports results of DiI labelling experiments performed by Yoshida *et. al.* (**C-D**, coronal section from animals 120 hours after DiI injection) where cells in areas corresponding to L1 and L3 exhibit extensive spreading. The calcified area of the frontal bone is indicated with arrow in **C**; the injection site of **D** indicated with arrow and cells have migrated into the frontal bone and to the tip of the head, indicated with a white arrowhead. Modified from Yoshida *et. al.* 2008, Figure 6.

d Dermis, **b** Brain

A-B Scale bar indicates 50μm. **C** Scale bar indicates 100μm.

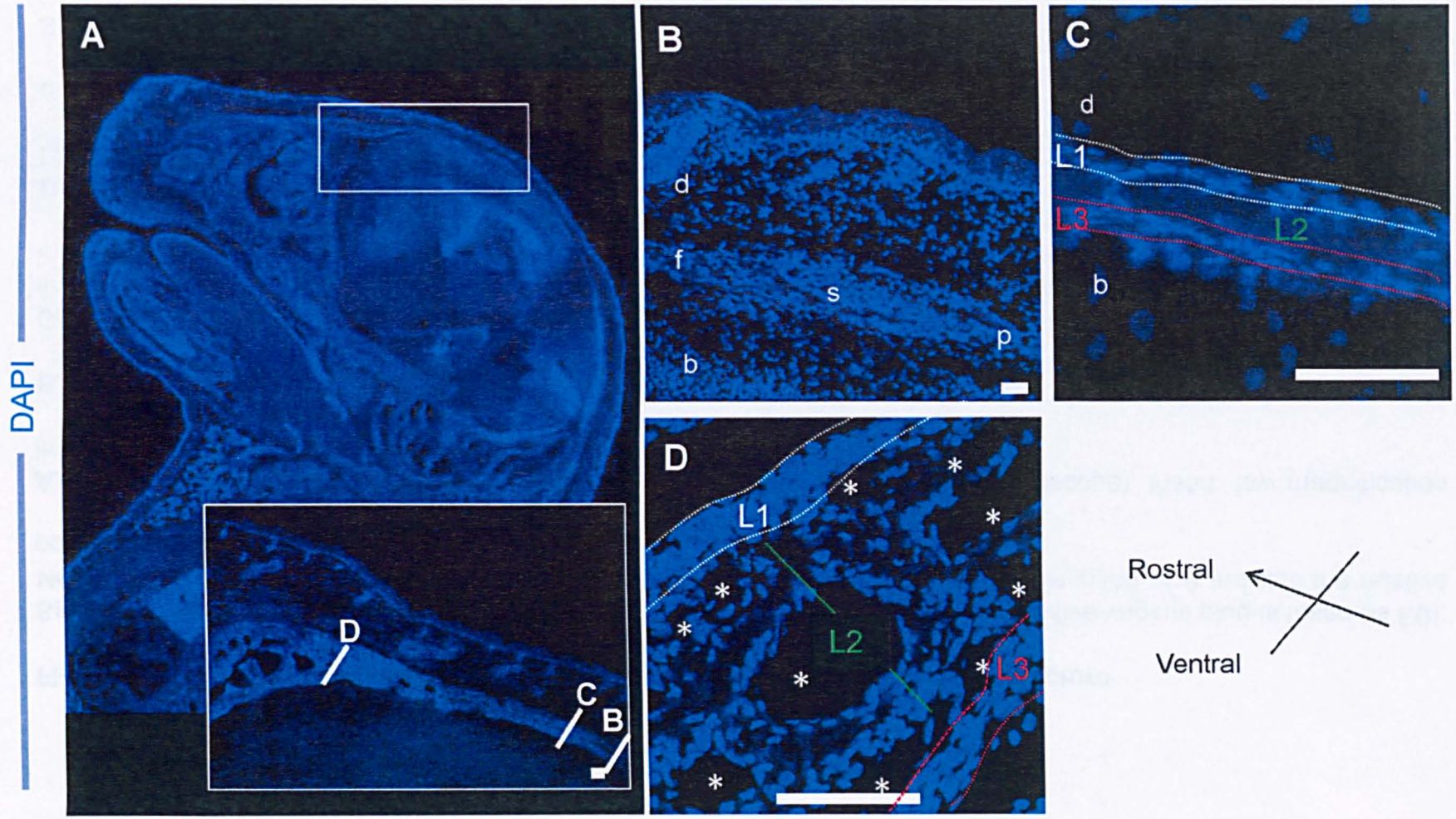
DAPI
A
D
C
B
B
d
f
s
p
b
C
d
L1
L3
L2
b
D
L1
L2
L3
Rostral
Ventral

Figure 1.6: The murine frontal bone at embryonic day E18, a tri-layered architecture

Sagittal section through the frontal bone at embryonic day E18 after conception (positive vaginal plug is taken as E0); *Wnt*1-Cre$^{+/-}$ x Rosa26LacZ$^{+/-}$ specimen. Nuclear stain (DAPI) in blue. Section lines in insert of **A** indicate the relative position of **B-D**. Layers 1, 2, and 3 are indicated as **L1**, **L2**, and **L3**, respectively.

A. Anatomical overview of the cranial region (image obtained on an Aperio microscope); insert: low magnification image of the frontal bone from the coronal suture to the nasal bone.

B. Magnification the coronal suture.

C. The most immature frontal bone, adjacent to the coronal suture. The cells of Layers 1 (area between white dotted lines) and 3 (area between red dotted lines) have physically separated and acquired a thin, flat morphology. The intervening space between the layers, which is initially very cell sparse, is termed Layer 2.

D. At a mature area of the frontal bone, the cancellous, trabeculated core of L2 remains sandwiched between L1 and L3, which are contiguous along the bone's length. Blood vessels are indicated (*).

d Dermis, **b** Brain, **s** Suture, **f** Frontal, **p** Parietal

Scale bar indicates 50µm.

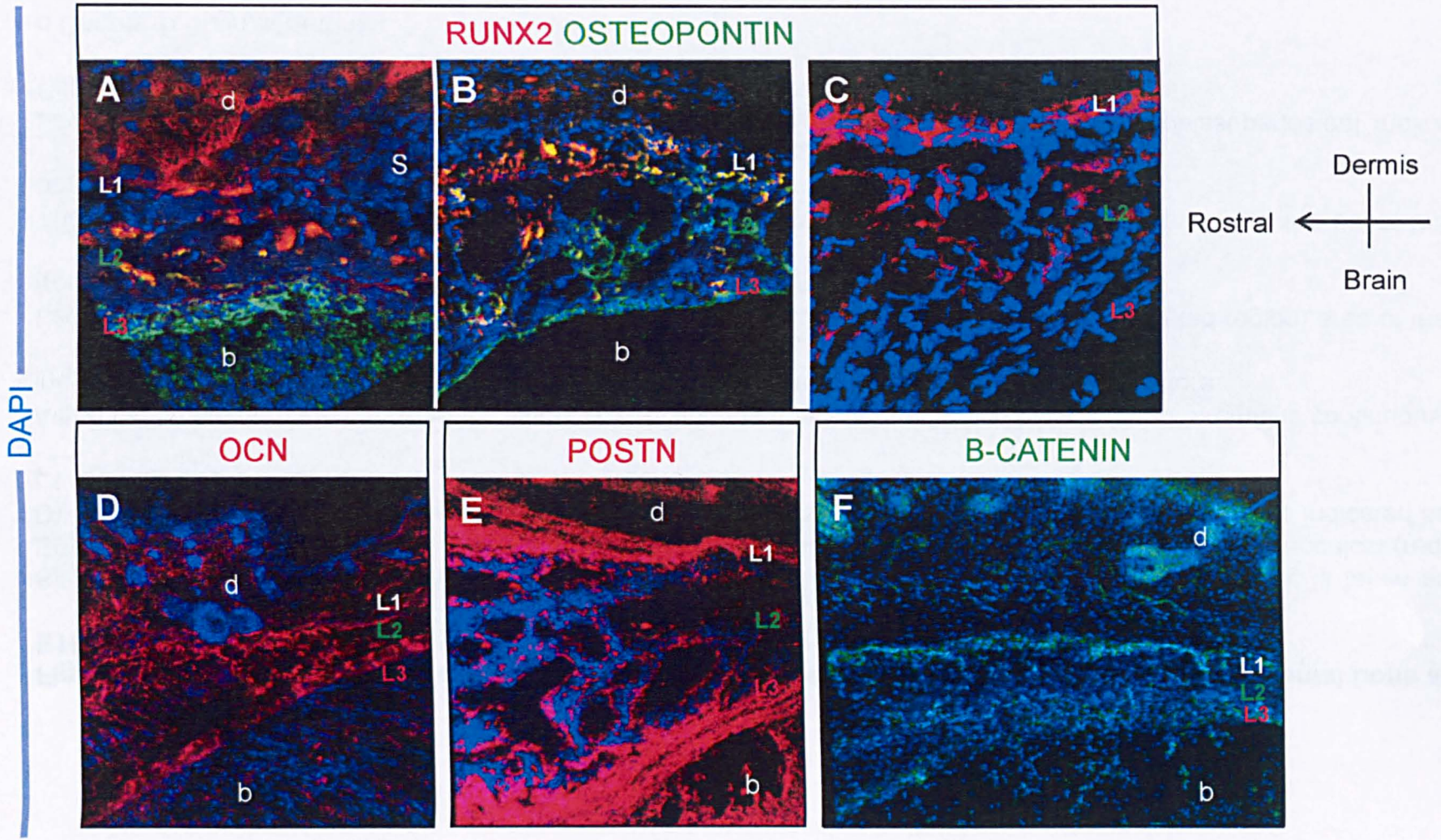
RUNX2 OSTEOPONTIN
A
d
S
L1
L2
L3
b
B
d
L1
L2
L3
b
C
L1
L2
L3
Dermis
Rostral
Brain
DAPI
OCN
D
d
L1
L2
L3
b
POSTN
E
d
L1
L2
L3
b
B-CATENIN
F
d
L1
L2
L3
b

***Figure 1.7*: Expression of markers in Layer 1 and 3 persist along the ventro-dorsal axis of the frontal bone at E18**

Sagittal sections through the frontal bone at embryonic day E18 after conception (positive vaginal plug is taken as E0); *Wnt*1-Cre$^{+/-}$ x Rosa26LacZ$^{+/-}$ specimen. IHC for Runx2 (red, **A-C**), Osteopontin (green, **A-B**), Osteocalcin (red, **D**), Periostin (red, **E**), and β-Catenin (green, **F**); nuclear counterstain DAPI (blue). Layers 1, 2, and 3 are indicated as **L1**, **L2**, and **L3**, respectively.

Along the length of the ventro-dorsal axis the expression of molecular markers in Layers 1 and 3 remains continuous, indicating expression within these layers, observed in the immature bone, is not a transient feature.

Layer 1 expresses Runx2 near the coronal suture (**A**) and at the most mature (highly trabeculated region) area of the frontal bone (**B**); this contrasts Layer 3, which expresses Osteopontin.

The expression domain of Osteocalin in a mature region of the frontal bone extends from Layer 1 to the Layer 2/3 border (**D**).

Layers 1 and 3 express the osteoblast marker β-Catenin (**F**) and the pre-osteoblast/osteoblast/periosteal maker Periostin (**E**).

d Dermis, **b** Brain, **s** Suture

Scale bar indicates 50μm.

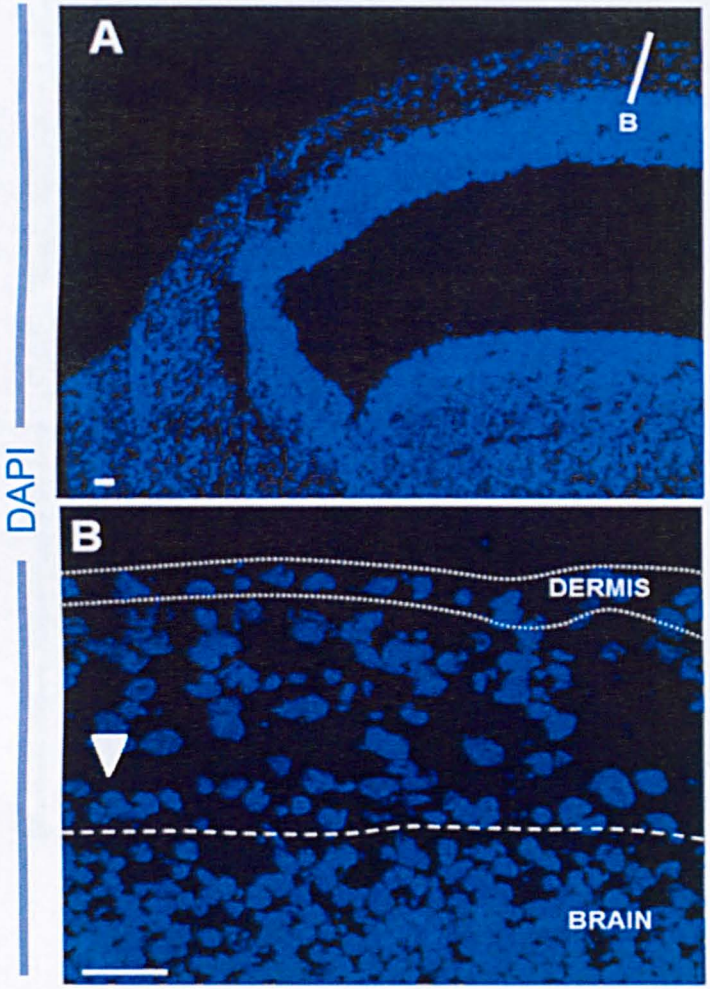

Figure 1.8: The murine frontal bone primordium at embryonic day E13

Sagittal section through the anlagen to the frontal bone at the condensed mesenchyme stage, embryonic day E13 after conception (positive vaginal plug is taken as E0); wild-type specimen. Nuclear stain (DAPI) in blue. Section line in **A** indicates the relative position of **B**.

A. Anatomical overview of the forebrain encased in the condensing mesenchyme at a low magnification.

B. Magnification of the condensing mesenchyme comprising the frontal bone anlage. The dermis comprises a single layer of aligned cells at the external margin of the tissue (indicated with white dotted line). The boundary of the forebrain is denoted with a dashed line and the single line of meningeal cells is indicated with an arrow. Cells within the condensation are morphologically indistinct and are largely blast-like.

Scale bar indicates 50µm.

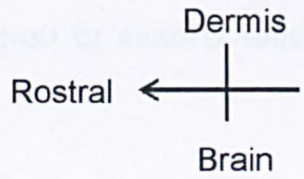

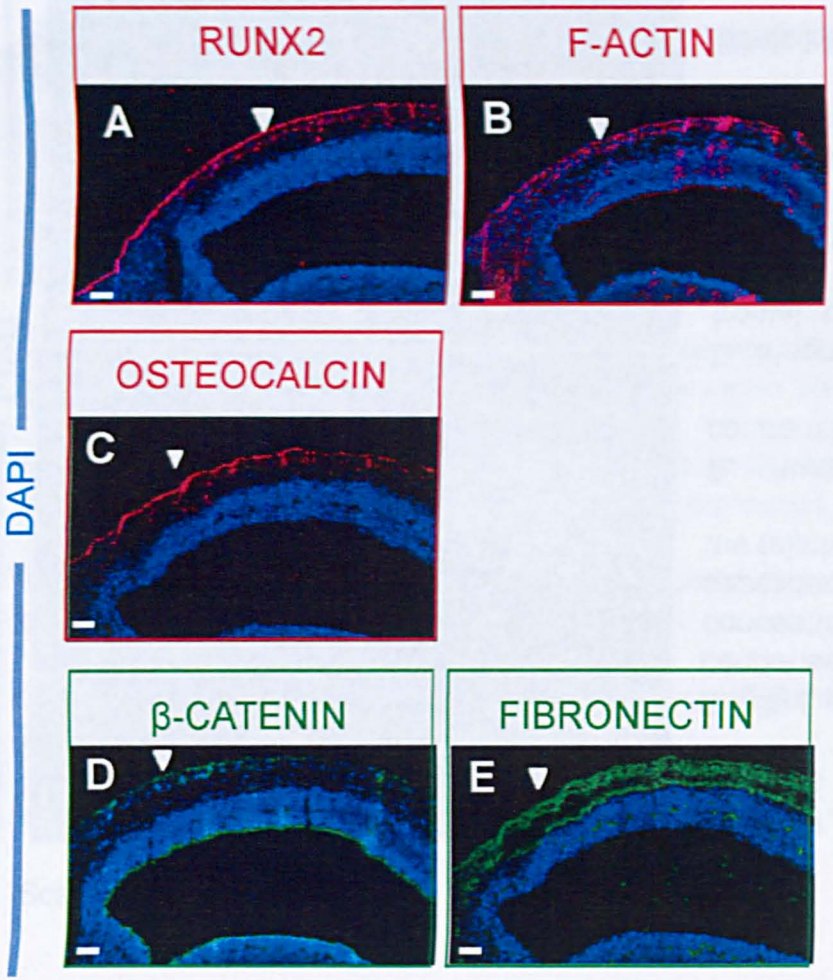

Figure 1.9: Dermal expression of several markers at embryonic day E13

Sagittal sections through the anlage of the frontal bone at the condensed mesenchyme stage, embryonic day E13 after conception; wild-type specimen. IHC for Runx2 (red, **A**), F-Actin (red, **B**), Osteocalcin (red, **C**), β-Catenin (green, **D**), Fibronectin (green, **E**); nuclear counterstain DAPI (blue).

A-E: Expression in dermis, indicated with white arrowhead. Red denotes expression in dermis and condensing mesenchyme; green denotes expression in dermis, condensing mesenchyme and meninges.

Scale bar indicates 50µm.

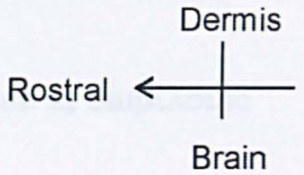

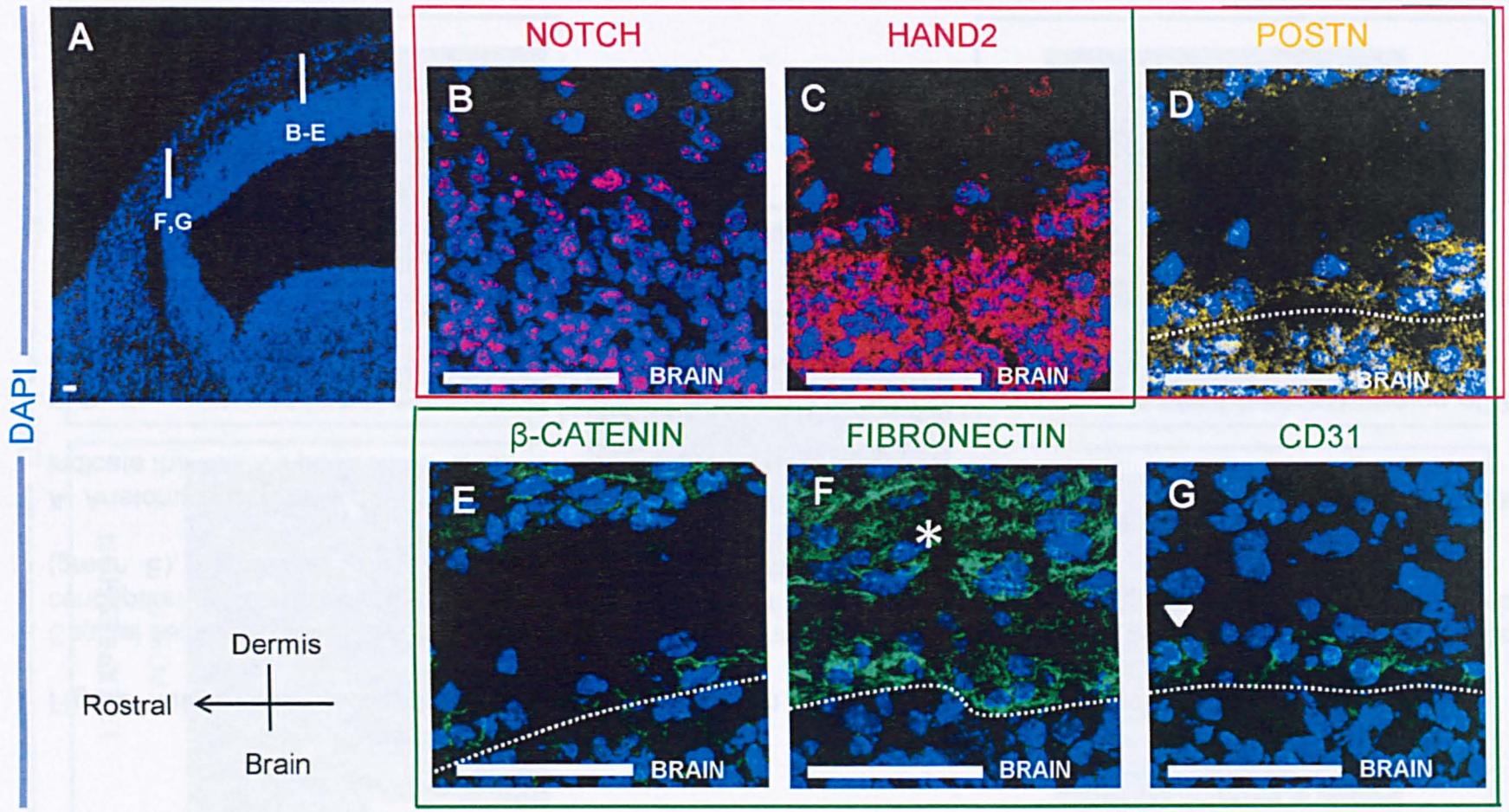
DAPI
A
B-E
F,G
NOTCH
HAND2
POSTN
B
C
D
BRAIN
BRAIN
BRAIN
β-CATENIN
FIBRONECTIN
CD31
E
F
G
*
BRAIN
BRAIN
BRAIN
Dermis
Rostral
Brain

Figure 1.10: Expression patterns of several markers in the forebrain and meninges at embryonic day E13

Sagittal sections through the forebrain and meninges at the condensed mesenchyme stage, embryonic day E13 after conception; wild-type specimen. IHC for activated Notch (red, **B**), Hand2 (red, **C**), Periostin (yellow, **D**), β-Catenin (green, **E**), Fibronectin (green, **F**), CD31 (green, **G**); nuclear counterstain DAPI (blue).

A. Anatomical overview of the forebrain encased in the condensing mesenchyme at a low magnification. Section lines indicate the relative positions of **B-G**.

B-G: Expression of Notch (**B**), Hand2 (**C**) and Periostin (**D**) in the developing forebrain (red box); expression of β-Catenin (**E**), Fibronectin (**F**) and CD31 (**G**) in early meningeal layer (green box).

The extent of the forebrain is indicated with a dotted line. In **F** the dense expression of Fibronectin in the condensing mesenchyme is indicated (*).

Scale bar indicates 50μm.

β-CATENIN HAND2
POSTN HAND2
A+B
B+C
L1 + L3 EXPRESSION
B
HAND2
A
C
β-CATENIN
POSTN
L1, L3 EXPRESSION
L3 EXPRESSION
DAPI

Figure 1.11: The frontal bone primordium is a bi-layered system at embryonic day E13

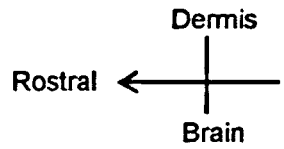

Sagittal sections through the frontal bone primordium at the condensed mesenchyme stage, embryonic day E13 after conception (positive vaginal plug is taken as E0); wild-type specimen. IHC for β-Catenin (green, **A, A+B**), Hand2 (red, **B, B+C**), Periostin (green, **C, B+C**); nuclear counterstain (DAPI, blue). Images are oriented cranial to the top and ventral to the left.

A. β-Catenin is expressed in the dermis (arrowhead in **A-C, A+B, B+C**), the meninges (*) and the most anterior region of the condensed mesenchyme; contrarily Hand2 (**B**) is expressed in a thin layer of cells at the posterior margin of the mesenchyme, as well as the meninges and brain. Similarly, Periostin (**C**) is expressed in posterior mesenchyme, meninges and brain.

A+B Displays the largely non-overlaping expression domains of β-Catenin and Hand2; while **B+C** shows the overlapping expression domain of Hand2 and Periostin. The anterior region is here defined as Layer 1, while the posterior compartment is termed Layer 3. Layer 1 comprises a wider physical area (white line) than Layer 3 (red line); while Layer 3 Is a more tightly packed tissue.

Scale bar indicates 50μm.

Wnt1-Cre x R26Lacz
E13

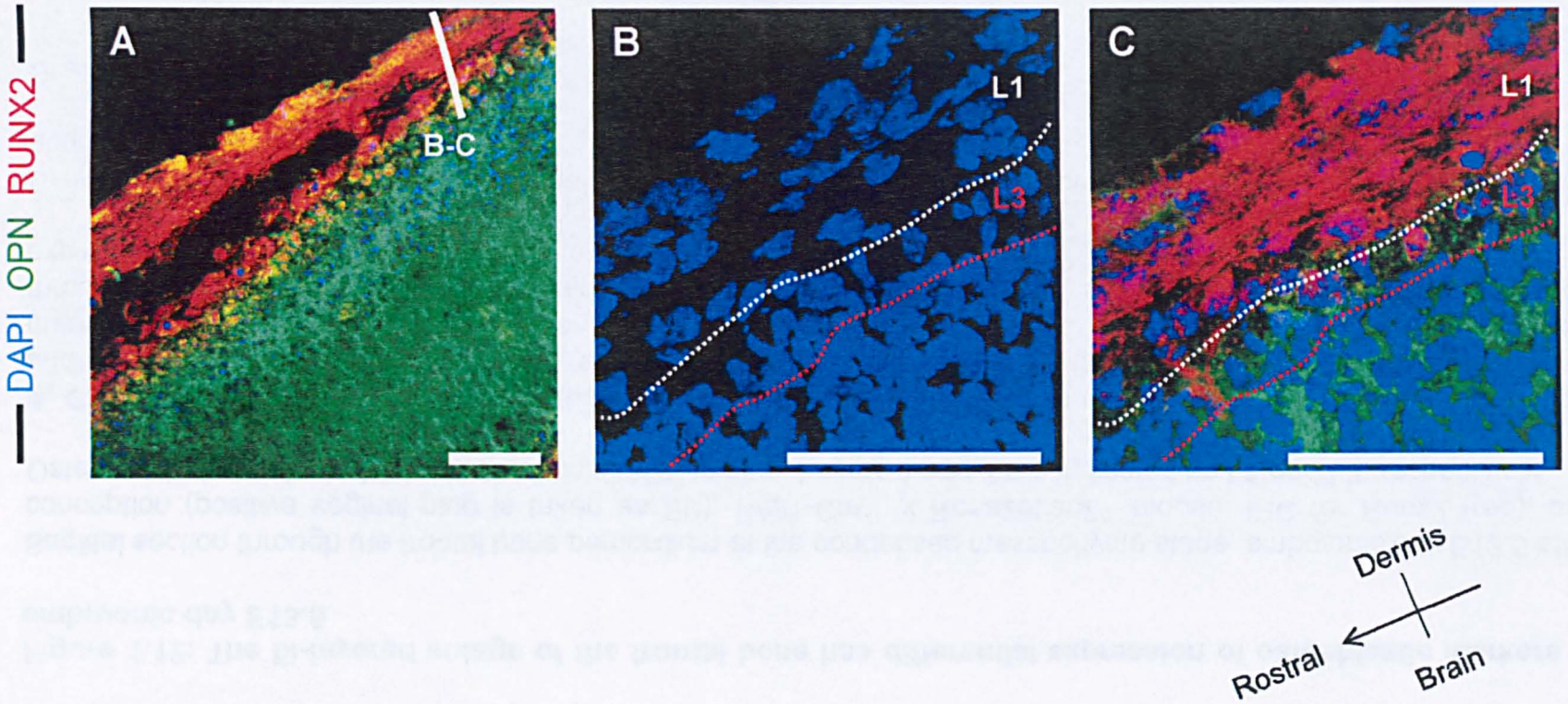

Figure 1.12: The bi-layered anlage of the frontal bone has differential expression of osteoblastic markers at embryonic day E13.5

Sagittal section through the frontal bone primordium at the condensed mesenchyme stage, embryonic day E13.5 after conception (positive vaginal plug is taken as E0); *Wnt*1-Cre$^{+/-}$ x Rosa26LacZ$^{+/-}$ mouse. IHC for Runx2 (red), and Osteopontin (green); nuclear counterstain (DAPI) in blue. Layers 1 and 3 are indicated as **L1** and **L3**, respectively.

A, C. Runx2 and Osteopontin have mutually exclusive expression patterns in the developing forbrain (OPN positive) and condensed mesenchyme (Runx2) except for the external margin of the dermis. Many of the cells of the mesenchyme have flattened and taken on a sheet-like appearance (**B**). Runx2 is expressed cytoplasmically throughout **L1**, with some cells in which expression is translocated into the nucleus. Osteopontin is strongly expressed in the brain and more weakly expressed in L3.

B. Within the area of the mesenchymal condensation comprising the precursor to Layer 1 (Runx2+) cells have acquired a slightly flattened morphology

Scale bar indicates 50μm.

1.2.1 Introduction

The vertebral head skeleton is divided into the neurocranium, the skeleton of the central nervous system, and the splachno- or viscerocranium, the skeleton of the lower face and branchial arches (Le Douarin and Kalcheim 1999). Within these divisions, the skeletal elements arise from either paraxial mesoderm or neural crest progenitors. The location of the neural crest:mesoderm boundary within the neurocranium has been heatedly disputed, with the margin of the neural crest territory alternatively hypothesized to be the frontal:parietal interface (Morriss-Kay 2001) or the parietal:occipital junction (Couly *et al.* 1993) The composition of the frontal bone has been argued to be entirely neural crest (Couly *et al.* 1993) or primarily mesodermal (Evans and Noden 2006). Notably, Couly *et al.*, who argue for an entirely neural crest-derived frontal bone, employ a standard grafting technique (quail-chick chimera) in their analysis, however, the final time-point of their study (just over mid-way through incubation) preceded definitive osteogenesis in the frontal and parietal areas examined. As such, their fate maps were generated at stage similar to E13 in murine development, as presented above, where the diploë architecture of the frontal bone is not yet established and any late invasion or contribution of mesodermal cells could not be analysed. Conversely, Evans and Noden maintain there is a large contribution of the mesoderm to calvarial tissues and their analyses occur at a slightly later time-point than Couly; however, their use of targeted injection of replication-incomplete retroviruses is not a *de rigueur* technique due to potential concerns over cross mesodermal:neural crest contamination.

Establishing a time-course of the contributions of the neural crest and mesoderm to both the generative layers (L1 and L3) and the fully formed L2 is a key component of understanding the cellular origins and histogenesis of the frontal bone, a bone for which homologies across vertebrates are well established (Rice 2008). As such, in addition to mapping the generative

architecture of dermal bone formation, the current study also aimed to resolve the widely contested issue of lineage origins of the frontal bone.

To examine the contributions of the neural crest and mesoderm to the frontal bone, lineage analysis was undertaken using Cre-mediated recombination: the *Wnt1* dorsal neural tube enhancer is expressed in the neural crest precursor population, and a *Wnt1*-Cre$^{+/-}$ strain of mouse will confer transgene expression to all neural crest cells and their resulting progeny, with the exception of neural crest from rhombomere 1 (Jiang *et al.* 2000; Ferguson and Graham 2004). When combined with Cre-reporter mice, carrying floxed resistance-pA cassettes, an excision event will occur and the neural crest cells can be permanently visualised. For the current study, lineage analyses were conducted using two strains of reporter mice: ROSA26LacZ$^{-/-}$ mice in which LacZ is under the control of the Rosa26 locus (Soriano 1999); and XZ-DR$^{-/-}$ mice with GFP under the control of the human Ubiquitin C minimal promoter (hUbC), shown to drive strong expression in mice (Zhang and Koentges unpublished ; Schorpp *et al.* 1996; Lois *et al.* 2002).

1.2.2 Results

From the earliest time-point analysed, E13, etiologically Layer 1 is neural crest, while Layer 3 is of mixed neural crest and mesodermal origins; the neural crest contributions to L3 are discernibly more minimal than the mesodermal component to that layer (Figure 1.13). From E13 through birth, the lineage composition of the layers is undisturbed: L1 remains neural crest and L3 is a mosaic of neural crest and mesoderm. The lineage heterogeneity in Layer 3 is reflected in Layer 2, which –from the most immature through mature states- contains cells of both origins (Figure 1.14). Notably, the mesodermal contributions to the neural crest do not appear to be confined to the vascular spaces (Figure 1.14).

The lineage mosaicism of the frontal bone was utilised to explore how L2 matures, as cells within L2 could derive from adjacent layers (1 and 3) and/or via endogenous cell division within L2. Within the most immature L2 the

sparse cells populating this intermediary layer carry the molecular signatures of either Layer 1 or 3 and have a rounded, blast-like morphology (Figure 1.15). The implication that these cells entered Layer 2 via direct deposition of cells from a generative layer would indicate an appositional mechanism of L2 maturation. A traditional model of appositional growth, developed for mesodermal long bones, would imply that cells percolate from a generative surface or surfaces directly into L2 without any constrained entry points as each mother cell within the respective layer would yield a daughter cell delving into the underlying matrix. This delamination of cells would lead to a columnar organisation of the expanding bone (Figure 1.16), akin to basic columnar organisation of progenitor cells migrating radially from a ventricular generative surface in the developing central nervous system (Price *et al.* 1987; Rakic 1988; Walsh and Cepko 1992; Walsh and Cepko 1993; Mountcastle 1997). This arrangement would yield bone matrix deposition in parallel sheets.

Cells within Layer 2 could alternatively (or in conjunction with apposition) experience clonal expansion; this mechanism of increasing L2 complexity would lead to the expectation of clonal nests or islands of cells derived from either mesodermal or crest progenitors, with little mixing between them within L2 (Figure 1.16). Furthermore, clonal expansion should lead to extensive amounts of discernable cells undergoing division within L2.

Contrasting with both these models, in an ontogenetic analysis, there does not appear to be homogenous deposition of cells from surfaces of either Layers 1 or 3, nor evidence of clonal expansion within L2. Instead, from E16 (the earliest time-point with a discernable L2), at specific points across the length of the developing bone, cells from L1 and L3 appear to invade the L2 space. Three-dimensional reconstructions of the developing bone show strings of neural crest cells (labelled) extending from L1 into L2 and touching the surface of L3, thus neural crest cells from one side extend across the different layers (Figure 1.17). The same is evident for mesodermal cell (non-labelled) from L3. Unusually, within this bee-line the cells in L2 continue to express the unique combination of markers of either Layer 1 or Layer 3

(Figure 1.18): i.e. Runx2+ cells from Layer 1 connect to Run2+ cells in Layer 2 and OPN+ cells in Layer 3 connect to OPN+ cells in Layer 2.

The lateral connections between L1 and L3 (across L2) are accomplished in the immature bone by only a single or few cells (Figures 1.17-1.19): cells from L1 enter L2 and form a bridge between the laminar layers in an organisation that appears akin to a handshake; these handshakes are hitherto referred to as 'clasps'.

Within the clasps, a physical link to the generative layers (L1 or L3) is maintained via cell-cell connections (Figures 1.17-1.19). The entry of cells into the L2 system does not appear to be confined to an immature phase of bone development, as the clasps are found along the length of the dorso-ventral axis from E16 through foetal and early post-natal development to P2 (the final time-point analysed). As L2 becomes increasingly trabeculated, clasps are maintained by increasing numbers of cells forming entire sheets inside L2 of the maturing bone (Figures 1.19-1.20). As the frontal bone increases in complexity, the lateral connections between layers also experience horizontal elaborations, however they are not engulfed directly by matrix (for details on aspects of biomineralisation refer to Chapter 3) (Figure 1.20). In this way, cells of both neural crest and mesodermal origins (both carrying markers of osteoblast lineages) intermingle and contemporaneously contribute to L2 development.

1.2.3 Conclusion

The molecular and morphogenic properties of L1 and L3 indicate their potential as generative layers of the frontal bone; the intervening space –L2- matures with bone development, increasing in cell density and thickness with time and carrying the osteoid and mineralised matrix (Described in Chapter 3). The mechanism by which L2 maturation occurs is at the heart of how dermal bones form. Evidence from the analysis of *Wnt*1-Cre$^{+/-}$ mice does not support either an appositional or clonal expansion model of L2 maturation, but instead favours the bidirectional intercalation of cells from L1 and L3

(Figure 1.21). The introduction of cells from the generative layers is highly constrained and accomplished via a 'threading in' mechanism whereby clasps act as conveyor belts, delivering new cells to L2. Continuous sheets of cells are formed within L2, while cells maintain the molecular profiles of the generative layer from which they originate. Although *de novo* expression of the markers from L1 or L3 within L2 cannot be ruled out, the traditional 'percolation' model of appositional growth from an internal surface is excluded on the basis that no columns of mesodermal cells (from L3) or neural crest cells (from L1 or L3) are observed. Instead, single cells appear to enter and expand L2 and at no point does either of the generative layers involute as whole entities, which would break the continuity of L1 and L3. Furthermore, the intriguing expression of markers of cellular mobility (Fibronectin, F-Actin, Periostin) and the periosteum (which are attractant to osteoblastic cells) in L1 and L3 is resolved when the migratory behaviour of L1 and L3 cells is understood. If L1 and L3 act as generative layers, cells within them must be capable of both integrating into L2 and performing the role of osteoblasts. The means by which the points of cellular entry into L2 are initiated and maintained are examined in Section 1.3, below.

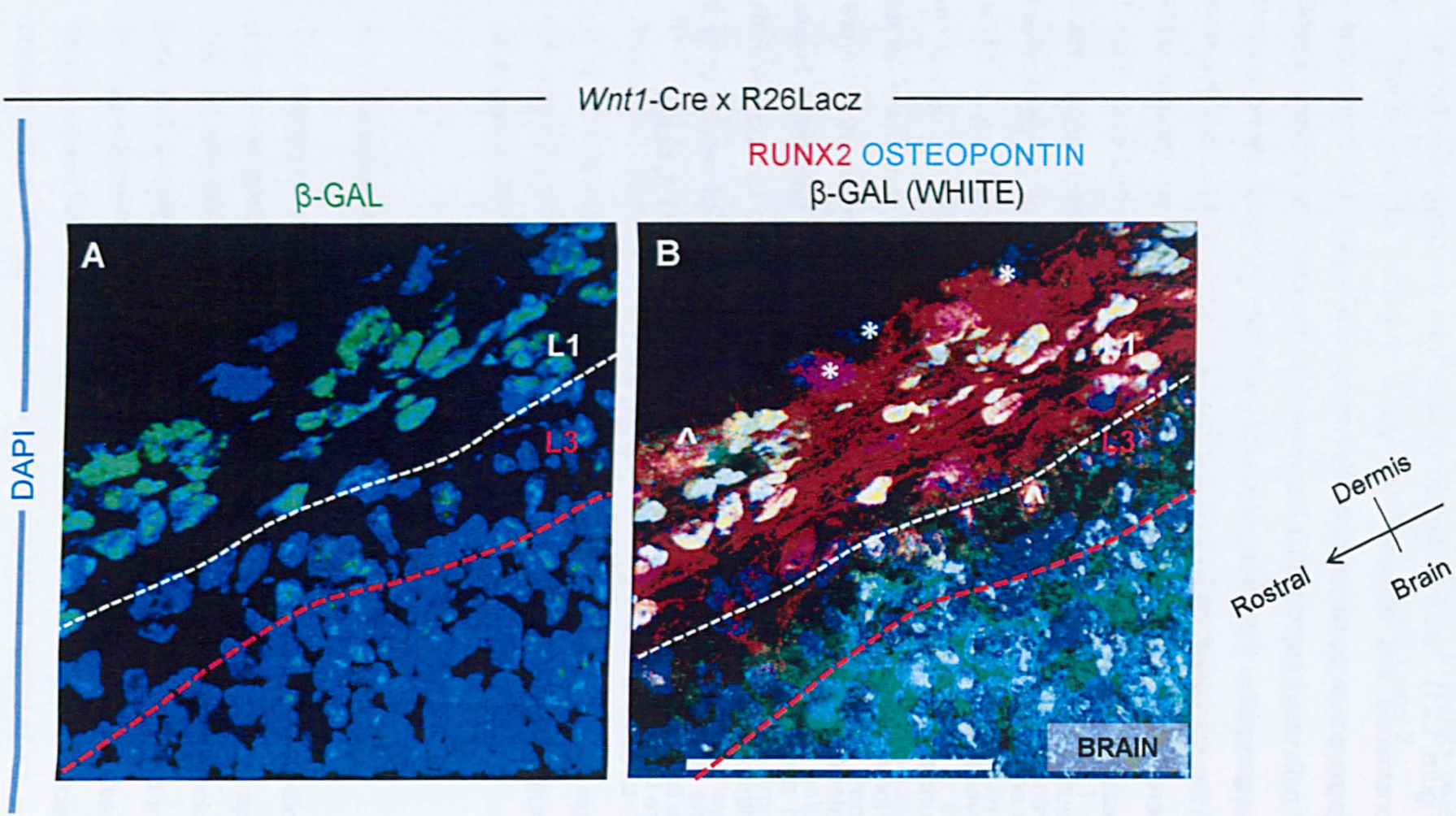
Wnt1-Cre x R26Lacz
RUNX2 OSTEOPONTIN
β-GAL
β-GAL (WHITE)
DAPI
A
B
L1
L3
BRAIN
Dermis
Rostral
Brain

Figure 1.13: The bi-layered anlage to the frontal bone is of mosaic lineage at embryonic day E13.5

Sagittal section through the frontal bone primordium at the condensed mesenchyme stage, embryonic day E13.5 after conception (positive vaginal plug is taken as E0); *Wnt*1-Cre$^{+/-}$ x Rosa26LacZ$^{-/-}$ mouse. IHC for β-Galactosidase indicating the neural crest cells (green, **A**; white, **B**), Runx2 (red, **B**), and Osteopontin (light blue, **B**); nuclear counterstain DAPI (blue). Layers 1 and 3 are indicated as **L1** and **L3**, respectively.

A. L1 (the region corresponding to Runx2 expressing cells in **B**) contains neural crest cells; at the external margin of the condensed mesenchyme, as well as within L3, cells of mesodermal origin are noted (*, in dermis), as indicated by a lack of β-Galactosidase activity.

B. Runx2 and Osteopontin expression domains are almost entirely mutually exclusive with a few noted exceptions (^). The forebrain is of neural crest origin and morphologically distinct from L3, although both express OPN. The extent of L3 is indicated with dashed lines.

Scale bar indicates 50μm.

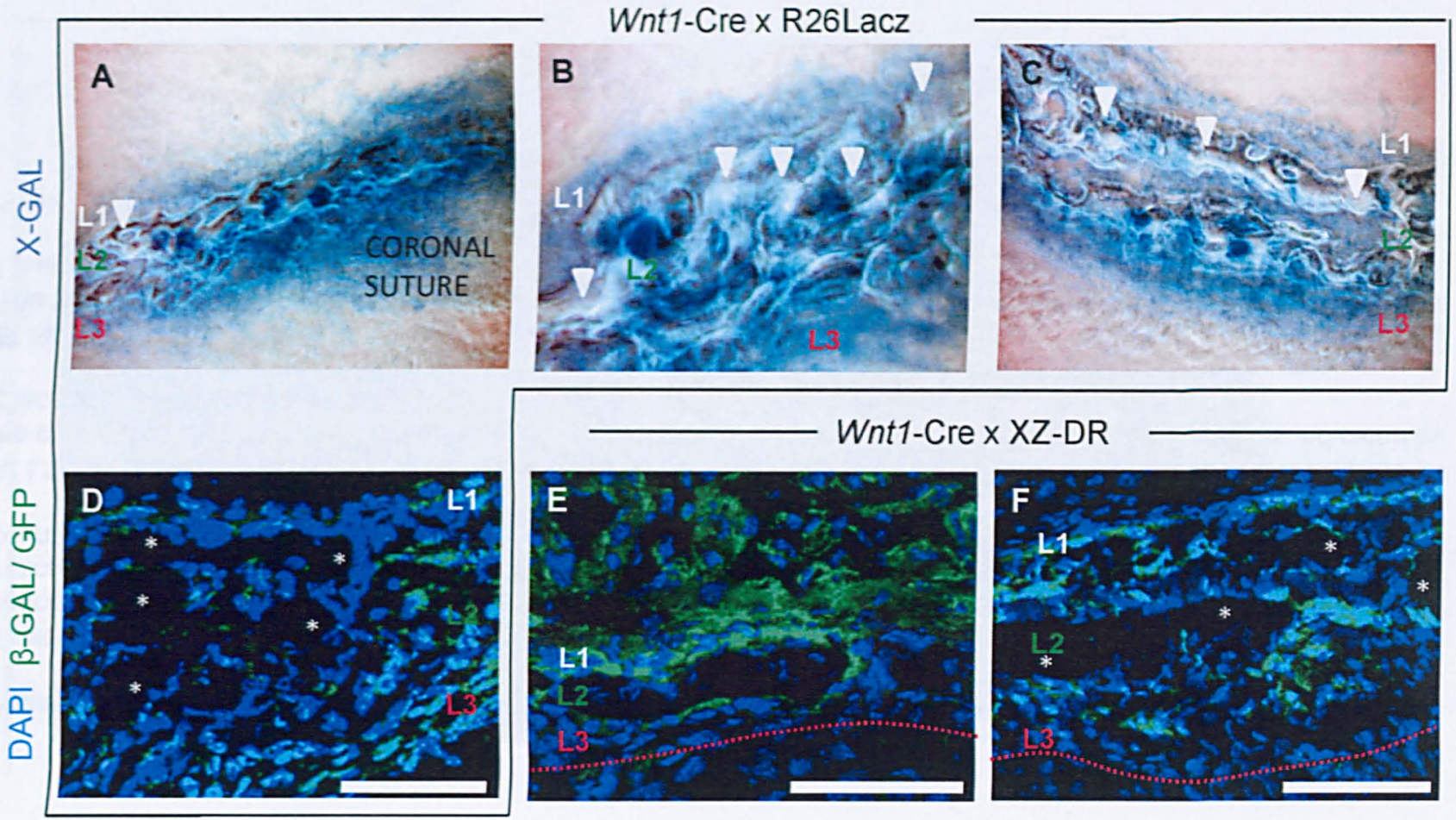
Wnt1-Cre x R26Lacz
X-GAL
A
B
C
L1
L2
L3
CORONAL
SUTURE
Wnt1-Cre x XZ-DR
DAPI β-GAL/ GFP
D
E
F

Figure 1.14: The frontal bone is of dual neural crest and mesodermal origin

Sagittal sections through the frontal bone at embryonic day E18 after conception (positive vaginal plug is taken as E0); *Wnt*1-Cre$^{+/-}$ x Rosa26LacZ$^{-/-}$ specimen **A-D**, *Wnt1*-Cre$^{+/-}$ x XZ-DR$^{-/-}$ specimen **E-F**. Layers 1, 2, and 3 are indicated as **L1, L2** and **L3**, respectively.

X-gal stain (**A-C**) and IHC (**D-F**) for β-Galactosidase showing neural crest cells in blue **A-C** and green **D-F**. Nuclear counterstain DAPI (blue) in **D-F**.

A-C. X-Gal stain of progressively more mature regions of the frontal bone. L1 and L3 regions sandwich the mineralised core of L2. **A**. Off the coronal suture, areas of non-reactivity, indicating tissues of mesodermal origin or those from rhombomere 1, are noted (white arrowhead) within L2.

B-C. In mature areas of the frontal bone areas without X-Gal labelling are not confined to blood vessel lining as they are within the bone matrix.

D-F. IHC of β-Gal (**D**) and GFP (**E-F**). L1 contains neural crest cells, while L2 and L3 have mosaic expression of the neural crest marker.

Scale bar indicates 50μm.

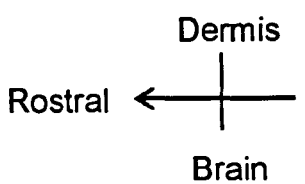

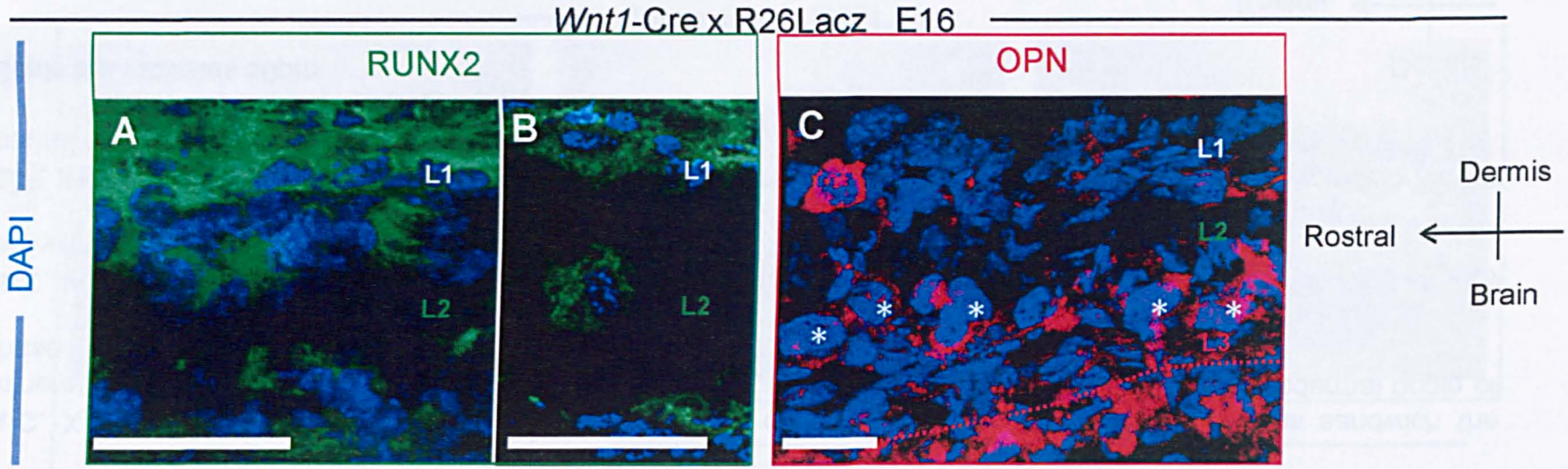

Figure 1.15: L2 is initially populated by blast-like cells expressing Runx2 or OPN

Sagittal sections through the most immature frontal bone displaying a diploe architecture at embryonic day E16 after conception (positive vaginal plug is taken as E0); *Wnt*1-Cre$^{+/-}$ x Rosa26LacZ$^{-/-}$ mouse. IHC for Runx2 (green, **A-B**), and Osteopontin (red, **C**); nuclear counterstain DAPI (blue). Layers 1, 2, and 3 are indicated as **L1, L2** and **L3**, respectively.

A-B. The initial cells on the L1-side of L2 are large and blast-like and express Runx2; this contrasts to many cells on the L2:L3 border (**C**) that have a similar morphology (blast-like) but express OPN (*). The external boundary between L3 and the brain is indicated in **C** (red dashed line).

Scale bar indicates 50µm.

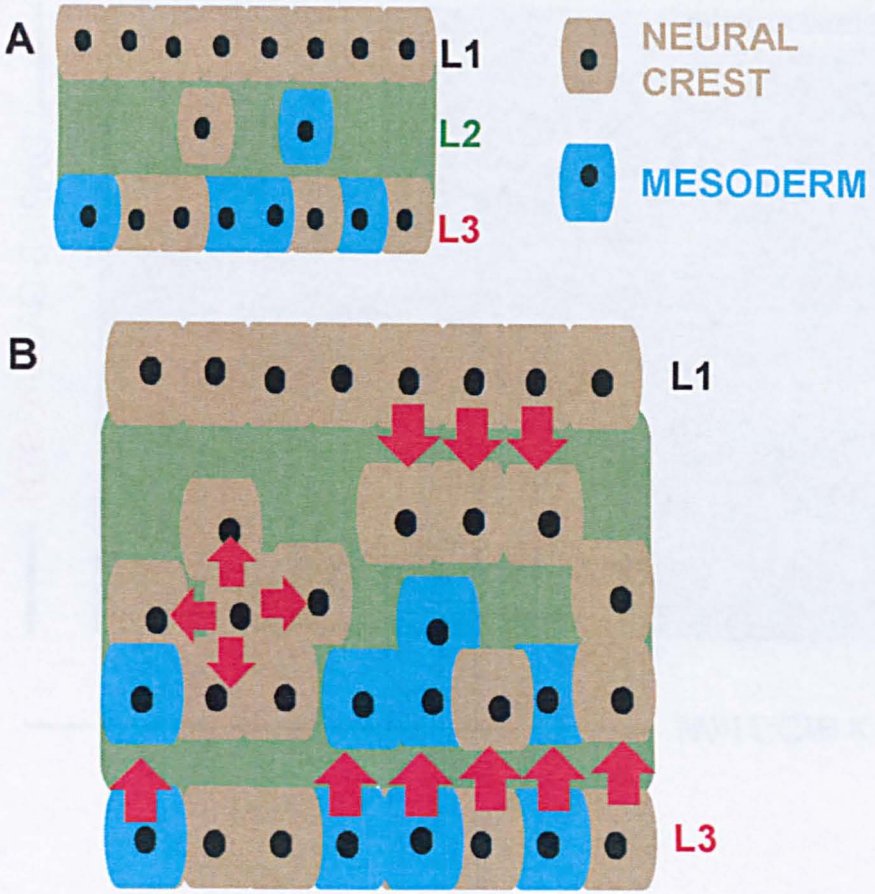

Figure 1.16: Competing models of the mechanisms for L2 growth

A. Schematic representation of an immature frontal bone at E16-18 as found in the current study. Layer 1 is entirely of neural crest origin, while L3 is a mosaic of neural crest and mesodermal cells. L2 is initially cell-sparse with cells of both lineages. In time L2 becomes more complex (not shown).

B. The appositional/clonal expansion model of L2 maturation. Cells from Layer 1 and 3 experience no lateral spread and deposit cells into L2 via direct apposition; these leads to clonal columns and a parallel-sheet organisation of L2. Cells within L2 could also divide, leading to clonal islands of cells within L2.

Wnt1-Cre x R26Lacz

DAPI β-GAL POSTN

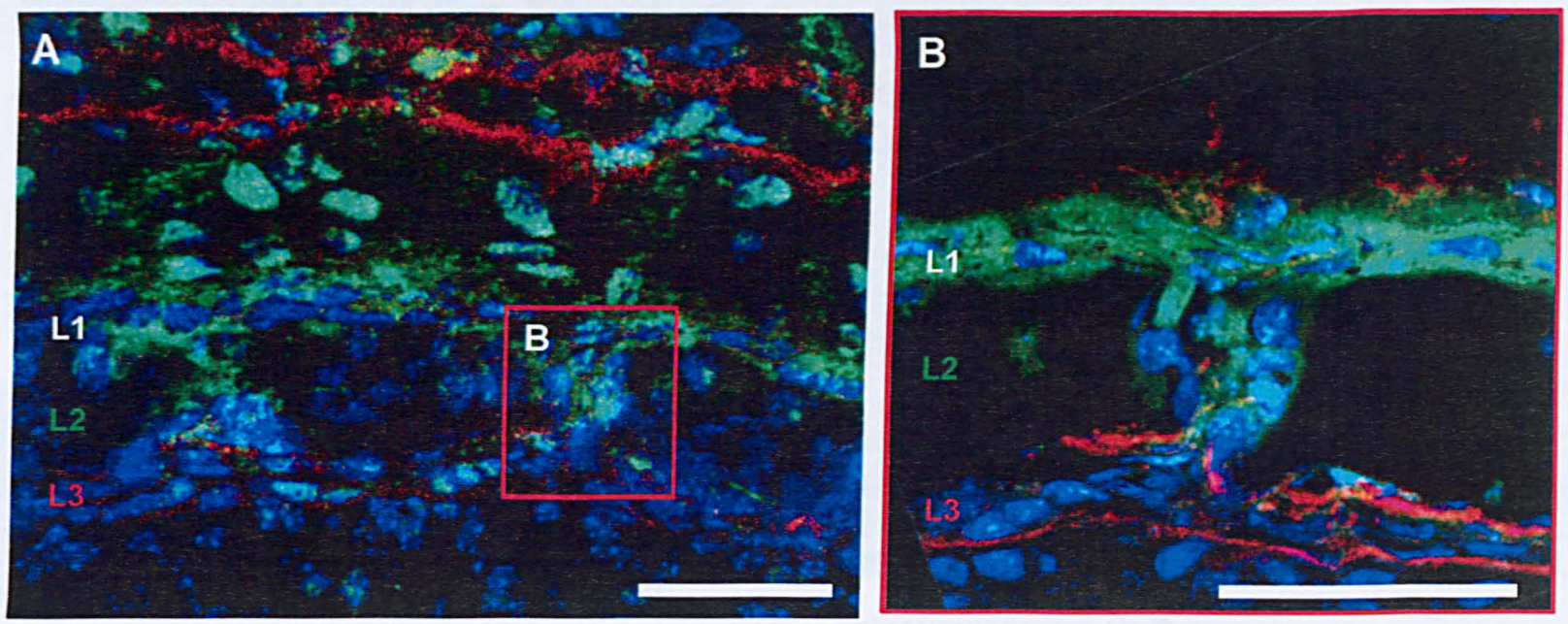

Dermis
Rostral
Brain

Figure 1.17: Evidence of bi-directional involution of cells from L1 and L3

Sagittal section through the frontal bone at embryonic day E18 after conception; *Wnt*1-Cre$^{+/-}$ x Rosa26LacZ$^{-/-}$ specimen. IHC for β-Galactosidase showing neural crest cells (green) and Periostin (red); nuclear counterstain DAPI (blue). Layers 1, 2, and 3 are indicated as **L1**, **L2**, and **L3**, respectively.

A. Cells from L1 and L3 invade L2 and form a bridge connecting the two generative layers. Red box indicates the location of **B.**

B. Optical section of the interaction between cells invading L2 from L1 and L3; this interaction is referred to as a 'clasp'. The cells within the clasp are sheet-like and maintain contact with the layer from which they originate.

Scale bar indicates 50μm.

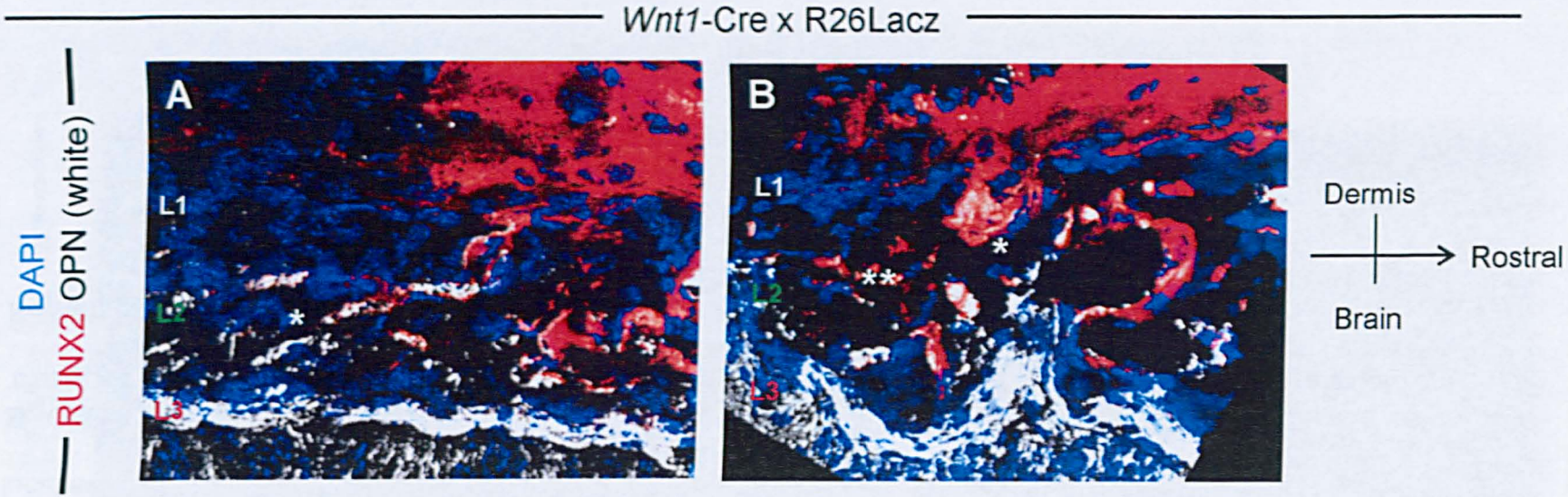

Figure 1.18: Clasp structures are formed by Runx2 and Osteopontin expressing cells

Sagittal section through the frontal bone at embryonic day E18 after conception; *Wnt*1-Cre$^{+/-}$ x Rosa26LacZ$^{-/-}$ specimen. IHC Runx2 (red) and Osteopontin (white); nuclear counterstain DAPI (blue). Layers 1, 2, and 3 are indicated as **L1**, **L2**, and **L3**, respectively.

Cells form a bee-line across L2, connecting L1 to L3; within this clasp cells are Runx2-positive, akin to Layer 1, or Osteopontin positive, akin to Layer 3. In less mature regions of the frontal bone clasps are formed by relatively few cells (* in **A**), compared to a fully trabeculated area from the same section where the clasps is maintained by significantly more cells and there appear to be horizontal extensions (**) from the predominant lateral clasp (*)

Wnt1-Cre x R26Lacz

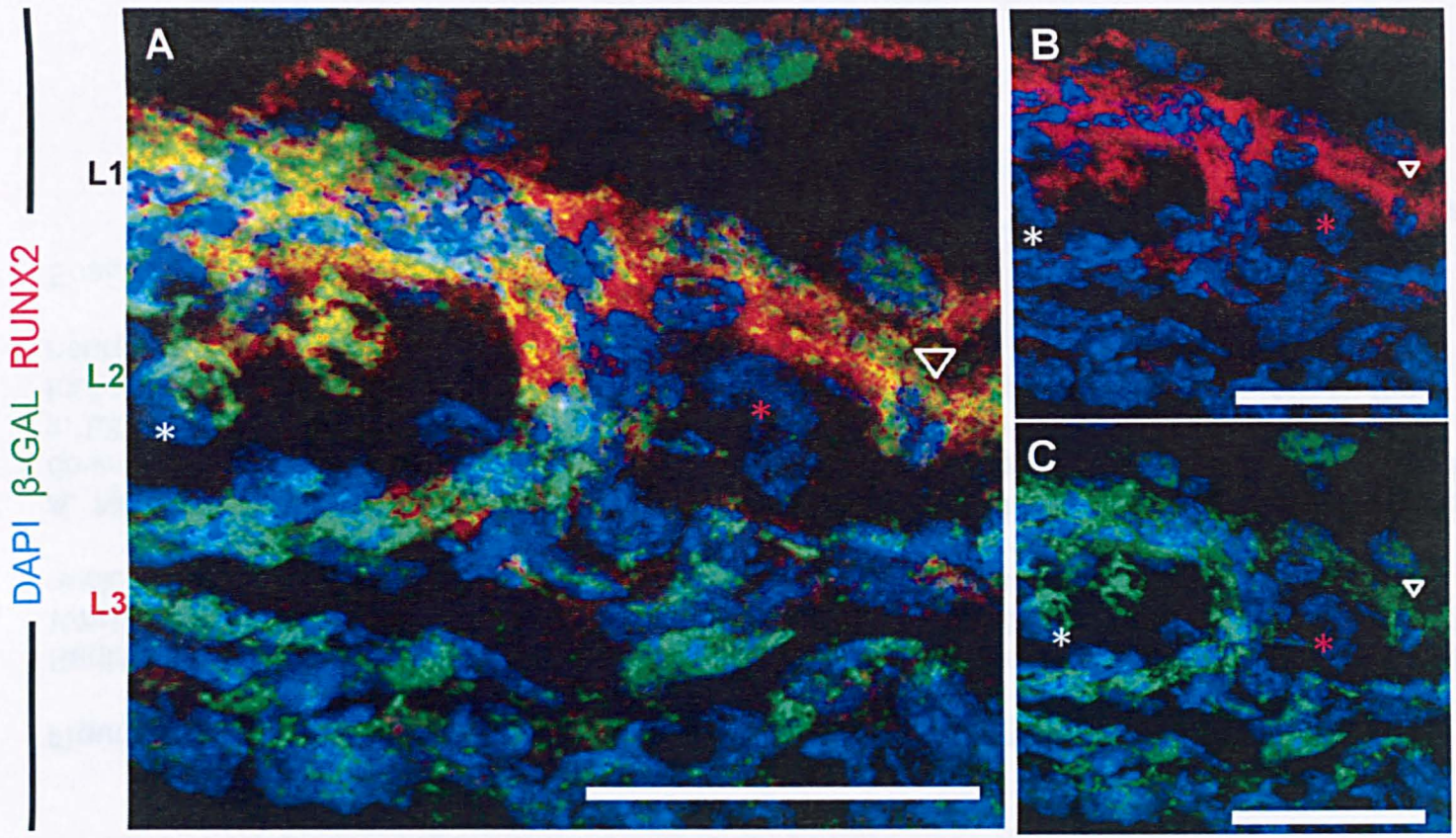

Figure 1.19: Following clasp formation L2 elaborates via continual cell involution

Sagittal section through the frontal bone at embryonic day E18 after conception (positive vaginal plug is taken as E0); *Wnt*1-Cre$^{+/-}$ x Rosa26LacZ$^{-/-}$ specimen. IHC for β-Galactosidase showing neural crest cells (green) and Runx2 (red); nuclear counterstain DAPI (blue). Layers 1, 2, and 3 are indicated as **L1**, **L2**, and **L3**, respectively.

A. Neural crest cells from L1, expressing Runx2, enter L2 and the clasp elaborates. Runx2 expression continues down the majority of the clasp (**B**) until it meets non-Runx2 expressing cells, which have lost expression or originated in L3. A nascent clasp is being formed by a cell intercalating into L2 (empty arrowhead). Large, blast-like cells are found encased in the clasp (white *) and associating with the outside of the clasp (red *); these cells are of mixed neural crest and mesodermal origin.

Scale bar indicates 50μm.

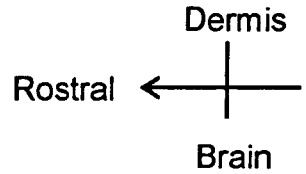

Wnt1-Cre x R26Lacz

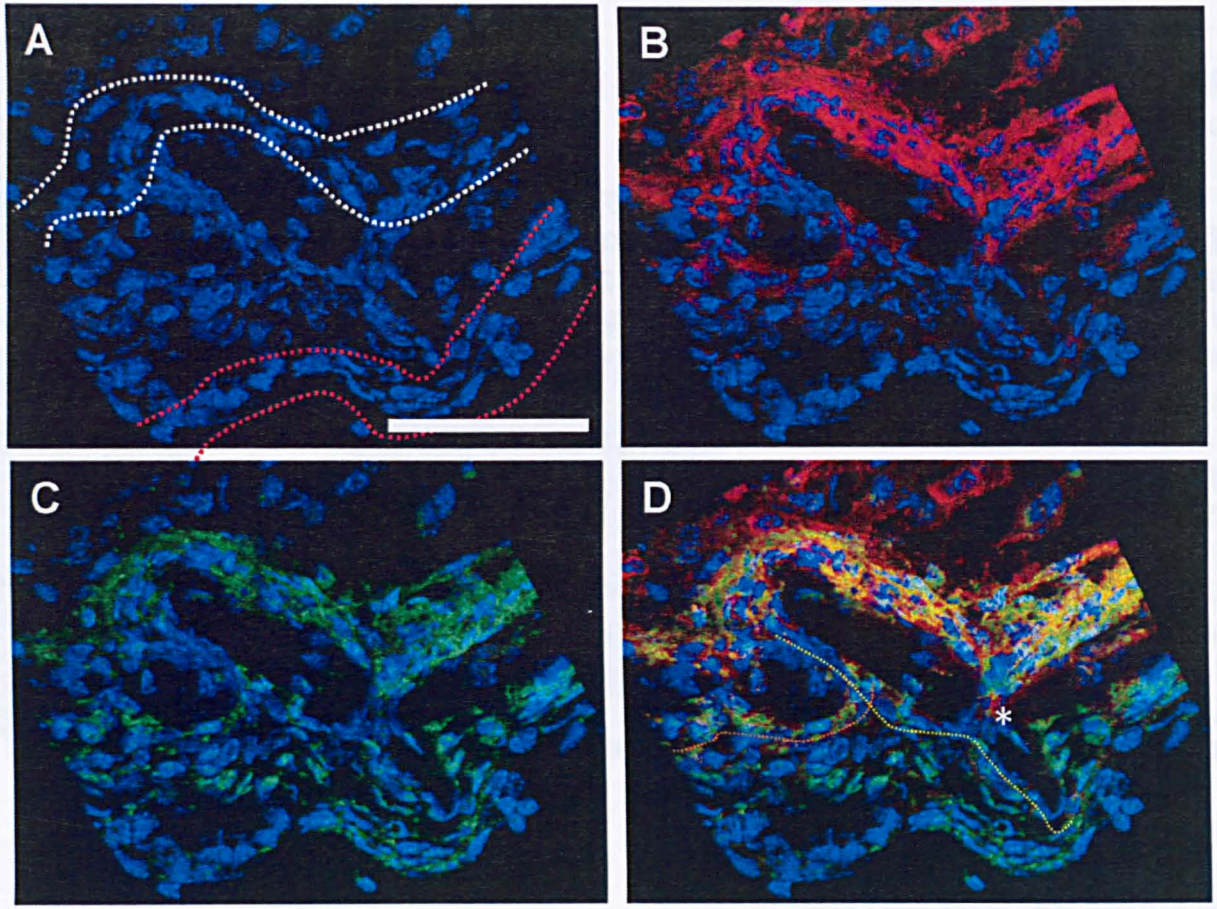

DAPI β-GAL RUNX2

Figure 1.20: In increasingly mature areas clasps experience vertical and horizontal elaborations

Sagittal section through the frontal bone at embryonic day E18 after conception (positive vaginal plug is taken as E0); *Wnt*1-Cre$^{+/-}$ x Rosa26LacZ$^{-/-}$ specimen. IHC for β-Galactosidase showing neural crest cells (green) and Runx2 (red) ; nuclear counterstain DAPI (blue). Layers 1, 2, and 3 are indicated as **L1**, **L2**, and **L3**, respectively.

A. In a semi-mature region of the frontal bone, long connections of cells forming sheets inside L2 are visible. Within these sheets cells are adjacent to other cells expressing the same marker (e.g. Runx2, **B**) and/or cells of the same etiological origin (e.g. neural crest versus mesodermal **C**).

In **D** a bee-line of cells of mesodermal origin can be see extending across the entire lateral space of L2, connecting the generative layers (line of cells indicated in yellow dashed line). This line is also bisected by a line of neural crest cells that all express Runx2 (outlined in orange dashed line) that are a horizontal elaboration of a clasp. At one point, cells of L1 (NC cells expressing Runx2) can be seen beginning to intercalate into L2 and sliding past the pre-exiting sheet of mesodermal cells (*).

Scale bar in **A** indicates 50μm.

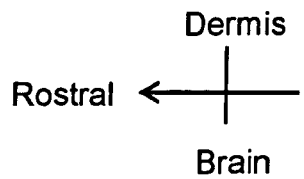

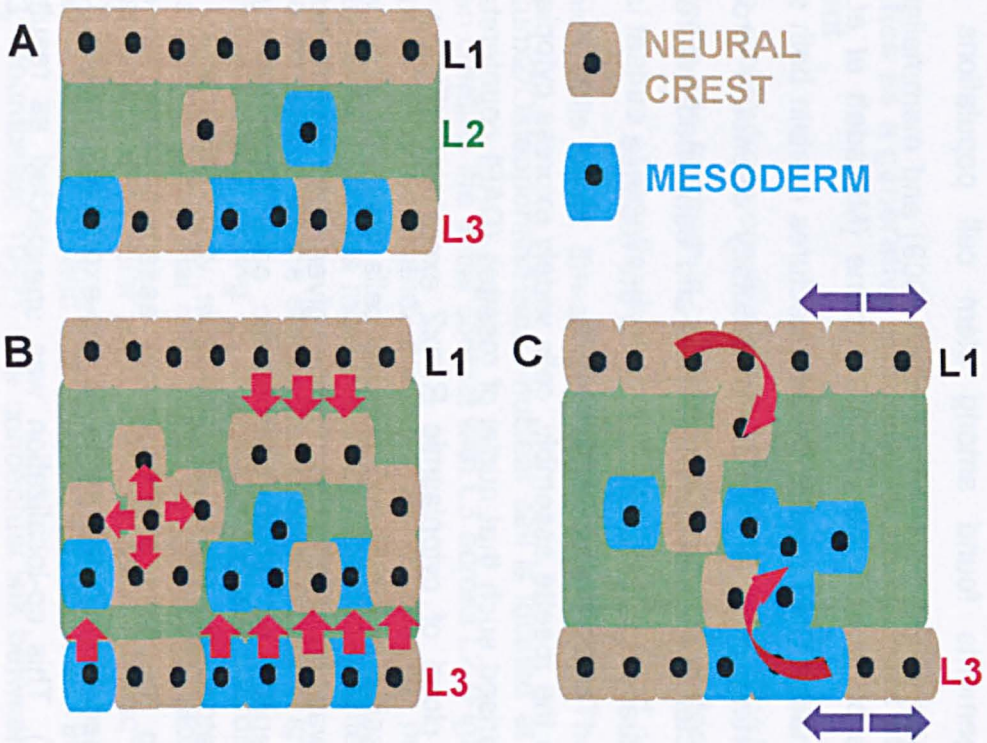

Figure 1.21: Contrasting modes of expanding L2

A. Schematic representation of an immature frontal bone at E16-18 as found in the current study. Layer 1 is entirely of neural crest origin, while L3 is a mosaic of neural crest and mesodermal cells. L2 is initially cell-sparse with cells of both lineages. In time L2 becomes more complex.

B. The appositional/clonal expansion model of L2 maturation. Cells from Layer 1 and 3 experience no lateral spread and deposit cells into L2 via direct apposition; these leads to clonal columns and a parallel-sheet organisation of L2. Cells within L2 could also divide, leading to clonal islands of cells within L2.

C. The bi-directional involution model of L2 maturation. Cells from Layers 1 and 3 spread laterally (purple arrows) and thread cells into L2 in a conveyor-belt delivery system. Cellular involution into L2 in constrained to specific notes and cells enter and form sheets on the inside of L2.

1.3 Discovery of the rosette system in dermal bone development

Having established the clasps as the point of initial contact between L1 and L3, my analysis subsequently focused on the process by which cells initiate their invasion of L2 from the generative layers. Three-dimensional reconstructions of the privileged points of cellular entry from L1 into L2 led to the discovery of a unique assembly of cells at the surface of L1. Cells around the entry point from L1 to L2 are oriented in a rosette-like architecture comprising ~6-8 flattened neural crest cells (Figure 1.22). These rosettes are observed along the length of the frontal bone at all places where cells from L2 connect to the generative layers.

1.3.1 Molecular composition of rosettes

The organisation of cells into a rosette formation is reminiscent of arrangements found among stem cell populations during neuromast formation in zebrafish (Hava *et al.* 2009) and mammalian neural stem cells on the surface of the ventricular zone (Mirzadeh *et al.* 2008). Within the mammalian CNS rosette-like architectures contain both stem cells and their supporting cells, which are molecularly distinct. I probed the molecular character of dermal bone rosettes and confirmed heterogeneity among the individual single cells contributing to the rosettes.

Within the rosette assembly, cells widely express cytoplasmic Runx2, which is polarised such that nuclei of rosettes (DAPI counterstained) appear to sit on a cloud of cytoplasmic Runx2 expression (Figure 1.22B). Notch co-expression in the Runx2-positive cells was also observed (Figure 1.22C), and was an interesting finding given that Notch activation acts as a mechanism by which osteoblastic cells have been shown to regulate haematopoietic stem cell niches *in vivo* (Calvi *et al.* 2003). Intriguingly, among the cells of the rosette assembly, one cell expresses nuclear-localised Runx2; the same cell co-expressed nuclear Osteopontin (Figure 1.22A). This co-localization was unexpected as results from dissociated calvaria concluded that double positivity of Runx2 and OPN does not exist;

indeed, such double positivity is also found within L2 (discussed in Chapter 3.4.2). The previously observed focal expression of Hand2 within L1 was also mapped to rosettes (Figure 1.22D), and nuclear Hand2 is found to be co-expressed in the nucleus of the Runx2/Osteopontin expressing cell. Hand2 has previously been found to be required for flattening up of cells in *Drosophila*, and a phylogenetically ancient role for the gene may be to coordinate the movements of cells in relation to one another (Ruest *et al.* 2003; Liu *et al.* 2009; Liu *et al.* 2009; Xiong *et al.* 2009). Hand2 also regulates Runx2, acting to supress intramembranous ossification by physically interacting with Runx2 and prohibiting proper osteoblast maturation via a mechanism that remains unclear (Funato *et al.* 2009). Therefore, Hand2, in the context of expression among dermal bone rosettes, may act to help cells of L1 coordinate their localised migration into L2 and prevent precocious osteogenesis from taking place within the rosettes.

1.3.2 Rosettes as a generative architectural component of frontal bone development

Beyond the molecular properties of the rosettes, their physical properties also indicated a role for them in coordinating the growth of dermal bones. An architectural feature of rosettes is they are organised around a physical hole, through which cells could thread into L2 (Figure 1.23). The single high-columnar Runx2/Osteopontin/Hand2-nuclear cell is located at the apex of a rosette, often creating the initial contact with L3 across L2 (Figure 1.24). This single Runx2/Osteopontin/Hand2-nuclear cell retains its position in the rosette as the clasp becomes more elaborate and non-rosette cells from L1 seem to use the rosette as the entry point to slide into L2 (Figure 1.24). The structure of the rosette, acting as a scaffold system coordinating cellular migration, is akin to radial glial cells acting as guideposts along which cells from the mammalian ventricular zone enter the cortex (Rakic 1972; Price *et al.* 1987; Rakic 1988; Walsh and Cepko 1992; Cepko *et al.* 1993; Walsh and Cepko 1993; Mountcastle 1997). The conceptual link between dermal bone rosettes and radial glial cells suggests a morphogenetic similarity,

underscoring the potential importance of rosettes in coordinating the structure of the frontal bone.

The startling finding of these rosettes, and the possibility that they might act as generative architectural components of bone formation coordinating the intercalation of cells from the generative layers into L2, necessitated a rigorous time-course analysis of rosette formation.

1.3.3 Ontogeny of rosette formation in the frontal bone

Rosettes are observed in the earliest formation of murine frontal bone development (E13) and can be identified in all stages of foetal development through birth (Figure 1.24). The rosettes act as points of cell invasion for cells of both the osteoblastic and vascular lineages (discussed further in Chapter 2.2). Rosettes were not identified within L3, potentially due to the higher cellular density of L3 compared to L1 complicating three-dimensional reconstruction of the L3 region.

To explore if rosettes persist as entities after birth, they were examined in the context of the two-dimensional space of L1 after a week of postnatal development. In addition to adding a later time-point of analysis, this would assess the relationship between cellular invasion and definitive matrix mineral deposition (the spatial relationship between rosettes and bone matrix deposition is detailed in Chapter 3). For these reasons I dissected the cranial region of a one-week old wild-type mouse: the frontal and parietal region was isolated and the frontal bone was flat-mounted; this was challenging as overlying dermis is difficult to remove, however, it is possible to confocal through the entire bone and reconstruct it in small 3D stacks. Using reflection imaging to exploit the birefringence of collagen fibres, rosettes can be seen sitting in distinct craters on the surface of L1 (Figure 1.25). In the centre of these craters small pores are visible (Figure 1.25), presumably the location through which other cells of L1 enter L2.

1.3.4 Rosettes: a common feature to both the frontal and clavicle bones

The implication that rosettes may be essential to dermal bone development would necessitate their presence not only across the entirety of dermal bone maturation, but also in all dermal bones. I confirmed the presence of rosettes in the dermal component of the murine clavicle. The clavicle undergoes both dermal and endochondral ossification (Figure 1.26). At the lateral end, where the clavicle meets the acromion, the bone develops via direct dermal ossification; more medially an endochondral core develops under a second dermal bone covering (Huang *et al.* 1997); with time the two dermal sheaths grow together. In addition to two forms of ossification, the clavicle derives from both mesodermal and neural crest precursors; an anterior neural crest component serves as the attachment regions of the sternocleidomastoid (SCM) and the coracobranchial muscles (Matsuoka et al, 2005), while the posterior dermal bone (serving as attachment region of pectoralis and other mesodermal muscles) is entirely mesodermal in origin. I focused my analysis on the neural crest-derived components of the dermal clavicle. The SCM was previously shown to be of neural crest origin (Matsuoka *et al.* 2005), and following the connectivity-rule I expected the underlying bone to be neural crest; as such my analyses focused on the area of the clavicle with SCM insertion points.

Investigations of the clavicle at the SCM lead to the identification of rosettes within L1 (Figure 1.27). Three-dimensional reconstructions again displayed the rosettes to be sitting in and along the walls of craters (Figure 1.27), which are shown to be Periostin positive with a discernible polarisation of POSTN localisation. The cells forming the rosettes of the clavicle displayed a similar molecular heterogeneity (with regard to Runx2 and Hand2) to those in frontal bone rosettes.

1.3.5 Conclusion

Rosette formations are located at the highly constrained points of cellular invasion from L1 to L2; this feature is conserved throughout bone

development into the postnatal condition. This supports the notion that that rosettes provide the basic units of cellular involution and ingrowth of cells necessary for the formation of L2.

Individual cells could enter L2 through the holes in rosettes (i.e. at focal places) and involution or invagination of the entire generative layer (similar to neurulation) is not observed. Furthermore, post-translational modification and protein re-localisation of Runx2 into the nucleus is a hallmark of single cells within the rosette formations at the apices of the observed rosette architectures and may be critical for the early establishment of L1 to L3 connections. This cell, at the apex of the rosette, expresses nuclear Osteopontin, Runx2 and Hand2, the implication of this co-expression being a fundamental role of Hand2 in the development of dermal bone. Hand2 is a known regulator of Runx2, although the mechanism by which this occurs is unclear: biochemical studies have identified the interaction domain of the two proteins, suggesting Hand2 prevents Runx2 from binding (Funato *et al.* 2009), but other (additional) means of *in vivo* control are possible.

Hand2 may play a role in coordinating the invasion of cells from L1 and L3 into L2, a requirement of layer-like elaboration of L2. While gene expression may be highly variable, the heterogeneity of marker expression within the rosettes appears to have significance for how the rosettes function.

In order to further elucidate the role of Hand2 in dermal bone formation, I analysed the phenotypes of two previously established strains of Hand2-transgenic mice, with specific regard to intramembranous ossification.

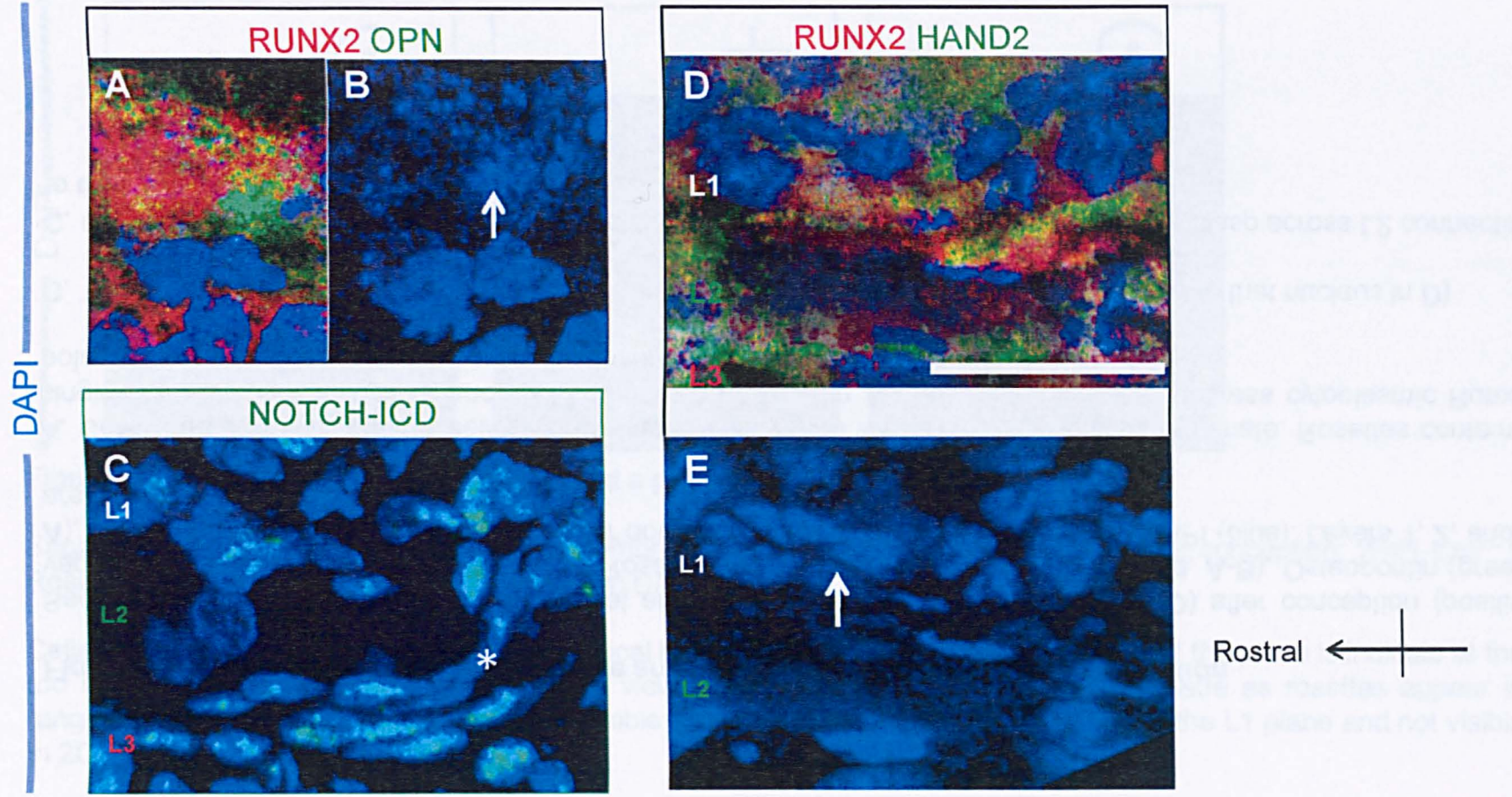
Wnt1-Cre x R26Lacz
DAPI
RUNX2 OPN
A
B
NOTCH-ICD
C
L1
L2
L3
*
RUNX2 HAND2
D
L1
L2
L3
E
L1
L2
Rostral

Figure 1.22: Cells at the apex of clasps are arranged in a pinwheel/rosette organisation

Sagittal sections through the frontal bone at embryonic days E13.5 (**A**) and E18 (**B-D**) after conception (positive vaginal plug is taken as E0); *Wnt*1-Cre$^{+/-}$ x Rosa26LacZ$^{-/-}$ specimen. IHC for Runx2 (red, **A-B**), Osteopontin (green, **A**), Hand2 (green, **B**) and Notch intra-cellular domain (green, **C**); nuclear counterstain DAPI (blue). Layers 1, 2, and 3 are indicated as **L1**, **L2**, and **L3**, respectively.

A. Cells organised into a pinwheel/rosette formation are found within L1 where clasps terminate. Rosettes contain a single cell with nuclear Runx2 and OPN expression (arrow in **A**), the remaining cells express cytoplasmic Runx2, polarised such that the cells appear to sit on clouds of Runx2 expression (**B & D**).

B. The cells that expresses nuclear Runx2 also co-expresses nuclear Hand2 (**D** and arrow to that nucleus in **D**)

C. Cells within the rosette also express an activated form of Notch1, as do the cells of the clasp across L2 connecting to the L1 rosette (*).

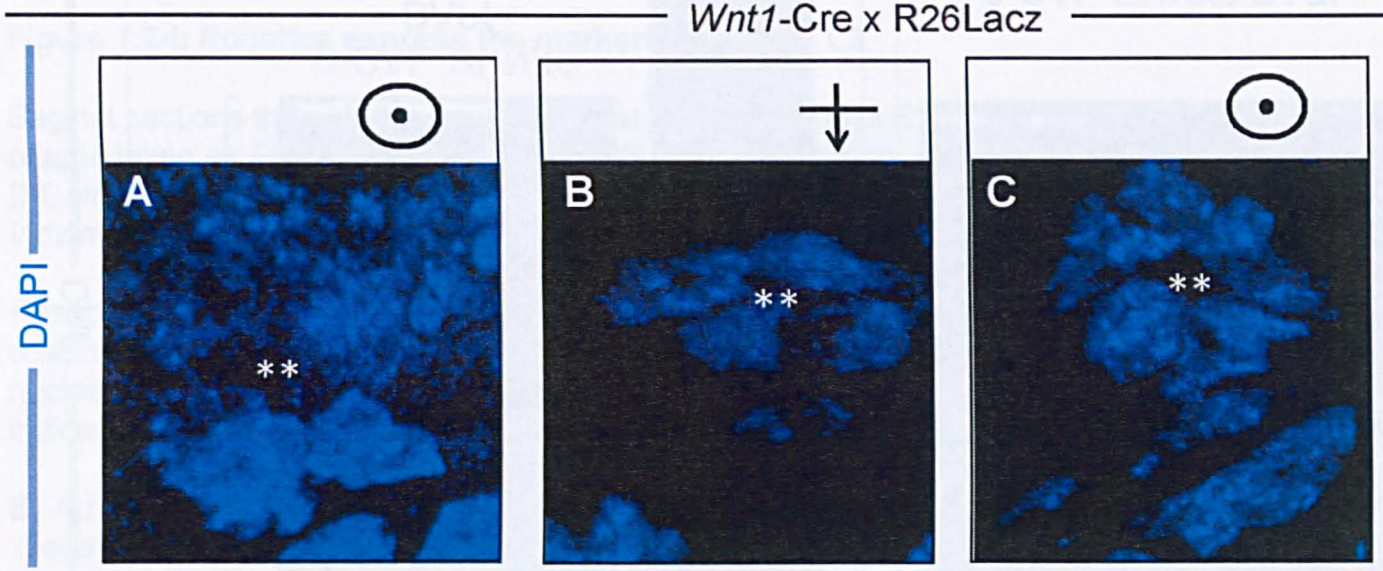

Figure 1.23: Rosettes are organised around a physical hole

Sagittal sections through the frontal bone at embryonic days E13.5 (**A**) and E18 (**B-C**) after conception; *Wnt*1-Cre$^{+/-}$ x Rosa26LacZ$^{-/-}$ specimen. Nuclear counterstain DAPI (blue).

Cells of rosettes are organised around a physical hole (indicated with **). The orientation of the plane is indicate at the top of each image (**A** and **C** are bird's eye views; versus **B**, an oblique view of a rosette as rosettes appear in tangential cross sections; rosettes are only visible using 3D reconstructions as they are in the L1 plane and not visible in 2D).

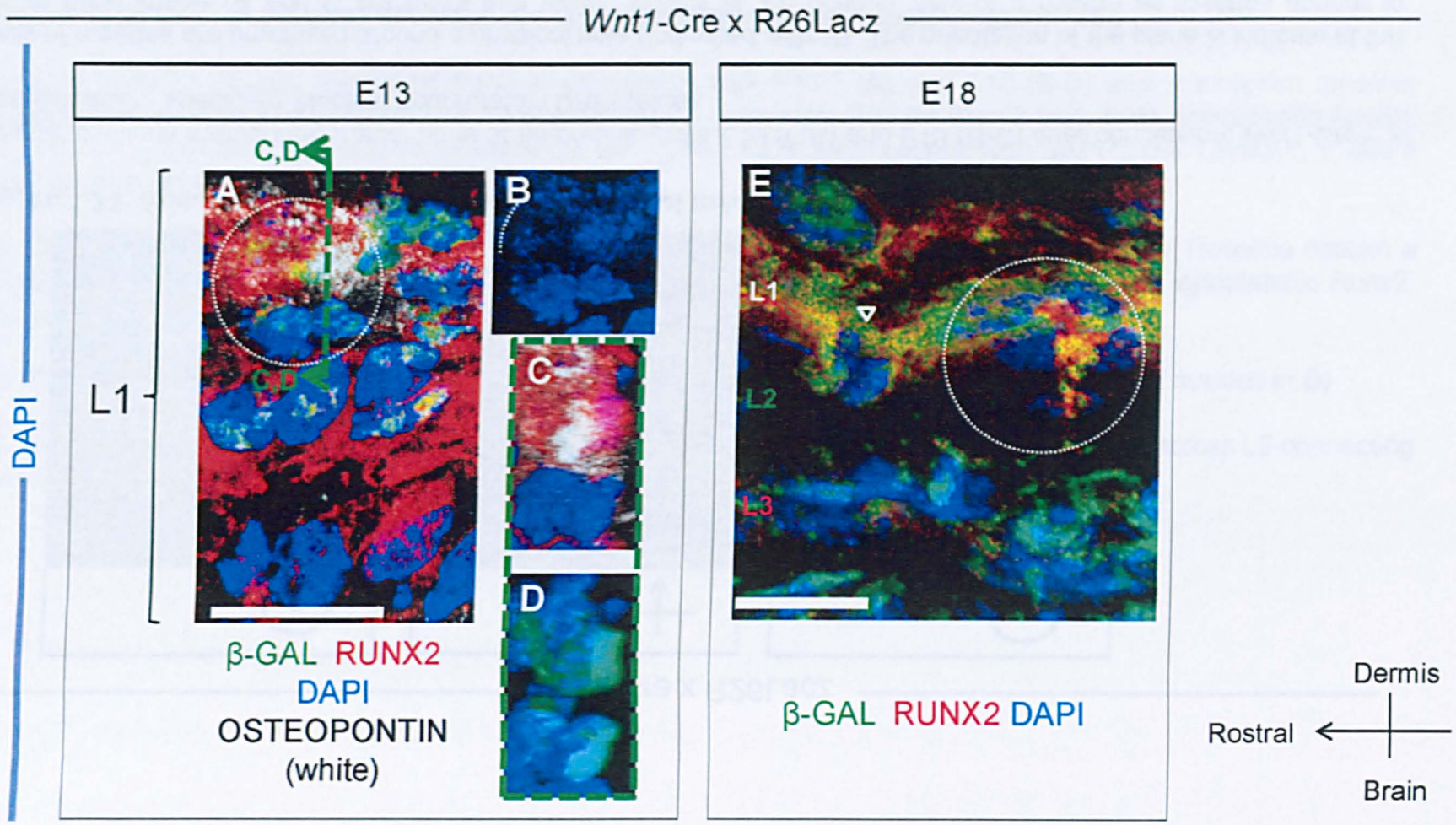
Wnt1-Cre x R26Lacz
E13
E18
DAPI
C,D
A
B
C
D
E
L1
L2
L3
β-GAL RUNX2
DAPI
OSTEOPONTIN
(white)
β-GAL RUNX2 DAPI
Dermis
Rostral
Brain

Figure 1.24: Rosettes express the markers of L1 and L3

Sagittal sections through the frontal bone at embryonic days E13.5 (**A**) and E18 (**B**) after conception (positive vaginal plug is taken as E0); *Wnt*1-Cre$^{+/-}$ x Rosa26LacZ$^{-/-}$ specimen. IHC for Runx2 (red, **A-B**), Osteopontin (white, **B**), and β-Galactosidase showing neural crest cells (green, **A-B**); nuclear counterstain DAPI (blue). Layers 1, 2, and 3 are indicated as **L1**, **L2**, and **L3**, respectively.

Rosettes are first identified in Layer 1 of the condensed mesenchymal precursor to the frontal bone at E13.5. The orientation of five cells into a rosette is visible in the DAPI channel in **B**. Within the rosette, a single cell expresses nuclear Runx2 and Osteopontin, as indicated by the sectional view of the nucleus in **C-D**, cut through the section line indicated in **A.** All cells of the rosettes, in the Runx2+/OPN+ cell, are of neural crest origin (**A, D**).

E. A rosette in L1 of an immature region of the frontal bone in an E18 mouse, where the majority of cells sit on a 'cloud' of Runx2 cytoplasmic expression. A single cell in the rosette with Runx2 nuclear expression has a cellular process extending into L2.

Scale bar indicates 25μm.

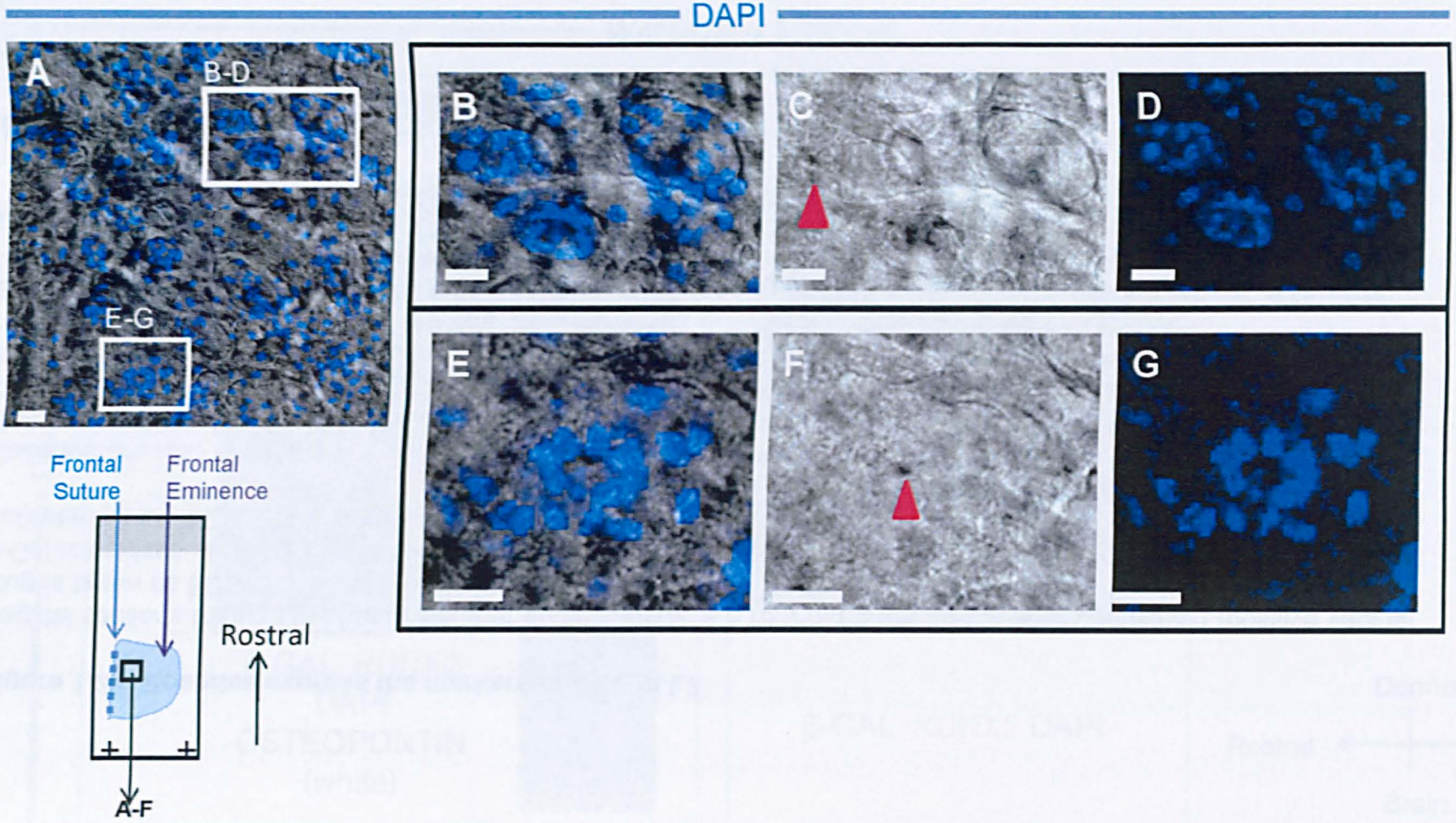
DAPI
A
B-D
E-G
B
C
D
E
F
G
Frontal Suture
Frontal Eminence
Rostral
A-F

Figure 1.25: Surface view of rosettes in L1

Flat mount of the frontal eminence of a wild-type mouse at postnatal day 3 (P2). Nuclear counterstain DAPI (blue) and reflection imaging to examine bone topography. Images are a surface view of **L1**, oriented rostral to the frontal suture to the left.

A. Low magnification of area of L1 near the frontal suture where rosettes sit along the entire image plane; the image series was acquired through a depth of 25µm of L1. The nuclei and reflection imaging were reconstructed in 3D, revealing rosettes sit along the walls of depressions in the bone; white boxes indicate the locations of subsequent panels.

B-D. The overlay of the DAPI and reflection channels and each individual channel. A cluster of three rosettes sit in craters. The three rosettes are at slightly different depths in the bone, such that the top right crater is imaged at a more superficial stage than the rosette to its left, which is imaged at the bottom of the crater and a small pore is visible at the base of the depression housing the rosette (red arrowhead, **C**).

E-G. The overlay of the DAPI and reflection channels and each individual channel. A rosette of several nuclei imaged at the bottom of the crater where a pore is visible (red arrowhead, **F**).

Scale bar indicates 50µm.

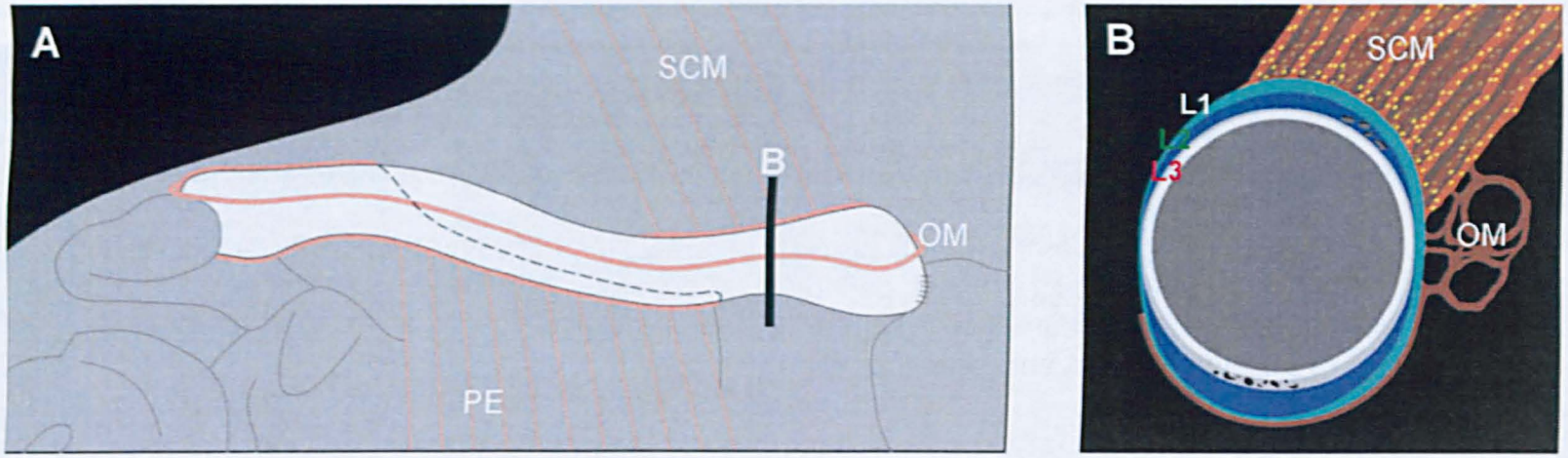

Figure 1.26: Diagrammatic representation of the clavicle

A. Coronal overview of the right murine clavicle (white). At the lateral end (left), toward the acromion, the clavicle undergoes direct dermal ossification; at the medial position, toward the sternum, an endochondral core develops under a dermal outer covering. The clavicle comprises cells from the neural crest (near the anterior sternocleidomastoid (SCM) muscle attachment) and lateral plate mesoderm (near the posterior attachment of the pectoralis (PE) muscle). A boundary between these zones is indicated with a dashed line. The omohyoideus 'sling' wraps around the clavicle (OM). The SCM, PE and OM are in pink. The section line (black) indicates the relative position of **B.**

B. A cross-section through the clavicle at the attachment of the SCM (orange and brown); the omohyodius is perpendicular to the SCM, dark brown). In the diagram, the endochondral core of the clavicle is dark grey and processing toward the external face are L3, L2 and L1.

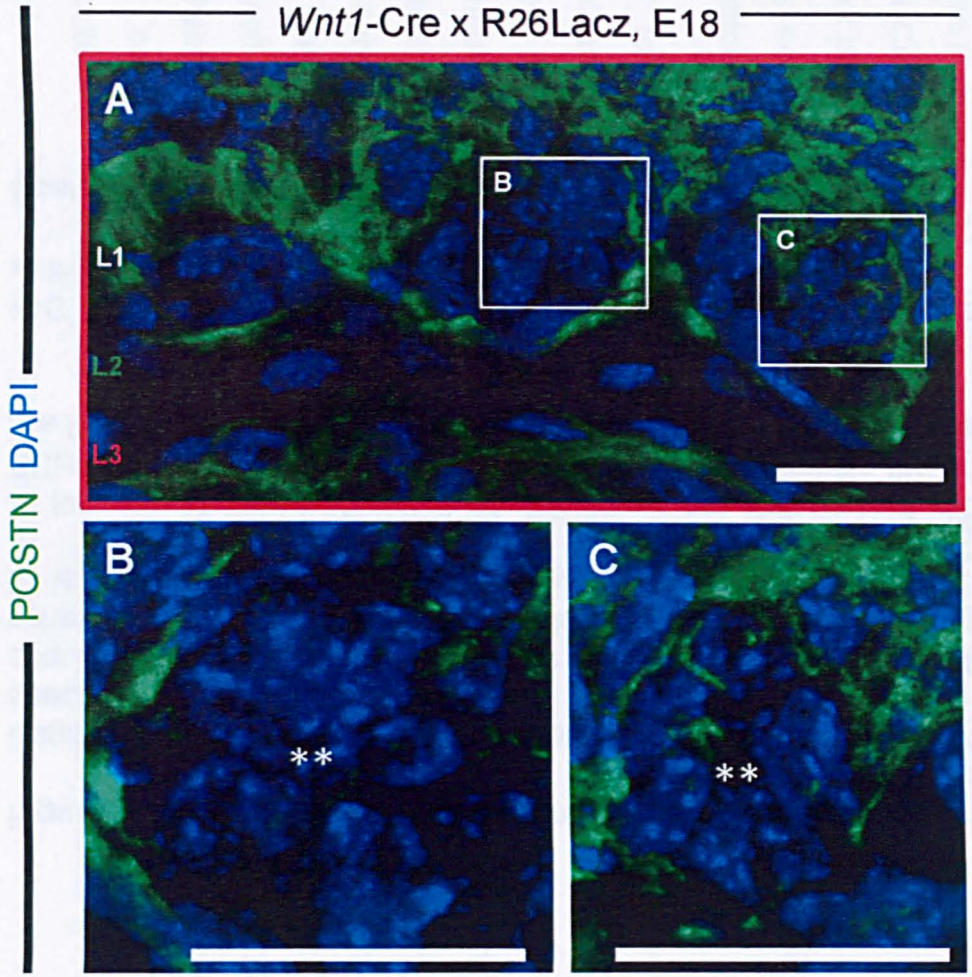
Wnt1-Cre x R26Lacz, E18
POSTN DAPI
A
B
C
L1
L2
L3
**
**

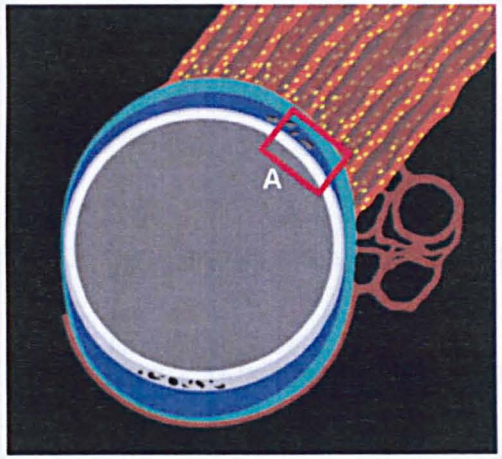
A

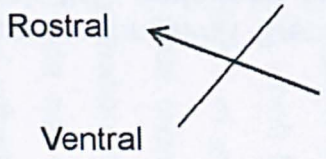
Rostral
Ventral

Figure 1.27: Rosettes within L1 of the dermal clavicle

Sagittal section through the dermal clavicle bone at embryonic day E18 after conception; *Wnt*1-Cre$^{+/-}$ x Rosa26LacZ$^{-/-}$ specimen. IHC for Periostin (green, **A-C**); nuclear counterstain DAPI (blue); IHC performed by B. Ryll, image acquisition and analysis performed by K. Jordan. Layers 1, 2, and 3 are indicated as **L1**, **L2**, and **L3**, respectively. A schematic representation of the clavicle at the attachment point of the SCM indicates the position of **A**. In the diagram L1 is light blue, L2 is blue/grey and Layers 3 is white.

A. Rosettes, first identified in the frontal bone, are also present in Layer 1 of the dermal clavicle at a region where the SCM inserts into the bone (attachment area is superficial to the area of **A**). Rosettes sit in craters, the walls of which are Periostin positive, allowing the depth of the craters to be assessed in 3D. White boxes indicate the locations of **B-C**.

B-C. The 3D reconstruction of **A** was rotated 180° to view the rosettes from behind, allowing visualisation of the pore at the base of the craters (**).

Scale bar indicates 25µm.

1.4 Hand2 mutant analysis: Disrupted layer morphogenesis

1.4.1 Introduction

The role of Hand2 in dermal bone formation was investigated using two previously established strains of mice in which Hand2 expression is ablated. The *Hand2*$^{fl/fl}$-*Wnt*1-Cre strain is a knockout transgenic which lacks *Hand2* expression specifically in neural crest cells (Hendershot *et al.* 2008). To visualise the Hand2-/- cells, *Hand2*$^{fl/fl}$-*Wnt*1-Cre mice were crossed with the ROSA26LacZ reporter. This cross enables the discrimination between cell-autonomous effects (in LacZ+ cells lacking Hand2) and non-autonomous phenotypic effects. To further specify if any observed effects of Hand2 deletion were the results of the loss of Hand2 function conferred by the so-called branchial arch enhancer (BAenh), I examined a strain of transgenic mouse lacking the BAenh region (*Hand2*BAenh) in parallel with the *Hand2*$^{fl/fl}$-*Wnt*1-Cre strain. Specimen from both strains were isolated for analysis at the day of birth (P0) to assess the resulting phenotype of Hand2 ablation during the processes of bone development previously analysed in the wild-type condition.

Prior to investigating the effects of Hand2 deletion on dermal bone development, the endogenous expression of Hand2 was confirmed in the system in question, namely the murine frontal bone and dermal clavicle. Immunohistochemistry results indicated that in immature dermal bones, expression of Hand2 is prolific in Layer 3; while in more mature areas Hand2 is widely expressed by cells populating Layer 2. Cytoplasmic Hand2 was also found to be expressed in the cells participating in rosettes, and crucially one cell of a rosette has a nuclear co-localisation of Runx2 and Hand2. *In situ* hybridisation (performed by B. Ryll) confirmed *Hand2* expression in an early condensation of L3 in the clavicle of an E14 *Hand2*-Cre$^{+/-}$ x ROSA26Lacz$^{-/-}$ animal (Figure 1.28) (Ruest *et al.* 2003); similarly to the frontal bone anlagen, the early condensation of L1 in the clavicle comprises more cell layers than L3 and L1 in the mature bone. *Hand2* mRNA expression at this stage was also observed at the muscle-bone interface in

the presumptive L1, in a less homogenous pattern than within L3 (Figure 1.28). Coronal sections through a more mature frontal bone (E16) show a wide expression of *Hand2* transcripts in L2 (primarily within osteoblasts, but also in the lining of blood vessels), and the dermis (Figure 1.28). Expression of *Hand2* mRNA in L1 and L3 at this stage is focal. Previous work in the laboratory confirmed the overlap of the endogenous and transgene expression patterns in craniofacial and clavicular structures of the *Hand2*-$Cre^{+/-}$ x ROSA26$Lacz^{-/-}$ transgenic strain (Ryll & Koentges, unpublished). For the purpose of the current study, only the endogenous mRNA expression and protein localisation of Hand2 was analysed.

1.4.2 Results

In *Hand2*$^{fl/fl}$-*Wnt*1-Cre x ROSA26LacZ specimen, Layers 1 and 3 are discernible by the alternating expression of Runx2 and OPN/Collagen I, respectively.

At the medial margin of the clavicle, there is an extreme proliferation of cells within Layer 1. Runx2 expression is considerably up-regulated and is entirely translocated to the nucleus, suggesting a cytoplasmic tethering of Runx2 by Hand2 protein *in vivo* (Figure 1.29B) occurs in the non-mutant condition. Cells along the external margin of the clavicle have achieved the thin, sheet-like morphology, which precedes L2 involution in the wild-type condition; however rosettes and their accompanying clasps are not evident and round, globular Runx2+ cells from L1 have filled the entire physical space up to L3. These cells are neural crest in origin (LacZ+) and appear unable to form sheets within L2. This appearance is akin to what is expected from a traditional 'percolation' model where cells would enter L2 without constraint.

The L1 to L3 boundary is discernible by the strong expression of Collagen I in L3 (Figure 1.29A); which also indicates the location of the dermal cover of the endochondral core as Collagen I is expressed by cells of osteobloastic but not cartilaginous lineages (Mundlos *et al.* 1990; Huang *et al.* 1997). There does not appear to be an extension of Collagen I expression into L2,

an expression profile indicating that cells within the initial generative layer L3 may be confined to this area in the mutant and not able to enter L2. Some cells of L3, akin to the external area of L1 cells, have flattened, however the characteristic bi-involution process is not evident and appears to be truncated by Hand2 ablation.

The attachment site of the SCM *per se*, where direct dermal ossification occurs, appears unaffected in *Hand2*$^{fl/fl}$-*Wnt*1-Cre x ROSA26LacZ mice (Figure 1.30), suggesting that the molecular mechanisms determining attachment regions are distinct from those responsible for the histogenesis (dermal or endochondral) of the underlying bone. This genetic separability might have relevance for the changes in ossification type within the shoulder region of tetrapods (Matsuoka *et al.* 2005).

Contrasting this, the organisation of the dermal bone layer along the diaphysis is severally disrupted. In the Hand2 knockout, cells of both L1 and L3 remain globular; the domain of L1 has expanded in the absence of a well-defined L2, while L3 consists of a single layer of cells (Figure 1.30). The organisation of POSTN expression becomes haphazard, with fibres spanning across the L1-L3 region, where clearly defined borders into what should be L2 are not evident (Figure 1.30). Within L1 rosettes are conspicuously absent and the cells' F-Actin fibres are radial giving the cells the appearance of being aligned along a vertical axis, further exaggerating that L1 cells have lost their horizontal-sheet arrangement (Figure 1.20).

An examination of the *Hand2*BAenh$^{-/-}$ strain yielded results indicating the *Hand2*BAenhancer ablation replicates the phenotype of crest-specific Hand2 deletion (Figure 1.31).

In the frontal bone of *Hand2*$^{fl/fl}$-*Wnt*1-Cre transgenic mice mirrors the condition of the clavicle with an expansion of L1 and L3 cells and arrest of L2 elaboration. Within L1 semi-flattened cells (LacZ-negative) sit adjacent to LacZ+ neural crest cells of globular morphology (Figure 1.32). Given that there is a successive invasion of neural crest from L1 into Layer 2 in the wild-type condition (see above), the globular cells within L2 at the L1/L2 interface might derive from L1 but be unable to form sheets within L2. Layer 1 is many

cell layers thick and the bone is lacking the characteristic clasp features connecting Layers 1 and 3. At points along the bone, single radial cancellar walls are formed in L2 of the mutants, largely by LacZ- cells, but these simple walls lack any further horizontal and radial elaboration (Figures 1.32-1.33). Where connections between the generative layers does occur, they are achieved by LacZ- cells, which do not carry the hallmarks of L1 given they are both Runx2 and OPN negative indicating these 'clasps' may be mesodermal blood vessels (Figure 1.33). The expression domains of Runx2 and OPN in the frontal have expanded, such that cytoplasmic Runx2 is found in L3, while OPN expression is observed in L1 and the dermis (Figure 1.33). Cells adjacent to the mesodermal vasculature are found to be large, round cells expressing both OPN and Runx2 (Figure 1.33).

1.4.3 Conclusion

The overall appearance of the dermal bones in both the *Hand2*$^{fl/fl}$-*Wnt1*-Cre and *Hand2*BAenh$^{-/-}$ strains are characteristic of an appositional growth mode via expansion of L1, while L3 cells appear to be more inhibited in their invasion of L2. In the mutants, cells are unable to enter L2 in a regulated manner, leading to many blast-like cells that are Runx2-nuclear within the space corresponding to Layer 2; the overabundance of L1 cells in the L2 space suggest either invasion of L2 from L1 or cells within L2 are undergoing rapid and unregulated division. Previous data suggested that Runx2 is a key regulator of invasion processes under metastatic conditions leading to osteolytic disease (Barnes *et al.* 2004; Pratap *et al.* 2006; Akech *et al.* 2010) and the invasive potential of Runx2+ cells seems to be maximised in the Hand2-mutant condition.

The regulators of confined entry into the developing L2 system, namely the rosettes, are not evident in either Hand2-mutant strain of mouse analysed, nor are there properly elaborated clasps. In the frontal bone, some areas with single canceller walls of cells within L2 are found, however, they are comprised mainly of cells of non-neural crest origin (LacZ-negative), in which Hand2 would not have been ablated. This implies an attempt at a

compensatory mechanism of the mesodermal cells, which contributes to the subtlety of the phenotype.

Interestingly, while the majority of cells are positive for LacZ, indicating they are Hand2-/- cells, the remarkable effect of Hand2 ablation on layer formation is most likely due to the loss of Hand2 function in coordinating cellular movements through the rosettes, established by the single Runx2/Hand2-nuclear expressing cell in each rosette. The consequence of the inability of cells to form proper laminae on vascularisation and biomineralisation are discussed in Chapters 2 and 3, respectively.

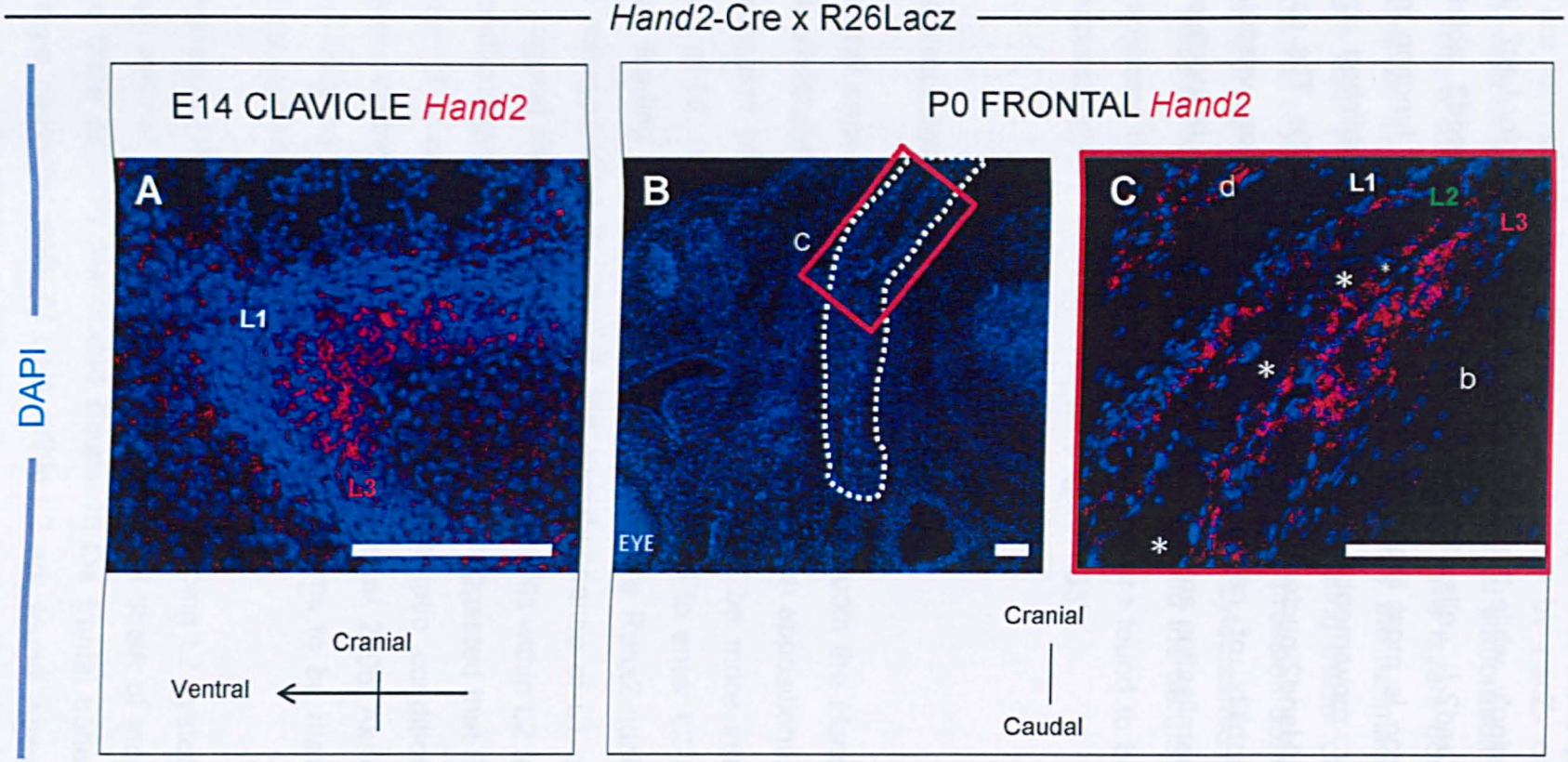
Hand2-Cre x R26Lacz
DAPI
E14 CLAVICLE Hand2
A
L1
L3
Cranial
Ventral
P0 FRONTAL Hand2
B
C
EYE
C
d
L1
L2
L3
b
Cranial
Caudal

Figure 1.28: Endogenous expression of *Hand2* mRNA in dermal bone

Sagittal section through the dermal clavicle bone at embryonic day E14 (**A**) after conception, and coronal section through the frontal bone at postnatal day 1 (P0) (positive vaginal plug is taken as E0); *Hands2*-Cre$^{+/-}$ x Rosa26LacZ$^{-/-}$ specimen. RNA fluorescent i*n situ* hybridisation for *hand2* (red); nuclear counterstain DAPI (blue); *in situ* performed by B Ryll, image acquisition and analysis performed by K Jordan. Layers 1, 2, and 3 are indicated as L1, L2, and L3, respectively.

A. At E14 the *hand2* transcripts are detected throughout L3 of the clavicle, as well as along the external margin of L1 and weaker expression is detected within the endochondral core of the clavicle.

B. Overview of the cranial region of a P0, the frontal bone is outlined (white dashed line).

C. Within the P0 frontal bone, *hand2* transcripts are detected in L2, as well as at focal points in L1 and L3. The majority of the *hand2* expression in L2 is confined to the bone proper, although weak expression in the lining of the vasculature is observed (blood vessels indicated, *).

d Dermis, **b** Brain

Scale bar indicates 50μm.

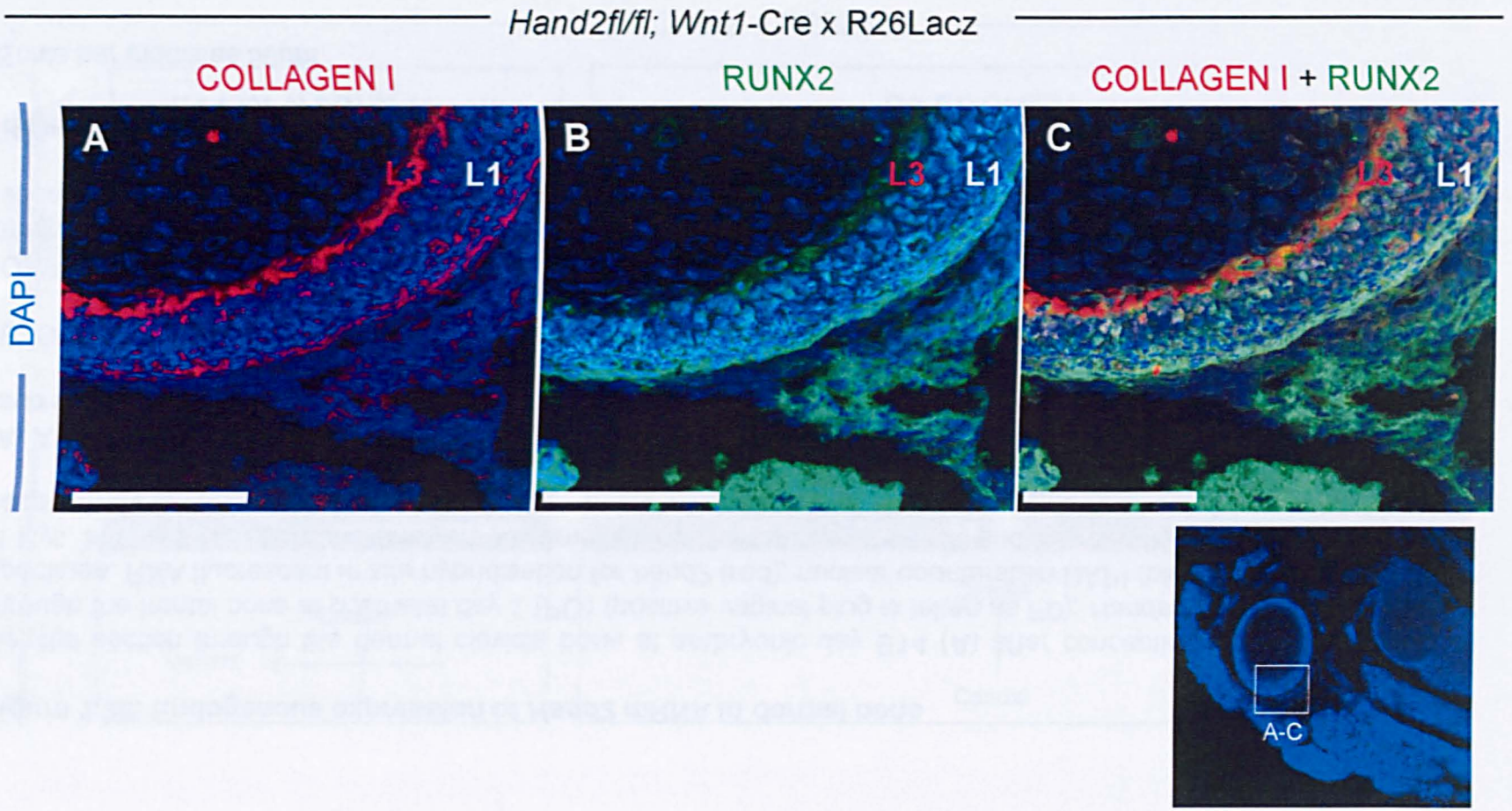
Hand2fl/fl; Wnt1-Cre x R26Lacz
COLLAGEN I
RUNX2
COLLAGEN I + RUNX2
DAPI
A
B
C
L3
L1
L3
L1
L3
L1
A-C

Figure 1.29: Loss of Hand2 leads to expansion of L1 and nuclear translocation of Runx2 expression

Sagittal section through the medial clavicle of postnatal day 1 (P0) transgenic knockout mouse; *Hand2fl/f-/-l; Wnt1-Cre*$^{+/-}$ x Rosa26LacZ$^{-/-}$ specimen. IHC for Collagen I (red, **A, C**), Runx2 (green in **B-C**); nuclear counterstain DAPI (blue. Layers 1 and 3 are indicated as **L1** and **L3**, respectively. Anatomical overview of counterstain, including the location of **A-C,** is indicated at bottom right.

Loss of Hand2 has resulted in a clavicle where L1 is expanded and L3 confined to a single layer of cells at the margin of the endodermal core; there is no discernable L2 space.

A. Collagen I expression is found in flattened cells at the external margin of L1 and within L3. Expression of Collagen I in a single layer of cells on the L1 side of L3 may indicate some cells from L3 have deposited via apposition into the area that should comprise L2.

B. Runx2 expression in L1 is ubiquitous and has been translocated into the nucleus in the absence of Hand2, indicating Hand2 may regulate Runx2 via a tethering mechanism. Within L3 there are some areas of Runx2 cytoplasmic expression.

C. Overlay of Collagen I and Runx2.

Scale bar indicates 50μm.

DAPI POSTN F-ACTIN
Hand2fl/fl; Wnt1-Cre x R26Lacz
β-GAL (white)
β-GAL
β-GAL
A
B
C
L1
L3
L1
L3
L1
L3
*
*
A-E
Rostral
Ventral
Wnt1-Cre x R26Lacz
D
E
L1
L3
L1
L2
L3

Figure 1.30: Loss of Hand2 disrupts layer formation of the dermal clavicle

Comparison of Hand2 knockout and control clavicles. **A-C**, Sagittal section through the dermal clavicle of postnatal day 1 (P0) transgenic knockout mouse in SCM attachment regions; *Hand2fl/fl; Wnt*1-Cre$^{+/-}$ x Rosa26LacZ$^{-/-}$. **D-E**, Sagittal section through the dermal clavicle of a non-mutant E18 mouse; *Wnt*1-Cre$^{+/-}$ x Rosa26LacZ$^{-/-}$ specimen. IHC for β-Galactosidase indicate neural crest cells in which Hand2 has been ablated (white in **A**, light blue in **B**, pink in **C**), Periostin (green in **A, B, D**), F-Actin (red in **A, C, E**); nuclear counterstain DAPI (blue). A schematic representation of the clavicle at the attachment point of the SCM indicates the position of **A-E.**

Loss of Hand2 has resulted in a clavicle where layer formation is disrupted. L1 is expanded and cells have not flattened up and involuted into an L2 region. The attachment region is notably unaffected. The region that should contain L2 is noted with a dashed green line in **A-C.**

A. Overlay of F-Actin, Periostin and β-Gal in the mutant clavicle.

B. The Periostin fibre system is disrupted in the mutant. Periostin fibres span the L1-L3 region and do not form the walls of craters as POSTN does in the presence of Hand2 (**D**); flattened cells that are POSTN+ and line L2 are no longer visible. Cells orienting themselves in circular formations, indicative of an attempt at crater formation, are noted (*) and are mainly negative for β-Gal indicating they have not had Hand2 ablated.

C. Cells in Layer 2 have acquired a vertical orientation in the Hand2 knockout mouse and appear more isolated from one another and have not created a meshwork of cells in a parallel sheet organisation (E).

Scale bar indicates 50μm.

DAPI
Hand2BAenh-/-
Hand2fl/fl; Wnt1-Cre x R26Lacz
F-ACTIN vWF
F-ACTIN, β-GAL
RUNX2 POSTN
POSTN,β-GAL
L1
L3
A
B
C
D
*
Rostral
Ventral
A-D

Figure 1.31: Loss of the Hand2 branchial arch enhancer disrupts layer formation of the dermal clavicle

Comparison of the clavicles of Hand2 knockout and Hand2BAenhancer knockout transgenic strains. **A-B**, Sagittal section through the dermal clavicle of postnatal day 1 (P0) transgenic knockout mouse in SCM attachment regions; *Hand2fl/fl; Wnt*1-Cre$^{+/-}$ x Rosa26LacZ$^{-/-}$. **C-D**, Sagittal sections through the dermal clavicle of a *Hand*2BAenh$^{-/-}$ specimen. IHC for β-Galactosidase indicate neural crest cells in which Hand2 has been ablated (pink in **A**, light blue in **B**), Periostin (green in **B, D**), F-Actin (red in **A, C**), vWF (green in **C**), and Runx2 (red in **D**); nuclear counterstain DAPI (blue). Layers 1 and 3 are indicated as **L1** and **L3**, respectively. A schematic representation of the clavicle at the attachment point of the SCM indicates the position of **A-D**.

Loss of the Hand2 branchial arch enhancer has resulted in a clavicle with a similar layer disorganisation as in the Hand2 knockout. L1 is expanded and cells have not flattened up and intercalated into an L2 region. The region that should contain L2 is noted with a dashed green line in **A-D**. The attachment region is notably unaffected.

A. Cells of Layer 1 are organised in a vertical manner and there is a total absence of flattened cells lining an L2 region; in the *Hand*2BAenh$^{-/-}$ knockout the L1 organisation in a columnar fashion is further exaggerated (**C**).
B. Periostin disorganisation in Hand2 knockout mice where POSTN fibres span L1-L3 and are strongest in the disorganised region between L1 and L3 that should contain L2. In the *Hand*2BAenh$^{-/-}$ mice POSTN is expressed at the margin of the attachment region and along the L1/L3 border (note: the globular appearance of POSTN in **D** is due to the antibody and not a phenotypic feature of the mutant).
C. The attachment region comprises a subsection of L1 with a meshwork of F-Actin expression and a high level of vascularisation. Contrasting this, L1 in non-attachment areas consists of cells in a vertical arrangement. Vascularisation of the L1 and L3 areas is impaired.
D. Runx2 expression in *Hand*2BAenh$^{-/-}$ animals is both nuclear and cytoplasmic in L1-L3. Cells of the layers remain round and blast-like and have not flattened. A nascent 'clasp' formation is noted (*), which is noticeably cell-poor and aberrantly constructed.

Scale bar indicates 50μm.

IHC in **A-B** performed by B. Ryll, IHC in **C-D** performed by K. Jordan, all image acquisition and analysis performed by K. Jordan.

Wnt1-Cre x R26LacZ

Hand2fl/fl; Wnt1-Cre x R26Lacz

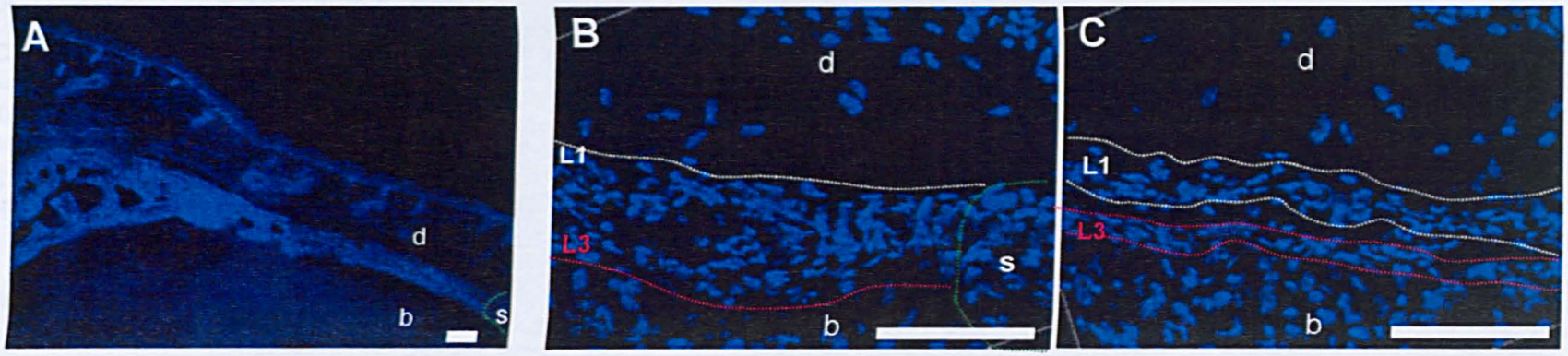

Dermis

Rostral

Brain

Figure 1.32: Loss of the Hand2 disrupts layer formation in the frontal bone

Comparison of Hand2 knockout and control frontal bone. **A**, Sagittal section through the frontal bone of a non-mutant E18 mouse; *Wnt*1-Cre$^{+/-}$ x Rosa26LacZ$^{-/-}$. **B-C**, Sagittal section through the frontal bone of postnatal day 1 (P0) transgenic knockout mouse; *Hand2fl/fl; Wnt*1-Cre$^{+/-}$ x Rosa26LacZ$^{-/-}$. Nuclear counterstain DAPI (blue). Images are oriented cranial to the top and ventral to the left. Layers 1 and 3 are indicated as **L1** and **L3**, respectively.

A. Anatomical overview of the frontal bone from the coronal suture to the nasal bone in a non mutant mouse. The bone becomes progressive more complex along the horizontal axis as it progresses toward the nasal bone.

B-C. In the mutant condition the layer formation is disrupted. At the coronal suture (**B**) the bone does not immediately resolve into L1, L2 and L3. The external margins of L1 and L3 are noted (white and red dotted lines, respectively), however their inner margins cannot be determined.

C. In the Hand2 knockout the bone becomes progressively **less** complex along its horizontal axis. **C.** is taken from a region adjacent to the nasal end, which should correspond to the most highly cancellous area of the bone. Layer 1 has expanded and a thin space, presumably L2, is noted between Layers 1 and 3.

d Dermis, **b** Brain, **s** Suture

Scale bar indicates 50μm.

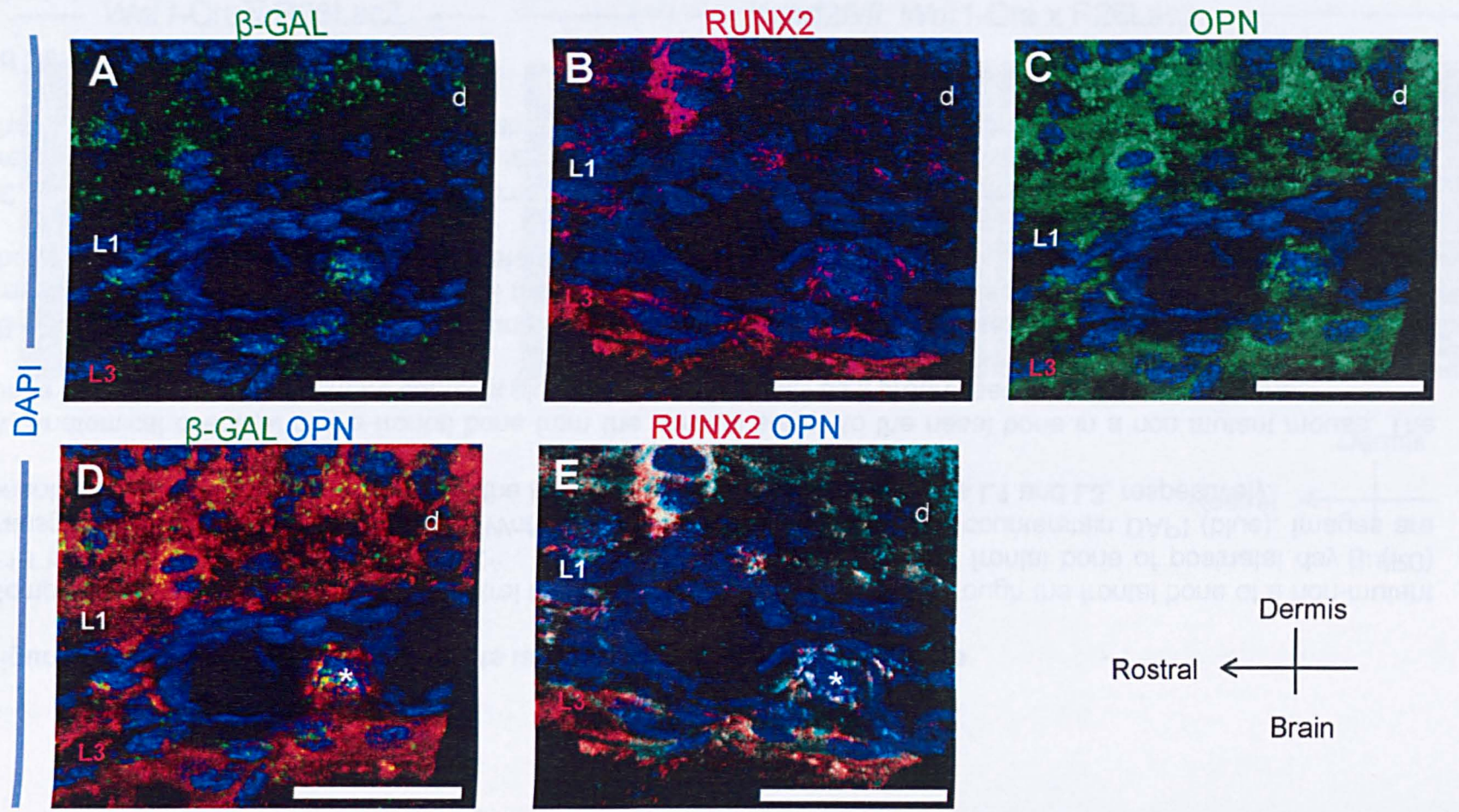
Hand2fl/fl; Wnt1-Cre x R26Lacz
β-GAL
RUNX2
OPN
DAPI
A
B
C
D
E
d
L1
L3
β-GAL OPN
RUNX2 OPN
*
Dermis
Rostral
Brain

Figure 1.33: Layer formation in the Hand2 knockout is achieved by mesodermal cells

Sagittal sections through the frontal bone of a postnatal day 1 (P0) transgenic knockout mouse; *Hand2fl/fl; Wnt*1-Cre$^{+/-}$ x Rosa26LacZ$^{-/-}$. IHC for β-Galactosidase indicate neural crest cells in which Hand2 has been ablated (green in **A, D**), Runx2 (red in **B**, **E**), Osteopontin (green in **C**, red in **D**, blue in **E**); nuclear counterstain DAPI (blue). Images are oriented cranial to the top and ventral to the left. Layers 1 and 3 are indicated as L1 and L3, respectively.

A. Cells of Layer 1 that have achieved a flattened morphology are negative for β-Gal indicating their non-neural crest origin meaning Hand2 has not been ablated in these cells. Horizontal elaborations within L2 are not found. Cells of Layer 2 forming a 'clasp' are not positive for Runx2 (**B**) or OPN (**C**) indicating they are likely to be blood vessels. Large, globular cells neural crest cells, positive for both Runx2 and OPN are noted within L2 (* in **D, E**).

B-C. The expression domains of Runx2 and OPN in the frontal have expanded. Cytoplasmic Runx2 is found in L3 (**B**), while OPN expression is observed in L1 and the dermis (**C**).

d Dermis

Scale bar indicates 50μm.

1.5 The PCP/non-canonical Wnt signalling pathway in dermal bone development

1.5.1 Introduction

The Hand2 mutants display a phenotype whereby the constrained cellular entry from L1 and L3 into L2 required for normal intramembranous formation of the frontal and clavicle bones is abrogated.

In the non-mutant condition, entry of cells from generative Layers 1 and 3 appears to involve the cells in closest proximity to the rosette scaffolds threading into the underlying L2, which is elaborated in time by the continual addition of new cellular material. The morphogenetic arrangements of sheets of cells threading into rosettes at defined places requires coordinated migration patterns and is a behaviour reminiscent of classically defined convergent extension movements, often regulated by the non-canonical *Wnt*/Planar Cell Polarity (PCP) pathway, usually associated with cellular polarisation (Darken *et al.* 2002; Wang *et al.* 2006; Simons and Mlodzik 2008). The PCP pathway regulates the organisation of cells along an epithelial plane and is involved in a diverse range of tissue formations, including gastrulation and neurulation, regulating aspects of development in an array of species including *Drosophilia*, *Xenopus*, zebrafish and mammals (Darken *et al.* 2002; Fanto and McNeill 2004; Karner *et al.* 2006; Karner *et al.* 2006; Simons and Mlodzik 2008). Components of the PCP pathway ensure proper sheet formation and overall cellular coordination (Myers *et al.* 2002). Mutations in this pathway lead to an inability of cells to coordinate their respective migration behaviours in groups, leading to the abolition of sheets and the isolation of cells that remain blast-like (Myers *et al.* 2002; Wu and Mlodzik 2009; Wansleeben and Meijlink 2011). This phenotype is replicated in the Hand2 mutants in the current study; the finding that LacZ+ cells lacking Hand2 remain blast-like and lose the polarisation of the markers they express (ex: Runx2, OPN, POSTN) indicate the membership of Hand2 in the PCP pathway. Although Hand2 is not a known member of PCP pathway, it is necessary for sheet formation in both zebrafish myocardial epithelium

outflow tract formation and murine palatal tissue development (Trinh *et al.* 2005; Xiong *et al.* 2009).

1.5.2 Results

The possibility that the PCP pathway is involved in layer morphogenesis of dermal bones is supported by our findings that components of the non-canonical *Wnt*/PCP pathway are expressed during the development of Layers 1, 2 and 3.

An activated form of Notch is widely expressed by cells of Layers 1 and 3 during early layer morphogenesis, including in cells participating in rosette formations and those cells that connect to the rosette and form a clasp across L2 (Figure 1.34). In epithelial tissues, the *Notch* pathway, in convergence with *Wnt* signalling and the *BMP* pathway, is transduced to the non-canonical *Wnt* pathway to control cell polarity and the canonical *Wnt* pathway to control tissue differentiation (Katoh 2007). Wnt5a is a key regulator of non-canonical *Wnt* signalling also known to direct cellular movements in the developing palate and is necessary for proper cranio-facial development (Oishi *et al.* 2003; He *et al.* 2008); this protein is expressed at focal points in Layer 1, within the majority of Layer 3 and, most interestingly, by cells that have intercalated into Layer 2 on both the L1 and L3 margins (Figure 1.34), further supporting the notion that cells invade L2 from the generative layers. Interestingly, a recent report describing a PCP-mutant phenotype (lacking PKC-delta) speculated that this pathway may regulate the more subtle features of osteogenesis beyond the final differentiation of osteocytes, a postulation supported by the current findings (Tu *et al.* 2007). The finding that the non-canonical *Wnt* pathway is involved in regulating the stacking of chondrocytes in endochondral ossification (Li and Dudley 2009) implies this pathway serves as a universal mediator of cellular orientation allowing cells to organise themselves with regard to their neighbours, a feature that would be required for the coordinated elaboration of sheets of cells forming L2. While the PCP-pathway has previously been linked to the

proper formation of cartilaginous elements of the cranio-facial skeleton (Dale *et al.* 2009), results from the current study indicate it may also be necessary for dermal bone development.

1.5.3 Conclusion

Taken together, results presented here in indicate the role of the PCP pathway in in establishing Layers 1 and 3 as sheets capable of intercalating cells into L2. This process is disrupted upon ablation of either Hand2 or the Hand2 branchial arch enhancer in neural crest cells, resulting in a columnar organisation of the dermal bones indicative of an appositional growth mode, supporting Hand2 as a possible component of the PCP/non-canonical *Wnt* signalling pathway under *in vivo* conditions. Thus the previously posited model for appositional growth most strikingly resembles what is observed in the Hand2 mutants – cells are able to percolate into L2 but are unable to self-organize within L2, nor able to establish proper communication to the underlying Layer 3.

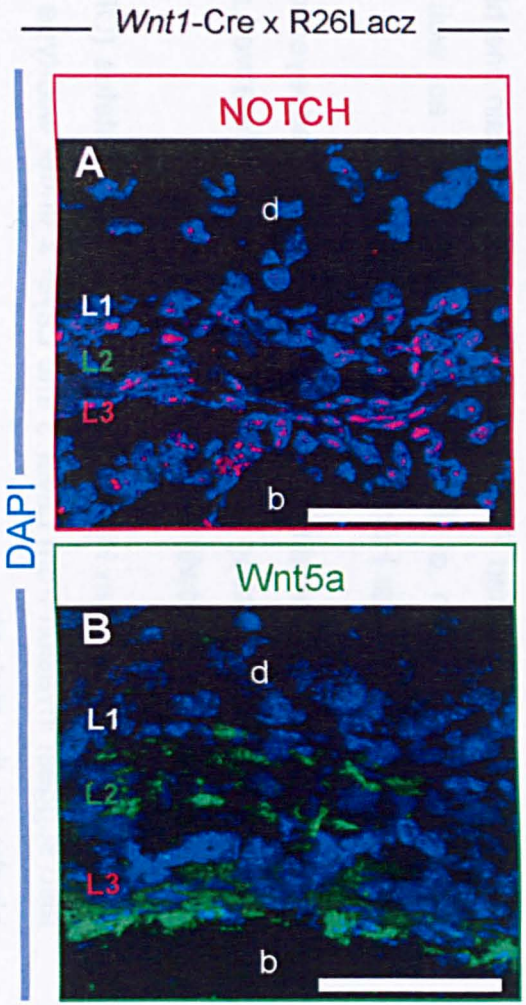

Figure 1.34: The non-canonical *Wnt*/PCP pathway is active in the generative layers of the frontal bone

Sagittal sections through the frontal bone at embryonic day E18 after conception; *Wnt*1-Cre$^{+/-}$ x Rosa26LacZ$^{-/-}$ - specimen. IHC for activated Notch (red, **A**), and Wnt5a (green, **B**); nuclear counterstain DAPI (blue). Layers 1, 2, and 3 are indicated as **L1**, **L2**, and **L3**, respectively.

Expression of markers of the non-canonical *Wnt*/PCP pathway in progressively more mature stages of frontal bone development.

A. An activated form of Notch is expressed by Layers 1 and 3 from the earliest stage of layer formation, as well as within cells of L2 and clasps that have achieved a flattened morphology. Notch is not expressed in cells that have remained round and not flattened up in Layer 2, as well as in the dermis.

B. Wnt5a is expressed focally in Layer 1, ubiquitously in Layer 3 and in cells that have entered L2.

d dermis, **b** brain

Scale bar indicates 50µm.

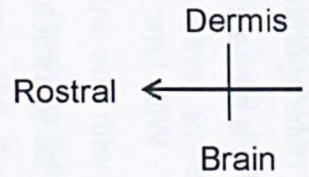

1. 6 Summary of findings

- The frontal bone primordium is a bilayered system comprising molecularly heterogeneous cells. External Layer 1 is neural crest in origin, while Layer 3 is a mosaic of neural crest and mesodermal cells;

- With time cells of Layers 1 and 3 flatten into laminar sheets and separate with the intervening space, termed L2, constituting the future cancellous bone structure that growths in thickness and complexity;

- During the elaboration of Layer 2, Layers 1 and 3 remain unchanged and continue to express the molecular markers combinations that serve as their signatures through bone maturation;

- Lineage mosaicism is used to explore the mechanism of L2 development and neither apposition nor clonal expansion is found to be the primary growth mode. Instead L2 is populated in time by the bi-directional movement of cells from L1 and L3 into L2 as a convergence extension process, and the horizontal elaboration of the sheets of cells in L2;

- There is no evidence of entire layer involution (neurulation-type behaviour) from L1 or L3 into L2;

- Cellular intercalation from L1 and L3 into L2 is constrained to specific nodes of entry; at these entry points in L1 cells are organised into rosette-like architectures;

- Rosettes have polarised POSTN expression and contain one high columnar cell with translocation of Runx2 into the nucleus, as well as nuclear Osteopontin and nuclear Hand2 expression;

- Loss of Hand2 in dermal structures results in disrupted layer formation and an organisation suggesting apposition from highly proliferative Layer 1 as the mechanism of bone growth in the mutants;

- Genetic evidence from Hand2 mutants and marker states (OPN+, Coll I+) also suggest invasion from Layer 3 into Layer 2 under wild-type conditions is blocked in the mutants.

- Translocation of Runx2 into the nucleus of *Hand2-/-* cells implies post-transcriptional tethering of Runx2 in the cytoplasm by Hand2 as the mechanism for regulation Runx2's action. Preventing Runx2 from entering the nucleus would deprive it from binding target genes. Such a mode of regulation is not dissimilar to the action of Twist and other transcription factors (Twist code);

- The PCP pathway is activated in Layers 1 and 3 and responsible for the convergent extension behaviours of cells threading from the generative layers into L2 in a highly regulated fashion;

- Hand2 is implicated as potential new component of the non-canonical *Wnt*/PCP pathway.

2. Vascularising dermal bone

2.1 Introduction

Bones are highly vascularised entities and angiogenesis is a key component of both endochondral and dermal ossification (Hall and Miyake 1992; Kanczler and Oreffo 2008). Proper bone development and maintenance requires a close physical proximity between vasculature and the osteogenic surface, without which bone integrity is lost and bone formation is abrogated (Coskun and Hirschi 2010). While initial stages of endochondral bone development occur under a-vascular conditions, dermal bone is believed to form around pre-existing vasculature (Figure 2.1) (Lieberman and Friedlaender 2005). In this model, the intramembranous skeleton arises from mesenchymal condensations that are highly populated by blood vessels; in the craniofacial skeleton this vasculature matures earlier in organogenesis from the cephalic mesoderm (Le Douarin and Kalcheim 1999). This means vasculature has temporal precedent and dictates the architecture of dermal bones in the conventional model of direct ossification: as mesenchymal cells differentiate into osteoblastic lineages they need to arrange themselves in close proximity to the blood vessels, without impinging upon the vasculature with capricious osteoid production (Figure 2.1) (Lieberman and Friedlaender 2005).

This model, whereby existing vasculature becomes enveloped by osteoblastic layers, is irreconcilable with results presented in Chapter 1, where Layer 2 is initially cell sparse and could not accommodate pre-existing vasculature nor does Layer 1 secondarily engulf vasculature in the overlying dermis. Moreover, it was previously assumed that blood vessel endothelia of dermal bones are mesodermal in origin within neural crest-derived skeletal elements on the basis of QH1 immunoreactivity and how mesodermal vasculature enters into a predominantly neural crest area has not been previously reconciled (Etchevers *et al.* 2001). Therefore, it became necessary to explore how vascular development is integrated into dermal bone formation. To accomplish this, the same technique was employed as

was used to explore layer morphogenesis: namely, a three dimensional time-course study of bone development from E13 through murine birth using molecular markers of vascular development.

Blood vessels (with the exception of capillaries) comprise three layers associated with both their function and the cell types within them (Figure 2.1C) (Lee 1989): at the internal (luminal) face the endothelial cells form the tunica intima. The tunica intima is ensheathed by the smooth muscle cells of the tunica media, reinforced by layers of the elastic laminae. The external adventia layer is composed of connective tissue and nerve fibres. Vascular development in dermal bones was analysed using three molecular markers, which preferentially labelled either the endothelia or smooth muscle lining of the vessels.

Endothelial cells were identified using the well-established markers von Willibrand factor (Factor VIII related factor) (vWF) and CD31 (PECAM1). vWF is synthesised by endothelial cells and megakaryocytes and is stored in intracellular granules or secreted into plasma; vWF is a component involved in platelet:vessel wall interactions (Denis 2002). Under some conditions, for example during tumorigenic angiogenesis, vWF immunolabelling is insufficient to identify all vessels, whereas CD31 has shown a wider area of expression among endothelial cells (Baderca *et al.* 2005). CD31 is produced by platelets and leukocytes, concentrated at the borders between endothelial cells (Simmons *et al.* 1990). Pericytes (or vascular mural cells) are embedded in the vascular basement membrane and their cytoskeleton can be labelled with α-smooth muscle actin (SMA); pericyte reactivity for SMA is not, however, entirely consistent: brain pericytes of chicken reportedly express SMA, while those in mice were unlabelled; even within individual micro-vessels SMA expression is patchy (Armulik *et al.* 2005).

A combinatorial approach, whereby markers of vasculature were examined in parallel with osteblastic markers, allowed a thorough investigation into the generation of the osteoblast-vasculature interface and the role of angiogenesis in dermal bone development.

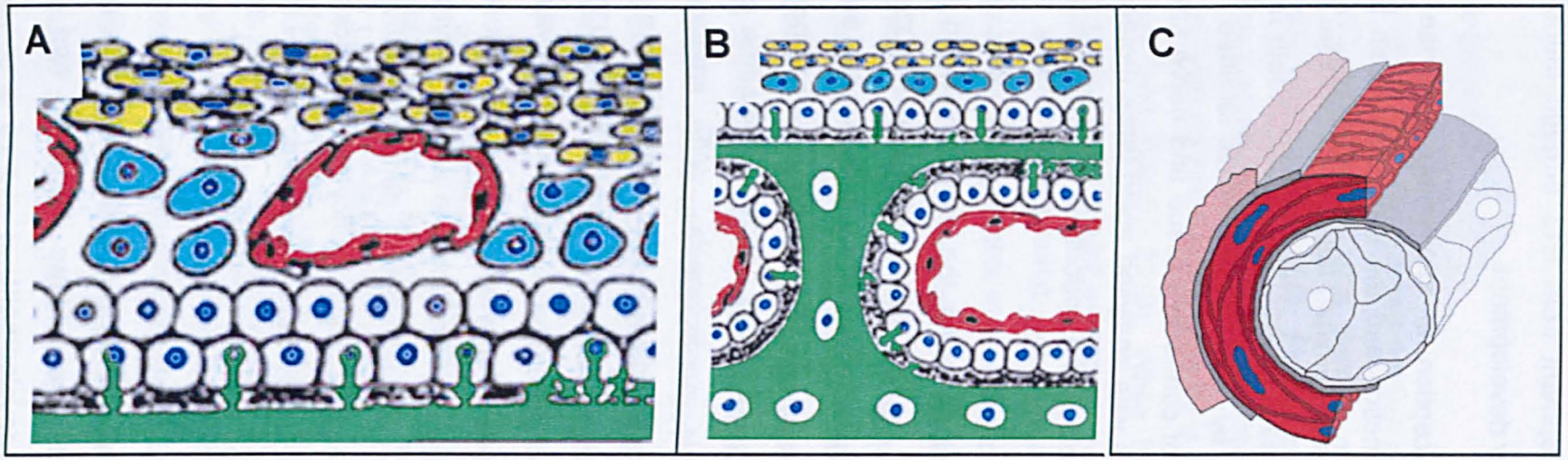

Figure 2.1 Vascularising dermal bones

A-B. Diagrammatic representation of the traditional model of intramembranous ossification in which the bone forms around pre-exisiting vasculature. The blood vessels (red) are engulfed by the growing bone front and osteoblasts (white) surround the vasculature and secrete osteoid (grey) and mineralised matrix (green) away from the vessels so as not to impinge upon them with precocious ossification.
Modified from Bruder & Scaduto in *Bone Regeneration and Repair,* 2005, Human Press Inc. Lieberman & Friedlaender, eds.

C. The structure of a blood vessel has three layers, separated by thin, elastic lamina (dark grey). At the internal (luminal) space, endothelial cells (light grey) of the tunica intima completely line the vessel. Endothelial cells are then sheathed on their external side by the smooth muscle cells of the tunica media (red). The most external area of the vessel is the connective tissue of tunica adventitia (pink).
Modified from Podell & DiGergorio, available at: http://www.freewebs.com/circulatorysystem/aboutbloodsystems.htm

2.2 Results

2.2.1 Generating the vasculature-osteoblast interface

Results presented in Chapter 1.1 indicate the mesenchymal condensation yielding the frontal bone is a bi-layered anlage comprising L1 and L3. At E13, the frontal bone primordium has a spatial molecular heterogeneity, with the lateral and medial aspects expressing the signature of L1 and L3, respectively. At this stage there is no intervening L2 nor any morphogenic evidence of pre-existing vasculature in the condensed mesenchyme. Expression of vascular markers at E13 is restricted to a border of cells at the margin of the brain (presumably the meninx) and to individual, blast like cells within L1 (Figure 2.2).

As foetal maturation progresses and rudimentary L2 is formed, there remains no evidence of fully formed vasculature within immature Layer 2 by day E16 (Figure 2.2). Conversely, Layer 1 and Layer 3 are extremely heterogeneous and comprise both osteoblastic *and* vascular CD31/vWF+ precursors (Figure 2.2). Analysis of *Wnt1*-Cre x ROSA26LacZ and *Wnt1*-Cre x XZ-DR mice indicate the CD31/vWF-positive cells are two populations: mesodermally-derived and neural crest-derived endothelia. The latter is surprising given that studies by LeDouarin *et al.* had not found neural crest to be able to form endothelia (Le Douarin and Kalcheim 1999).

If L1 and L3 are closed systems that provide osteoblastic cells to populate L2, without pre-existing vasculature there is the possibility that L1 and L3 also act as generative layers for the endothelia. Indeed, examining early clasp formations in *Wnt1*-Cre$^{+/-}$ x XZ-DR$^{-/-}$/ROSA26LacZ$^{-/-}$ mice reveals pairs of neural crest (LacZ/GFP-positive) cells entering L2 from the generative layer L1; these pairs contain cells of two separate fates, osteoblasts that are Runx2+/CD31- and Runx2-/CD31+ endothelial precursor cells (Figure 2.3), in direct proximity to each other. This is the first time, to our knowledge, neural crest cells have been shown to form endothelia in the frontal bone, although they have been previously documented within the bone marrow of

adult animals (Nagoshi *et al.* 2008). The mosaic expression of bone and vascular markers in L1 is reflected in L3, indicating L3 may also contribute both osteoblastic (OPN+) and vascular (CD31+/vWF+) cells to L2 (Figure 2.2).

As cells continue to invade L2, the bone structure becomes continually more elaborate along the dorso-ventral axis and through a time-course of development. Osteoblastic cells in L2 contribute to matrix deposition while CD31/vWF-positive cells participate in angiogenesis. The proximity of the osteoblastic and vascular cells is continually maintained such that the vascular and bone architectures develop concurrently (Figure 2.4). The *de novo* formation of the bone vasculature from CD31/vWF-positive cells from L1 and L3 results in a mature frontal bone containing both neural crest and mesoderm-derived vasculature (Figure 2.5). In areas with advanced stages of bone maturation, L3 becomes increasingly vascularised and is many cell layers thick, with the cells in a parallel-sheet orientation (Figure 2.5). Contrasting this, L1 only ever comprises 1-3 cell sheets and the relative proportion of osteoblast and vascular cells remains stable from E16 through birth.

2.2.2 Rosettes and the pore-canal system

Results from Chapter 1.3 indicate rosettes are the entry point for the osteoblastic cells, and additional evidence supports them being the introduction site of the endothelia. Intriguingly, when examined with vascular markers, single cells within rosettes were also found to be positive for endothelial markers (Figure 2.6). In early ontogeny, rosettes were not the exit or sprouting points of pre-existing dermal vasculature, but were hubs of endothelial intercalation. At a future time-point, late in ontogeny (E18 and beyond), rosettes appear to also be docking points, connecting vasculature in the dermis to the generative layer (Figure 2.7).

The physical topography of the rosette environment, namely a pore in the centre of a crater at the bone-dermis interface, are reminiscent of the pore-

canal system of fossil fish (Gross 1956; Donoghue and Sansom 2002; Le Guellec *et al.* 2004). A schematic representation of the pore-canal system in the basal jawed-vertebrate osteostracans displays a remarkable similarity to the surface view of rosettes in L1 (Figure 2.8). The pore canal system exists in heterostracans, osteostracans and lungfish, where the dermoskeletan is laced with canals that communicates with the external surface via a series of pores whose morphogenetic significance has remained elusive (Donoghue and Sansom 2002); these canals were initially believed to act as electroreceptive organs (given the similarity between the pore-canal morphology and ampullary organs in chondrichthyans) or spacing agents for mechanoreceptors and later understood in the classical framework of ossification as a secondary consequence of vascular involution and remodelling (Gans and Northcutt 1983; Northcutt and Gans 1983; Maderson 1987; Gans 1988; Gans 1989; Hanken and Hall 1993). This notion was problematic as only placoderms display clear evidence of bone remodelling. If, however, the system has been retained through evolution and now comprises rosettes and their scaffolds, the pore canal system can be understood not as a consequence of remodelling, but part of dermal bone development involving active and constant insertion of new cellular material (osteoblastic and vascular) in the initial modelling process. Under these conditions one can start to re-examine classical acellular bone such as that found in heterostracans where classical 'remodelling' has not been found.

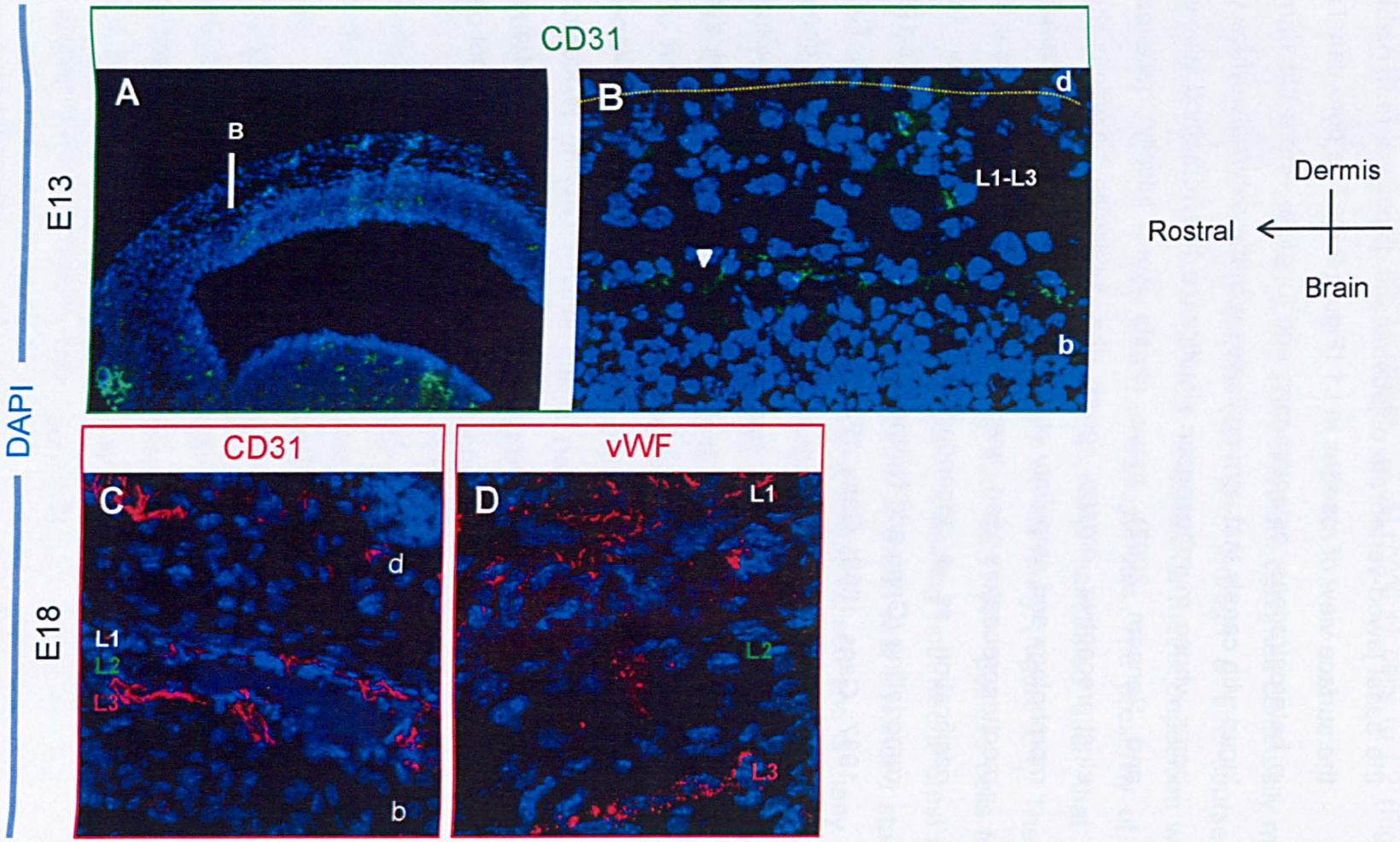
CD31
A
B
B
d
L1-L3
b
E13
DAPI
CD31
vWF
C
d
L1
L2
L3
b
D
L1
L2
L3
E18
Dermis
Rostral
Brain

Figure 2.2: Location of endothelial cells in the developing frontal bone from E13-E18

Sagittal sections through the frontal bone at embryonic day E13 (**A-B**) and E18 (**C-D**) after conception; *Wnt*1-Cre$^{+/-}$ x Rosa26LacZ$^{-/-}$. IHC for CD31 (green, **A-B**; red, **C**), and vWF (red, **D**), indicating endothelial cells; nuclear counterstain DAPI (blue). Layers 1, 2, and 3 are indicated as **L1**, **L2**, and **L3**, respectively.

Location of endothelial cells in the developing frontal bone.

In the mesenchymal anlage to the frontal bone (**A-B**) CD31 expression is confined to a single layer of cells at the brain:mesenchyme interface (presumably the meninges) and to a few cells within the mesenchyme. Notably, none of these cells has achieved the flattened appearance of fully differentiated endothelial cell.

C-D. In immature regions of the frontal bone at E18 there are very few endothelial cells within L2, instead L1 and L3 are both populated by vascular cells, intermingled with non-vascular cells (presumably osteoblasts).

d Dermis, **b** Brain

Scale bar indicates 50μm.

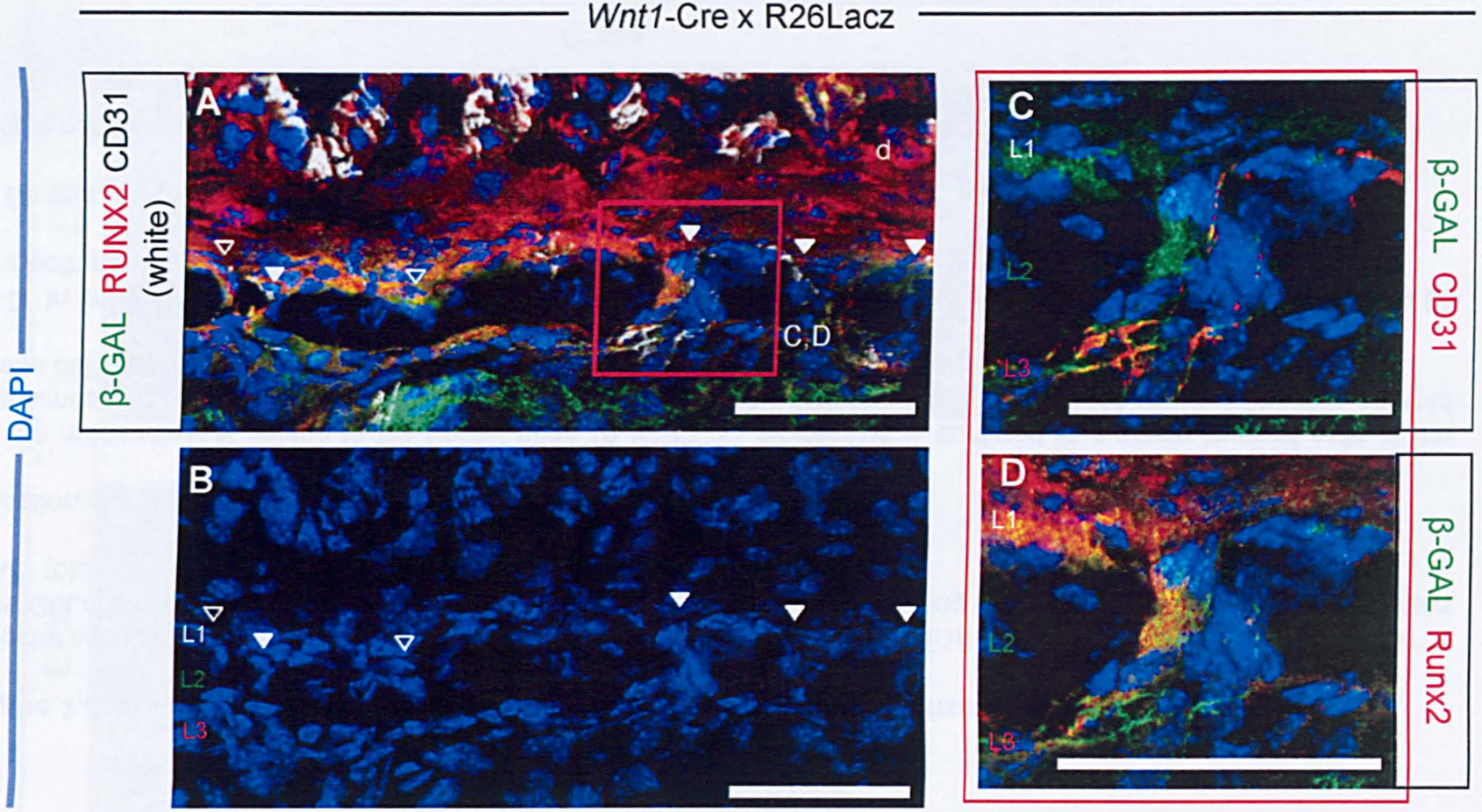
Wnt1-Cre x R26Lacz
DAPI
β-GAL RUNX2 CD31 (white)
A
d
C,D
B
L1
L2
L3
C
L1
L2
L3
β-GAL CD31
D
L1
L2
L3
β-GAL Runx2

Figure 2.3: Osteoblastic and vascular cells enter L2 via clasps in a twinned manner

Sagittal section through the frontal bone at embryonic day E18 after conception; *Wnt*1-Cre$^{+/-}$ x Rosa26LacZ$^{-/-}$ specimen. IHC for β-Galactosidase showing neural crest cells (green), Runx2 (red in **A, D**) and CD31 (white **A**, red in **C**); nuclear counterstain DAPI (blue). Layers 1, 2, and 3 are indicated as **L1**, **L2**, and **L3**, respectively.

A. In an immature region of the frontal bone clasps can be seen in different stages of development. Mature clasps (filled arrowhead) are interspersed with nascent clasps (empty arrow head). Red box indicates the location of **C** and **D**.

B. Anatomical overview of L1, L2, L3 and clasps.

C-D. Cells in a mature clasp enter L2 in a paired-manner where one cell is a Runx2+ osteoblast and the other is a CD31+ endothelial cell. Both cells are of neural crest origin.

d Dermis

Scale bar indicates 50μm.

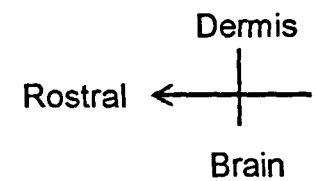

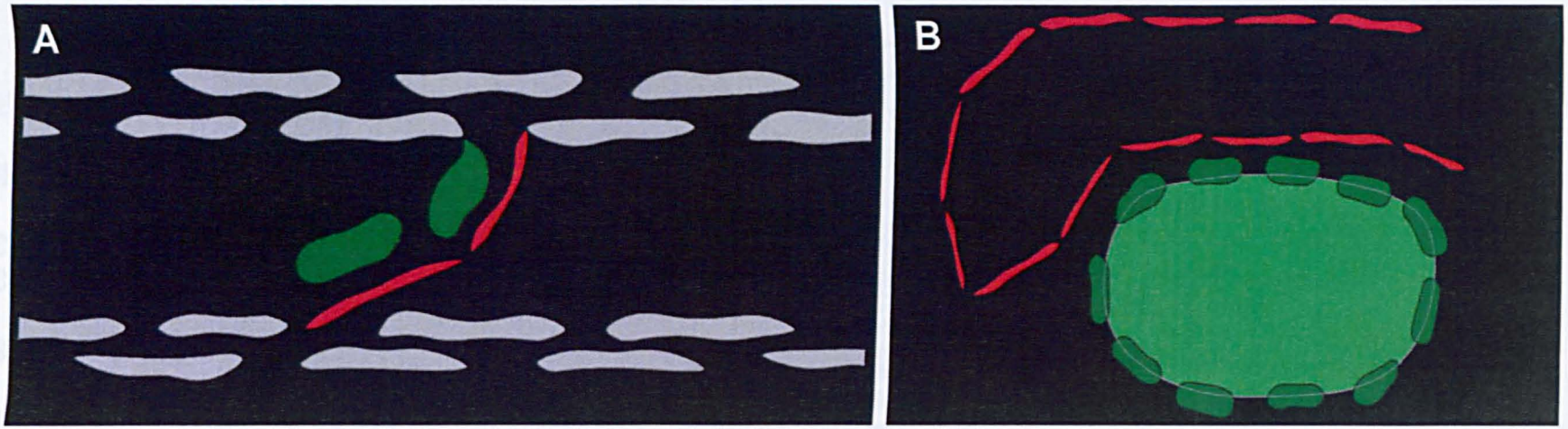

Figure 2.4: Diagram of parallel vasculature and bone morphology development

A. In an immature frontal bone vascular cells (red) and osteoblastic cells (green) enter L2 from the generative layers L1 and L3 (grey) in a twinned manner. The close proximity of the cells indicates the cooperative manner of establishing the layer morphogenesis and vasculature.

B. As the bone develops the osteoblastic cells (green) surround the bone matrix (light green) while the vasculature (red) develops in parallel and surrounds the matrix via *de novo* tube formation.

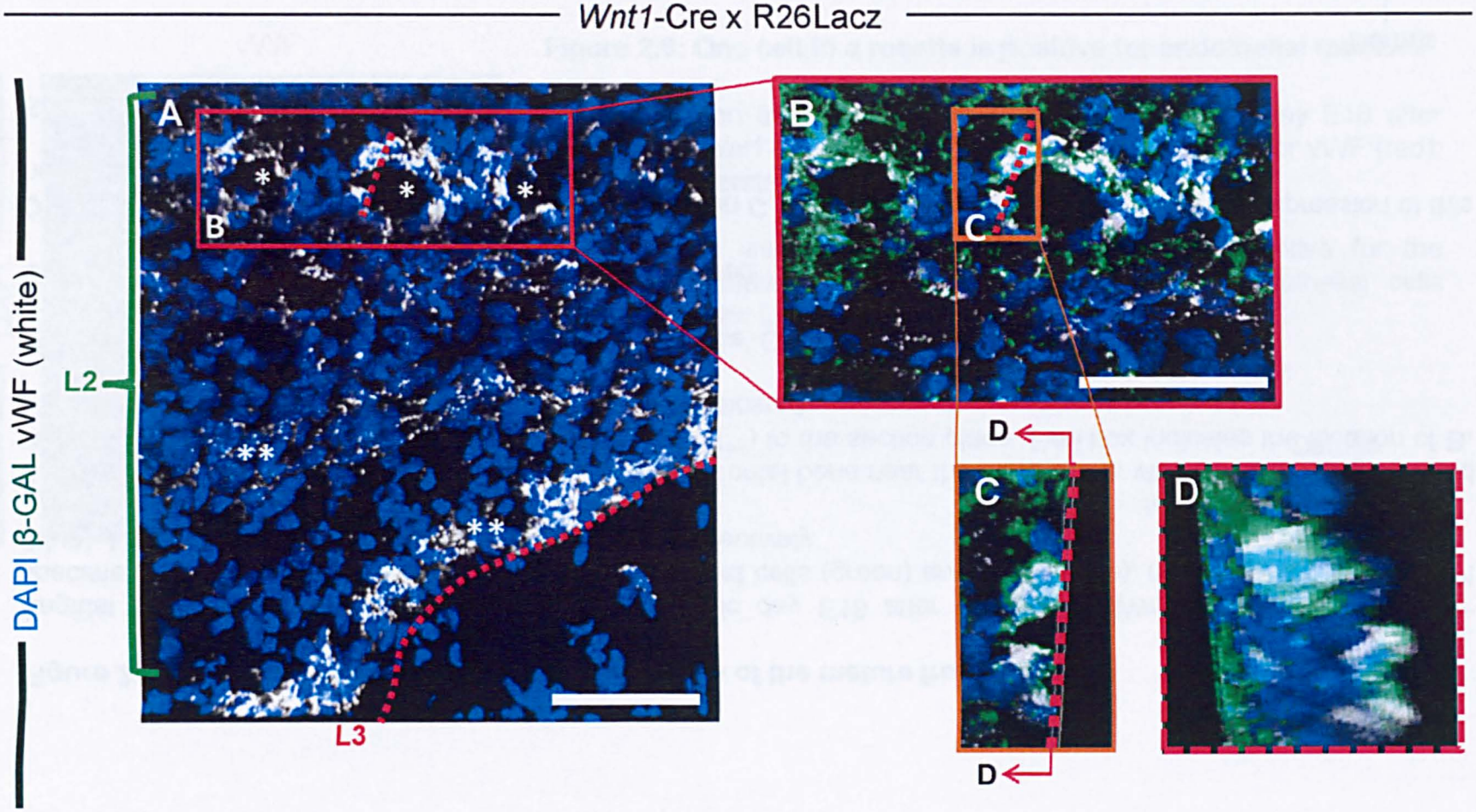
Wnt1-Cre x R26Lacz
DAPI β-GAL vWF (white)
A
B
C
D
L2
L3

Figure 2.5: Neural crest contributes to the endothelia of the mature frontal bone

Sagittal section through the frontal bone at embryonic day E18 after conception; *Wnt*1-Cre$^{+/-}$ x Rosa26LacZ$^{-/-}$ specimen. IHC for β-Galactosidase showing neural crest cells (green) and vWF (white); nuclear counterstain DAPI (blue). Layers 2, and 3 are indicated as **L2**, and **L3**, respectively.

A. Overview of the vasculature of a mature area of the frontal bone near the nasal bone. vWF-positive lining of blood vessels are seen running perpendicular (*) and parallel (**) to the section plane. Red box indicates the location of **B.** L1 is above the plane of the image and L2 and L3 are indicated.

B. Zoom of the neural crest vasculature in the frontal bone. Orange box indicates the location of **C.**

C. Frontal view of the section line along which **D** is oriented.

D. Plane cut through the axis indicated with section line in **C**, confirming the double β-Gal and vWF expression of this neural crest-derived endothelia.

Scale bar indicates 50μm.

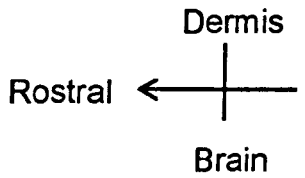

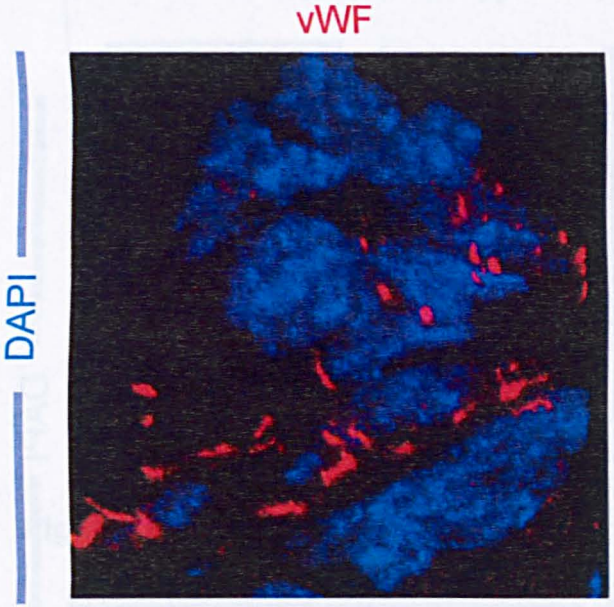

Figure 2.6: One cell in a rosette is positive for endothelial markers

Sagittal section through the frontal bone at embryonic day E18 after conception; *Wnt*1-Cre$^{+/-}$ x Rosa26LacZ$^{-/-}$ specimen. IHC for vWF (red); nuclear counterstain DAPI (blue).

A single cell within the rosette formation (L1) is positive for the endothelial marker vWF; this cell interfaces with endothelial cells beneath it at the L1:L2 interface.

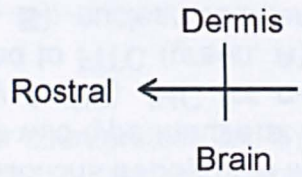

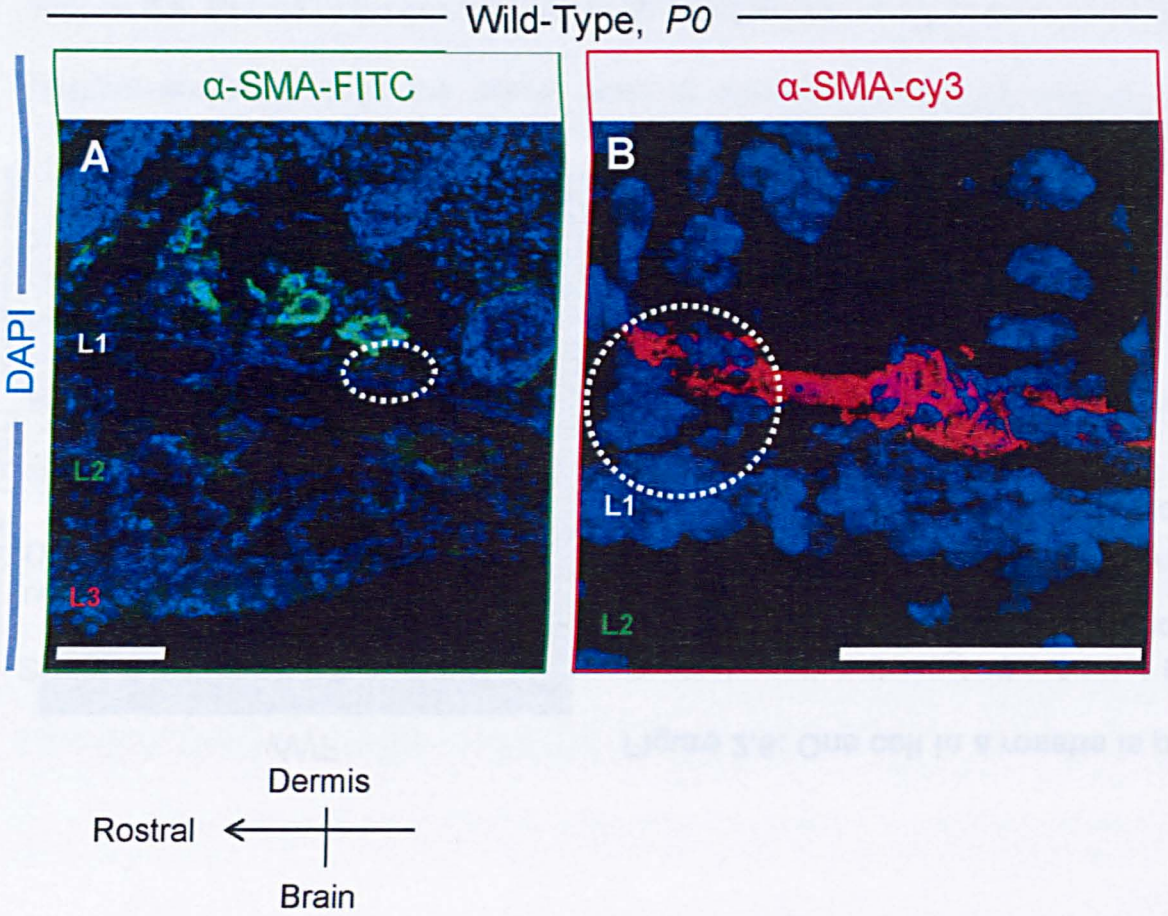

Figure 2.7: Rosettes connect the bone to dermis vasculature

Sagittal sections through the frontal bone of a wild-type mouse at post-natal day 1 (P0). IHC for α-SMA conjugated to FITC (green, **A**) and cy3 (red, **B**); nuclear counterstain DAPI (blue). Layers 1, 2, and 3 are indicated as **L1**, **L2**, and **L3**, respectively.

Rosettes connect to external (dermis) vasculature late in development. **A.** Mature area of the frontal bone where nascent blood vessels in the dermis, positive for the pericyte marker α-SMA, connect to a rosette (circled). **B.** Magnification of an area where an L1 rosette ties to a blood vessel in the dermis skirting the top of the bone.

Scale bar indicates 50μm.

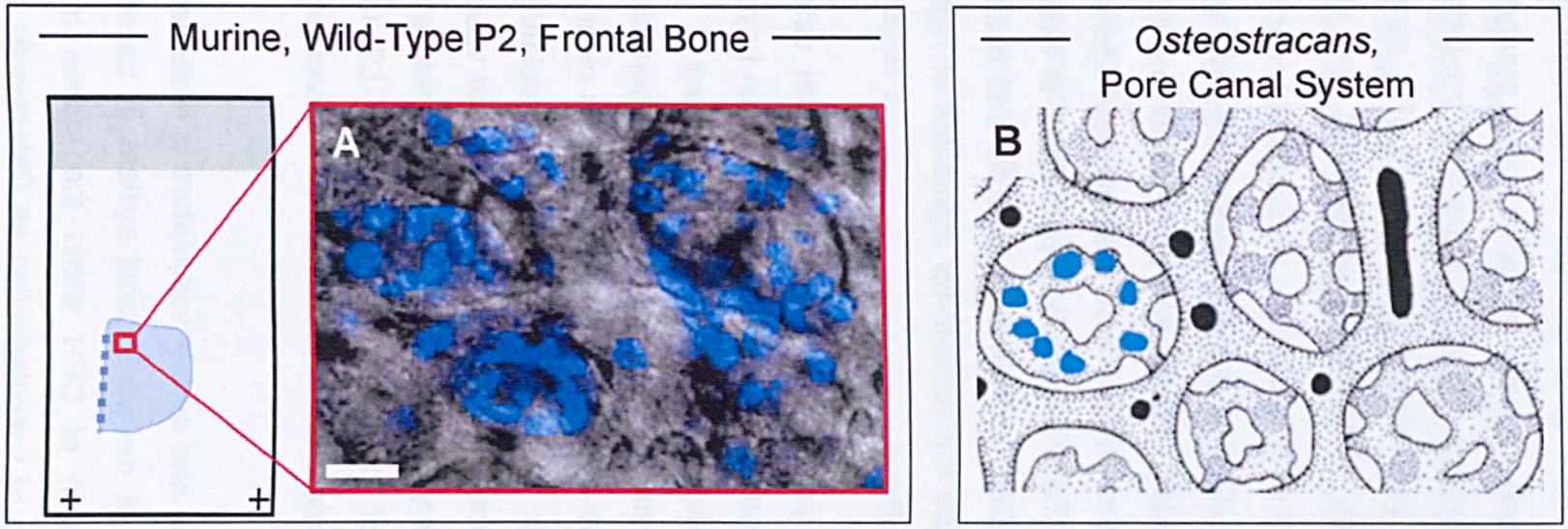

Figure 2.8: Rosettes are similar to the pore-canal system of basal vertebrates

A. Flat mount of the frontal eminence of a wild-type mouse at postnatal day 3 (P2). Nuclear counterstain DAPI (blue) and reflection imaging to examine bone topography. Three rosettes sit along the walls of craters formed by depressions in the bone surface. At the base of the crater a pore connects L1 to L2.

B. Diagrammatic surface view of the pore canal system of osteostracans, a clade of fossil, armoured jawless vertebrates from the Silurian and Late Devonian eras. The orientation of the system is similar to that of the rosette system. Modified from Gross 1956.

Scale bar indicates 50μm.

2.3 Conclusion

The observation that endothelial precursors enter L2 in a concomitant manner with osteoblastic cells is in contrast to the traditional model of intramembranous ossification whereby the bone forms around pre-existing vasculature. The current findings show that there is no pre-patterning of the bone by the vasculature, but rather a development of a cancellous bone structure by the expansion of sheets of osteoblastic and vascular cells intercalating into L2.

There is no evidence of involution of entire vessels from the dermis, as L1 and L3 create a closed system and the only entry points into L2 are through rosettes. The early clasp structures are surprisingly heterogeneous: cells of both neural crest and mesodermal origin co-participate in individual clasps and clasps can simultaneously contain both vascular and osteoblastic cells (Figure 2.9). Clasps provide the scaffold for ingression of highly migratory osteoblastic cells and endothelia.

Three-dimensional histological analysis shows that both osteoblasts and adjacent endothelial cells generate internal surfaces within Layer 2 that later connect up with vasculature on the outside of Layers 1 and 3. This observation is not commensurate with traditional angiogenesis modes that rely on 'sprouting' from pre-existing vessels as I find no clear-cut evidence for a direct physical link between early dermis vasculature and bone vasculature. The connection between the bones internal vascular network and external vessels is only evident in late stages of maturation, following extensive establishment of the internal organisation of L2, indicating that bone vasculature development is not predicated on contact with the dermis vasculature.

The late link between bone and dermis vasculature is facilitated by rosettes fulfilling the ancient role of the pore canal system in basal vertebrates. Interestingly, the expression of OPN within the rosette has additional significance in the context of vascularisation as Osteopontin expression is attractant for vasculature and plays a role in hematopoietic stem cell niches in bone (also termed osteoblastic niches) (Nilsson *et al.* 2005; Yin and Li

2006); as such the OPN+ cell of the rosette could play a role in attracting the endothelia of L1 to the rosette or mediating the late interface of L1 and external blood vessels.

Results from both Chapter 1 and 2 support a mode of dermal bone development where the generative architecture of the bone is dictated by *de novo* sheet formation within L2. The concomitant development of layer morphogenesis and angiogenesis is achieved by the paired entry and persistent juxtaposition of osteoblast and endothelial precursors, a spatial relationship that ensures mutual benefits to both cell types: osteoblasts are supplied with nutrients, while the vasculature can influence the bone development to prevent precocious ossification. In this model, co-development would further support a mechanism of growth that did not require re-modelling by osteoclasts to accommodate any additional vascular development after the establishment of mineralised matrix, explored further in Chapter 3.

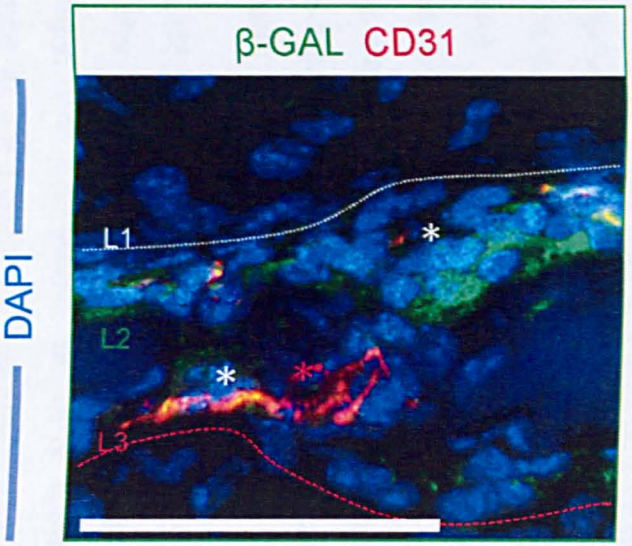

Figure 2.9: Clasps are formed by diverse cell types

Sagittal section through the frontal bone at embryonic day E18 after conception; *Wnt*1-Cre$^{+/-}$ x Rosa26LacZ$^{-/-}$ specimen. IHC β-Galactosidase showing neural crest cells (green) and CD31 (red) indicating endothelia; nuclear counterstain DAPI (blue).

A nascent clasp across L2 connects L3 to a rosette in L1 (the pore in the centre of rosette indicated *). This clasp comprises a neural crest cell, which is not endothelial, from L1 connecting to an endothelial cell of mesodermal origin (red *). The mesodermal endothelial cell is adjacent in Layer 3 to a neural crest-derived endothelial cell (white *).

Scale bar indicates 50μm

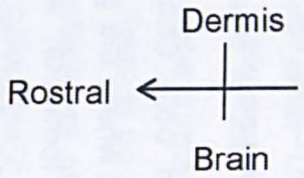

2.4 Summary of findings

- The development of intramembranous layer morphogenesis and *de novo* vasculature are paired; vasculature does not pre-pattern the bone's organisation;

- Vasculature in the frontal bone is of both neural crest and mesodermal origins;

- Both osteoblastic cells and endothelial cells enter the maturing L2 system via the rosettes;

- Rosettes also serve as anchor points for dermal bone vasculature to connect to the bone late in frontal bone maturation;

- Rosettes and the clasp system may be the mammalian counterparts of the pore-canal system in basal vertebrates and provide a framework for re-examining acellular bone in the gnathostome stem group.

3. Biomineralisation of dermal bones

3.1 Introduction

The establishment of layer morphogenesis and the parallel development of the bone vasculature led to a further analysis of another key process to bone maturation: matrix deposition and biomineralisation.

Biomineralisation is the process by which the mineral phase is added to the organic matrix leading to the hardened bone tissue (Bala *et al.* 2010). In the case of vertebrates, the mineral phase of bone, dentine and tooth enamel predominantly consists of calcium phosphate (hydroxyapatite) crystal formation along a collagen scaffold (George and Veis 2008; Weiner 2008). The organic phase (the osteoid) is primarily comprise collagens, but also contains proteoglycans and acidic non-collagenous proteins containing glycosaminoglycans (Golub 2009) and the process by which the hydroxyapatite crystals form in the osteoid *in vivo* is highly contentious. Alternate theories for the initial nucleation have been proposed, with the most widely supported being the heterogeneous nucleation theory, favouring direct formation of apatite from soluble inorganic ions on organic and inorganic precursors (Veis 1981). Irrespective of how nucleation commences, it is generally accepted that biomineralisation is essentially the process by which the crystals form along the collagen scaffold nucleating on the collagens themselves, by entering the collagen pore and growing in between collagen fibres or by growing along the fibres as thin platelets perpendicular to the longitudinal axis of the fibres (Gajjeraman *et al.* 2007); biomineralisation in vertebrates may or may not involve an early unorganised mineral being replaced by a more stable structured mature crystalline phase, a mode of growth found in invertebrates that can be induced in mammalian tissues (Crane *et al.* 2006; Weiner 2006).

The issue of remodelling the bone matrix is complex: remodelling is a constant feature of some endochondral bones, however some species (such as rodents) display little secondary remodelling (Bala *et al.* 2010), in these

animals –as in dermal bones- the initial mineral deposition may be highly controlled and coordinated if later remodelling is not expected.

Several genes play a role in directing the process of biomineralisation: Osteopontin has the contrasting functions of both promoting mineralisation and also capping it in a directional manner: growth of HAP crystals can only occur away from the Osteopontin protein core and the polarisation of Osteopontin localization has direct implications for the directionality of emerging HAP crystals (Boskey *et al.* 1993; Boskey 1995). Similarly in calcified cartilage Fibronectin also acts to mediate the mineralisation process (Burton *et al.* 1996) and Collagen itself is implicated in crystal modulation (Gajjeraman *et al.* 2007). Many extracellular matrix proteins are acidic and inhibit calcification by binding Ca^{2+} and there is enough calcium phosphate in bone tissue that crystal inhibitors are required to prohibit spontaneous mineralisation leading to a hyper-calcification (Marcus *et al.* 2008; Weiner 2008; Golub 2009). The roles these genes play in the biomineralisation of dermal bone has not been extensively studied *in vivo*, despite mutants being available for many of them (Aubin *et al.* 1995; Norris *et al.* 2007; Frazen *et al.* 2008; Farrow *et al.* 2009); indeed the process of biomineralisation is typically explored in endochondral bones as dermal bone ossification was perceived as a variant of endochondral ossification. Outstanding issues of dermal bone biomineralisation include: to what extent the initial mineralisation process is controlled by the osteoblasts expressing Runx2, OPN and/or Fibronectin; additionally, the pre-eminence of either initial mineral deposition or later remodelling remains to be clarified.

For the purpose of the current study, the aim was to explore how the forming bone architecture and gene expression influences mineralisation of dermal bones: the newly identified mechanism of continually supplying cells to the bone as it grows in thickness would be expected to have implications for the process of biomineralisation. To this end, I examined the ontogeny of dermal bone biomineralisation, and conducted a study of the process of collagen synthesis, cleavage and concomitant matrix production *in* and *ex vivo.*

3.2 Normal time-course of matrix deposition in dermal bone

The process of bone mineralisation was examined *ex vivo* by the histological addition of calcein, a fluorescent chelating agent that marks bone mineralisation by incorporating into areas where calcium-phosphate (hydroxyapatite) has been added to the osteoid (Hale *et al.* 2000; O'Brien *et al.* 2002; Kihara *et al.* 2004). During a time-course of development from E12 through birth, the presence of mineralised osteoid in dermal bone was confirmed at E14.

Early mineralisation occurred within very immature regions of L2, near the coronal suture, in distinct 'clouds' or 'islands' (Figure 3.1). Each calcein+ island was separated from its neighbour by the clasps across L2, which remained unmineralised, and the extent of the mineralisation did not reach L1 or L3 (Figure 3.1B). In a more mature region of L2, the mineralised islands formed a single plane of mineralisation. As development progressed, sheets of mineralised matrix form parallel to the surface of the bone. These calcein planes were physically separated by non-mineralised sheets of cells, which reached from L1 to L3, connected to the clasps/rosettes identified above (Figure 3.1C). The calcein planes were, therefore, like tectonic plates or plywood that could be moved as the system increased in complexity, allowing thickness growth to occur without stunting the lateral and vectorial growth of the bone taking place simultaneously. Curiously, the planes of mineralisation were located centrifugally, an unusual feature that counters the classical concept of apposition, which would imply the planes should be stacked from L3 towards L1.

In the clavicle at E18, the blocks of mineralisation are fully surrounded by Undulin positive flattened cells, giving the impression that calcein carrying areas are packaged by the Undulin+ cells producing the matrix (Figure 3.2). These cells are adjacent to small blood vessels observed within the spongious matrix, giving the appearance of a contiguous growth surface of Undulin+ osteoblasts and endothelial cells within Layer 2. This observation would be commensurate with a *de novo* sheet formation within Layer 2 as,

again, the points of entry are focal and involution of entire Layers 1 and 3 was not observed,

Cells trapped within the mineralised matrix, presumably producing the osteoid, were unexpectedly heterogeneous: all cells at the margin of the calcein-positive areas were Undulin-positive; conversely Runx2-expression was variable and the cells surrounding and within the mineralised areas were largely, but not entirely Runx2-positive (Figure 3.3). The expression pattern of Osteocalcin (OCN) was equally intermittent: Osteocalin expression appeared confined to cells that were not fully embedded in the mineralised front. In the immature condition a discernible cleft is evident between the margin of OCN and the calcein-positive island (Figure 3.4); in the mature bone, cells surrounded by calcein are largely OCN-negative, especially toward the internal margins of the bone away from L1 (Figure 3.4). Osteocalcin negativity in mineralised areas was unexpected as Osteocalcin is reportedly a marker of late osteoblasts and osteoclasts.

Taken together, results of the *ex vivo* study indicate the biomineralising zone changes significantly with time (from clouds-like structures, to flat sheets within L2, to multi-layered planes interconnected by radial areas of mineralisation) suggesting a remodelling process. However, in light of the irregular pattern of Runx2 and OCN expression within the biomineralising zone, it is impossible from the *ex vivo* study to determine the identity of the cells producing the matrix and, potentially, accomplishing the remodelling.

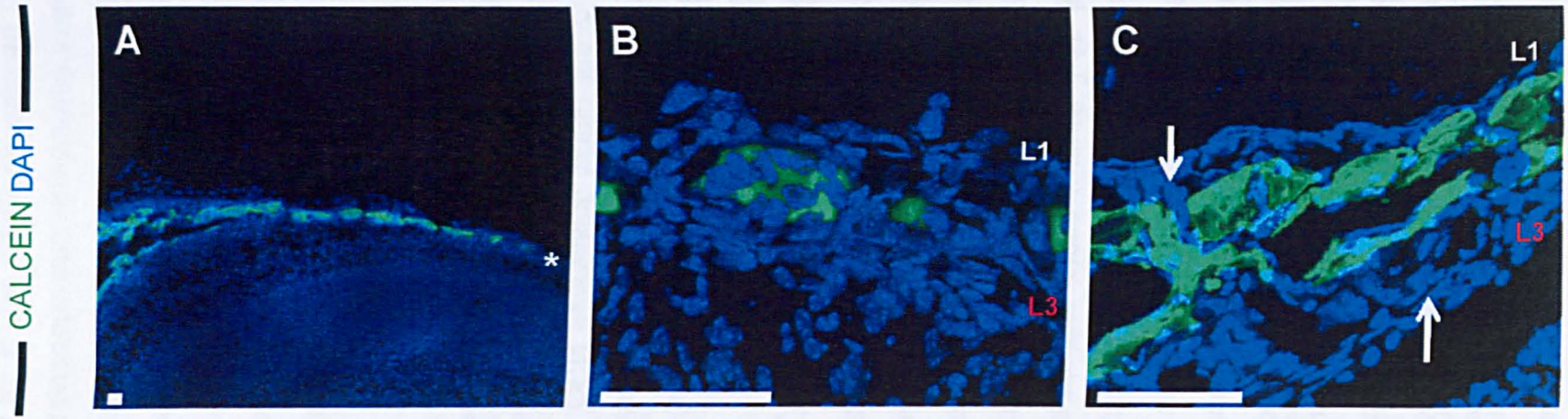

Figure 3.1: Mineralisation begins as islands and becomes planes surrounded by non-mineralised walls

Sagittal sections of a wild-type frontal bone at embryonic day E16 after conception (positive vaginal plug is taken as E0). Histological addition of calcein (green) stains the mineralised matrix; nuclear counterstain DAPI (blue). Layers 1 and 3 are indicated as **L1** and **L3**, respectively.

A. Overview of calcein positive areas along the frontal bone. Mineralisation begins adjacent to the coronal suture (*). Matrix mineralises in individual islands (**B**) surrounded by un-calcified clasps.

C. In the most mature region two planes of mineralisation form in parallel and sheets of cells still connect unmineralised L1 to unmineralised L3 (arrows). Calcified areas are found toward the centre of L2.

Scale bar indicates 50µm.

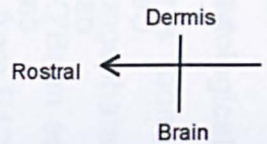

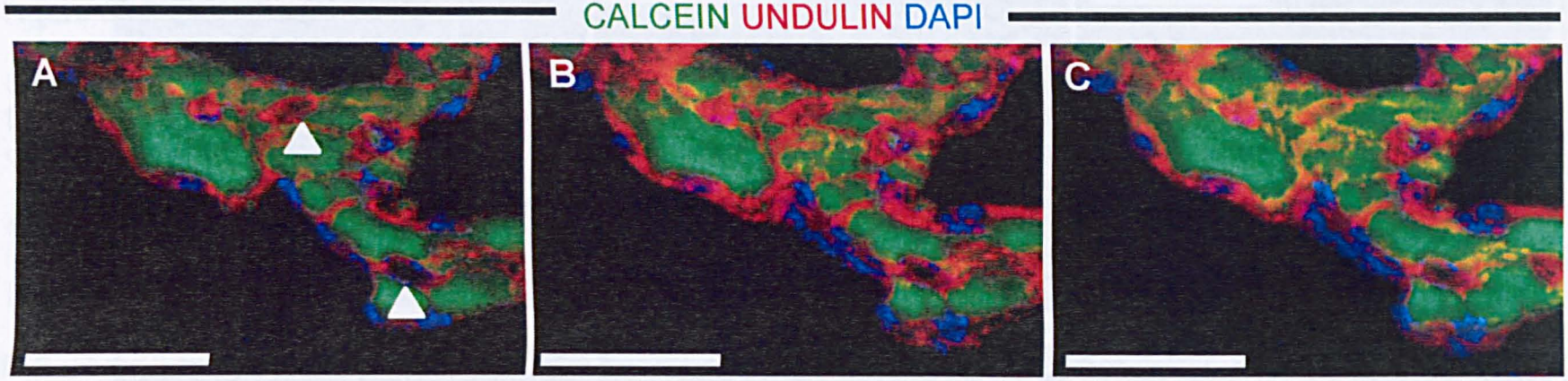

Figure 3.2: Undulin-positive cells surround and package mineralised islands

Sagittal sections of a wild-type clavicle at embryonic day E18 after conception. Calcein stain of mineralised matrix (green); IHC for Undulin (red); nuclear counterstain DAPI (blue).

A-C. Calcein was reconstructed in 3D and the nuclei and Undulin from three optical sections was stacked to show the Undulin+ projections of cells encompassing the mineralised islands. In **A** blood vessels are indicated (white arrowheads); the top blood vessel is inside the calcified area and the stacks indicate a contiguous growth surface of Undulin+ osteoblasts and endothelial cells inside the spongious Layer 2.

Scale bar indicates 50µm.

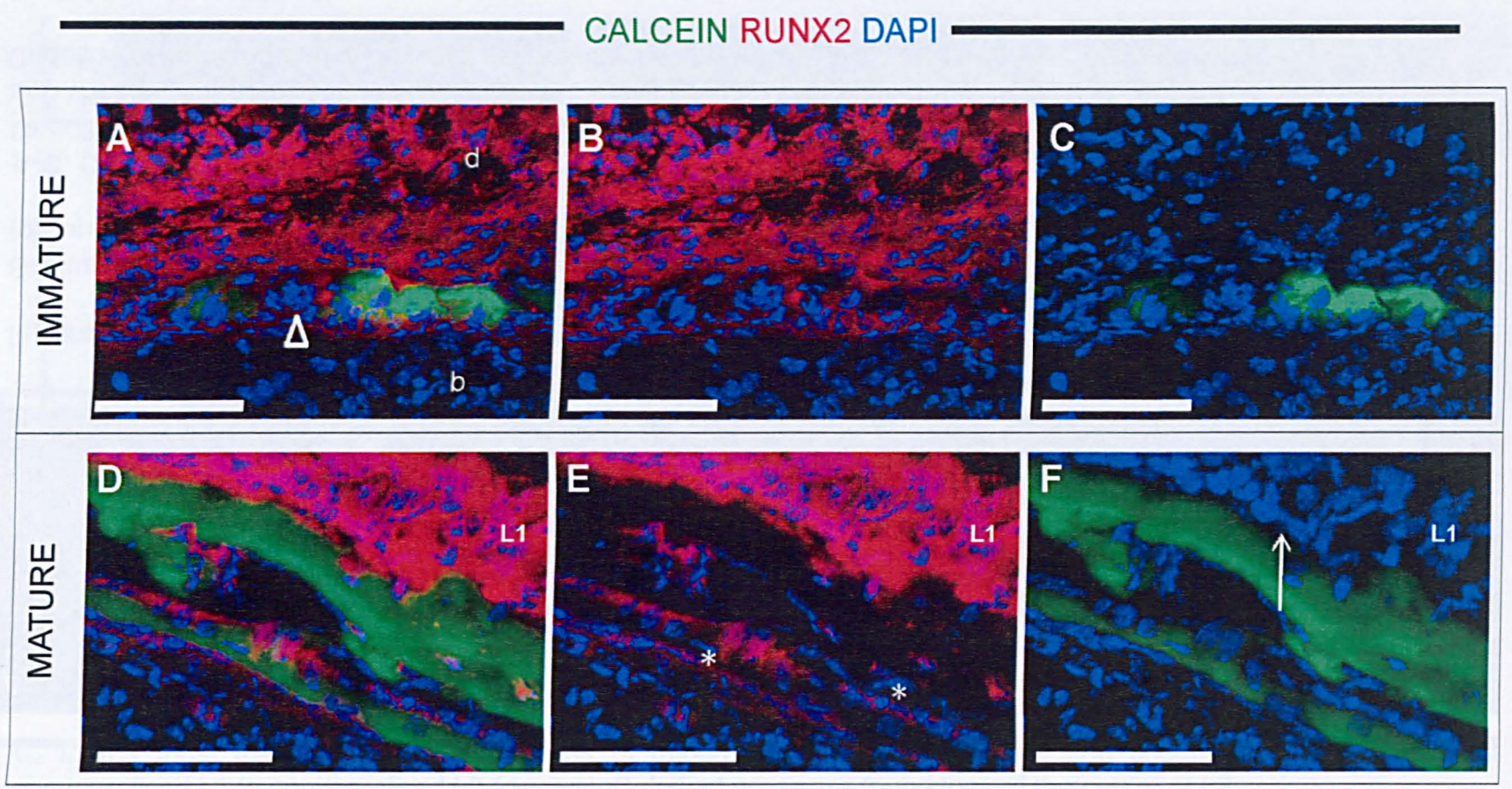
CALCEIN RUNX2 DAPI
IMMATURE
MATURE
A
B
C
D
E
F
d
b
Δ
L1
L1
L1
*
*

Figure 3.3: Runx2-positive osteoblasts in the mineralised matrix

Sagittal sections of a wild-type frontal bone at embryonic day E16.5 after conception (positive vaginal plug is taken as E0). Calcein stain of mineralised matrix (green); IHC for Runx2 (red); nuclear counterstain DAPI (blue). Images are oriented cranial to the top and ventral to the left.

A-C. Bird's eye-view of Layer 1:2 interface showing Runx2 expression in relation to matrix mineralisation in the immature frontal bone. Cells sitting on top of calcein 'clouds' are Runx2+. Notably, this Runx2 expression is weaker than expression within L1. Part of a rosette (arrowhead) is seen separating the two mineralised clouds.

D-F. Runx2 expression in the most mature aspect of L2 in the frontal bone of an E16.5 mouse; two planes of mineralised matrix are surrounded by Runx2+ cells (with a cleft between the calcein and the generative Layer 1, arrow in **F**). The majority of the cells sitting in calcified matrix are Runx2, with some exceptions (*).

d Dermis, **b** Brain

Scale bar indicates 50μm.

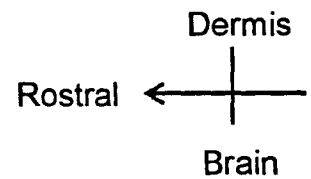

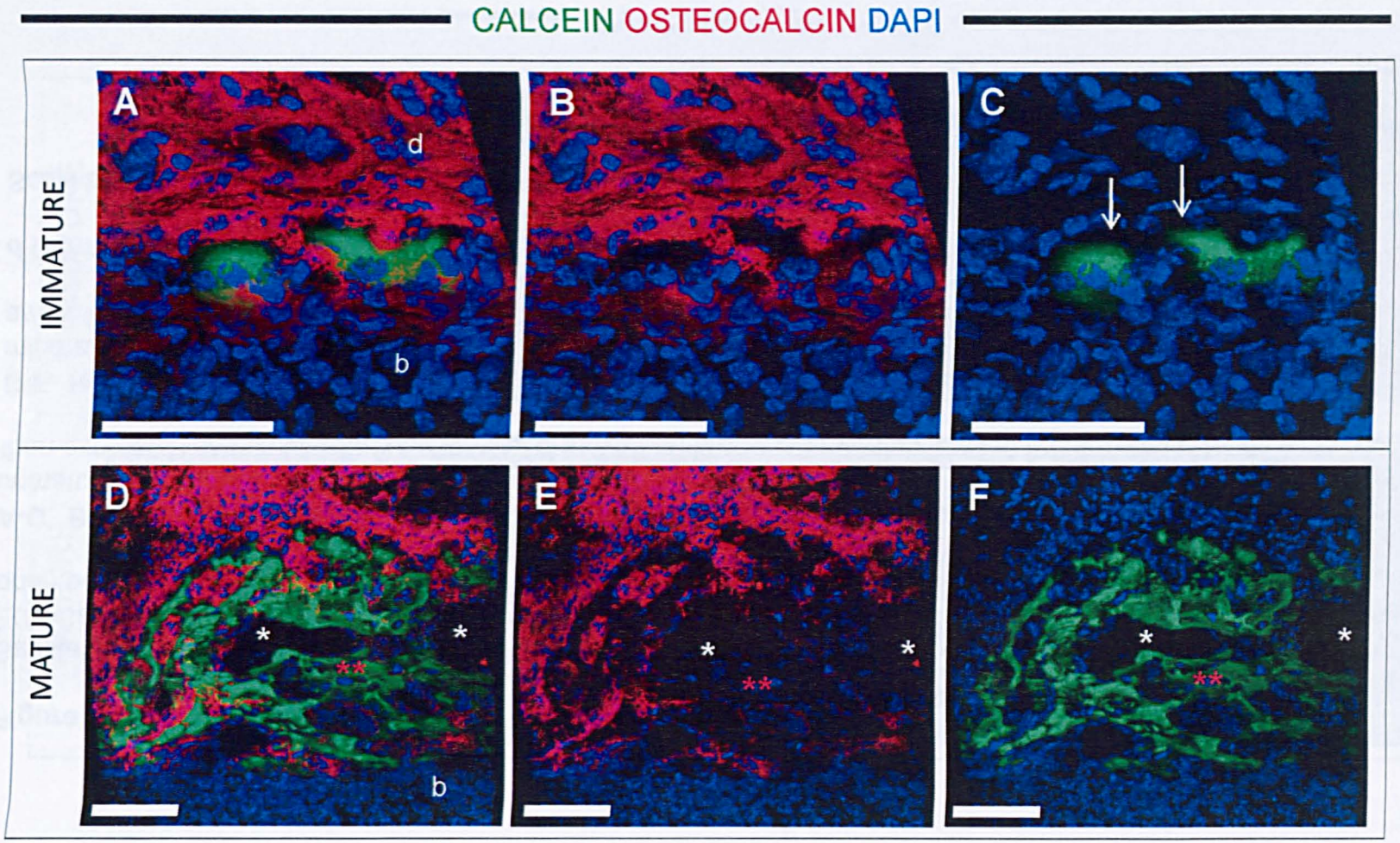
CALCEIN OSTEOCALCIN DAPI
IMMATURE
MATURE
A
B
C
D
E
F
d
b
b
*
**

Figure 3.4: Osteocalcin-positive osteoblasts surround the mineralised matrix

Sagittal sections of a wild-type frontal bone at embryonic day E16.5 after conception. Calcein stain of mineralised matrix (green); IHC for Osteocalcin (red); nuclear counterstain DAPI (blue).

A-C. Osteocalcin expression in relation to matrix mineralisation in the immature frontal bone. Cells along the margin of the calcified area (not within it) are Osteopontin positive. There is a cleft (indicated with an arrow in **C**) between OCN expression and the mineralised matrix, visible comparing **B** and **C**.

D-F. Osteocalcin expression in the most mature aspect of the E16.5 frontal. Osteocalcin expression is confined to the exterior aspects of the bone. Cells at the internal calcification are negative for OCN expression or only very weakly positive (red **). Blood vessels are indicated (white *).

d Dermis, **b** Brain

Scale bar indicates 50µm.

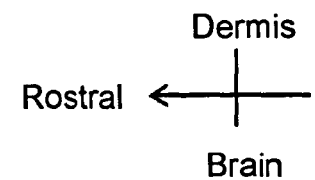

3.3.1 Introduction

I designed an *in vivo* time-course experiment to explore the exact spatial extent of the mineralising zone in dermal bones and its changes in time. Two alternative cellular models of biomineralisation were feasible in light of the results of the *ex vivo* calcein study (namely the molecular heterogeneity of the cells in the mineralising zone and the apparent remodelling of the mineral phase) (Figure 3.5):

A) Apposition: non-mineralised cells could sandwich the mineralised area and lay osteoid appositionally.

B) Nesting: osteoblasts could invade the mineralised matrix and continually remodel the bone as it grows from within.

The former model, A, would require the younger matrix to be deposited on top of the previous matrix; the finding that the mineralised areas are always located centrifugally would indicate cells enter from Layer 1 and 3 and encase previous matrix with new osteoid. Alternatively, model B would lead to remodelling taking place within (and outside of) previously established mineral and new osteoid would be located within a shell of older matrix (Figure 3.5).

For *in vivo* analyses, fluorescent chelating agents would be injected into pregnant dams at concentrations high enough to confer the dye to the embryos without producing pharmalogical side effects (ex: high doses of tetracyclines can alter osteoblastic metabolic rhythms and impair bone formation *in vitro* (Tam and Anderson 1980; Simmons *et al.* 1981)). At a later time-point a second dye would be injected, and an analysis of the dye configuration would yield an insight into the patterns of biomineralisation, including any remodelling taking place. Injections would be made into the peritoneal cavity and the physical proximity of the osteoblasts and blood vessels in the bone would ensure dye delivery to the target matrices. The

labelling experiments would address the two models of bone mineralisation supported by the *ex vivo* calcein experiments (Figure 3.5) and support the model of layer morphogenesis (namely, two generative layers) hypothesized in Chapter 1. If the mineralisation occurs purely appositionally and there are two generative surfaces (L1 and L3), the first injected colour is expected to be sandwiched by the second colour injected; alternatively if deposition is appositional from a single generative surface, the second colour will be external to the first. Alternatively, a more unusual alternative would be if cells continually invade and nest into the previously established matrix resulting in the second colour found inside areas labelled by the first injection. The appropriate license for the experiments was procured and the following controls conducted prior to commencing the experiments:

3.3.2 Controls for *in vivo* labelling experiments:

3.3.2.1 Histological addition of chelating agents to confirm there is no spectral overlap. The labelling agents chosen for the *in vivo* analyses had previously been used in *in vivo* studies of endochondral bone repair, where they were successfully imaged without overlap (Pautke *et al.* 2005). To confirm it is possible to image the labelling agents without overlap, previously untreated slides from wild-type mice were subjected to histological addition of each agent (at *in vivo* concentrations) and imaged. Despite the previously published report, I found a high level of spectral overlap between the compounds (Figure 3.6, Technical Appendix 11.1). The slides were deemed to be over stained as the actual concentration of dye incorporated into the matrix *in vivo* would be significantly less than the histological preparations using the injection concentration. Using confocal microscopy, a wave-length spectrum for each labelling agent was established that diminished the overlap between the emissions of the various dyes, and this optimal range was used in all ensuing experiments. However, to ensure maximal confidence in the experiment it was decided that the two dyes most frequently used would be calcein and xylenol orange, due to their largely

non-overlapping spectra. If a third dye was to be added, it would be doxycycline, added in a sequence guaranteeing no time overlap with calcein.

3.3.2.2 Time-course of dye retention. To confirm the individual labelling agents would clear the system prior to the addition of the next compound, a single labelling agent was added to a dam between E11-12 and the offspring were isolated at two time-points, E18 and P2. Matrix mineralisation first occurs at E14, so any labelling agent present still from the E11-12 injection that was retained in the system for more than 2 days would incorporate into the matrix. The 2 day gap between injection and mineralisation was chosen as 2 days was the desired minimum injection period between addition of labelling agents in the later experimental phase of the project. Analysis revealed the matrix of the animals injected between E11-12 did not contain any labelling agents, when examined at E18 and P2 (Figure 3.7). Examining the two time-points of sacrifice was done to ensure that any areas that were labelled by the E11-12 injections were not missed due to subsequent remodelling *in vivo* (leading to the erroneous conclusion that the dye had not been retained through the mineralisation). I conclude from these findings that the dye does not circulate within the system for more than 2 days and incorporation times closely matched the injection times.

3.3.2.3 Dye swap. The next control was to ensure that different fluorescent dyes would not preferentially label different types of matrix and would not differ significantly in their ability to penetrate through tissues. To this end dye swap experiments were performed such that each labelling experiment was conducted as a pair involving a dye reversal; ie calcein injection at E14 and xylenol orange at E18 has the dye swap control of xylenol orange injection at E14 and calcein at E18. Patterns produced by the labelling regime could be confirmed in the dye swap to validate they were not a result of –for example- preferential binding of one labelling agent.

3.3.3 Results of *in vivo* labelling experiments

The initial labelling experiment (EX1) consisted of a calcein injection at E14, followed by xylenol orange injection at E16 and specimens were isolated and analysed at postnatal day 3 (P2). Analysis revealed an inside-out arrangement with the majority of xylenol orange labelling nested inside calcein labelling (Figures 3.8-3.9); the implication that cells dug into the calcein-labelled matrix is supported by focal areas where xylenol orange extended from the inside of the calcein block to its external face, presumably indicating the cell's entry point into the previously mineralised area. Notably, at high magnification, the areas were largely green *or* red, and although closely nested, they were not yellow, demonstrating the matrix was deposited by two separate cells (as a single cell carrying both dyes would incorporate the dyes into the matrix at a spatial resolution leading to a yellow appearance). Neither L1 nor L3 was labelled, and the cleft between the generative layers and the mineralised matrix suggests osteoid secretion occurs only after cells have invaded L2.

The short interval between the injections, and the resulting nested pattern, illustrated the dynamic nature of the L2 mineralising area and the fast pace of matrix production and subsequent remodelling. A successive experiment (EX2) lengthened the time between injections (calcein injection E14, xylenol orange injection E18) and results indicated a pattern where xylenol orange encased calcein, which in turn surrounded a xylenol orange core (Figure 3.10). This xylenol-calcein-xylenol pattern indicates that between E18 and birth (the timeframe for xylenol to be present in the system) some cells remodel the existing calcified matrix, while others enter the system and start depositing new mineralised matrix. The orientation of the calcein toward the centre of L2 is reminiscent of the *ex vivo* experiments, implying that as cells enter L2 from L1 and L3, the generative layers progressively move away from each other and new cells enter L2, sheathing the pre-existing L2 architecture. There was a tendency for unlabelled areas (calcified after both dyes had cleared) to be more extensive toward L1, raising the possibility that L1 is more active than L3 in inserting cells into L2 in the two days following birth (Figure 3.10).

A specimen from the dye swap of EX2, with the injection regimen E14-Xylenol Orange;E18-Calcein, matured to P8, was then analysed to examine the extent of the remodelling through the first week of murine postnatal development. Similarly to the specimen isolated immediately after birth, the initial xylenol orange labelling is found toward the centre of L2, furthest from L1 and L3 (Figure 3.11). One cell within L2 can be seen carrying the second colour (calcein), which has dug into the area that is otherwise xylenol labelled (Figure 3.11). An additional cell is observed traversing the calcein front; the radial collagen fibres emanating from this cell are visualised using refection imaging, showing this cell carries no label, indicating remodelling is actively taking place even in the postnatal condition when the dyes are no longer being incorporated by the cells. Indeed, the degree of remodelling is evidenced by the extensive area within the mature frontal bone of the P8 specimen that is unlabelled.

After the first week of post-natal development there are striking changes within L1 and L3. At the L1:L2 border there is a region where cells from L1 appear to have deposited a thin layer of unlabelled matrix appositionally onto the top of L2 (Figure 3.11), giving this region the appearance of a characteristic compacta. Even more dramatically, the condition of L3 at P8 is extremely altered from that of a littermate examined at P2. Immediately after birth the thin stacks of cells in L3 were unmineralised and tightly packed, contrasting this a week later, L3 has mineralised and the cell sheets within L3 are widely spaced apart and cell sparse: this arrangement is reminiscent of a classical appositional model of matrix deposition whereby cells deposit matrix (either polarised toward L2 or in all directions) and become separated from one another, trapped in the secretions from themselves and the osteoblasts surrounding them.

Intriguingly, reflection imaging in the late L3 condition displays plywood-like crossed bundles of collagen fibres, indicative of what in basal vertebrates is termed the isopedine layer (Gross 1956; Donoghue and Sansom 2002).

3.3.4 Conclusion

Results from *in vivo* labelling experiments indicate a dual mechanism of dermal bone biomineralisation; from E14 through birth the mineralising zone is a dynamic space with L2 being actively remodelled by cells intercalating from L1 and L3, and after birth there is a later stage of appositional addition of matrix from L1 and L3 (Figure 3.12). The secondary invasion of cells into areas already arranged into collagen fibres is similar to the process by which scales mineralise in zebrafish (Le Guellec *et al.* 2004), potentially highlighting that remodelling by invading cells is a conserved feature between teleosts and mammals. Mineralisation is known to be guided along a collagen scaffold (Golub 2009) and our reflection imaging appeared to show the collagen within the bone; I next investigated the collagen system and its relationship to the biomineralisation pattern observed *in vivo*.

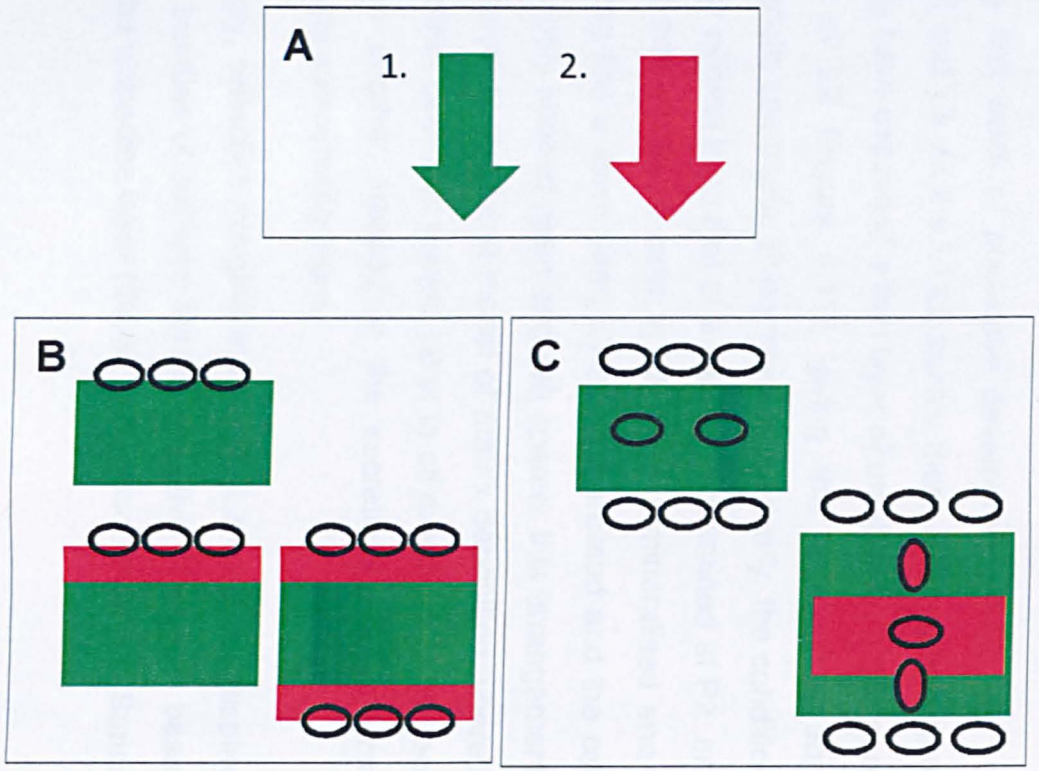

Figure 3.5: *In vivo* biomineralisation experiment designed to assess the growth mode of the mineralising zone

A. Two fluorescent dyes (green and red) will be sequentially delivered to the mineralising bone of murine embryos via intraperitoneal injection to pregnant dams. The resulting pattern of the dyes will indicate the mode of growth.

B. Appositional biomineralisation. Osteoblasts from one or two generative surfaces will secrete osteoid that becomes mineralised; the first mineralised matrix will be labelled green and will be sandwiched by the second colour (red).

C. Deposition of osteoid in a nested pattern. Cells produce osteoid only once inside L2 and mineralised matrix can be remodelled by subsequent osteoblasts entering the system carrying the second dye. The second colour is sandwiched inside the first.

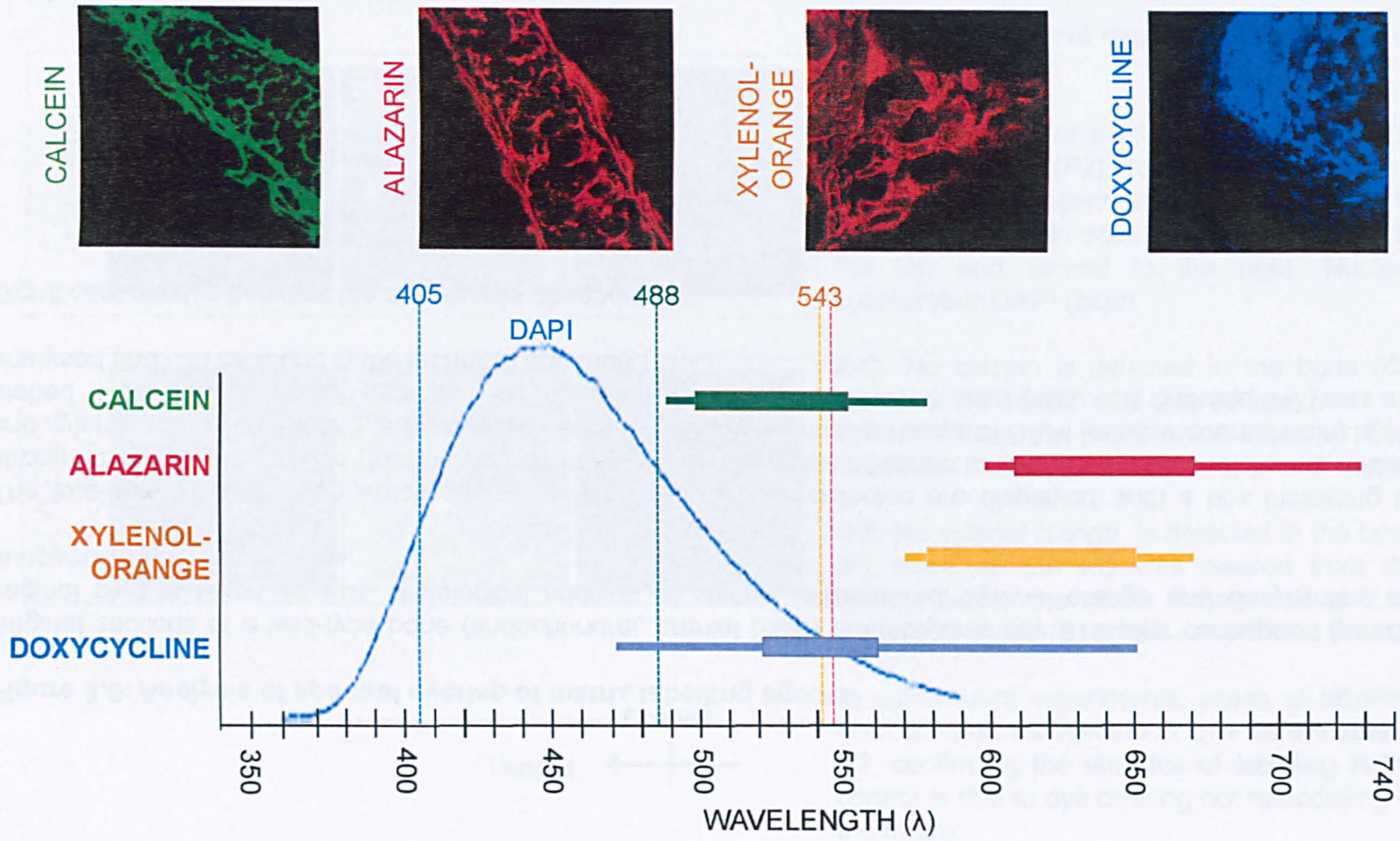
CALCEIN
ALAZARIN
XYLENOL-
ORANGE
DOXYCYCLINE
405
488
543
DAPI
CALCEIN
ALAZARIN
XYLENOL-
ORANGE
DOXYCYCLINE
350
400
450
500
550
600
650
700
740
WAVELENGTH (λ)

Figure 3.6: Analysis of spectral overlap of matrix labelling agents

Sagittal sections of a wild-type bone (endochondral, cranial base) at embryonic day E18 after conception (positive vaginal plug is taken as E0). Histological addition of calcein, alizarin red, xylenol orange and doxycycline and subsequent spectral analysis.

The total emission range in which each labelling agent can be detected are displayed, with a box indicating the strongest area of expression (from which the images were collected). Calcein was excited off the 488 laser, alizarin and xylenol orange off the 543, and doxycycline off the 405. The emission curve of DAPI (nuclear counterstain) is also plotted. The emission of each potential labelling agent when excited with each laser (405, 488, 543 and 647) was also analysed and can be found in the technical appendix (11.1).

Significant overlap between the agents was observed.

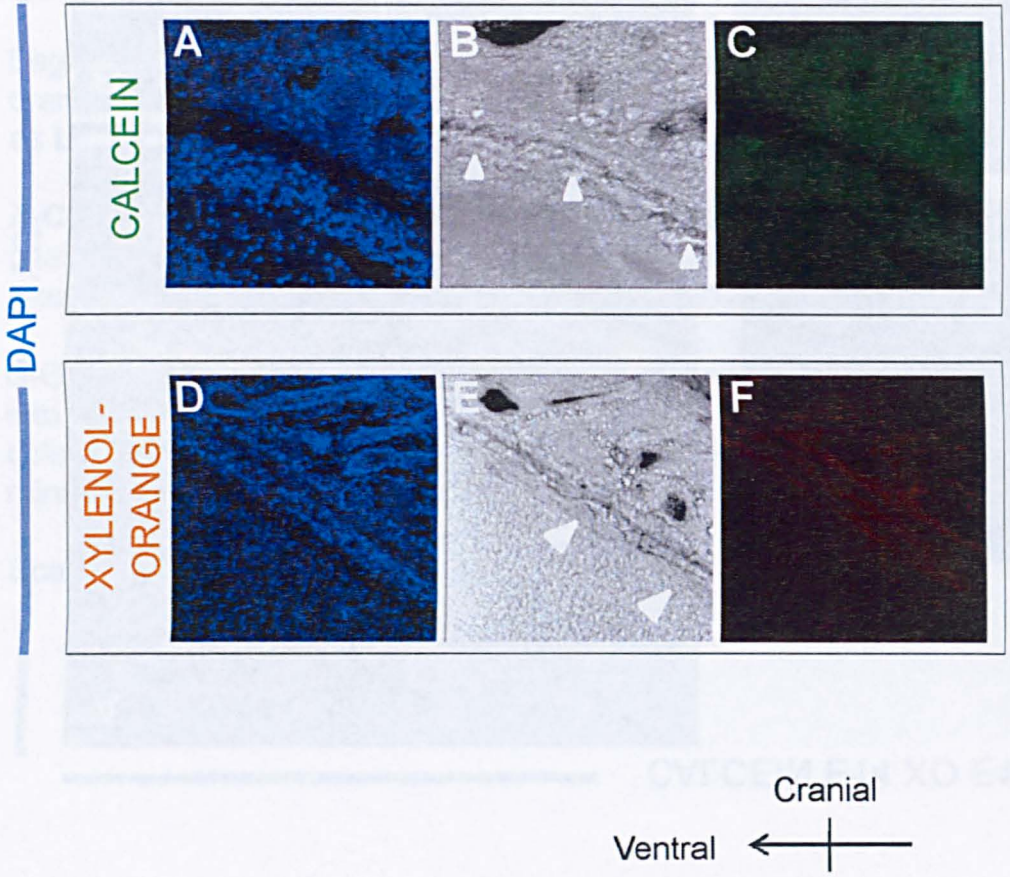

Figure 3.7: Control experiment: analysis of dye clearing

Sagittal sections of a wild-type frontal bone at postnatal day 3 (P2), following injection of a single labelling agent at embryonic day E11 after conception. Images are oriented cranial to the top and ventral to the right. Nuclear counterstain DAPI (blue).

A-C. No calcein is detected in the bone (**C**), therefore the calcein was cleared from the system before the matrix mineralised at E14. Reflection image (**B**) shows mineralised areas.

D-F. No xylenol orange is detected in the bone (**F**), therefore the XO was cleared from the system before the matrix mineralised at E14. Reflection image (**E**) shows mineralised areas.

In subsequent experiments, areas of labelling from compounds injected at E14 were visible at P2, confirming the absence of labelling in the control is due to dye clearing not remodelling of the matrix.

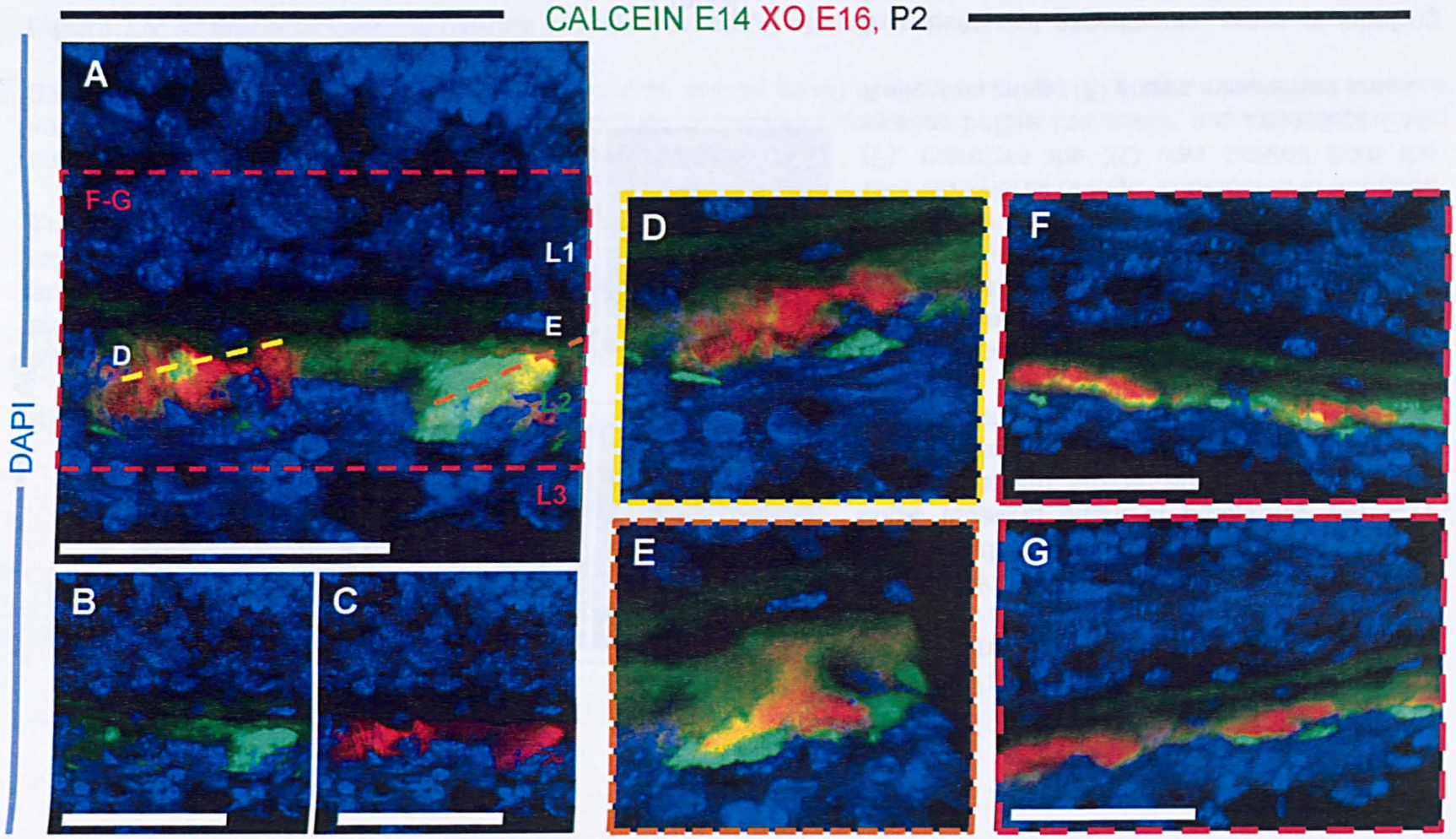
CALCEIN E14 XO E16, P2
DAPI
A
F-G
L1
E
D
L2
L3
B
C
D
F
E
G

Figure 3.8: Labelling Experiment 1: A nesting pattern of labelling agents

Sagittal sections of a wild-type frontal bone at postnatal day 3 (P2), following injections of calcein at E14 and xylenol orange at E16 (positive vaginal plug is taken as E0). Nuclear counterstain DAPI (blue). Layer 1, 2 and 3 are indicated as **L1**, **L2** and **L3**, respectively.

A-C. Overview of calcein and xylenol orange patterns in an immature frontal bone region; overlay in **A** and individual channels **B-C** show that xylenol orange labelled matrix (second colour injected) is found nested inside calcein positive areas (first colour injected). The section lines of **D-G** are indicated.

D-G. The surface of the 3D reconstruction was sectioned through (clipping plane into the plane of the image) to look into the cross section of the nested expression. The second colour injected (xylenol orange) is found inside the first colour (calcein) indicating the system was remodelled allowing additional osteoid (red) to be laid within the previously mineralised area (green).

Scale bar indicated 50μm.

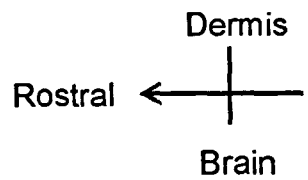

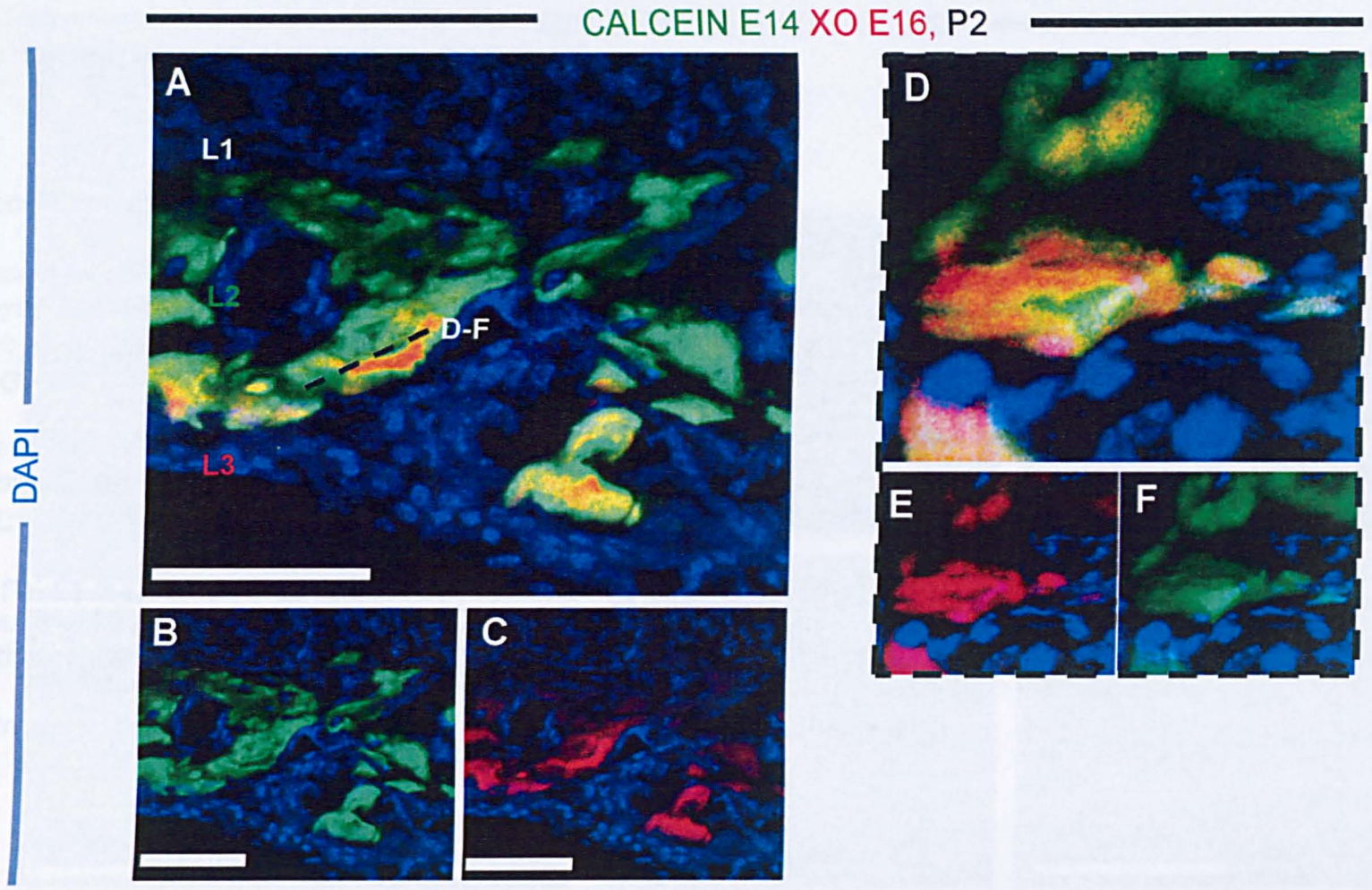
CALCEIN E14 XO E16, P2
DAPI
A
L1
L2
L3
D-F
B
C
D
E
F

Figure 3.9: Labelling Experiment 1: The biomineralising zone is subject to remodelling

Sagittal sections of a wild-type frontal bone at postnatal day 3 (P2), following injections of calcein at E14 and xylenol orange at E16 (positive vaginal plug is taken as E0). Nuclear counterstain DAPI (blue). Layer 1, 2 and 3 are indicated as **L1**, **L2** and **L3**, respectively.

A-C. Overview of calcein and xylenol orange patterns in a mature frontal bone region; overlay in **A** and individual channels **B-C** show that xylenol orange labelled matrix is found nested inside calcein positive areas. The section lines of **D-F** are indicated.

D-F. The surface of the 3D reconstruction was sectioned through (clipping plane into the plane of the image) to look into the cross section of the nested dyes. The second colour injected (xylenol orange) is found inside the first colour (calcein) indicating the system was remodelled. At places the line of xylenol orange expression extends to the external face of the calcein island, indicating a potential entry point of the cell delivering the xylenol labelled-mineral.

Scale bar indicated 50μm.

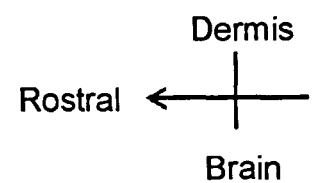

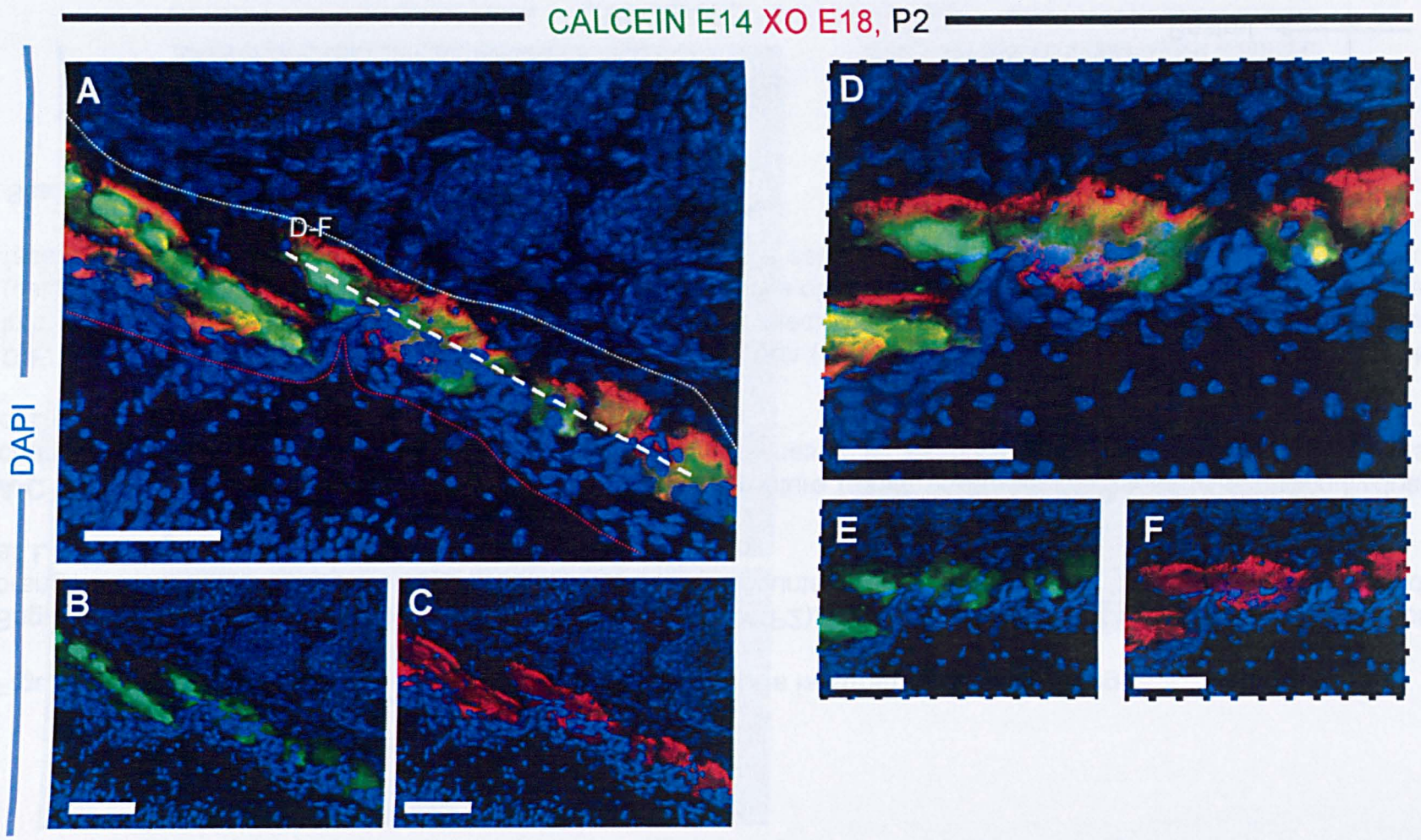
CALCEIN E14 XO E18, P2
DAPI
A
D-F
B
C
D
E
F

Figure 3.10: Labelling Experiment 2: Cells remodel previously calcified matrix and secrete new osteoid

Sagittal sections of a wild-type frontal bone at postnatal day 3 (P2), following injections of calcein at E14 and xylenol orange at E18 (positive vaginal plug is taken as E0). Nuclear counterstain DAPI (blue). Layer 1, 2 and 3 are indicated as **L1**, **L2** and **L3**, respectively.

A-C. Overview of calcein and xylenol orange expression patterns in an immature frontal bone region; overlay in **A** and individual channels **B-C** show that xylenol orange expression is found nested inside calcein positive areas, as well as external to the calcein areas where new cells enter the system and secrete matrix that becomes mineralised. The section lines of **D-F** are indicated. The external boundaries of L1 and L3 are indicated with white and red dotted lines, respectively.

D-F. The surface of the 3D reconstruction was sectioned through (clipping plane into the plane of the image) to look into the cross section of the nested labelling pattern. The second colour injected (xylenol orange) is found nested inside the first colour (calcein) indicating the system was remodelled; and xylenol-positive areas outside the calcein-reactive border indicates that new cells enter from L1 and L3 and secrete new matrix that subsequently mineralises.

Scale bar indicated 50μm.

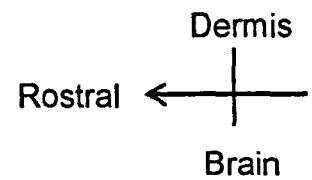

DAPI XO E14 CALCEIN E18, P8

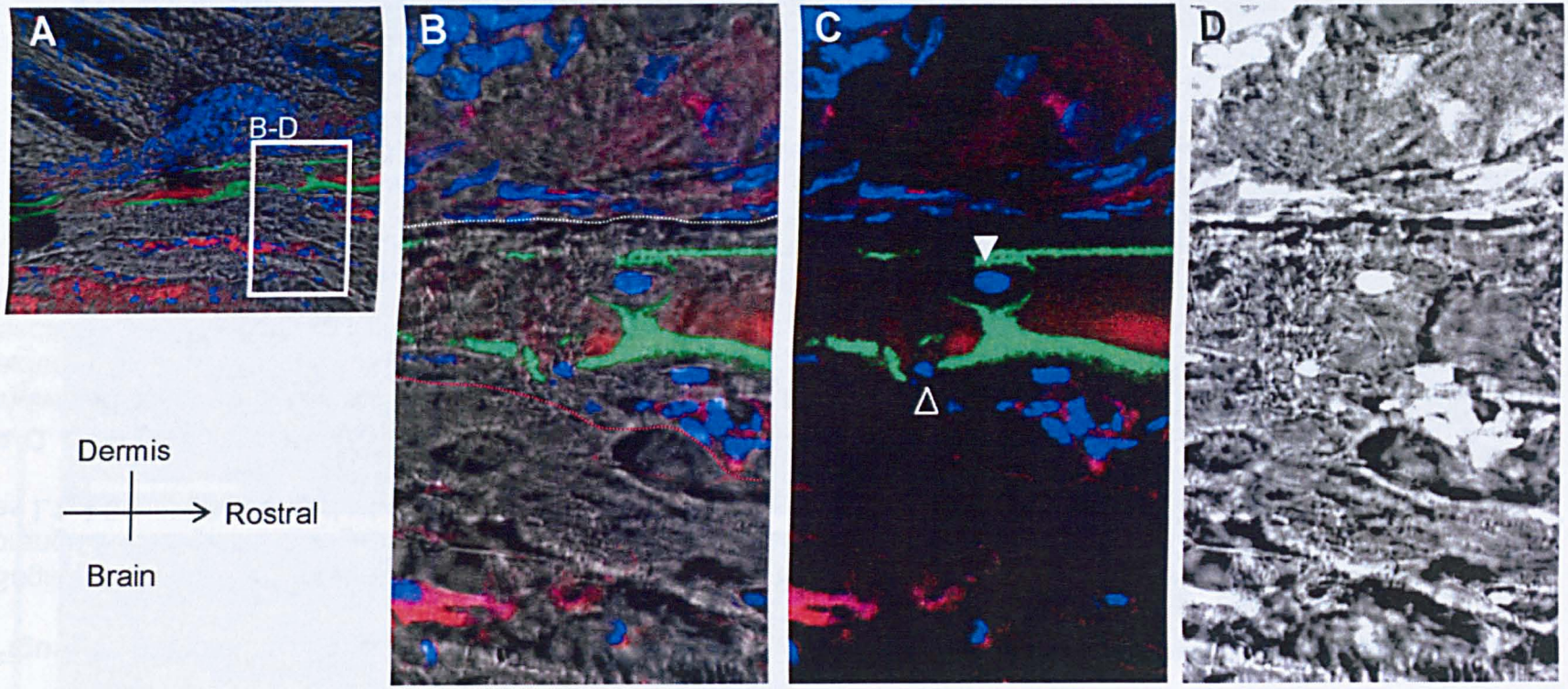

Figure 3.11: Labelling Experiment 2 Dye Swap, P8: Evidence of osteoblast remodelling and late apposition of matrix deposition from L1 and L3

Sagittal sections of a wild-type frontal bone at postnatal day 9 (P8), following injections of xylenol orange at E14 and calcein at E18 (positive vaginal plug is taken as E0). Nuclear counterstain DAPI (blue).

A-C. Overview of a mature frontal bone where only a thin margin of labelling within the bone is noted as the early matrix has been remodelled. Xylenol orange has lingered in the vasculature. The location of **B-D** is indicated.

B. Overlay of the xylenol orange, calcein, DAPI and reflection imaging (birefringence of collagen fibres) from the region indicated in **A**. Zoom indicates the frontal bone that has been remodelled with very little matrix that was labelled between E14 – P1 remaining in L2. The L1-L2 boundary is noted with a white line, and the L2-L3 boundary is indicated in red. One cell (filled arrow head, **C**) still carrying calcein has burrowed into the remaining xylenol-labelled area. An additional cell (empty arrowhead in **C**) can be seen that is etching through a green line of matrix labelling, carrying no labelling agent; in **D** the reflection imaging shows the fibres from this cell are radial.

Reflection imaging highlights that L3 is arranged in parallel sheets of mineralised matrix, indicating a late apposition of matrix from L3 cells.

Scale bar indicated 50μm.

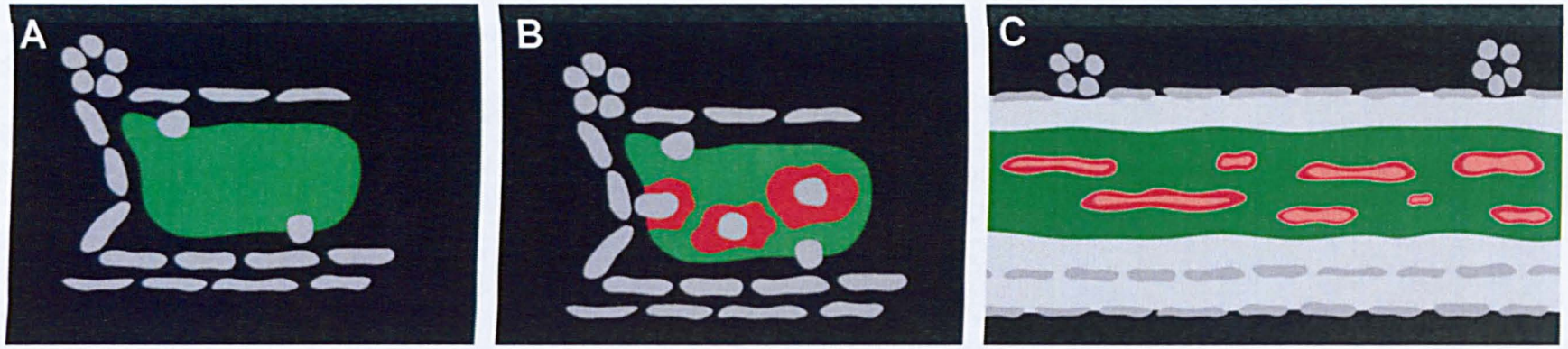

Figure 3.12: Diagrammatic representation of biomineralisation process as modelled on the current results of *in vivo* labelling experiments

A. Mineralisation occurs as soon as the diploe architecture of the bone is formed. Initial mineralisation occurs in distinct 'clouds' or 'islands' (green), cells on the outside of which encase the mineralised areas in Undulin. The mineral phase does extend to the generative layers (L1 and L3) and each island is separated from its neighbour by unmineralised sheets of cells.

B. As new cells enter the L2 area they dig into previously laid mineral and add new matrix into the internal space. The results of this, in *in vivo* labelling experiments, is the second injected colour being nested inside the first (in **B** it's red inside green).

C. Remodelling of the mineralised area results into a core of L2 that has amorphous mineral (dark green); at a time-point after birth L1 and L3 add matrix to this, laid appositionally, generating the characteristic outer compacta and sheets of mineral found in a mature bone (light grey).

3.4 Building and remodelling collagen scaffolds

3.4.1 Introduction

Results from *in vivo* matrix mineralisation labelling experiments indicate a high level of remodelling takes place in dermal bones; what remains elusive is the mechanism by which this can occur in the absence of osteoclasts and in the sole presence of osteoblasts (Runx2+ or OPN+) and endothelial precursors.

AFM studies have shown that HAP crystals sit on collagen fibres and the organisation of collagens is fundamental to the biomineralisation process (George and Veis 2008); as such the building and reorganising of collagen scaffolds might be critical for remodelling biominerals within Layer 2. Notably, high concentrations of Collagen I can form liquid crystals, i.e. they have a self-organising capability whereby they generate crossing stacks of fibres on their own (Giraud-Guille *et al.* 2000; Giraud-Guille *et al.* 2003; Kikuchi *et al.* 2004). As such, high expression of Collagen I in an enclosed space *in vivo* might lead to a crossed-fibre stacking morphology, as observed in Layer 3 (whose physical location corresponds to the basal layer in fish scales and the isopedin of fossil gnathostomes (Le Guellec *et al.* 2004; Donoghue *et al.* 2006)).

In addition, mixtures of different collagens can render fibrous collagen into an amorphous substance and HAP associated proteins (such as OPN) can define the directionality of crystal growth (Nishiyama *et al.* 1994). For this reason, the exact position of collagens with regard to the osteoblasts populating L2 was examined *in vivo*.

My analysis of the collagen system in dermal bones focused on collagens I and II. Collagen I is believed to be up-regulated in cells of the osteoblastic lineage (preosteoblasts, osteoblasts, and osteocytes) (Huang *et al.* 1997) and constitutes the majority of the scaffold of the bone matrix (Whelan and Senger 2003; Abzhanov *et al.* 2007; Shapiro 2008). Conversely, Collagen II was previously associated with cartilaginous development, but has recently

been found to be expressed by pre-osteoblasts and an intermediary cell type of the osteoblastic lineage, termed chondrocyte-like osteoblasts (CLO cells) (Abzhanov *et al.* 2007; Shapiro 2008).

3.4.2 Results

Analysis of the immature frontal bone at E16.5 yielded the surprising result that Collagen II was present in L2 prior to Collagen I (Figure 3.13). Collagen II is identified within L2 at the margin of L1 as soon as the diploë architecture of the layers is established, potentially indicating an early infusion of Collagen II into the L2 area by the cells of L1 (Figure 3.13). In a short developmental timeframe, Collagen II quickly spreads to fill the entire L2 space (Figure 3.13). The expression of Collagen II in the immature frontal bone overlapped with Runx2 expression at the L1:L2 interface, although Runx2+ cells in the external margin of L1 do not secrete Collagen II. Collagen II expression did not overlap with Collagen 1 (Figure 3.13). As the bone matures, the majority of the matrix remains weakly positive for Collagen II (Figure 3.14).

Initial Collagen II expression in L2 takes place during a time in which Collagen I is synthesized only on the internal margins of L3 (toward, but not within, L2), as well as in the dermis (Figure 3.13). As L2 matures, Collagen I is noted within this layer but confined to the area of clasps (Figure 3.14); based on Collagen I expression mapped in previous studies, expression of Collagen I in clasps and L3 could be attributed to either early osteoblasts or the endothelial precursors in the generative layers (Whelan and Senger 2003; Shapiro 2008). To confirm the Collagen I expression pattern was true (and not an artefact of using a monoclonal antibody or epitope sensitivity to fixation), a polyclonal Collagen I antibody was used, which confirmed the previously defined boundaries of Collagen I.

In the mature areas of an E18 frontal bone, Collagen I expression was wider, but not ubiquitous (Figure 3.14). This finding contradicts the widespread

notion that Collagen I forms the majority of the L2 matrix or may indicate the antibody may only be binding to areas that have not crystallised.

Confirming the expression found in the prenatal frontal bone, in the clavicle of a newborn mouse, Collagen I was present in cells of L3, as well as along the clasps across L2 and at the connection points of muscle to the bone, again confined to un-mineralised areas (Figure 3.14D).

Collagen I and Osteopontin are widely co-expressed throughout the frontal bone, most conspicuously along vascular margins of the bone matrix:blood vessel interface, as well as along the seams between mineralised regions (Figure 3.15). Late in ontogeny some Runx2-positive osteoblasts also co-express Collagen I (Figure 3.16). The previously noted co-expression of Runx2 and Osteopontin (Chapter 1) was mapped in detail and Runx2+/OPN+ cells were found in mature regions of the frontal bone, focused around the sites of vasculature/bone interfaces, with OPN polarised toward the vasculature (Figure 3.17). As OPN acts to cap mineralisation, this arrangement presumably prevents mineralisation from impinging on blood vessel formation (Kawasaki and Weiss 2008).

3.4.3 Conclusion

The larger expression domain of Collagen II compared to Collagen I in the immature frontal bone was unexpected. Results presented here indicate the initial collagen scaffold of the frontal bone may composed of Collagen II, secreted by Runx2+ cells of an osteoblastic lineage; later Collagen I secretion is achieved by both Runx2+ and OPN+ cells. The finding that Collagen II is closely associated with Runx2 is not surprising, given that previous dissociation studies had categorised an intermediary cell type (between pre-osteoblasts and fully functional osteoblasts) called chondrocyte-like osteoblasts (CLO cells) that co-expressed these markers (Abzhanov *et al.* 2007). In that study, Collagen I expression was co-localised with Osteopontin expression in cells believed to be osteoblasts, a cell type the authors believed to be developmentally later than CLO cells. What is

noteworthy from the current results is that co-expression of Runx2 and Collagen II does *not* precede osteoid secretion (which was previous thought to be accomplished by OPN+ osteoblasts). In fact, the Runx2+/Collagen II+ cells are contemporaneous with the early OPN+/Collagen I+ cells and, therefore, segregation of cells by their marker profiles is spatial and not temporal. Additionally, in late ontogeny, cells that are Collagen I-positive also express Runx2. Results presented here highlight the importance of examining the marker combinations *in vivo* and stresses that there may be a dynamic relationship between the expression of the markers and the role of the cell: i.e. early Runx2+/Coll II+ cells may establish the initial matrix, which Runx2+/Coll I+ and OPN+/Coll I+ cells remodel.

The issue of remodelling, first introduced by the *in vivo* labelling studies, and highlighted here by the intriguing pattern of collagen crystals, warrants further investigation. Hydroxyapatite crystals grow with collagen fibre systems as their guide-posts, given that the shape of the biomineralised zone changes significantly with time (from clouds, to sheets, as described above), a reorganisation of the collagen system would be needed to provide the flexibility requires for elaboration and embellishment of the mineral structure independent of the function of osteoclasts.

Collagen I expressing cells may have a role in remodelling the mineralising zone which would necessitate the cleaving and etching of the pre-existing fibres by proteases, namely members of the matrix metalloproteinase (MMP) family. MMPs would be utilised by cells intercalating into L2 after an initial osteoid or mineral phase had been established; MMPs could be used to dissolve pre-existing collagen scaffolds, including amorphous HAP (calcein-positive) mineral deposits. To confirm there is a remodelling of the collagens, and explore which cells are capable of remodelling, I investigated the expression of MMPs within the forming intramembranous bones.

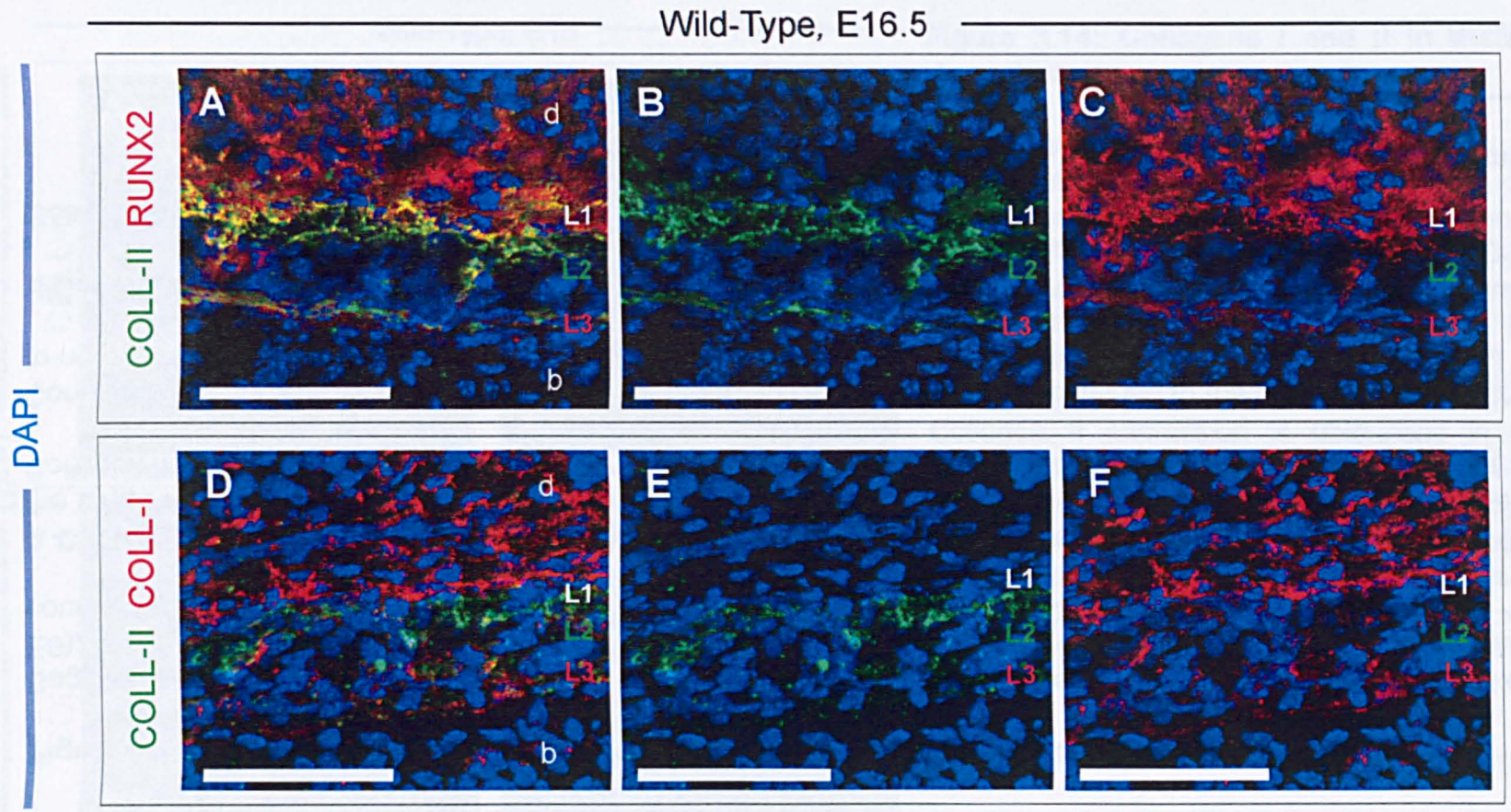
Wild-Type, E16.5
DAPI
COLL-II RUNX2
COLL-II COLL-I
A
B
C
D
E
F
d
b
L1
L2
L3

Figure 3.13: The initial osteoid is Collagen II rich and Collagen I poor and laid by Runx2+ cells

Sagittal sections through the frontal bone at embryonic day E16.5 after conception (positive vaginal plug is taken as E0); wild-type specimen. IHC for Collagen II (Green **A-F**), Runx2 (red, **B-C**), Collagen I (red, **D-F**); nuclear counterstain (DAPI) in blue. Layers 1, 2, and 3 are indicated as **L1**, **L2**, and **L3**, respectively.

A-C. Overlay (**A**) and individual channels showing Collagen II is widely expressed along the anterior margin of L2 (at the L1:L2 interface) in cells that also express Runx2; on the external side of L1, Runx2-positive cells do not secrete Collagen II.

Contrasting the pattern of Collagen II, in **D-F** the expression of Collagen I is confined to the dermis and L3, with little to no overlap between the collagens in the immature frontal bone.

d Dermis, **b** Brain

Scale bar indicates 50μm.

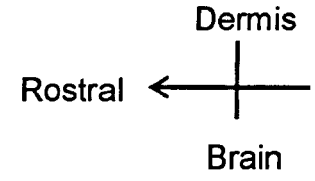

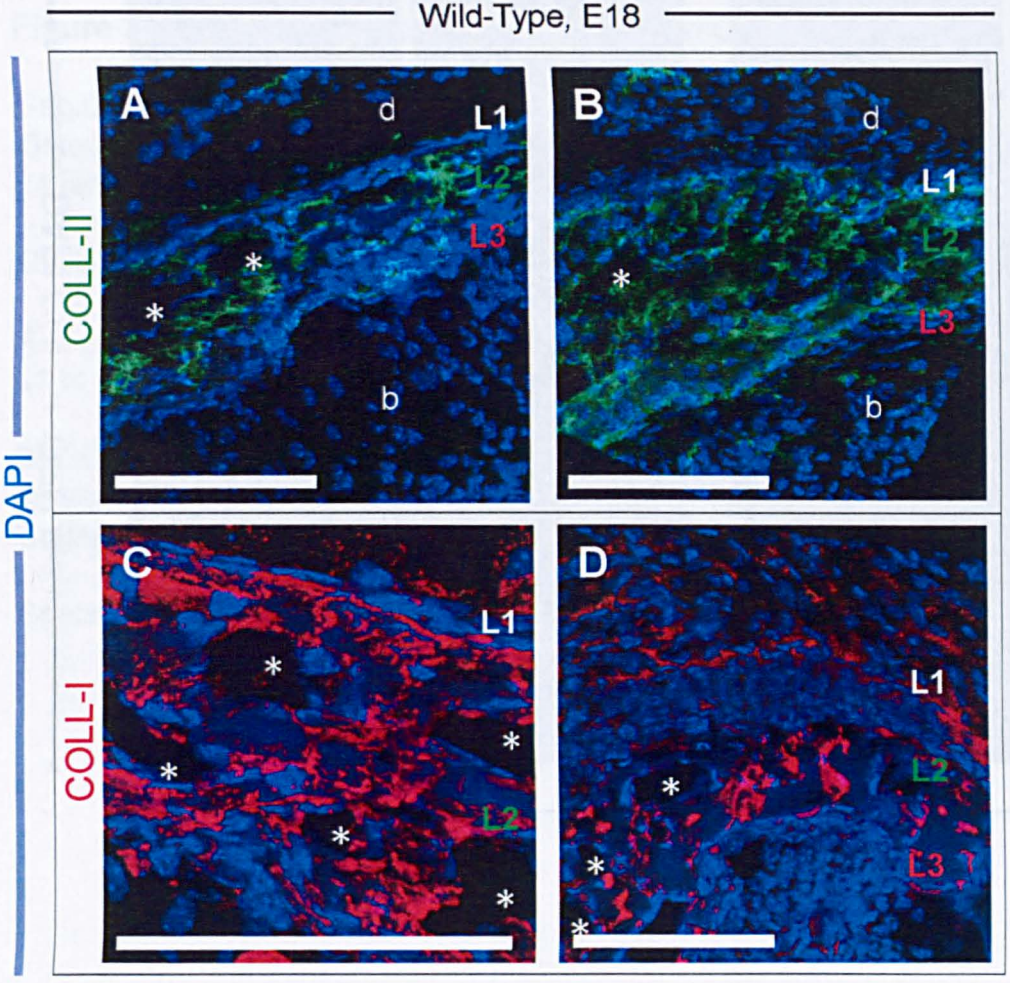

Figure 3.14: Collagens I and II in mature dermal bone

Sagittal sections through wild-type frontal (**A-C**) and clavicle (**D**) bones at embryonic day E18 after conception. IHC for Collagen II (Green **A-B**), and Collagen I (red, **C-D**); nuclear counterstain (DAPI) in blue. Layers 1, 2, and 3 are indicated as **L1**, **L2**, and **L3**, respectively. Blood vessels are indicated (*)

Collagen II expression is ubiquitous in the matrix of the mature frontal bone (**A-B**). Alternatively, Collagen I expression (**C-D**) is more pronounced but not ubiquitous. Collagen I expression appears confined to edges of mineralised and unmineralised areas, as well as the muscle-bone interface in the clavicle (**D**).

d Dermis, **b** Brain

Scale bar indicates 50μm.

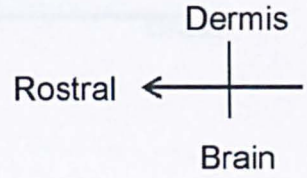

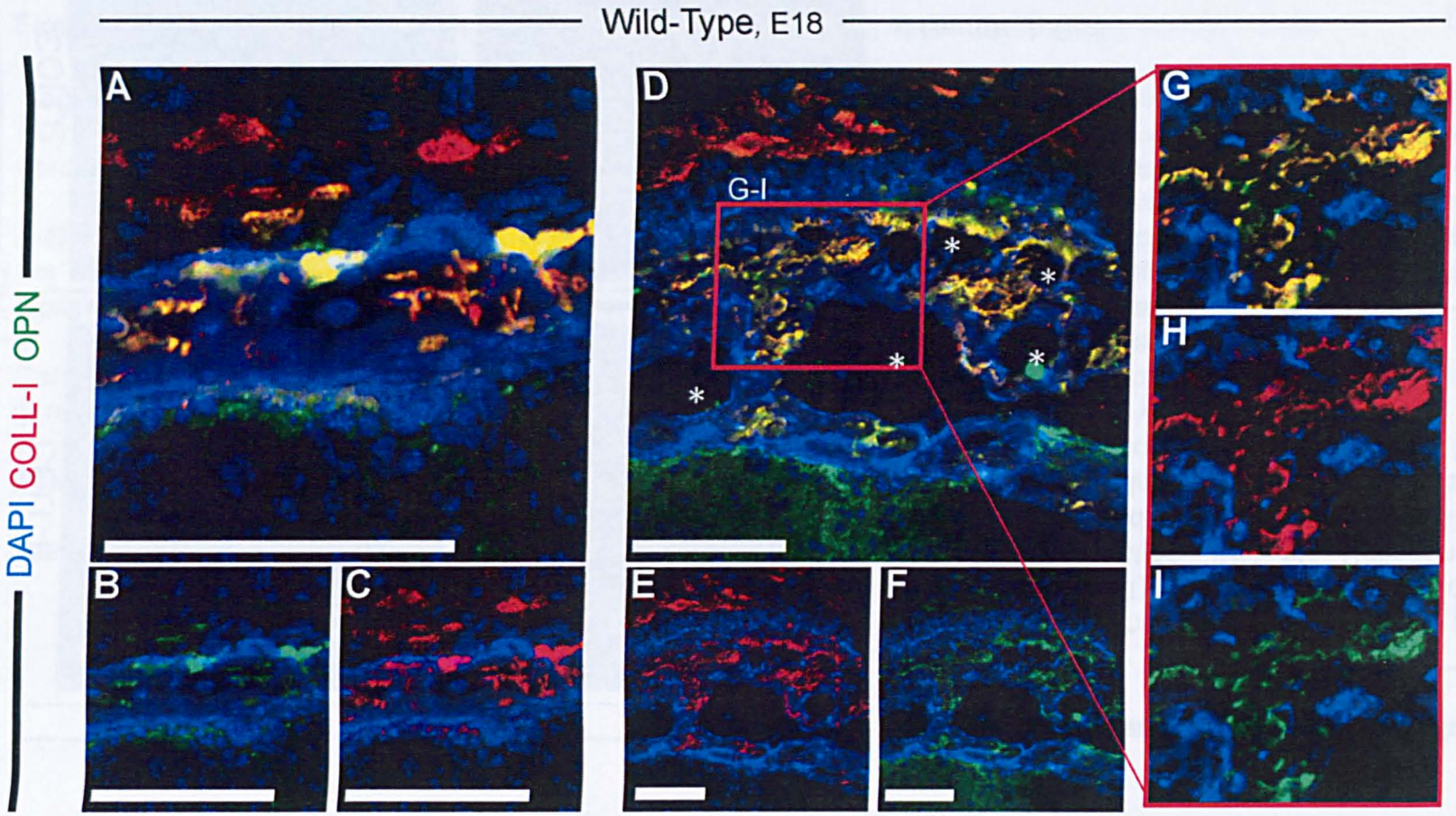
Wild-Type, E18
DAPI COLL-I OPN
A
B
C
D
G-I
E
F
G
H
I

Figure 3.15: Co-expression of Collagen I and Osteopontin

Sagittal sections through a wild-type frontal bone at embryonic day E18 after conception. IHC for Collagen I (red), and Osteopontin (green); nuclear counterstain (DAPI) in blue. Images are oriented cranial to the top and ventral to the left. Layers 1, 2, and 3 are indicated as **L1**, **L2**, and **L3**, respectively. Blood vessels are indicated (*)

Collagen II and Osteopontin are co-expressed in the developing frontal bone.

A-C. In immature areas Osteopontin is weakly expressed in L3, and co-expression of Osteopontin and Collagen 1 in L1 is focal (potentially mapping to rosettes). Overlay in **A** and individual channels **B-C**.

D-I. Co-expression of Osteopontin and Collagen I in a mature region of the frontal bone. Expression of both markers is widespread and overlapping in L2. A magnification of the region indicated by a red box in **D** shows that OPN and Collagen I expression is in the seams of the matrix and around blood vessels.

Scale bar indicates 50μm.

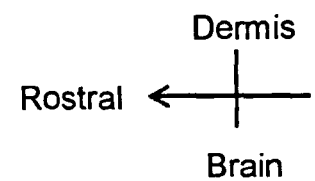

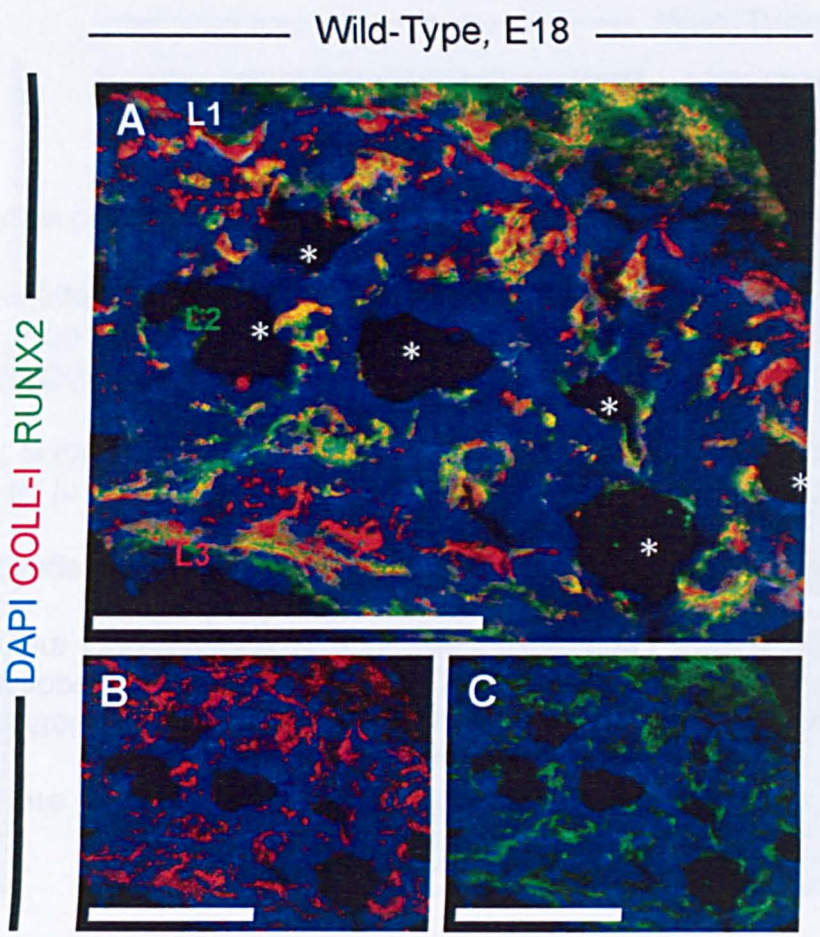

Figure 3.16: Co-expression of Collagen I and Runx2

Sagittal section through a wild-type frontal bone at embryonic day E18 after conception (positive vaginal plug is taken as E0). IHC for Collagen I (red), and Runx2 (green); nuclear counterstain (DAPI) in blue. Layers 1, 2, and 3 are indicated as **L1**, **L2**, and **L3**, respectively. Blood vessels are indicated (*)

Runx2 and Collagen 1 have wide areas of co-expression (overlay in **A**, individual channels in **B** and **C**) in a mature region of the frontal bone; however, the majority of the bone matrix that is mineralised (indicated by the DAPI 'sheen') is negative for both markers.

Scale bar indicates 50µm.

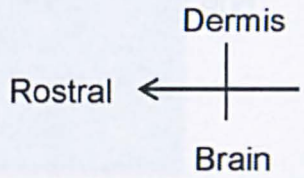

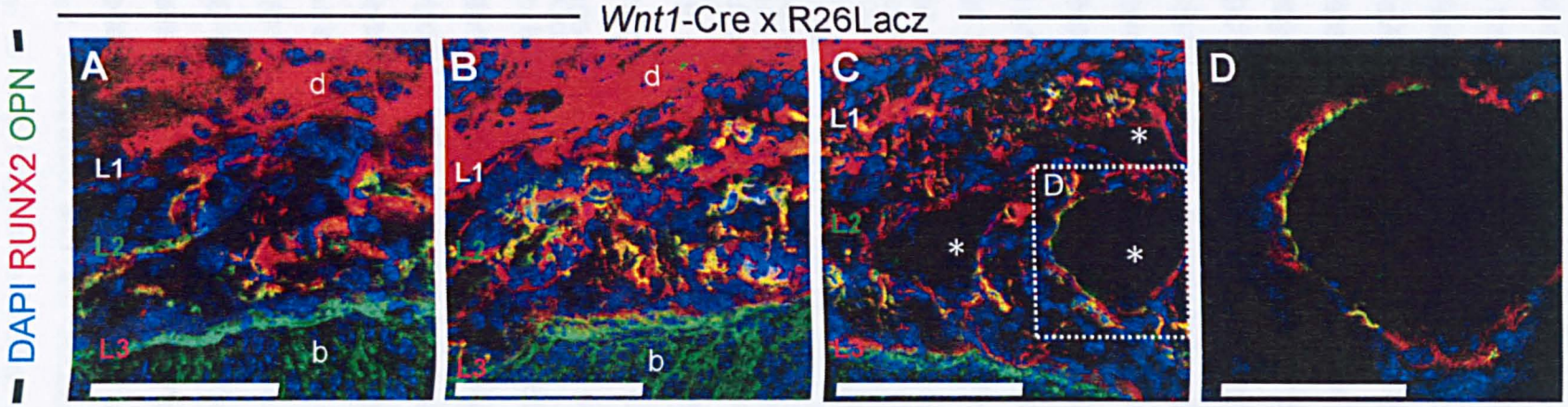

Figure 3.17: Expression of Osteopontin and Runx2 in the frontal bone

Sagittal sections through the frontal bone at embryonic day E18 after conception; *Wnt*1-Cre$^{+/-}$ x Rosa26LacZ$^{-/-}$ specimen. IHC for Runx2 (red), and Osteopontin (green); nuclear counterstain (DAPI) in blue. Layers 1, 2, and 3 are indicated as **L1**, **L2**, and **L3**, respectively. Blood vessels are indicated (*)

Runx2 and Osteopontin have focal co-expression in mature L2. **A**. In an immature condition areas of yellow overlap are not noted. But as L2 matures (**B-C**) areas of co-expression are discernible. In the most developed region of L2 these co-expressing cells are at boundary of the vasculature-matrix interface. An optical slice (**D**) of a blood vessel shows polarity within the cell, with OPN expression on the external margin toward the blood vessel.

d Dermis, **b** Brain. Scale bar indicates 50μm.

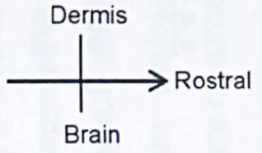

3.5.1 Results

Both Collagens I and II, which are expressed throughout the dermal bone, are substrates for MMPs -1, -8 and -13 (Egeblad and Werb 2002). My analysis focused on MMP13 as recent evidence indicates MMP13 is secreted by osteoblasts and degrades Collagen I and Collagen II as part of endochondral bone-remodeling processes (Nakamura *et al.* 2004). Collagen II appears to be the first collagen to generate a scaffold in dermal bone formation and MMP13 cleaves Collagen II 40-fold more effectively than MMP1 (Golub 2009). Once Collagens I and II are subjected to the initial cleavage, they can then be degraded by gelatinases, including MMP9 (Golub 2009).

To confirm MMP13 has a role in remodeling the matrix, I explored MMP13 expression in combination with histological calcein staining. At early stages of bone maturation MMP13 is localised within L3 and at focal points in L1, as well as along the Layer 3/brain interface (Figure 3.18) As L2 elaborates, MMP13 was found within all of the calcified areas, inside all of the individual calcein+ parcels described earlier (Figure 3.19). This arrangement indicates an external shell of mineralisation surrounds a pliable core, enabling mineral remodeling and further matrix deposition within each initial calcein parcel. Cells entering these calcein-carrying matrix islands would be able to etch into the existing matrix and continue to secrete new osteoid, with the calcified exterior expanding outwards (Figure 3.12); this mode of action would be in line with the results of the *in vivo* labeling experiments where nested patterns of matrix were observed. The co-expression of MMP13 by Runx2+ osteoblasts invading the L2 matrix was confirmed (Figure 3.18). Notably, widespread areas of MMP13 expression where Runx2 was absent were also observed, and may correspond to areas where OPN+ cells from L3 are entering L2 (Figure 3.18).

Blood vessels were previously found nested inside mineralising areas and the theory that the morphology, biomineralisation and vascularisation are developing in parallel would necessitate the ability of the vasculature to also etch into pre-existing matrix. MMP9 is expressed by pericytes and endothelial cells and is critical for vascularisation of endochondral growth plates (Vu *et al.* 1998; Egeblad and Werb 2002). MMP9 is found to be widely expressed in L1and co-expression of MMP9 and Collagen I in flattened cells entering L2 from L1 and L3 in areas that have the characteristic 'sheen' (DAPI channel) indicating osteoid/matrix (Figure 3.20). As it stays confined to the clasp regions themselves, this unique localisation would enable integration of new cells onto the surfaces of pre-existing mineralized areas. MMP9 is a gelatinase that digests Fibronectin, and expression within L1 may make L1 a more permissive environment to aid cellular invasion into L2 through the threading in process described in Chapter 1. In the mature bone, several areas of overlap between MMP9 and Collagen I were found within the bone matrix, and along the edge of blood vessels (Figure 3.20). As Undulin is also a substrate for MMP9, MMP9 expression could be involved in breaking down the ties around the calcein blocks to aid the remodeling (Sigma 2001).

3.5.2 Conclusion

Collectively, the results of our exploration of the biomineralisation of dermal bones indicate the matrix is not static but is instead a dynamic space that serves as a malleable substrate for rapid thickness growth. The development of the mineralising areas is dictated by the simultaneous development of the bone morphology and vasculature. There was a notable distribution of the MMPs whereby MMP9 is superficial and found at the osteoblast:endothelial interface within Layer 2, while MMP13 is injected into the core of the biomineralised matrix itself. The inference from this is that these MMPs have different substrates and the substrates would be distributed in a similar manner to their respective MMPs. With regard to Layer 2 elaboration, this would mean that MMP9 mediates an increase of the osteoblast:vasculature

interface, while MMP13 mediates an extension of the biomineralising zone by internally cleaving the collagen fibre system. This provides an understanding of how the *in vivo* labeling results can be achieved, with a later dye found inside a previously-labeled area.

The most important implication of the current results is that the Runx2+ osteoblasts themselves are the ones that modulate the collagen depositions, which they and their predeceasing cells have accomplished - without the need of osteoclasts. MMP13 has been shown to be directly regulated by Runx2 at the transcriptional level (Jimenez *et al.* 1999), a notion established in tissue cultures whose *in vivo* relevance may be to enable remodeling by Runx2-positive osteoblasts. MMP-mediated bone remodeling, as shown here, supports previous work on *MMP13* null mice that indicates the knockout has abnormalities in the growth plate and delayed ossification during endochondral ossification, (Inada *et al.* 2004). However, dermal bones have not been studied in these mutants.

The unusual finding that osteoblasts themselves remodel the mineralised matrix supports recent work by Witten (Witten and Huysseune 2009) on osteoblasts/osteoclasts in zebrafish and can shed light on the molecular and cellular mechanism of how bone mineral may have changed in fossil fish in the gnathostome stem group, which did not possess osteoclasts. Placoderms are the earliest evolutionary group displaying classical bone remodelling akin to that observed in newborn or adult mice (Donoghue *et al.* 2006), which occurs at a significantly later stage of development than that of the current study.

Matrix remodeling is predicated on the invasion of cells from the generative layers, a process that was clearly disrupted in the Hand2 mutant strains. To establish the effect of the disrupted layer formation on the biomineralisation of Hand2-mutant strains, I examined the mineralising zone of *Hand2*$^{fl/fl}$-*Wnt1*-Cre mice *ex vivo*.

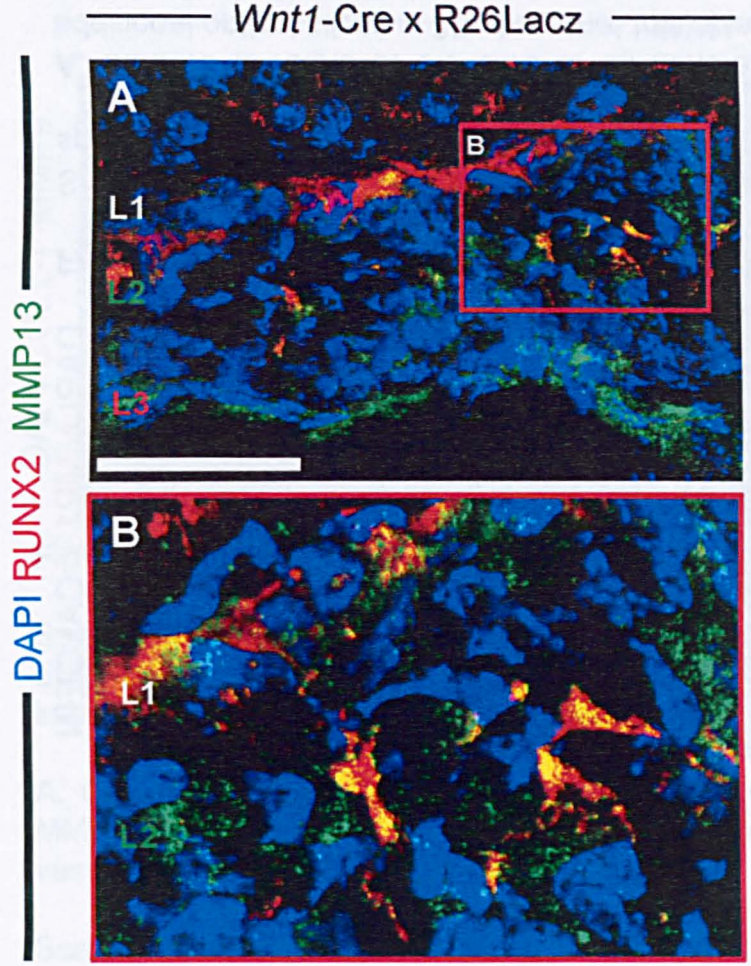

Figure 3.18: Runx2 expressing osteoblasts dig into matrix via MMP13 expression

Sagittal section through the frontal bone at embryonic day E18 after conception (positive vaginal plug is taken as E0); *Wnt*1-Cre$^{+/-}$ x Rosa26LacZ$^{-/-}$ specimen. IHC for MMP13 (green) and Runx2 (red); nuclear counterstain (DAPI) in blue.

A-B. Overview (**A**) and magnification (**B**) of MMP13 and Runx2 co-expression (yellow) in a semi-mature frontal bone. Co-expression of Runx2 and MMP13 in L2 and isolated MMP13 expression throughout the L2 matrix and in L3.

Scale bar indicates 50µm.

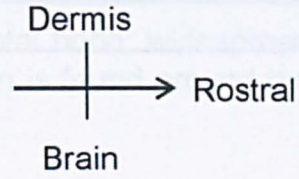

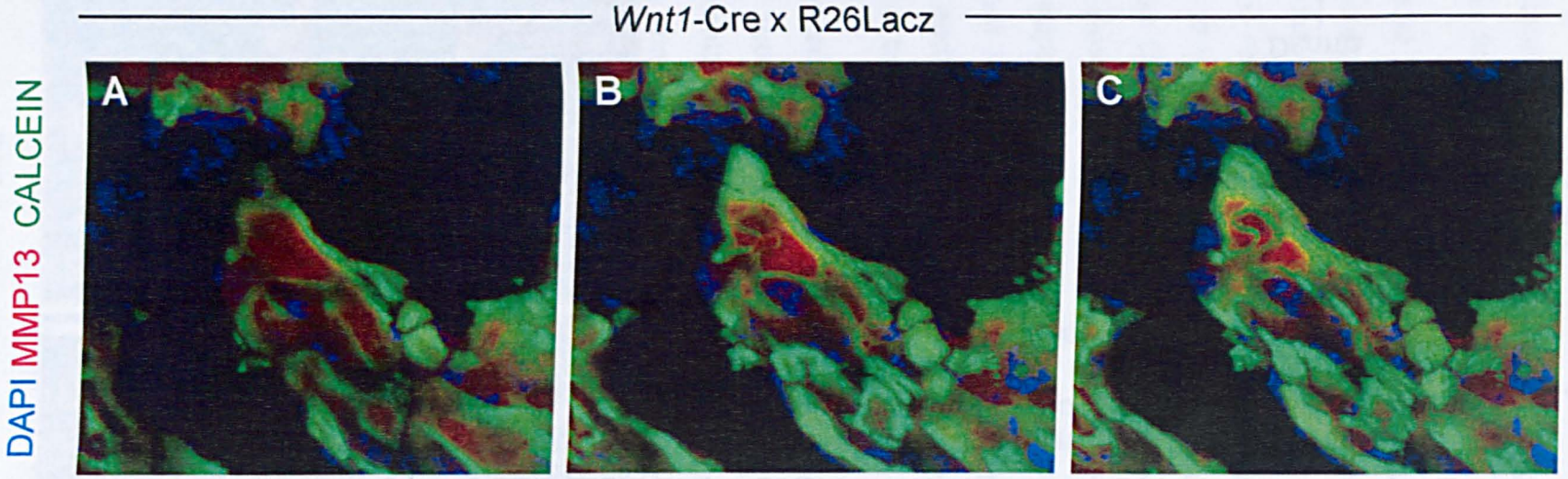

Figure 3.19: MMP13 is at the core of mineralised islands

Sagittal sections through the frontal bone at embryonic day E18 after conception; *Wnt*1-Cre$^{+/-}$ x Rosa26LacZ$^{-/-}$ specimen. IHC for MMP13 (red); calcein stain (green); nuclear counterstain (DAPI) in blue.

A. MMP13 is found at the core of all mineralised areas (calcein shell around MMP13+ centre). **B-C.** Stack of additional optical slices in 3D show that this arrangement can be found in all the mineralised areas, which are distinct islands of calcein positivity.

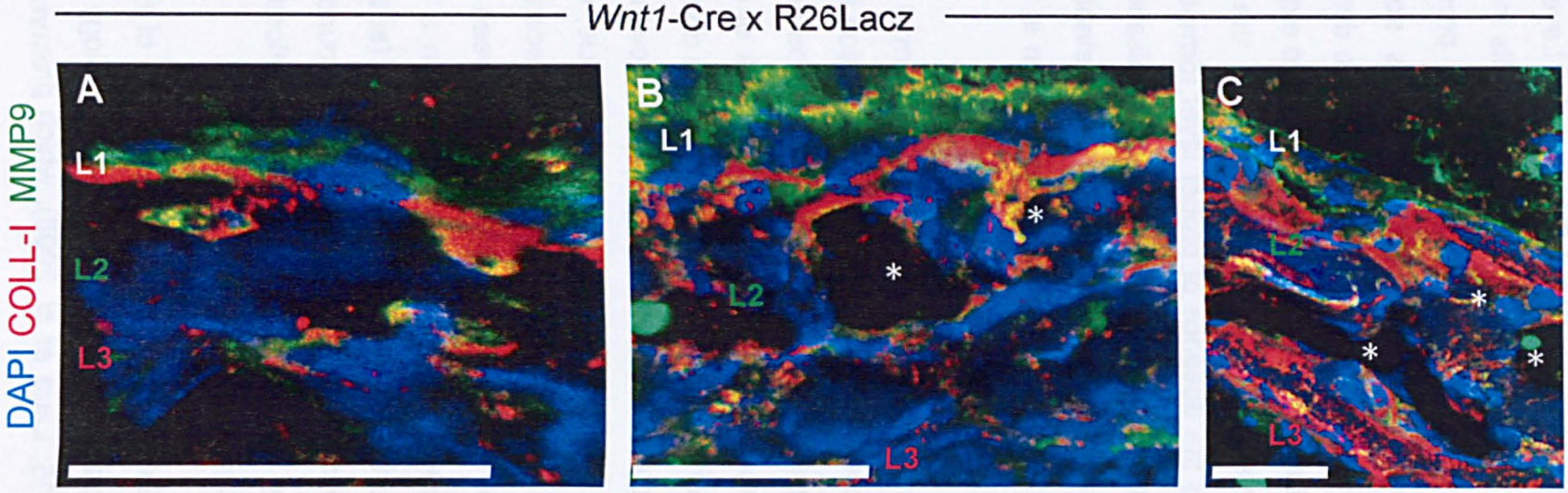

Figure 3.20: MMP9 expression in the developing frontal bone

Sagittal sections through the frontal bone at embryonic day E18 after conception (positive vaginal plug is taken as E0); *Wnt*1-Cre$^{+/-}$ x Rosa26LacZ$^{-/-}$ specimen. IHC for MMP9 (green) and Collagen I (red); nuclear counterstain (DAPI) in blue.

A. Co-expression of Collagen I and MMP9 in a few thin cells within L2 in the immature frontal bone; widespread MMP9 expression in L1. In more mature regions (**B-C**). MMP9 and Collagen I co-expression is found around the vasculature.

Scale bar indicates 50µm

3.6 Hand2 mutant analysis: biomineralisation

In the dermal bones of *Hand2*$^{fl/fl}$-*Wnt*1-Cre mice there is an abrogation of clasp structures leading to an unregulated filling of the Layer 2 space by Runx2+ osteoblasts. This appositional growth mode results in a lack of any internal osteoblast:endothelial layer formation. Results presented above indicate that mineralisation of dermal bone begins as soon as diploë architecture is achieved in the wild-type condition, and the dynamic process of mineralising the matrix involves excessive remodelling to expand the bone in thickness and complexity and to accommodate the concurrently developing vasculature. In the absence of proper layer formation, where an appositional mode of growth is favoured, biomineralisation would be expected to commence as soon as precocious Runx2+ osteoblasts invaded Layer 2, and continue until a single plane of mineralisation is formed, which would not be remodelled.

Indeed, *ex vivo* histological application of calcein to dermal bones of the *Hand2*$^{fl/fl}$-*Wnt*1-Cre mice confirmed aberrant biomineralisation in the absence of proper layer morphogenesis. In both the frontal bone and dermal clavicle, the mineralised zone comprises a single contiguous block of calcein. In the frontal bone, a thin sheet of calcification extends along the dorso-ventral axis and the bone does not increase in complexity along its growth plane (Figure 3.21). In the neural crest components of the mutant clavicle, calcified areas were dramatically different in appearance to adjacent unaffected, mesodermal areas (Figure 3.22A). The juxtaposition between mineralisation in the affected versus non-affected regions is evident on a single section where the mesodermal-derived component of the clavicle (at the attachment of the pectoralis) has a wide zone of mineralisation surrounding numerous trabeculations, contrasting to the single band of calcification along the attachment of the SCM (Figure 3.22).

The appearance of the mineralised zone in dermal bones of *Hand2*$^{fl/fl}$-*Wnt*1-Cre mice is similar to a classical hyperossification pathology (Hessle *et al.* 2002; Anderson *et al.* 2005; Laue *et al.* 2008), which presumably results in

the Hand2-mutants from the combination of Runx2-deregulation and a lack of remodelling.

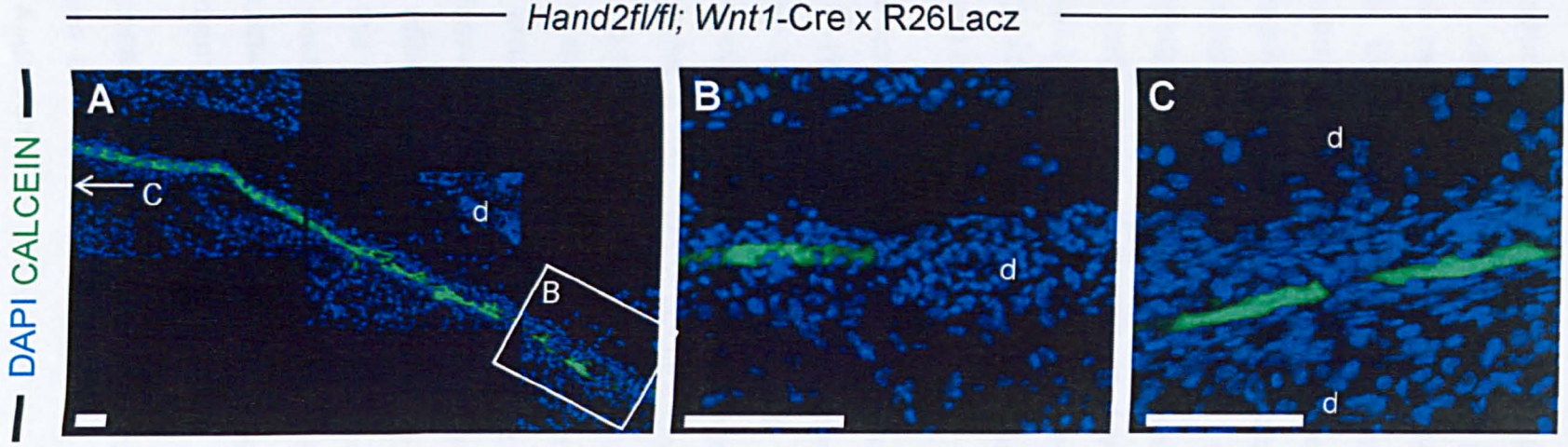

Figure 3.21: Biomineralisation in the frontal bone of *Hand2fl/fl; Wnt1-Cre* mice

Sagittal sections through the frontal bone at postnatal day 1 (P0) in a Hand2 knockout mouse; *Hand2fl/fl; Wnt*1-Cre$^{+/-}$ x Rosa26LacZ$^{-/-}$ specimen. Calcein stain (green); nuclear counterstain (DAPI) in blue.

A. Overview of the single plane of biomineralisation in the frontal bone of Hand2-knockout mice. The coronal suture is in the white box, indicating the magnification in **B.** In **B-C** the mineralised area is seen as a single sheet at the coronal suture (**B**) and the most mature region of the bone (**C**).

d Dermis, **b** Brain, **s** Suture

Scale bar indicates 50µm.

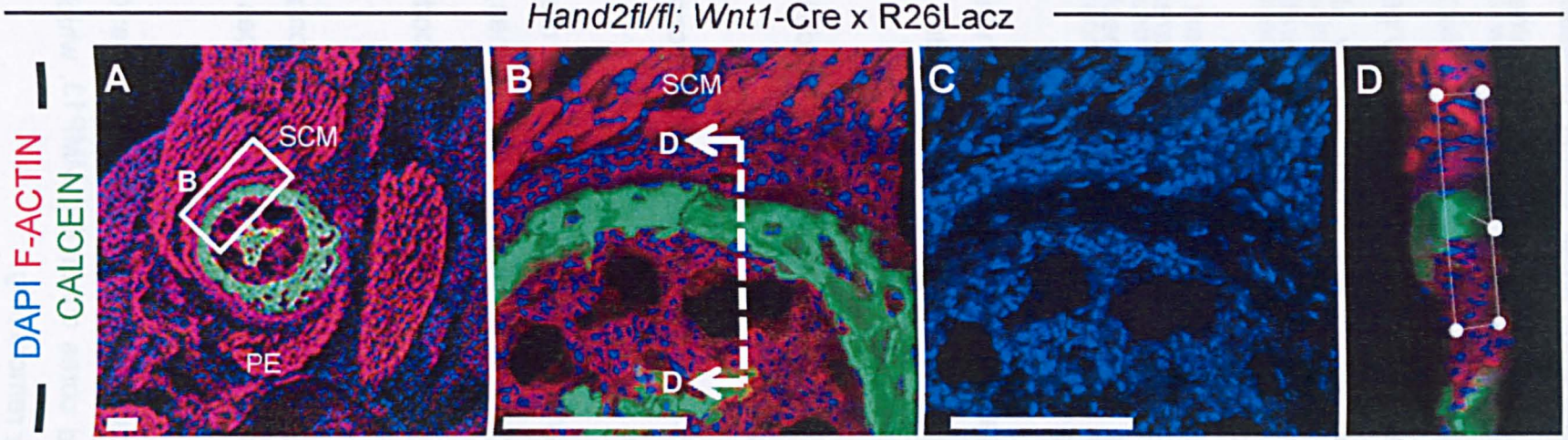

Figure 3.22: Biomineralisation in the clavicle of *Hand2fl/fl; Wnt1-Cre* mice

Sagittal sections through the clavicle at the SCM attachment at postnatal day 1 (P0) in a Hand2 knockout mouse; *Hand2fl/fl; Wnt*1-Cre$^{+/-}$ x Rosa26LacZ$^{-/-}$ specimen. Calcein stain (green); IHC for F-Actin (red); nuclear counterstain (DAPI) in blue.

A. Overview of the clavicle; at the SCH attachment biomineralisation is a single plane, versus at the pectoralis (PE) where Hand2 has not been ablated, the clavicle is trabeculated and the biomineralised area is expanded. **B-C**. The biomineralised area is a single plane though a cell-sparse L2; a section through the calcein (**D**) shows it is a solitary, dense block.

Scale bar indicates 50μm.

3.7 Summary of findings

- Early biomineralisation occurs when small 'clouds' or 'islands' of osteoid within L2 are calcified; these islands are separated by unmineralised clasps of cells, capped by rosettes;

- As biomineralisation progresses the calcified areas form planes, focused toward the centre of L2 and are always surrounded by sheets of non-mineralised cells that connect to the un-mineralised generative layers (L1 and L3) allowing for lateral and vectorial growth of the bone;

- An *in vivo* time-course of bone mineralisation indicates areas of calcified matrix are remodelled as the bone develops through a mechanism where matrix is continually expanded from within;

- Remodelling of the biomineralising zone continues through the first week of murine post-natal development and after birth matrix is added appositionally from the generative layers;

- Osteoblasts within calcified areas express Runx2 and Undulin and Undulin cloaks the individual calcein islands;

- The initial osteoid is rich in Collagen II, produced appositionally by Runx2+ osteoblasts at L1/L2 interface;

- Collagen I does not comprise the majority of the L2 matrix, however, Collagen II is widespread in the matrix of mature dermal bones;

- Collagen I is deposited later than Collagen II by both Runx2 and Osteopontin expressing cells;

- Runx2 and Osteopontin are co-expressed in mature frontal bones, with principle co-expression centred around vascular spaces providing a boundary between the matrix and the blood vessels;

- Remodelling the collagen scaffolds is established by MMPs: Calcified areas are mineralised shells around cores containing MMP13, which would make the centre area permissive for remodelling;

- Runx2+ and Runx2- cells express MMP13, presumably as part of matrix remodelling;

- Cells with vascular-like morphology express MMP9, often in conjunction with Collagen I, presumably as a part of vascular remodelling of the biomineralising zone;

- Osteoblasts may have the potential to remodel the biomineralised zone in the absence of osteoclasts;

- In Hand2 mutants biomineralisation is confined to a single layer calcification, underscoring the importance of the dynamic co-development of layer morphogenesis, vasculature and the ensuing biomineralisation.

4.1 Introduction

Bones play a crucial role in mediating movement, a function enabled by bone-muscle attachments; toward this end, several dermal bones have muscle insertion sites (entheses). Entheses comprise the connective tissue of the muscle and the corresponding bony attachment site, each of which forms from independent progenitors of the same embryonic origin (Matsuoka *et al.* 2005; Ahlberg and Koentges 2006) (known as the 'connectivity rule' whereby neural crest connective tissue inserts into a neural crest derived site on the bone, and the same from somitic/mesodermal tissues).

Entheses are classed into two group describing the mechanics of the bone:connective tissue interface; in direct insertion (commonly near joints) there is a four zone arrangement of the tendon/ligament, non-calcified connective tissue, calcified cartilage, and the bone (Hashimoto *et al.* 2007); alternatively, indirect insertion (usually found in a diaphysis) connects the tendon to the periosteal surface of the bone and may also be termed 'fibrous' insertion (Hashimoto *et al.* 2007). Intriguingly, there does not appear to be a link between the form of ossification (intramembranous or endochondral) and the character of the enthesis (Hems and Tillmann 2000). Furthermore, while skeletal muscle attachment to bone is always mediated by a form of connective tissue, there is a large breadth of intermediates ranging from tendons to ligaments to indistinct connective tissues (Benjamin *et al.* 2002). To date, little is known about the molecular composition of entheses and the majority of the literature focuses on the development of the muscle-bone interface in endochondral formations.

Results from Chapter 1 indicate Layer 1 is a periosteal-like tissue, therefore, it may be assumed that entheses of dermal bones are achieved via L1, an assumption underscored by the physical location of L1 at the external margin of the bone, where a musculoskeletal attachment would form. However, the abnormal layer formation displayed in the Hand2 mutants (both the *Hand2*$^{fl/fl}$-

*Wnt*1-Cre and *Hand*2BAenh$^{-/-}$ strains) did not disturb the muscle-bone interface of the clavicle, indicating the enthesis may not be established by Layer 1. To clarify the role of Layer 1 in forming entheses and to contextualise muscle:bone attachment in light of the current findings on the diploë architecture of dermal bone development, immunohistochemistry was combined with three-dimensional imaging to characterise the attachment point of the sternocleidomastoid to the dermal clavicle.

4.2.1 Musculoskeletal attachment is achieved by a molecularly discernible subdivision of Layer 1

In areas with no muscle attachment (such as the frontal bone) Layer 1 has a dual function whereby it houses the rosettes and acts as a generative layer providing both osteoblastic and vascular cells to the developing cancellous structure (Layer 2) (See Chapters 1-2). In the frontal bone there is no physical separation between the rosettes and the surrounding cells, in fact the adjacent proximity is what allows the osteoblastic and vascular cells to migrate from L1 into L2.

At the site of muscle attachments, however, Layer 1 has further subdivided, such that a subsection of L1 provides the attachment point of the skeletal muscle. This area is physically separated from the remainder of L1 at the most exterior margin (Figure 4.1). This sub-section of L1, termed here L1-attachment (L1-A), has cortical expression of Periostin (an ancient homophilic binding protein (Takeshita *et al.* 1993)) which can be used to visualise the unique physical topography of the region: in three-dimensional reconstructions the attachment site resembles a tube in cross section (Figures 4.1-4.2). This docking area is conspicuous in all regions around the circumference of the clavicle where muscles attach, and notably flattened in areas lacking any insertion points (Figure 4.2). The cells within the L1-attachment region have a prominent orientation whereby their nuclei are arranged perpendicularly to the rest of L1, which renders them in a parallel orientation with the muscles that are inserting into the layer.

To confirm the docking region is truly a sub-division of L1, its molecular characteristics were further explored. The region of L1 that acts a generative surface for osteoblasts and endothelial cells widely expresses Undulin and has polarised POSTN expression within rosettes (see Chapter 1.3); Runx2 expression by osteoblasts within the layer is cytoplasmic except within the rosettes and cells entering L2, and Hand2-nuclear expression also localises

to rosettes (see Chapter 1.3). Compared to this, cells in L1-attachment widely express Periostin, however, there is no expression of Undulin (Figure 4.3). The majority of cells within L1-attachment do not express Runx2; the notable exception to this are the muscle fibres themselves at the insertion point, which terminate with a nucleus that is Runx2- and Hand2-positive (Figure 4.4); these Runx2/Hand2-nuclear cells appear to capture muscle fibres prior to insertion into L1, effectively acting as docking points (Figure 4.4). In some areas, immediately prior to the docking being established, expression of Hand2 is not observed, although the muscle fibre connection point to L1-A after the docking is established is Hand2+; this potentially indicates a highly confined temporal pattern of Hand2 expression in mediating muscle attachment to L1-A (Figure 4.4).

The expression profile of L1-docking, therefore, largely resembles that of previously established regions of L1, with an intriguing protein re-localisation in L1-attachment.

4.2.2 β-Catenin, a potential lineage-specific marker of attachment

The canonical *Wnt* pathway acts to mediate the muscle position relative to the bone prior to muscle insertion (Kardon 1998; Kardon *et al.* 2003); to explore this further, β-Catenin expression was mapped in L1-attachment. β-Catenin is widely expressed in L1 in non-attachment regions of the frontal bone and by some cells within L2 and L3 (see Chapter 1.1). In the murine clavicle, the Runx2-expressing cells mediating the muscle-fibre L1-A attachment also express cytoplasmic β-Catenin (Figure 4.5). β-Catenin expression maps to areas of sternocleidomastoid insertion and the omohyoideus, but *not* to deltoid or pectoralis insertion on the same section (Figure 4.6). Moreover, β-catenin positive neural crest cells also contribute to entheses of intercostals muscles (Figure 4.6C). Thus, the β-Catenin expression pattern correlates with the neural crest-derived muscles but is notably absent from regions of mesodermal insertions (Matsuoka *et al.* 2005). While this was an interesting and unexpected finding, further analyses

would be required to see if this pattern holds true for all neural crest-derived muscle insertions.

Wnt1-Cre x R26Lacz

DAPI POSTN

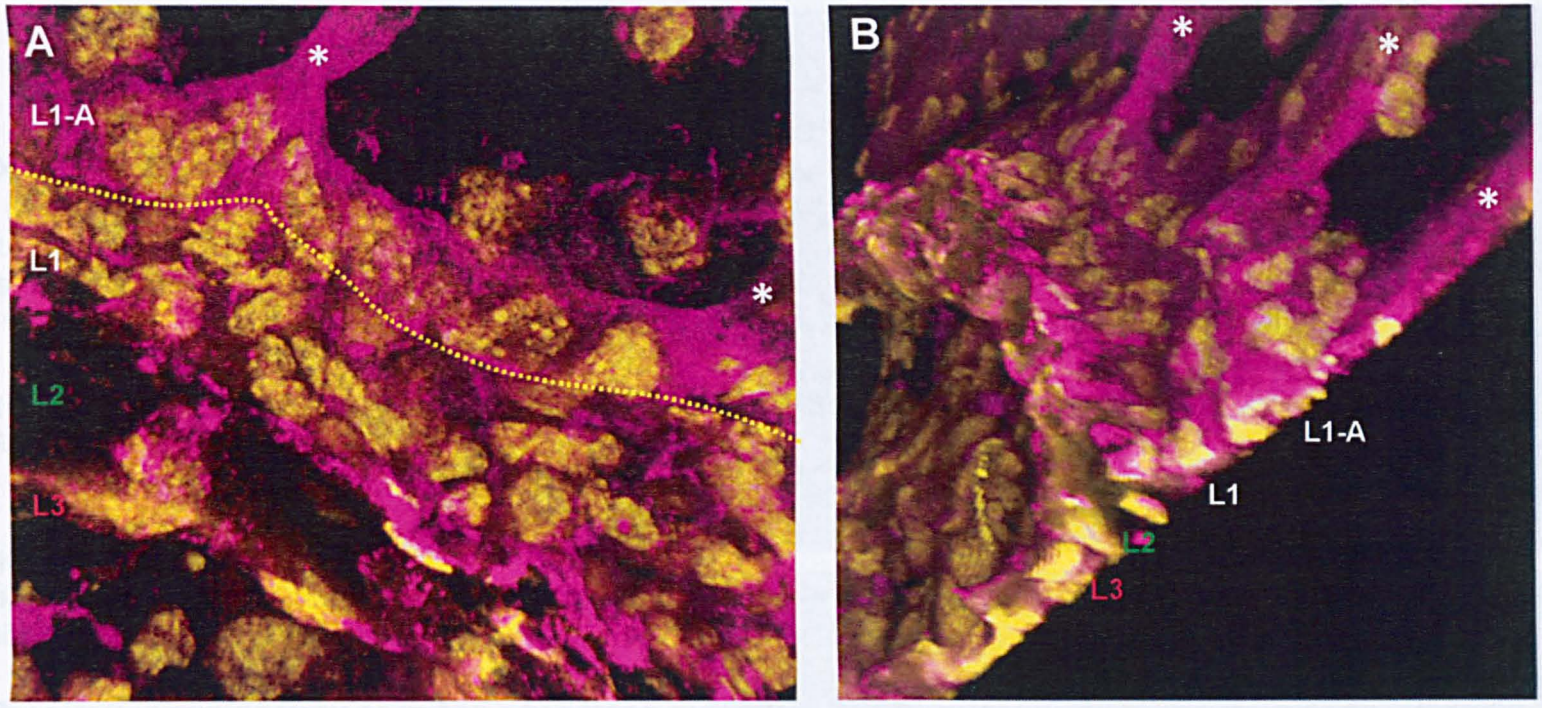

Figure 4.1: A sub-section of Layer 1 provides the bone:muscle attachment of the SCM to the clavicle

Sagittal sections through the clavicle at the SCM attachment at embryonic day E18 after conception (positive vaginal plug is taken as E0); *Wnt*1-Cre$^{+/-}$ x Rosa26LacZ$^{-/-}$ specimen. IHC for Periostin (purple); nuclear counterstain (DAPI) in gold. 63x magnifications.

A. At the SCH attachment, Layer 1 comprises a wide physical area and houses rosette formations at the L1:L2 interface, as well as a sub-partition that forms the enthesis. At the muscle:L1 interface, here termed L1-Attachment (L1-A), POSTN expression is cortical. The boundary of L1-A is indicated with a yellow dashed line.

B. An oblique section showing the 3D topography of the clavicle at the SCM enthesis. The bone is a raised plateau, lined by L1 and L3. L1-A has a unique architecture and appears like a tube in cross section. Three individual muscle fibres (*) are connected to L1-A.

63x magnification + zoom

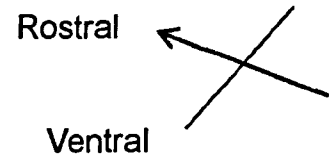

Wnt1-Cre x R26Lacz

DAPI RUNX2 POSTN (white)

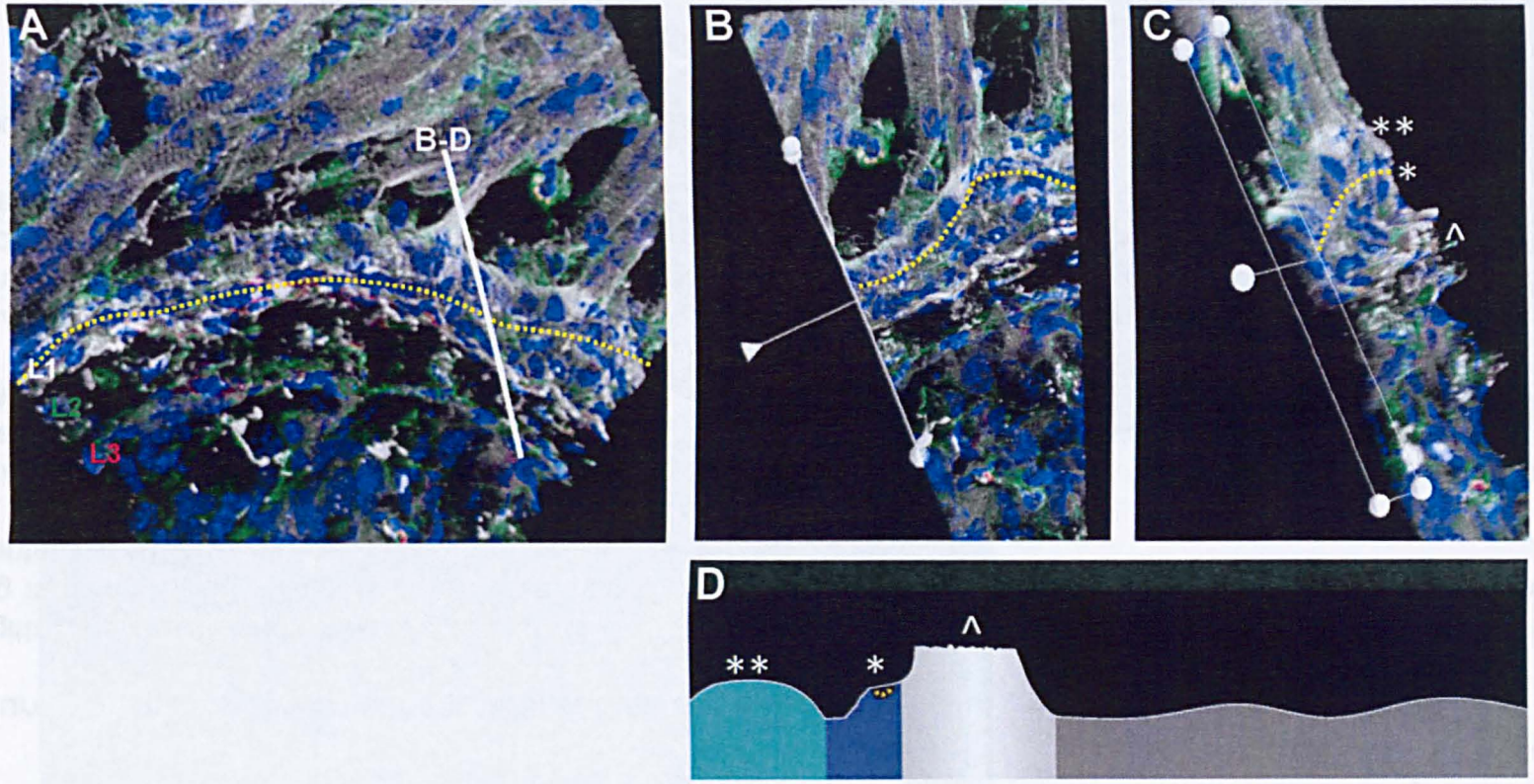

Figure 4.2: The topography of the SCM enthesis

Sagittal sections through the clavicle at the SCM attachment at embryonic day E18 after conception (positive vaginal plug is taken as E0); *Wnt*1-Cre$^{+/-}$ x Rosa26LacZ$^{-/-}$ specimen. IHC for Periostin (white) and Runx2 (green) ; nuclear counterstain (DAPI) in blue.

A. At the SCH attachment, L1-A is a subsection of L1 that formed the enthesis. The clipping plane in **B** shows the location through which the oblique 3D cross section of **C** is taken. The boundary of L1-A:L1 is indicated (yellow dashed line).

D. A diagrammatic representation of the clavicle at the SCM enthesis. L1-A (**), into which individual muscle fibres connect, is in teal and is physically raised from the remainder of L1 (blue, *), which houses rosettes, osteoblasts and endothelial cells. The bone proper (including the L1:L2 interface, L2, and the L2:L3 interface) is a raised plateau (^). The cartilaginous core of the clavicle is represented in dark grey.

40x magnifications.

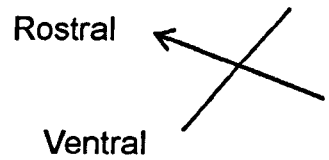

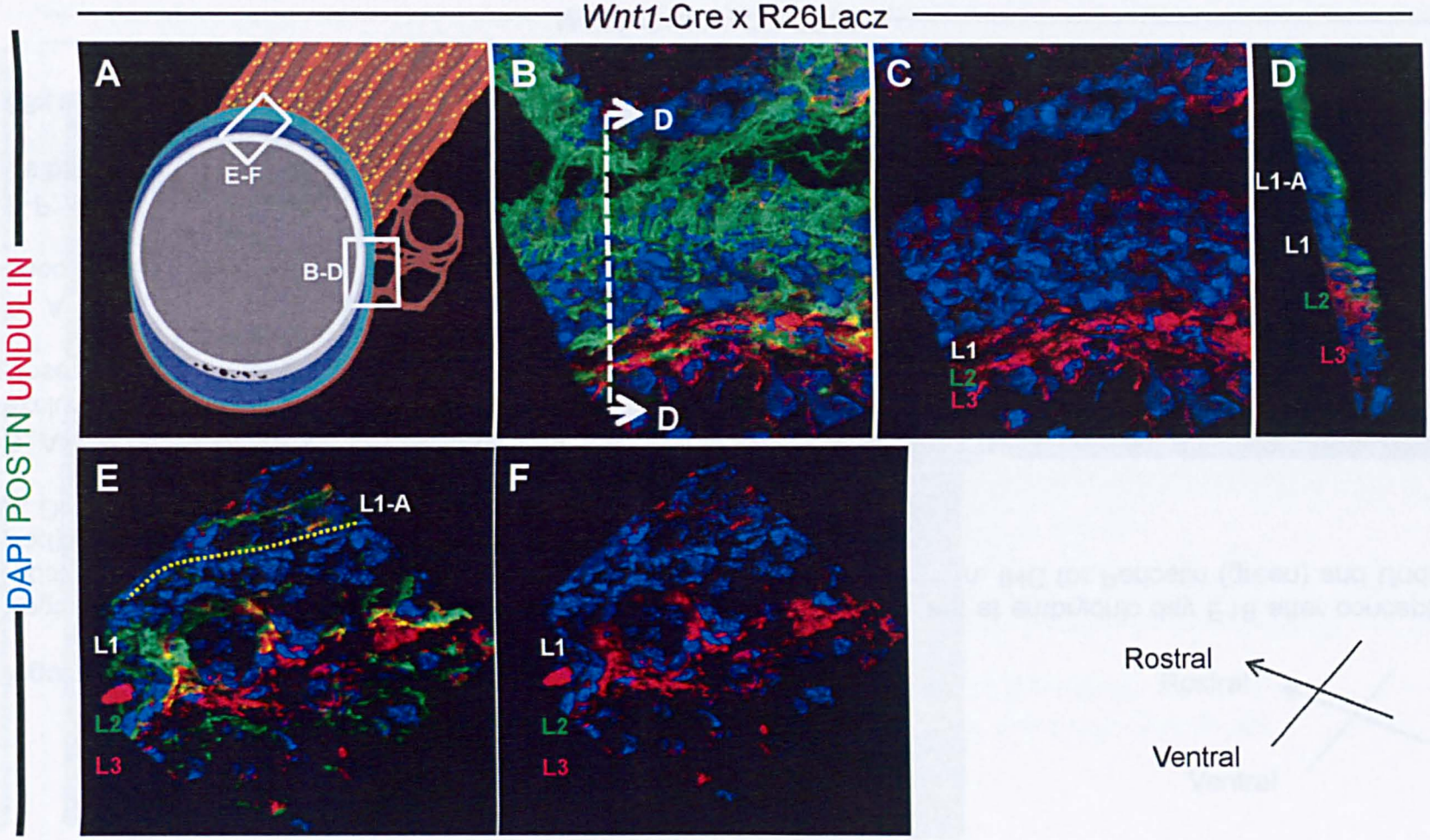
Wnt1-Cre x R26Lacz
DAPI POSTN UNDULIN
A
E-F
B-D
B
D
D
C
L1
L2
L3
D
L1-A
L1
L2
L3
E
L1-A
L1
L2
L3
F
L1
L2
L3
Rostral
Ventral

Figure 4.3: Undulin is not expressed by the cells of L1-A

Sagittal sections through the clavicle at regions of muscle:bone attachment at embryonic day E18 after conception (positive vaginal plug is taken as E0); *Wnt*1-Cre$^{+/-}$ x Rosa26LacZ$^{-/-}$ specimen. IHC for Periostin (green) and Undulin (red); nuclear counterstain (DAPI) in blue.
A. Diagrammatic representation of the clavicle showing the positions of **B-F.**

B. At the omohyoideus L1-A is discernible by the cortical expression of POSTN; without the POSTN channel (**C**) the exclusion of Undulin in the attachment region is notable. Cells of the wide intermediary area between L1-A and L1 closest to the L2 interface are also largely Undulin-negative .

D. A cross section through L1-A (region of cross section indicated in **B**) shows the cortical expression of POSTN encompasses the entire attachment region.

E-F. At the attachment of the SCM Undulin expression in L1 again excludes the attachment region, L1-A. There is a visible line of Undulin expression at the margin of L1-A and L1.

63x magnifications

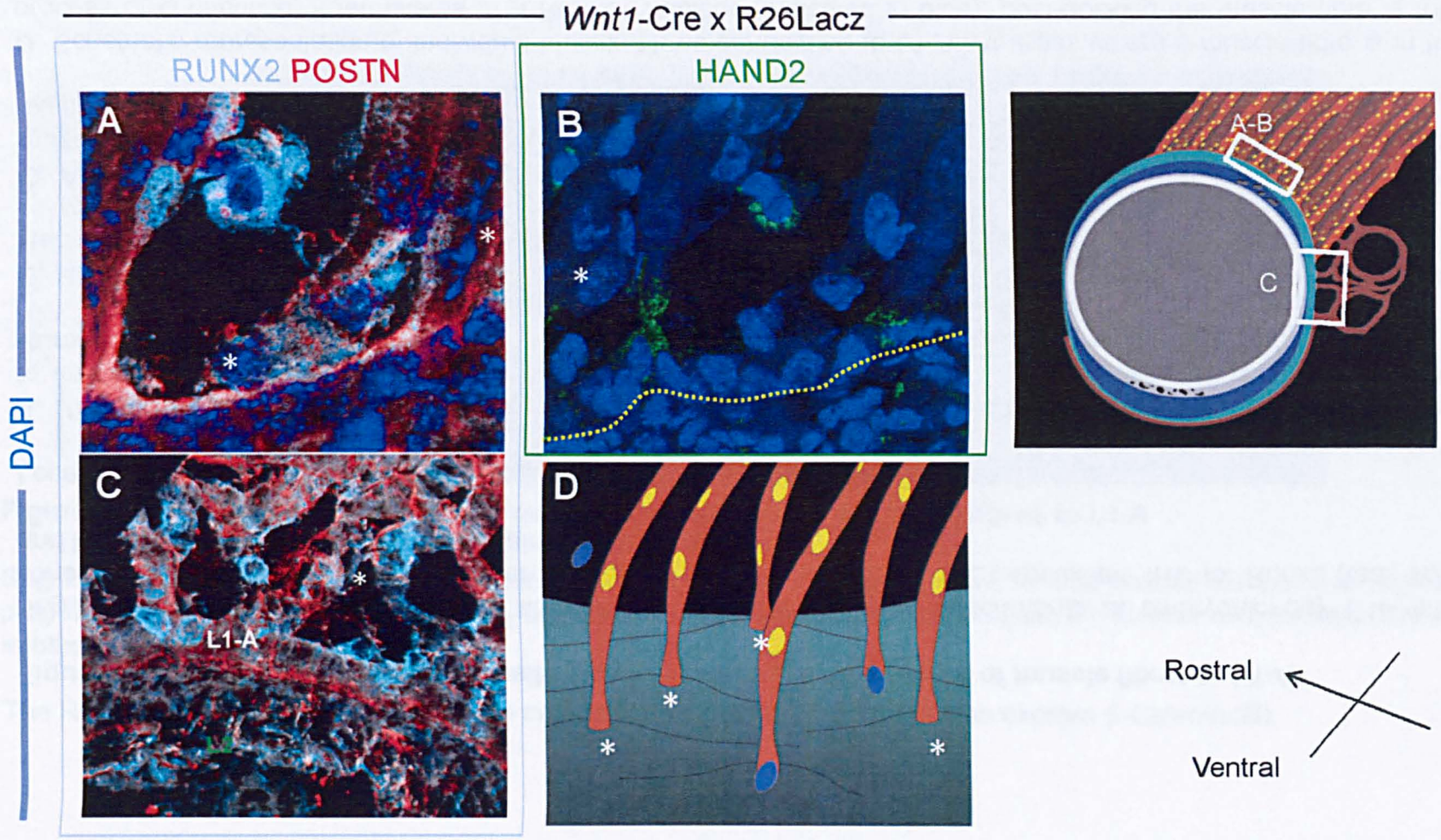
Wnt1-Cre x R26Lacz
RUNX2 POSTN
HAND2
DAPI
A
B
C
D
A-B
C
L1-A
Rostral
Ventral

Figure 4.4: Runx2-positive, Hand2-positive cells mediate the attachment of muscle fibres to L1-A

Sagittal sections through the clavicle at the SCM and omohyoideus attachments at embryonic day E18 after conception (positive vaginal plug is taken as E0); *Wnt1*-Cre$^{+/-}$ x Rosa26LacZ$^{-/-}$ specimen. IHC for Runx2 (teal, **A,C**) and Hand2 (green **B**); nuclear counterstain (DAPI) in blue.

Locations from which **A-C** are taken is indicated on the schematic of the clavicle, far right.

A. High resolution image (100x) of three individual muscle fibres connecting to L1-A. Cells expressing Runx2 appear to mediate the interface of the enthesis. Two of the fibres (far left and far right) have already connected and are Runx2-negative; this contrasts to the central fibre, which terminates in two Runx2-positive nuclei.

B. Hand2 expression in the same region as **A**; unlike Runx2, the two muscle fibres docked into L1-A are positive for Hand2, as is the single nucleus external to muscle fibres.

C. At the interface of the omohyoideus and the clavicle, several Runx2-positive nuclei are visible mediating the muscle:L1-A interface. Runx2-expression is abundant at the end of each muscle fibre before it connects to L1-A, an example is highlighted (*).

D. Schematic representation of individual muscle fibres connecting to L1-A. At areas where a muscle fibre is in the process of connecting, it terminates in a Runx2+ nucleus (indicated in blue); post-docking the muscle fibre is fully embedded in L1-A (*) and the connection point is positive for Hand2.

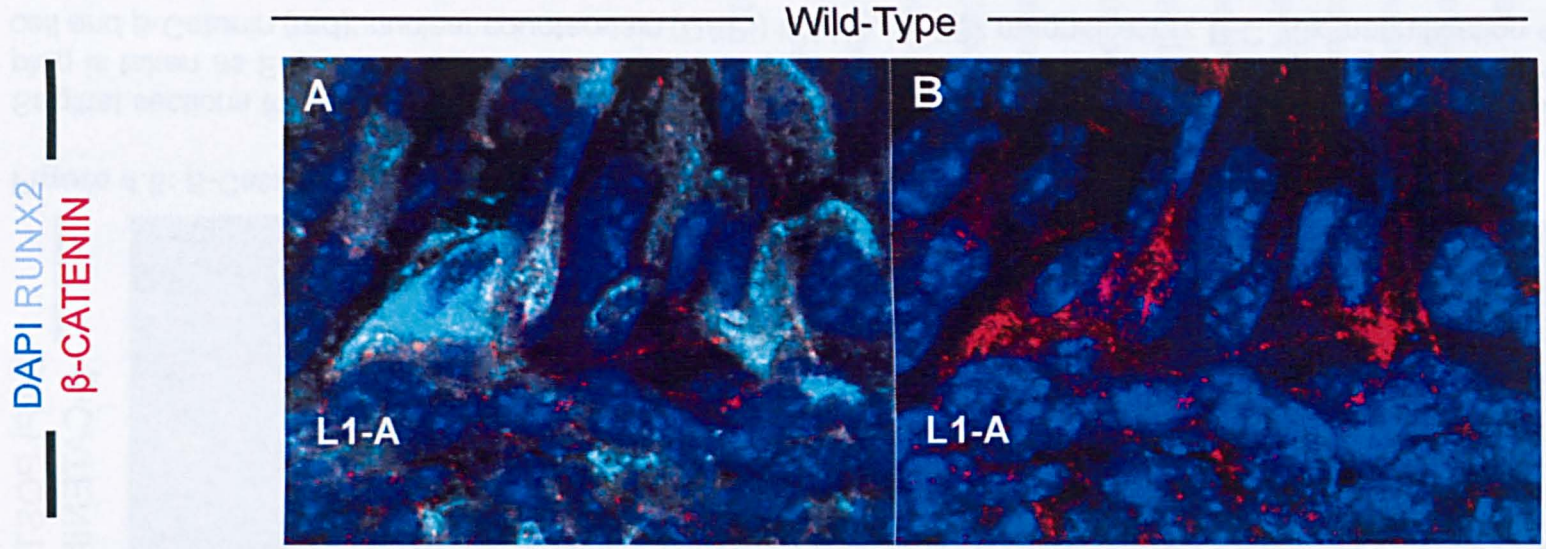

Figure 4.5: β-Catenin expressing cells mediate the attachment of muscle fibres to L1-A

Sagittal sections through the clavicle at the SCM attachment at embryonic day E18 after conception (positive vaginal plug is taken as E0); Wild-type specimen. IHC for Runx2 (teal, **A**) and β-Catenin (red, **B**); nuclear counterstain (DAPI) in blue. 100x magnification + zoom.

The Runx2-positive cells that mediate the muscle fibre attachment to L1 (**A**) also express β-Catenin (**B**).

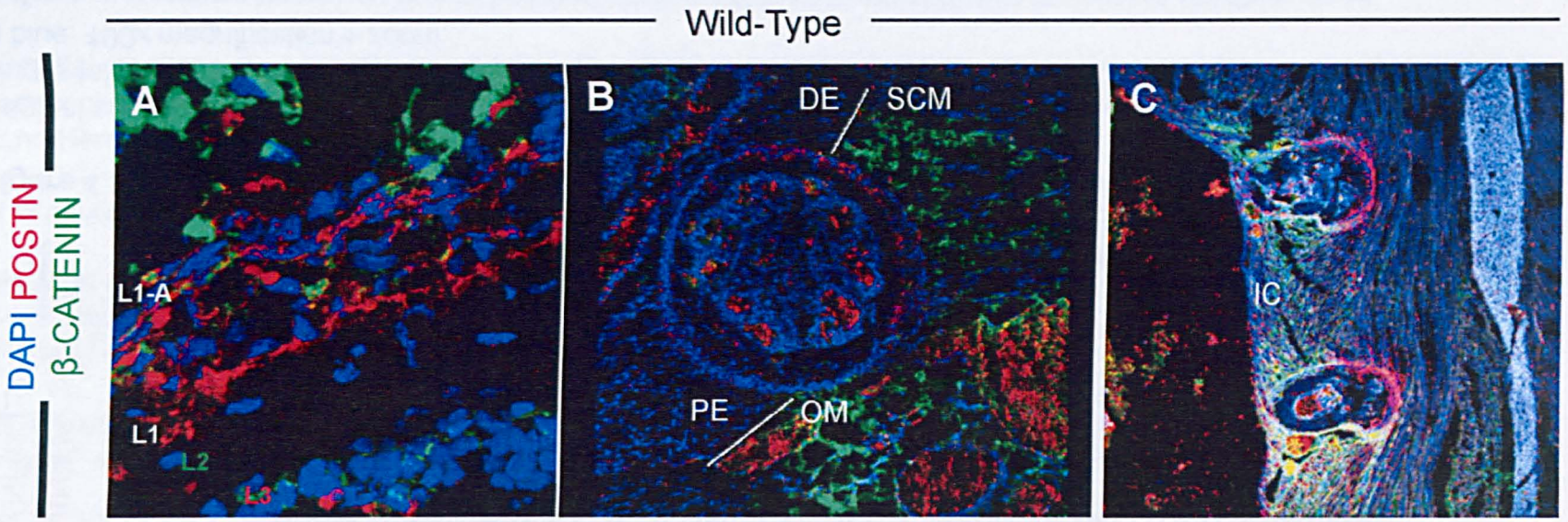

Figure 4.6: β-Catenin expressing cells are confined to entheses of neural-crest derived muscles

Sagittal sections through the clavicle at the SCM attachment at embryonic day E18 after conception (positive vaginal plug is taken as E0); *Wnt*1-Cre$^{+/-}$ x Rosa26LacZ$^{-/-}$ speciman. IHC for β-Galactosidase (green) indicating neural crest cell and β-Catenin (red); nuclear counterstain (DAPI) in blue. **A.** 63x magnification; **B-C** 20x magnification + zoom.

In the clavicle, β-Catenin is expressed by cells at the entheses of neural crest-derived muscles, such as the SCM (**A-B**) and omohyoideus (OM), but not the pectoralis (PE) or deltoid (DE) (**B**); this is also true for the intercostal muscles (IC) (**C**) between ribs.

4.3 Conclusion

Results presented here suggest that the establishment and maintenance of skeleto-muscular patterning is a separate process from that of Layer 2 elaboration. Thus dermal bones and muscle attachments could evolve separately. The finding that L1 has a discrete, molecularly distinct, sub-structure to facilitate the muscle:bone interface resolves previous findings by other groups where expression of ethesis markers did not penetrate into the bone proper (Benjamin *et al.* 2002). The organisation of L1, separating L1-attachment into its own autonomous sub-structure, explains how muscle attachments are maintained through ontogeny while the cancellous bone structure (L2) is formed, another hitherto unexplained complication of the traditional appositional bone growth model.

As β-Catenin is a molecular sensor for mechanical stress (Armstrong *et al.* 2007; Case *et al.* 2008), its expression was expected along all tendino-periosteal interfaces; however, it was confined in the clavicle to attachment regions that are neural crest-derived and may, therefore, constitute the first lineage specific attachment marker (if future work supports the current findings).

4.4 Summary of findings

- The entheses of the clavicle are formed by a sub-section of L1 (L1-attachment) that is physically separated from the remainder of L1 housing rosettes and the generative cells of L2;

- Partitioning of L1 enables muscle attachments to be established early in ontogeny and maintained even as the architecture of the cancellous structure of the bone increases in complexity through development;

- L1-attachment is characterised by cortical expression of Periostin; Undulin expression is excluded from attachment regions;

- At the point of muscle insertion, the muscle fibre docking into L1-attachment is mediated by a neural crest cell with nuclear Runx2 and nuclear Hand2 expression,

- In entheses of the clavicle, expression of β-Catenin, a component of canonical *Wnt* signalling that senses mechanical stress, appears confined to areas where neural crest-derived muscles attach to the clavicle and excluded from mesodermal insertion sites.

5. Discussion & concluding remarks on dermal bone formation

I chose to focus my investigations of intramembranous ossification on the murine frontal bone and dermal component of the clavicle as their structure, development and homologies are accepted as characteristic of membranous bones. The vectorial growth of the frontal bone permits simultaneous observation of different stages of maturation in an unbroken temporal and spatial continuity at a given time; while in the clavicle, the parallel development of the dermal and endochondral components allows the easy juxtaposition of the different mechanisms of growth between the two forms of ossification. I analysed bone maturation during a time-course of ontogeny from E13 through post-natal day 8, using molecular markers traditionally associated with long-bone development and progression through the osteoblastic lineage (from pre-osteoblast through mature osteoblast and osteocyte).

I explored the hypothesis that dermal bones expand in thickness via appositional deposition of cells and matrix in an area pre-patterned by the existing vasculature; in contrast to this, findings presented here suggest an alternative model of dermal bone formation in which the external envelope, comprising L1 and L3, is established before these layers act as generative surfaces contributing cells to the embellishment and radial growth of in intervening space, L2, housing the mineralised matrix and cancellous core of the bone.

The establishment of the two generative layers in the frontal bone (L1 and L3) by embryonic day E13 indicates a molecular heterogeneity of the morphologically homogenous mesenchymal condensations and an early pre-patterning of the frontal bone primordium. The expression pattern and morphology of the two generative layers continues through bone development and birth (notably, cell layer definitions were based on majority expression as the generative layers were heterogenous due to their mosaic nature whereby they comprise both osteoblastic and vascular cells). The

integrity of the molecularly defined Layers 1 and 3 is not broken at any stage of development, essentially creating a closed system. Thus, involution or wrapping of these layers around pre-existing dermal blood vessels could not be found as one would expect to find at least grooves of partially engulfed dermal vasculature, which were never observed. Neither was uncontrolled entry of cells from the generative layers observed, as would be predicted by the appositional model of bone development; instead the entry points of cells in L2 were highly constrained to areas where cells in L1 are organised into rosette structures, reminiscent of stem cell populations in the both mammalian CNS and teleost fish (Mirzadeh *et al.* 2008; Hava *et al.* 2009).

These newly discovered rosette formations may act as a dermal bone stem cell niche, although such an assertion cannot be definitively made without further examination of the molecular characteristics and cell division dynamics within rosettes. Cells within Layer 1 of both osteoblastic and vascular lineages use the rosette as the entry point into Layer 2. Rosettes are the *only* entry point for cells into L2 and we show in a single embryonic time slice and across ontogeny that L2 grows in thickness as additional cellular material is added to it from generative layers L1 and L3. In the most immature stage of frontal bone development where diploë architecture (L1-L2-L3) is evident, L2 is a cell sparse region; as maturation progresses increasing numbers of cells invade L2 in pairs of Runx2-positve osteoblasts and CD31/vWF-positive endothelial cells. This twinning can serve as a mechanism to ensure that although these osteoblasts later secret matrix in a polarized fashion, osteoblasts are always supported by vasculature that forms in direct juxtaposition. This proximity is also the precondition for labels (such as calcein etc.) to reach the osteoblasts and the matrix they secrete.

The ability of the generative layers to give rise to cells that bee-line into L2 and there form a sheet-like architecture resembles convergence-extension like behaviour dependent on both the PCP pathway and the transcription factor Hand2, as evidenced by the disrupted formation of dermal bones in the Hand2-mutant strains of mice. Hand2 joins the group of other interactors

of Runx2 that can block and modulate its function by direct binding. Here I find evidence of a tethering mechanism that ensures that although Runx2 is expressed in the developing bone, it cannot act as it is prevented from entering the nucleus in the entirety of L1, except the few 1-2 cells within rosettes and cells entering L2. Upon Hand2 removal we see significant deregulation of this process and re-localisation of Runx2 to the nuclei of cells within L1 and L2; the bone becomes a permissive environment with uncontrolled cell entry into L2 and subsequent inability of cells within L2 to form sheets, a key hallmark for the growth of L2 in wild types.

We posit that acquisition of a Hand2-dependent molecular programme by the neural crest was a key preadaptation for the elaboration of dermal bone (L2) beyond that of single radial cancellar walls. The level of disruption of bone formation in the Hand2-mutants was surprising, including effects observed in very medial areas of the clavicle that have contradictorily been described as forming via dermal or endochondral ossification (Huang *et al.* 1997). These results could alternatively suggest a dermal method of ossification of this area, or a role of Hand2 in the endochondral development of the outer layers of the clavicle.

In the wild-type condition, the L2 system is highly dynamic, with the layer morphology, vascularisation and biomineralisation developing in parallel, with evidence of continual remodelling within the bone through foetal development and the first week of birth.

Remodelling of the bone is an important feature of the new model proposed herein for dermal bone formation. A time course of *in vivo* matrix production revealed the surprising result that osteoblasts are the key agents not only of initial matrix secretion but also in remodelling the matrix that they (or preceding osteoblasts) have laid down. Results suggest the first collagen scaffold in the bone is formed by Collagen II, secreted appositionally by cells at the L1 margin of L2. I then observe a remarkable mechanism of L2 invasion and immediate matrix deposition in 'cloud' or 'bag' like

arrangements, followed by a bidirectional invasion of cells into the mineral phase of L2 and subsequent internal remodelling of the calcified areas. This counters classical models of mineral accretion on a pre-existing scaffold as, in contrast, the collagen scaffold is continually being remodelled. Osteoblasts dissolve the existing mineral with MMP13 (rendering the calcified matrix flexible), which is initially on the outside of L2 and becomes injected radially into the mineral cores by virtue of invading osteoblasts. MMP13 is a direct target of Runx2, allowing cells to switch easily between osteoid/matrix dissolution and production (Nakamura *et al.* 2004). Vascular cells also remodel the previously established osteoblast-endothelial sheets inside L2 by secreting MMP9 which stays confined to these sheet-like inner surfaces. We posit that this is used to expand the number of cells taking part in sheet formation. Interestingly, MMP9 is able to cleave Osteopontin (Nilsson *et al.* 2005), indicating the MMP9 carrying vasculature could invade the OPN+ vasculature-matrix boundary as part of the remodelling.

Introduction of MMPs to the L2 system, as well as mixtures of different collagens within L2 (such as Collagen I, Collagen II and Collagen XIV (Undulin)) changes the mixtures of fibrous versus amorphous collagens, which has previously been speculated to be a key mechanism by which woven bone could come into being. PMT imaging of a P8 murine frontal bone displays the biomineralised zone contains an amorphous core of mineralised islands surrounded by a late appositional matrix. The appearance of appositional matrix surrounding amorphous inner matrix is a feature retained throughout evolution from the earliest examples of fossilised biomineralised tissues in Anaspids (Figure 5.1). Halstead and others previously discussed whether these centres of cancellar walls are cellular or not (Halstead and Sarjeant 1995). The osteoblast-endothelial interface, which we find can be derived from the same ancestral cell population and emerges as the result of a convergence-extension motion into and out of the rosette system, could provide a cellular framework in which biomineralization occurs in fossil fish (Jordan, Koentges and Donoghue, unpublished). Here I have described a model of mineralisation and its remodelling that entirely

rests on the protean ability of this osteoblast-endothelial surface and that may have been conserved through over 420 million years of evolution (Figure 5.1).

The establishment of the bone morphogenesis, vascularisation and mineralisation precedes the introduction of osteoclasts to the system. I base this supposition on several factors: the majority of the frontal bone is of neural crest origin (including the vasculature) and I have found no evidence indicating monocytes and megakaryocytes (the precursors to osteoclasts (Geissmann *et al.* 2010)) derive from the neural crest. Osteoclasts are introduced to the bone via the vasculature, which we have shown here develops in parallel with the morphology and biomineralisation; ergo, the only way osteoclasts would be introduced during the time-course of our analysis would be if the mesodermal cells found within the early bone differentiate into osteoclasts. Additionally, I do not observe cells within the bones at this stage of maturation that display the classic morphological indicators of osteoclasts, namely mutli-nucleation, characteristic F-Actin rings, or nuclei containing a high proportion of vesicles (Nijweidi *et al.* 1986; Vaananen *et al.* 2000; Buccione *et al.* 2004).

In addition to bone layer morphogenesis, vascularisation and biomineralisation, the establishment of the skeletal muscle:bone interface was also examined. The structure of L1 mediates the enthesis, whereby it is sub-compartmentalised into an area where Runx2/Hand2-nuclear expressing cells dock the skeletal muscle fibres into a periosteum-like tissue. This arrangement allows an early connection to an area of L1 that is physically connected to the bone proper, but does not insert muscle fibres into an area that will be remodelled; in this arrangement, bone development can progress without being impinged upon by mechanical strain and bone thickness growth is not stunted.

The major differences between the traditional and new models of bone development are described in Table 5.1 and Figures 5.2-5.6.

The success of the current study was predicated on the type of analysis conducted: a time-course of immunohistochemsitry combined with high resolution imaging and three-dimensional analysis of bone development. The extensive cohort of markers examined at single-cell resolution was an attempt to interlink all the crucial aspects of bone development, including layer morphogenesis, vascularisation, biomineralisation and muscle:bone connectivity. Although the majority of these markers have been well-characterised in endochondral formation, they have not been used for analyses of direct ossification.

Crucially, I observe the expression pattern of bone-related markers is determined by their position rather than temporally by stage in development. For example, the establishment of periost/perichondrium-like tissues (L1 and L3) is prior to the generation of an embellished L2; and the osteoblasts did not progress through stages of development marked by alternating Runx2 and Osteopontin expression. Remarkably, co-expression of several markers and post-translational modifications appear to be critical for dermal bone formation.

The discrepancy between current findings and previous studies is attributable to three features: firstly, the use of immunohistochemistry, rather than *in situ* hybridisation; secondly the analysis of these markers in undisturbed conditions (avoiding the use of dissociation or explant techniques); and thirdly the extensive time-points analysed as single time-point studies could not map the continuity of Layers 1 and 3, nor explore the mechanism of L2 expansion. Immunohistochemistry was favoured over *in situ* due to the many post-translational modifications and protein localisation events that effect the function of some of the genes that were to be analysed (ex: Runx2 (Harada *et al.* 1999; Westendorf 2006; Jonason *et al.* 2009). By exploring the protein localisation of the markers in question in a time-course of development under *in vivo* conditions at single-cell resolution, we were able to discern the fine detail of the bone development. For example, this technique enabled me to identify previously repudiated co-expression of

Runx2 and OPN, which appears to define the matrix-vasculature interface and may have been overlooked in previous studies due to the minority of cells exhibiting co-expression.

I have, therefore, classified the cell types analysed in the current study by their unique molecular properties and the functions they appear to play in intramembranous ossification. This classification includes: rosettes, motile osteoblasts, osteoblasts with remodelling potential and those at the boundary of biomineralised areas and the mineral:vasculature interface; additionally, I differentiate between generic vasculature and the endothelia capable of remodelling. Molecular maps of marker co-expression, and corresponding diagrams of the model of intramembranous ossification based on current results, are found in Figures 5.7-5.13.

The mechanism of generating the architecture of dermal bone described herein would have existed before endochondral ossification, a feature that is phylogentically more recent than intramembranous ossification (Donoghue and Sansom 2002). The model of dermal bone formation based on the current study is predicated on the continual intercalation of both neural crest and mesodermal cells into the developing bone, revealing the highly dynamic nature of intramembranous ossification. Interestingly, because of the evolutionary precedence of dermal over endochondral bone, one can consider that certain aspects of indirect ossification follow similar generative rules to those observed in the current study; for example, the invasion of vasculature to the cartilaginous template of endochondral bones. As such, a reanalysis of the process of bone remodelling during endochondral ossification may be warranted, as this process is often studied in adult animals in the context of bone injury, which may be very different from the early development of endochondral structures (Lieberman and Friedlaender 2005). By examining the various features of dermal bone formation, this study aimed to put the ontogenetic features of bone development in the correct phylogenetic order, based on the assumption that it is endochondral

bone formation that co-opts its mechanism of growth from the older form of dermal ossification.

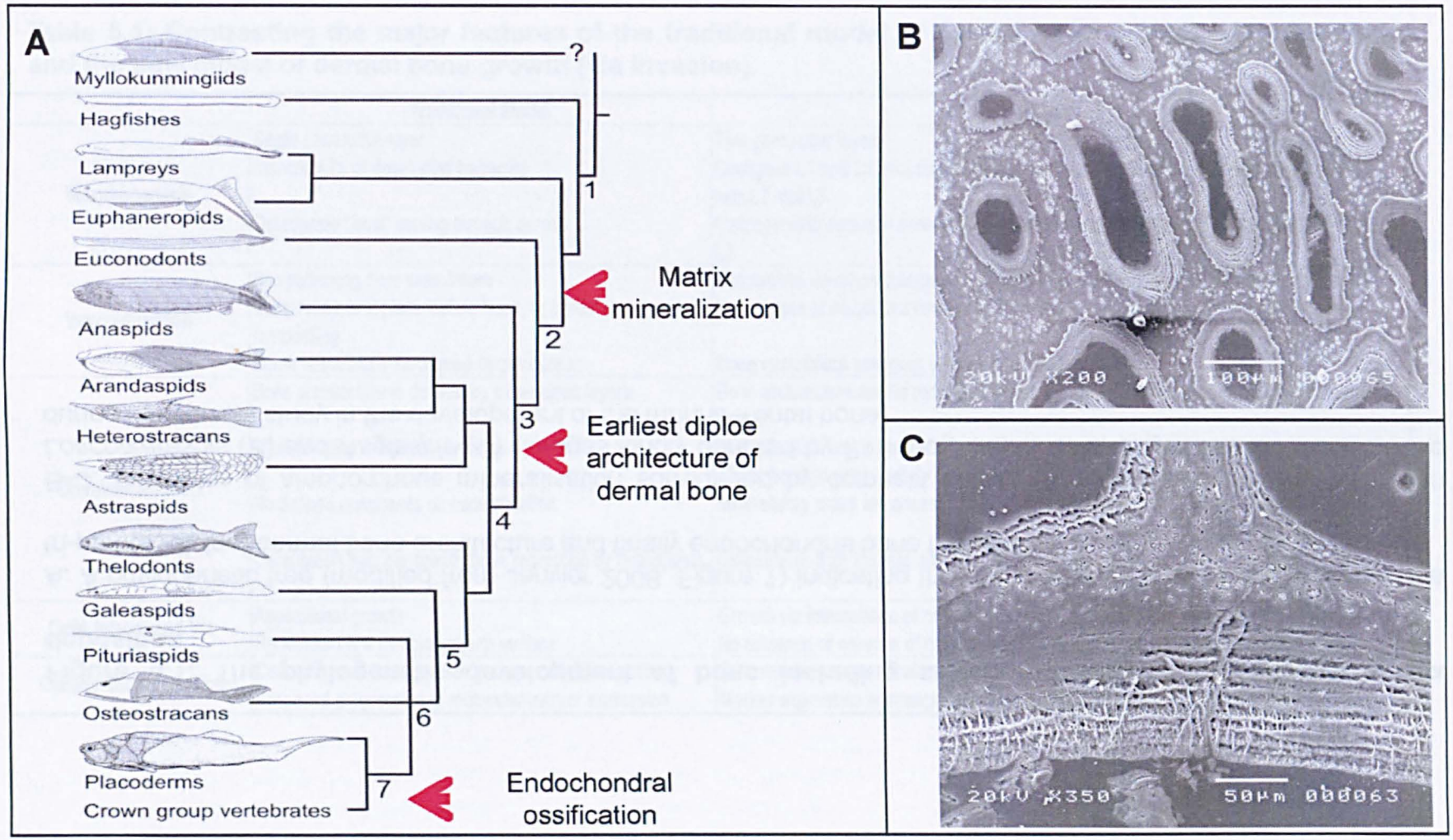
A
Myllokunmingiids
Hagfishes
Lampreys
Euphaneropids
Euconodonts
Anaspids
Arandaspids
Heterostracans
Astraspids
Thelodonts
Galeaspids
Pituriaspids
Osteostracans
Placoderms
Crown group vertebrates
?
1
2
3
4
5
6
7
Matrix mineralization
Earliest diploe architecture of dermal bone
Endochondral ossification
B
20kV X200
100µm 000063
C
20kV X350
50µm 000063

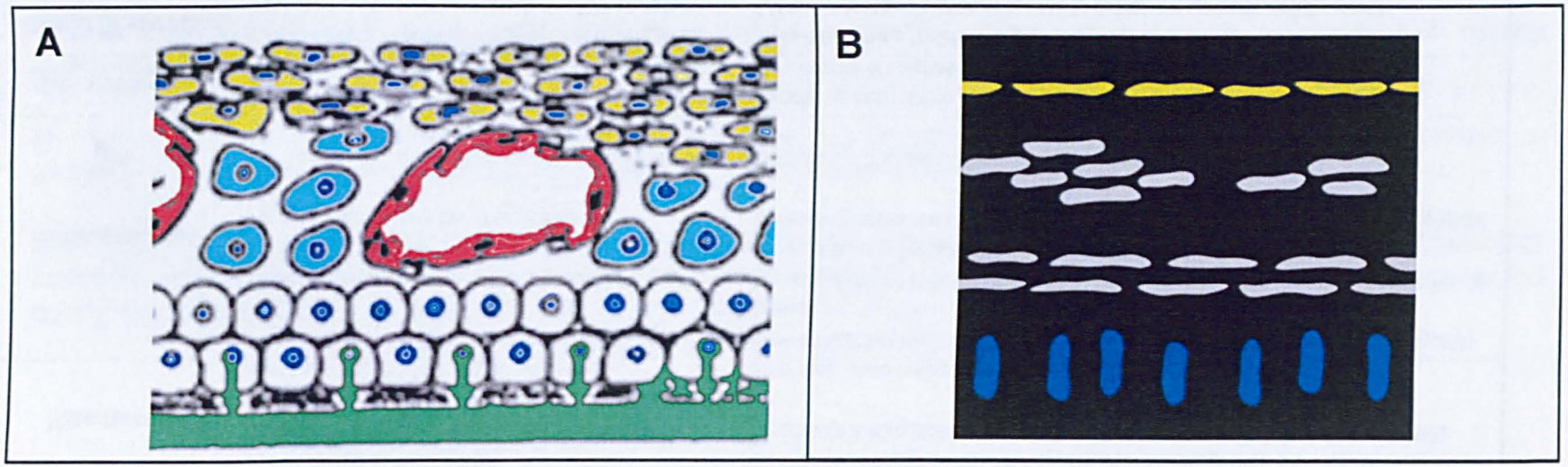

Figure 5.2: The traditional model of dermal bone development contrasted to the alternative model supported by the current data: Initialising bone development

Contrasting models of dermal bone development.

A. The traditional model of dermal bone development favours an appositional mode of growth. The early mesenchymal condensation features pre-osteoblasts (turquoise) in the vascularised dermis (early condensed mesenchyme/dermis in yellow). Pre-osteoblasts differentiate into osteoblasts (white) and secret matrix (grey) which mineralises (green). Modified from Bruder & Scaduto in *Bone Regeneration and Repair,* 2005, Human Press Inc. Lieberman & Friedlaender, eds.

B. The model supported by the current findings: in the earliest stages (E13) the mesenchymal condensation (grey cells) is already a bi-layer comprising osteoblastic and vascular cells (grey), that sits beneath the dermis (yellow) and above the brain (blue).

Figure 5.1: The phylogenetic development of bone including amorphous versus appositional matrix deposition

A. A phylogenetic tree (modified from Janvier 2008, Figure 1) indicating the first instances of a mineralised matrix, a tri-partite (diploe) dermal bone architecture and finally endochondral bone formation.

B-C. Examples of amphorphous mineralisation surrounded by compact sheets of mineralisation in the fossil fish *Loricopteraspis* (**B**) and *Anglaspis* (**C**) (images kindly donated by P. Donoghue). This arrangement is also observed during the current study in the development of the murine frontal bone.

Table 5.1: Contrasting the major features of the traditional model of dermal bone growth (via apposition) and the new model of dermal bone growth (via invasion).

	Traditional Model	New Model
Morphogenesis	Single generative layer Discontinuity of developing trabacles Osteogenic "front" moving through dermis	Two generative layers Contigous L1 and L3 encasing L2 which matures in time and is in constant communication with L1 and L3 Osteogenesis occurs in controlled and coordinated manner by increasing the complexity of L2
Vascularisation	Pre-patterning from vasculature Vasculature is in place before bone, or introduced via remodelling Some vasculature introduced by periosteum	Vasculature develops co-commitantly with layer morphogenesis and biomineralisation Vasculature is introduced via rosette formations, in conjunction with osteoblastic cells Bone vasculature contigous with L1 and L3 vasculature
Biomineralisation	Bone architecture is defined by mineralised layers Mineralisation in distinct layers or trabacles No defined constraints on mineralisation Osteoblasts secrete ostoid; bone resorption by osteoclasts	Bone architecture can be remodelled even after mineralisation, accomodating tangential growth Mineralisation first in clouds/islands, then horizontal sheets and later radial connection; this allows bone to grow radially Mineralising areas are encased by non-mineralising cells with distinct molecular signature Osteoblasts both secrete and remodel the osteid matrix
Cells Introduced Via	Appositional growth Periosteum is a cambial growth surface	Growth via intercalation of cells from L1 and L3 mediated by rosettes No evidence of columns of cells across layers deposited in a cambial fashion
Cellular Differentiation	Cells progress through distinct stages of differentiation Proposed progression of molecular marker expression	Cells maintain the molecular signature of their layer of origin Marker expression is strongly related to spatial, not temporal, cellular identity

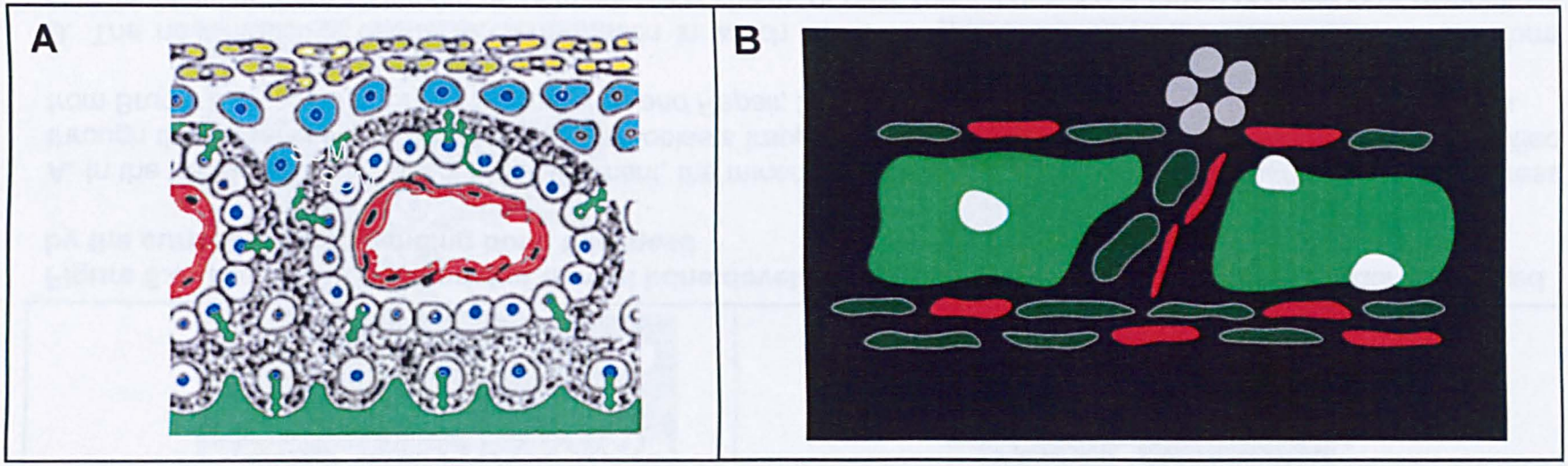

Figure 5.3: The traditional model of dermal bone development contrasted to the alternative model supported by the current data: Early mineralisation

A. In the traditional model of intramembranous ossification, the osteoblast front grows and cells that were pre-osteoblasts (turquois) in Figure 5.2 differentiate into osteoblasts, around the pre-existing vasculature. Osteoblasts secrete and are trapped in the osteoid (grey), which becomes mineralised (green). Modified from Bruder & Scaduto in *Bone Regeneration and Repair,* 2005, Human Press Inc. Lieberman & Friedlaender, eds.

B. The alternative model of dermal bone development features cell invasion from two generative layers as the mode of growth. An early bi-layered mesenchyme matures when cells of the bi-layers flatten and move apart with the intervening space carrying the matrix (green). The two generative layers comprise osteoblastic (dark green) and vascular (red) cells and carry periost markers from an early stage. Cells from these layers enter into the space between them at points dictated by the presence of rosette formations. Mineralisation is seen in distinct islands from E16 (green), cells producing the matrix are of osteoblastic origin (Runx2 or OPN expressing cells) (white).

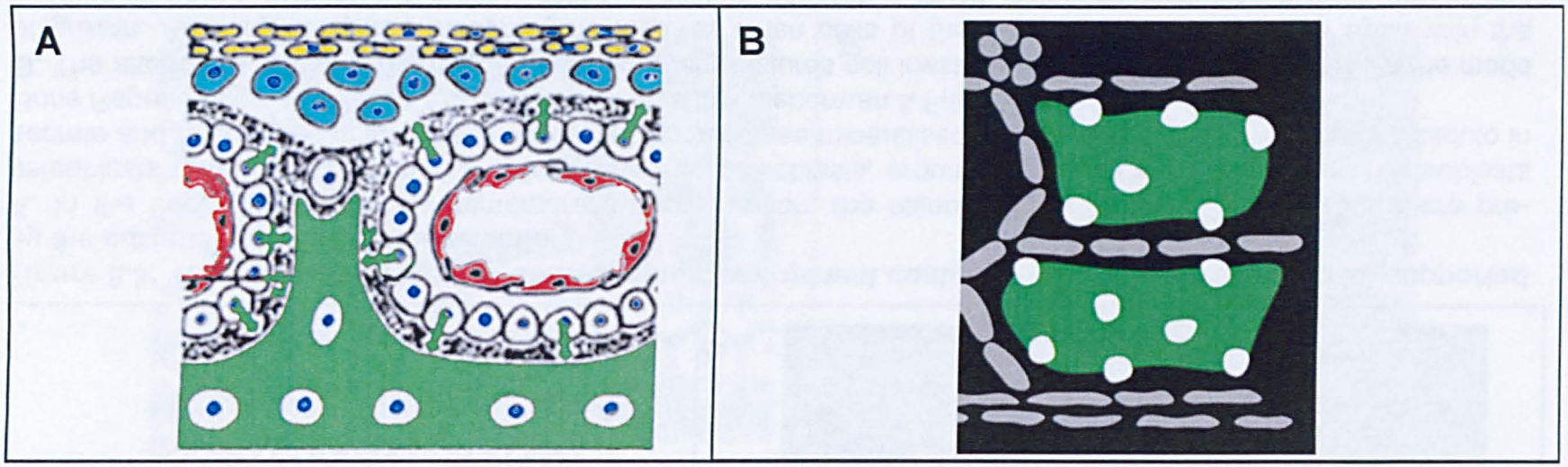

Figure 5.4: The traditional model of dermal bone development contrasted to the alternative model supported by the current data: Expanding bone thickness

A. In the traditional model of bone development, the mineralisation occurs as a single front that continues to progress through the mesenchymal condensation. Osteoblasts trapped in osteoid further differentiate into osteocytes. Modified from Bruder & Scaduto in *Bone Regeneration and Repair,* 2005, Human Press Inc. Lieberman & Friedlaender, eds.

B. The new model of dermal bone formation in which the biomineralisation occurs in parallel sheets that form concomitantly and are separated by unmineralised sheets of cells (grey indicating a mixed population of osteoblasts and vascular cells) maintaining contact with the generative layers. The unmineralised sheets experience horizontal elaboration within the cancellous bone and supply both osteoblastic and vascular cells to the growing system. The mineralised areas can be moved and remodelled during their formation, without the presence of osteoclasts.

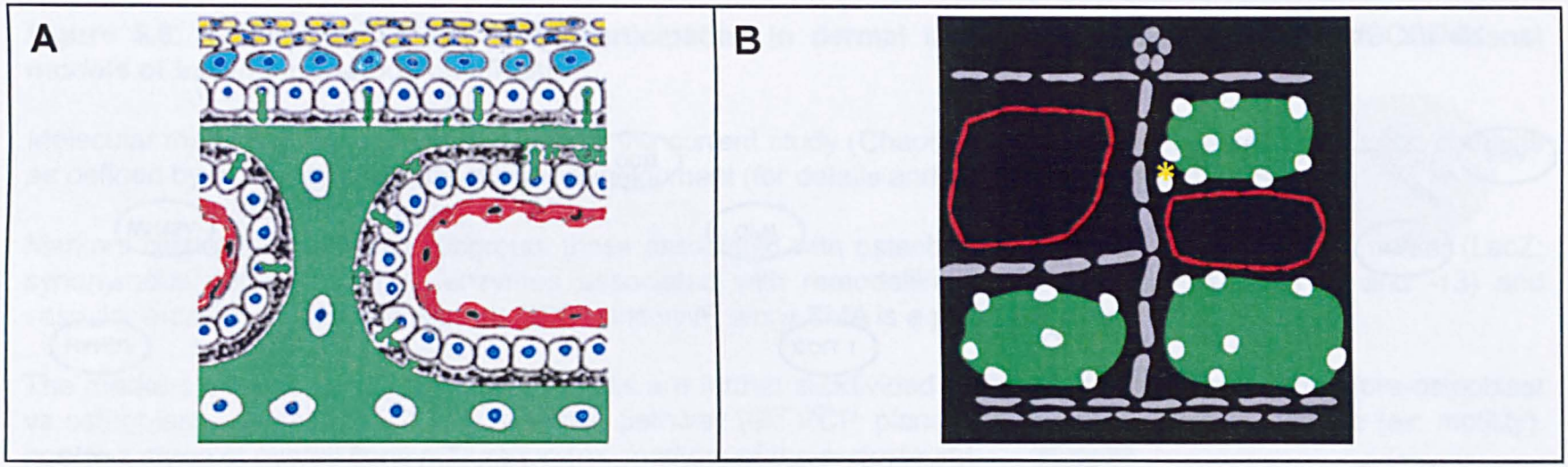

Figure 5.5: The traditional model of dermal bone development contrasted to the alternative model supported by the current data: Further maturing the bone

A. The bone continues to mature as additional sheets of mineralisation are added in an appositional manner. At a final stage of development the periost surrounds the bone and the spongious core of the bone is surrounded on either side by compact bone (not shown on this diagram). Modified from Bruder & Scaduto in *Bone Regeneration and Repair,* 2005, Human Press Inc. Lieberman & Friedlaender, eds.

B. In the invasive model of dermal bone development, the layer morphogenesis, vasculature and biomineralised areas develop in parallel and are subject to remodelling. The biomineralised areas are expanded from cells burrowing in (example of a cell leaving from the sheet of unmineralised cells and approaching the mineralised area to burrow in indicated with *) and increasing the mineralised area from within; simultaneously, the vasculature invades the growing bone. The cells invading from the generative layers (grey) continue to provide material for bone expansion. The mature bone structure features a spongious layer surrounded by late appositionally added compact bone (late apposition from L1 and L3 not shown on this diagram).

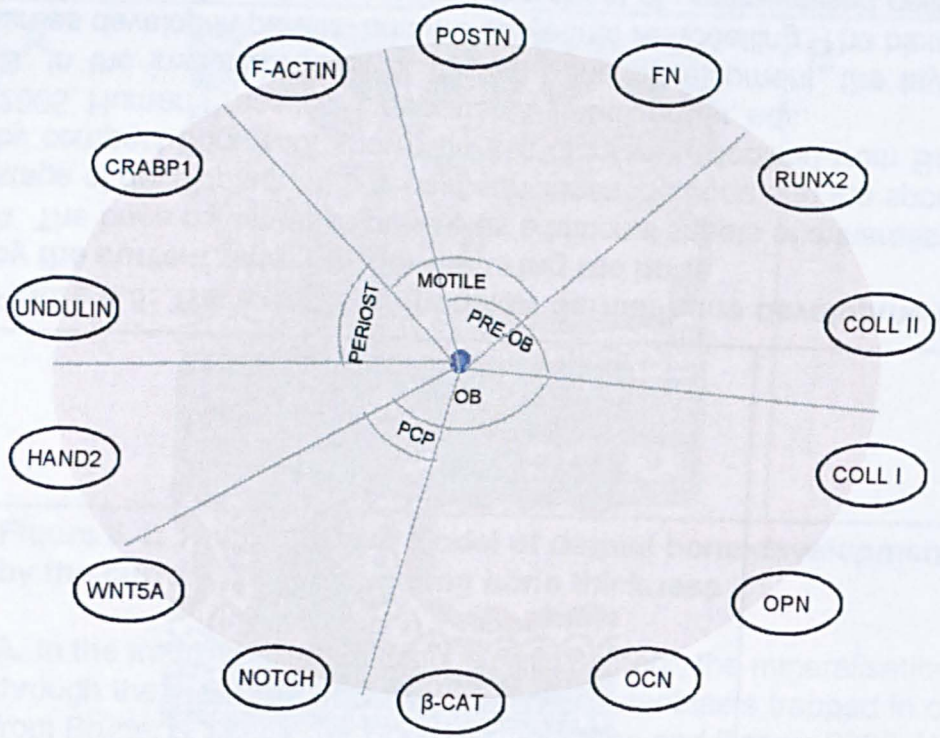

NEURAL CREST

REMODELLING

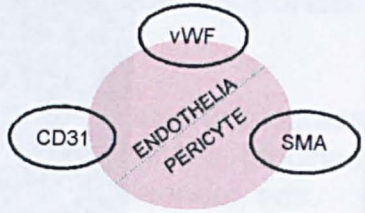

VASCULAR

Figure 5.6: Molecular profile of cells participating in dermal bone development according to traditional models of intramembranous ossification

Molecular map of all the markers assayed in the current study (Chapters 1-5) and the expected expression domains as defined by published analyses of bone development (for details and references, see text).

Markers cluster into 4 distinct subgroup: those associated with osteoblastic lineages, the neural crest marker (LacZ; synonymous here with GFP), enzymes associated with remodelling (matrixmetalloproteinases -9 and -13) and vascular markers (endothelia express CD31 and vWF, while SMA is a pericyte marker).

The markers associated with osteoblastic cells are further subdivided by the stage of cell maturation (pre-osteoblast vs osteoblast), an association with a certain pathway (ex: PCP, planar cell polarity), a notable feature (ex: motility), and/or a stage of overall bone maturation (ex: markers of the periosteum).

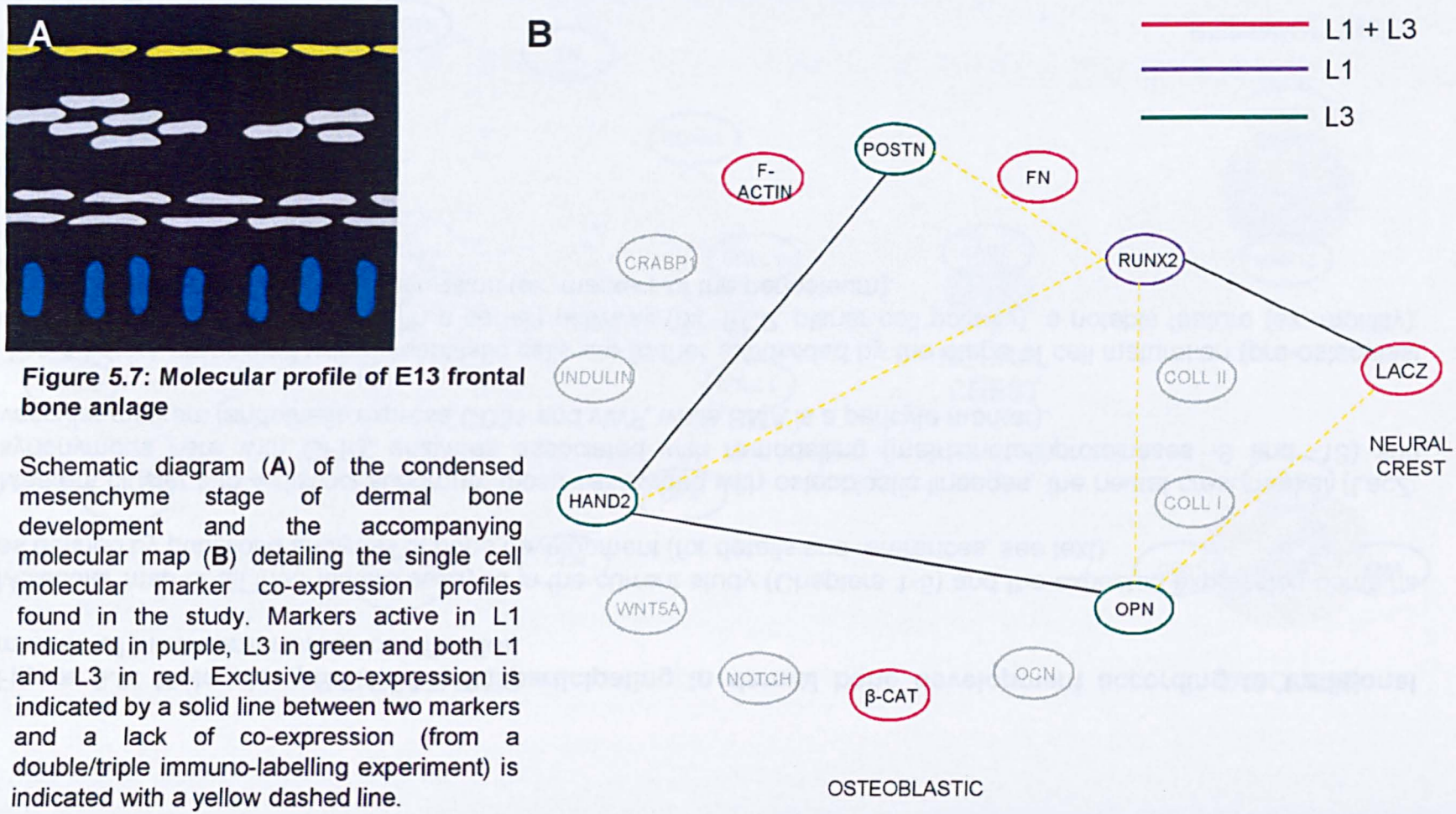

Figure 5.7: Molecular profile of E13 frontal bone anlage

Schematic diagram (**A**) of the condensed mesenchyme stage of dermal bone development and the accompanying molecular map (**B**) detailing the single cell molecular marker co-expression profiles found in the study. Markers active in L1 indicated in purple, L3 in green and both L1 and L3 in red. Exclusive co-expression is indicated by a solid line between two markers and a lack of co-expression (from a double/triple immuno-labelling experiment) is indicated with a yellow dashed line.

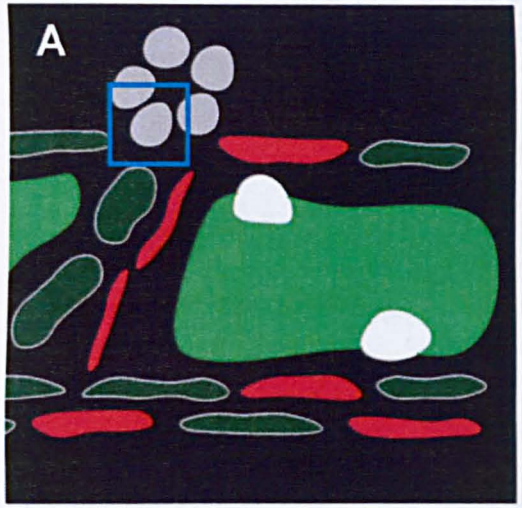

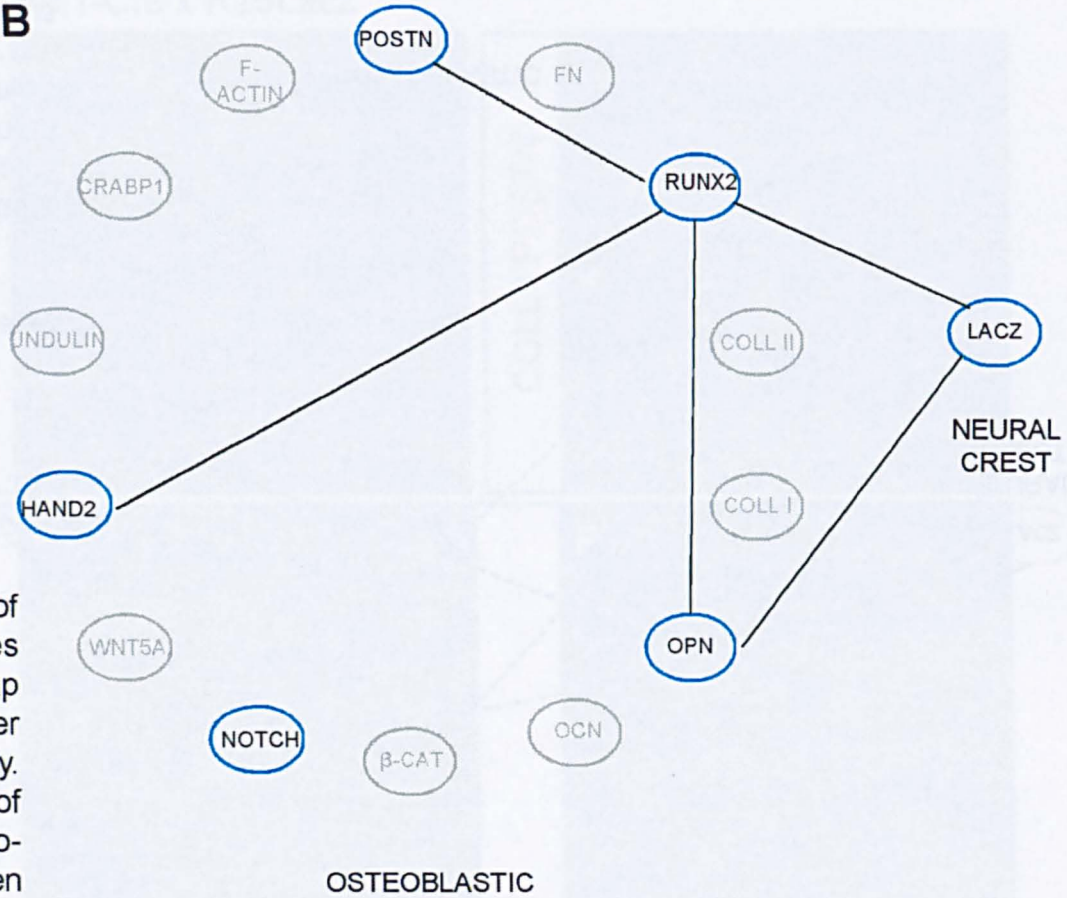

Figure 5.8: Molecular profile of rosettes

Schematic diagram (**A**) of an early stage of dermal bone development including rosettes in L1, and the accompanying molecular map (**B**) detailing the single cell molecular marker co-expression profiles found in the study. Markers active in the cell at the apex of rosettes are highlighted in blue and co-expression is indicated by a solid line between two markers.

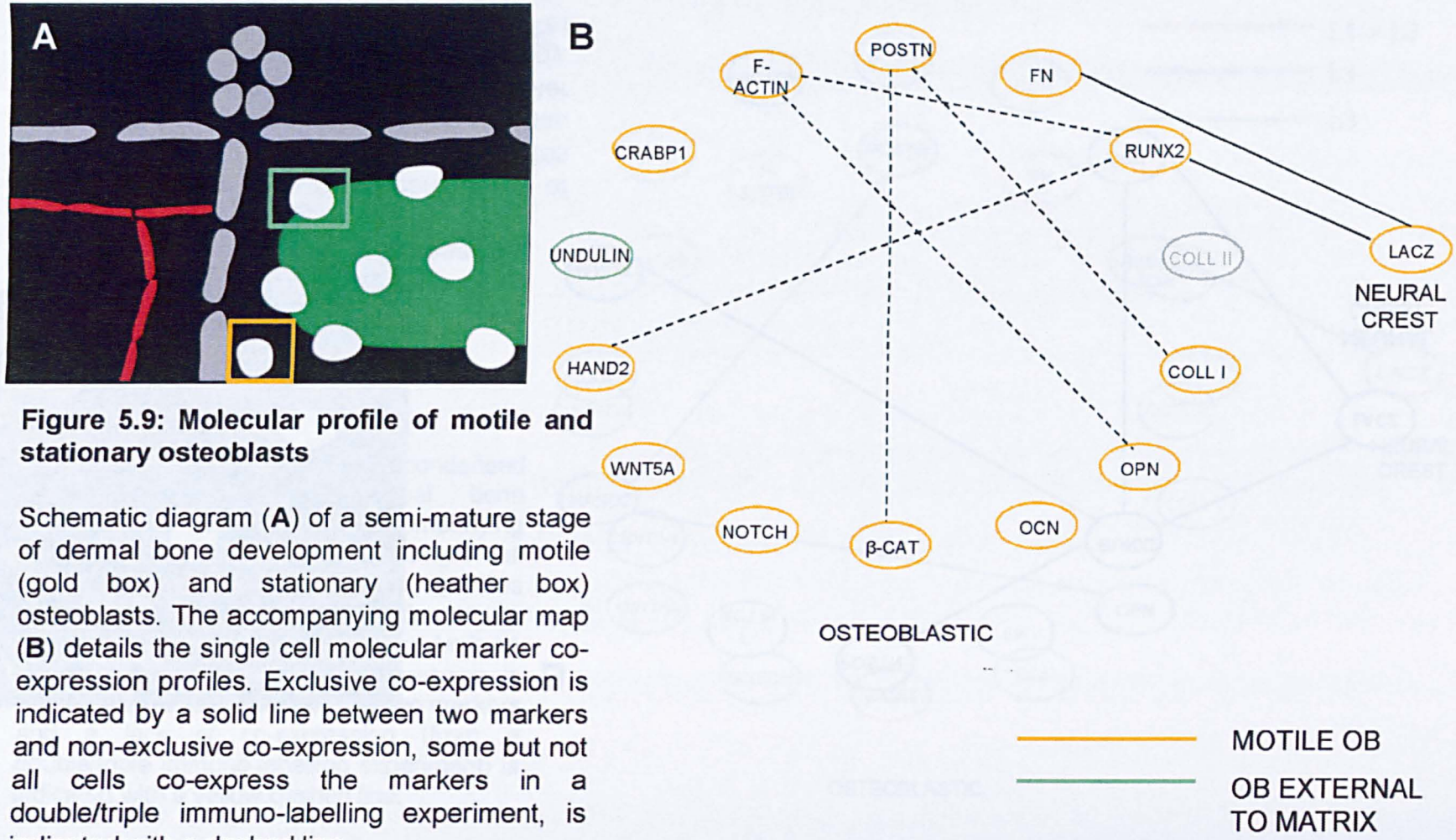

Figure 5.9: Molecular profile of motile and stationary osteoblasts

Schematic diagram (**A**) of a semi-mature stage of dermal bone development including motile (gold box) and stationary (heather box) osteoblasts. The accompanying molecular map (**B**) details the single cell molecular marker co-expression profiles. Exclusive co-expression is indicated by a solid line between two markers and non-exclusive co-expression, some but not all cells co-express the markers in a double/triple immuno-labelling experiment, is indicated with a dashed line.

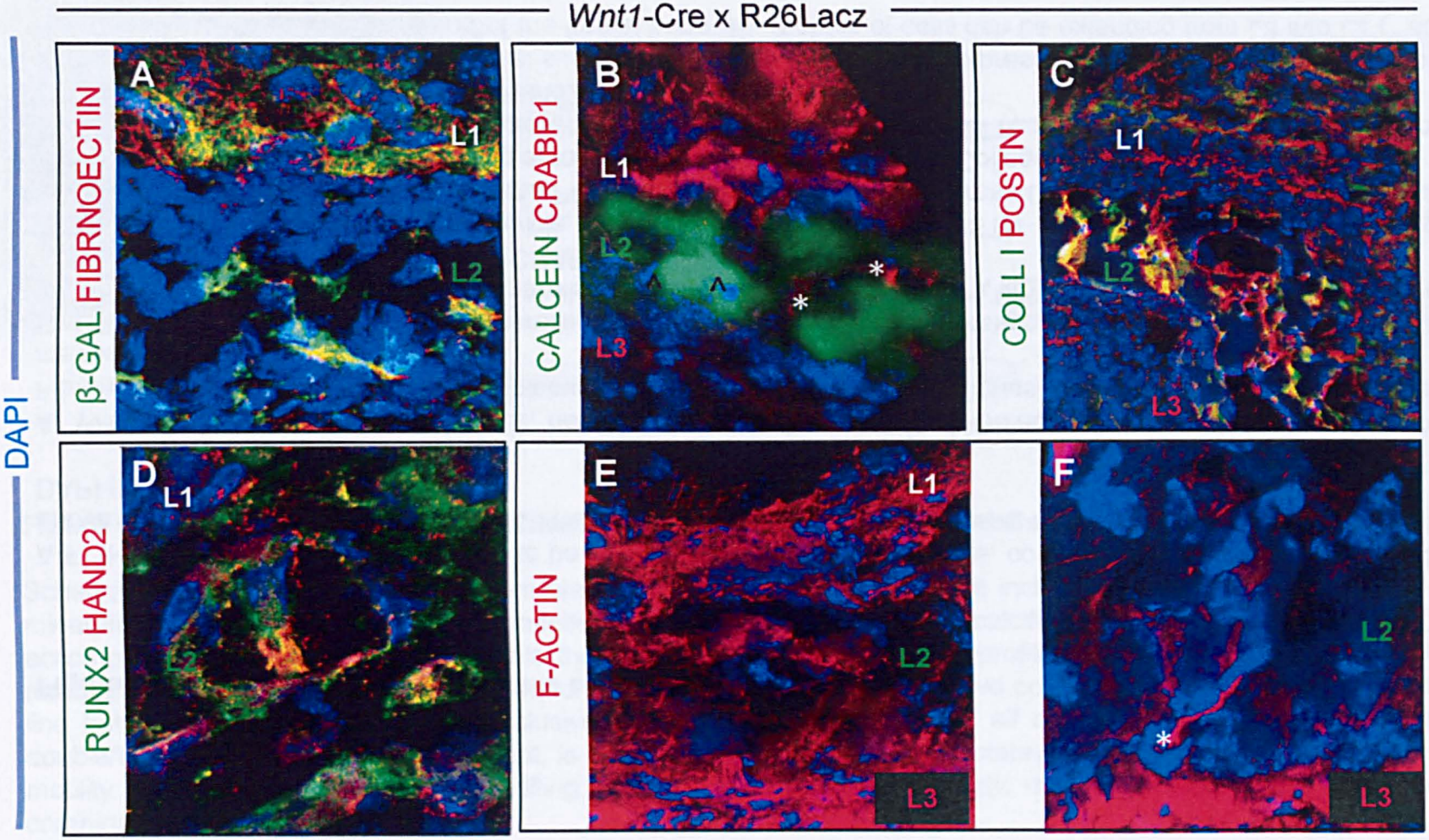
Wnt1-Cre x R26Lacz
DAPI
β-GAL FIBRNOECTIN
A
L1
L2
CALCEIN CRABP1
B
L1
L2
L3
COLL I POSTN
C
L1
L2
L3
RUNX2 HAND2
D
L1
L2
F-ACTIN
E
L1
L2
L3
F
L2
L3

Figure 5.10: Additional images of motile osteoblast cells

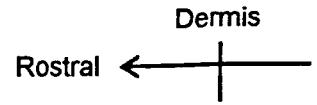

A-F. IHC for molecular markers found to be expressed by motile osteoblasts, combinations described in Figure 5.9, above. All 63x magnifications from E18 *Wnt1*-Cre$^{+/-}$ x Rosa26LacZ$^{-/-}$ transgenic mice. All have nuclear counterstain DAPI (blue).

A. Within L1 and at some points in L2, neural crest cells (indicated by β-Galactosidase reactivity, green) express Fibronectin (red), a cell-adhesion molecule. Notably, in this region, L2 has an unusually high population of mesodermal cells.
B. CRABP1 (red); calcein stain of mineralised area (green); nuclear counterstain DAPI (blue). Motile cells in L1 and those in L2 that are remodelling the mineralised area are CRABP1 positive (*), while those that secrete the matrix and are embedded within it do not express CRABP1 (^).
C. The dermal component of the clavicle, where it meets the SCM. POSTN (red) is found at the muscle-bone interface and within L1, L2 and L3. Some POSTN expressing cells also express Collagen I (green) although, notably, osteoblasts of clasps of cells traversing across L2 are the most reactive for Collagen I.
D. The dermal component of the clavicle where there is a wide expression of Runx2 (green) within L1 and L2; some cells within L2 are also co-expressing Hand2 (red).
E-F. In the frontal bone near the coronal suture (**E**), all of L1 and L3 cells express F-Actin (red, rhodamine phalloidin stain), while at the most mature end of the frontal bone (**F**), a chain of cells can be extending from L3 into L2 (* at L3 base of chain).

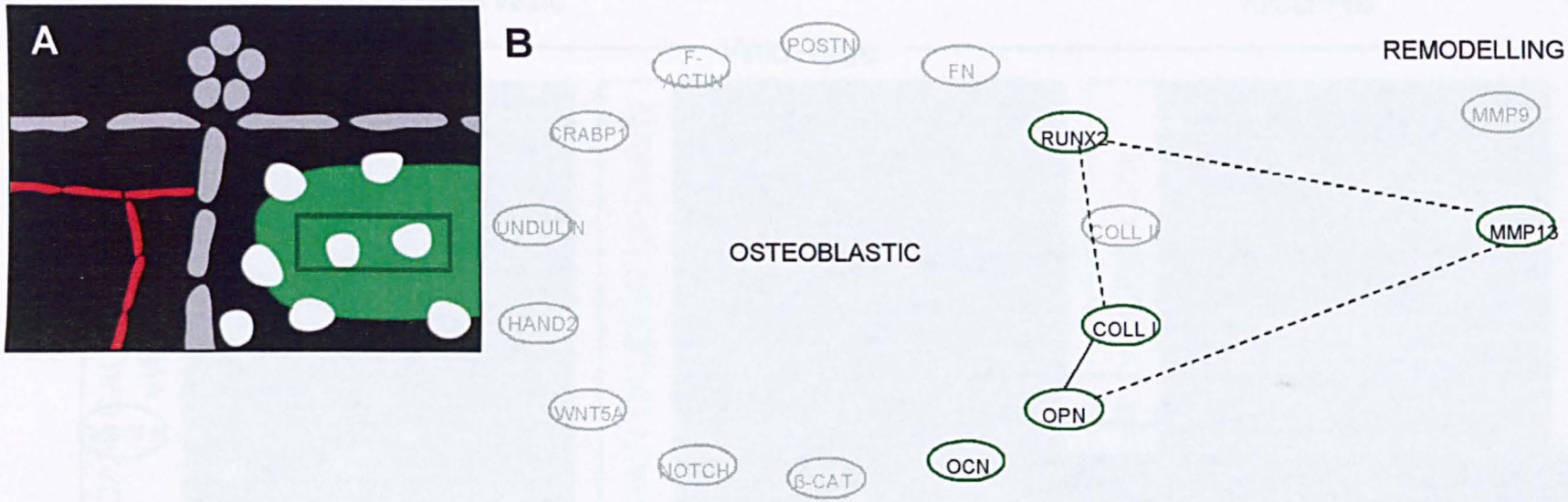

Figure 5.11: Molecular profile of osteoblasts found at the centre of re-modelled mineralised areas

Schematic diagram (**A**) of a semi-mature stage of dermal bone development including osteoblasts in the centre of mineralised matrix that has been remodelled from within the previously calcified areas (dark green box). The accompanying molecular map (**B**) details the single cell molecular marker profiles of cells at the centre of these remodelled areas (from a double/triple immuno-labelling experiment). Exclusive co-expression is indicated by a solid line between two markers and non-exclusive co-expression, some but not all cells co-express the markers in a double/triple immuno-labelling experiment, is indicated with a dashed line. Notably, any osteoblast that is capable of motility may also be capable of remodelling, however the specific osteoblastic markers indicated were assayed in combination with the MMPs.

.

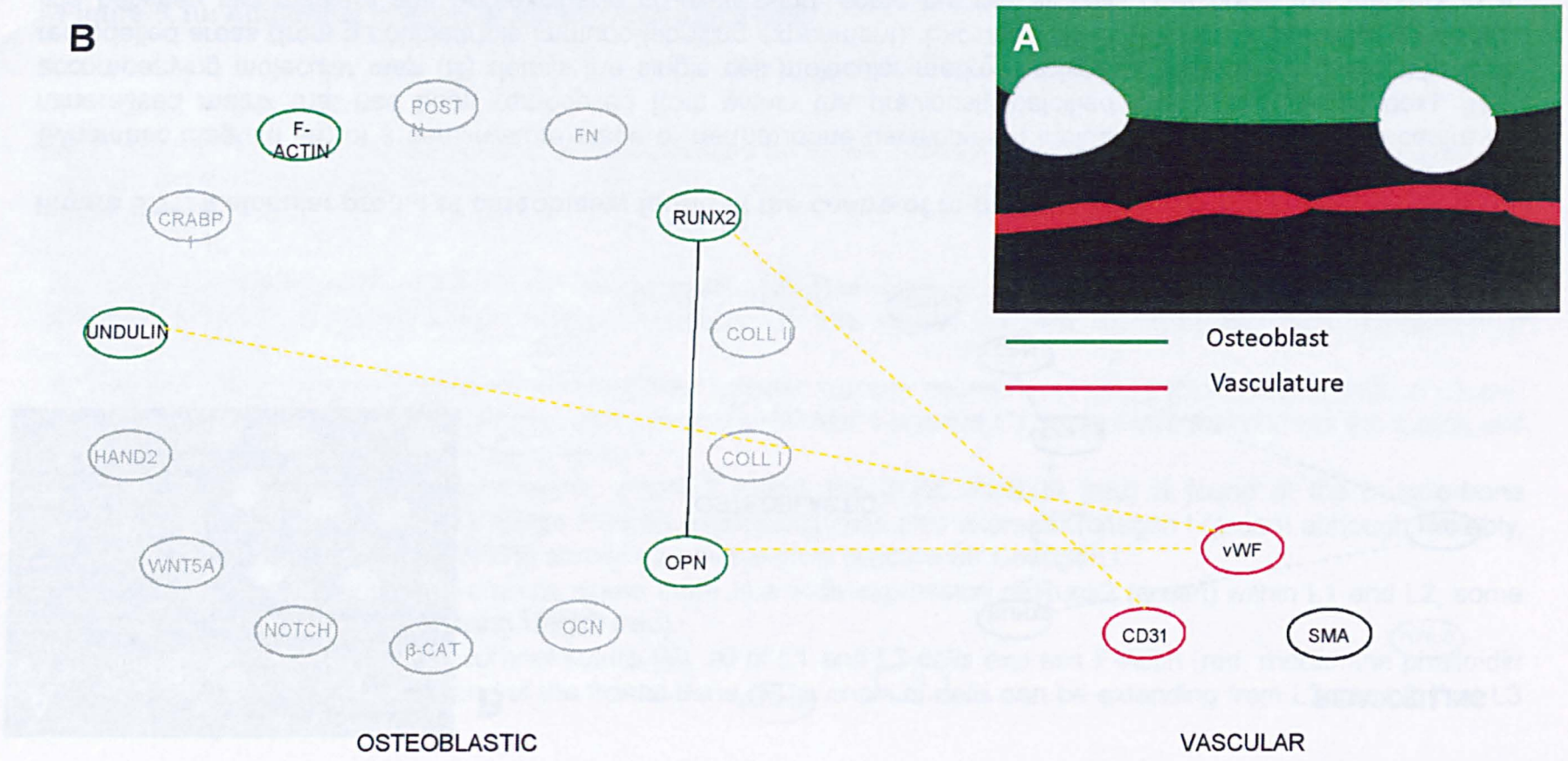

Figure 5.12 continued on the next page

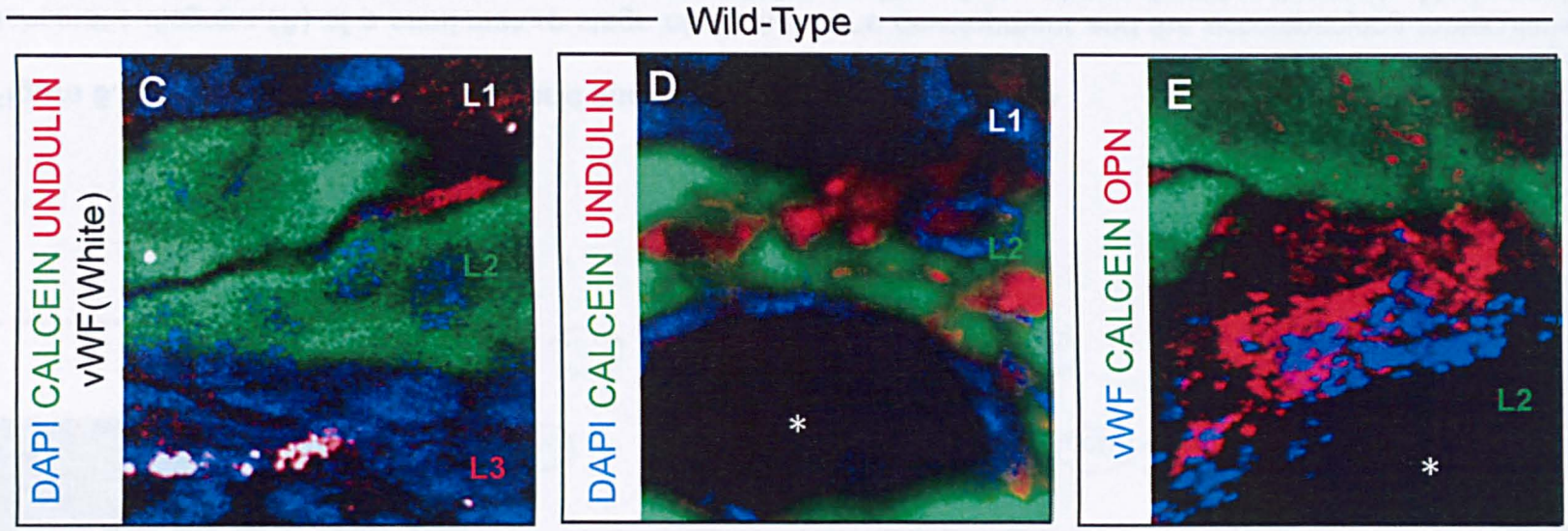

Figure 5.12: Molecular profile of cells at the vasculature-mineralisation boundary

Schematic diagram (**A**) of the vascular bone interface; the accompanying molecular map (**B**) details the single cell molecular marker profiles of cells at this border. Exclusive co-expression is indicated by a solid line between two markers and a lack of co-expression (from a double/triple immuno-labelling experiment) is indicated with a yellow dashed line.

C-D. IHC for Undulin (red) and vWF on a section with histological addition of calcein; in an immature part of the frontal bone Undulin expression is found at the margins of all areas that are mineralised but not in the developing vascular cells; in a semi-mature clavicle (**D**), Undulin is notably absent from the lining of vascular space (BV indicated with *)

E. At the blood vessel (*):bone interface, the endothelia is von Willibrand Factor positive (blue) and there is a border of Osteopontin expression between the calcein carrying mineralised area and the vasculature. OPN caps mineralisation and is always found at the bone-vasculature interface.

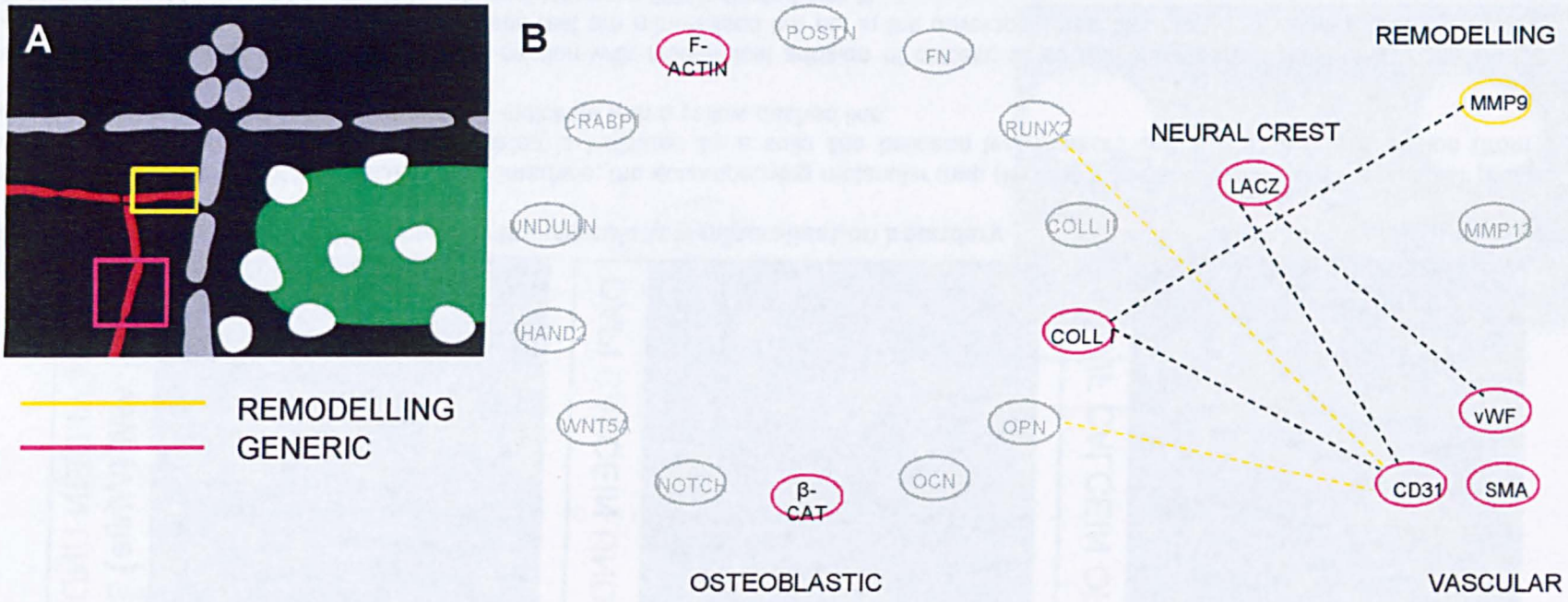

Figure 5.13: Molecular profile of generic and motile/digging vasculature

Schematic diagram (**A**) of a semi-mature stage of dermal bone development and the accompanying molecular map (**B**) detailing the single cell molecular marker co-expression profiles of vasculature found in the study. Markers active in generic vasculature are highlighted in pink; vasculature capable of remodelling also expressed MMP9 (gold). Exclusive co-expression is indicated by a solid line between two markers and non-exclusive co-expression, some but not all cells co-express the markers in a double/triple immuno-labelling experiment, is indicated with a dashed line. A lack of co-expression (from a double/triple immuno-labelling experiment) is indicated with a yellow dashed line.

PART II:

EXPLORING THE CHIARI MALFORMATION AS A NEUROCRISTOPATHY

6. Chiari and the neural crest

6.1 Introduction: Chiari malformations and the neural crest

Work undertaken in our laboratory in 2005 used genetic lineage analysis (Cre-recombinase-mediated transgenesis) to map the neural crest and mesodermal contributions to the head and neck, leading to the discovery of the 'connectivity' rule in mammals (also known as the 'scaffold model', previously illustrated in lower vertebrate species (Huang *et al.* 2000; Olsson *et al.* 2001)) and the contribution of neural crest cells to territory previously believed to arise from mesodermal progenitors (Matsuoka *et al.* 2005). This finding held clinical significance for a number of human syndromes as areas primarily affected in several conditions were now shown to derive from a specific sub-population of cells, the post-otic neural crest (PONC). The implication that one syndrome, the Chiari malformation, is a neurocristopathy was further investigated in the current study.

The Chiari syndromes are characterized as malformations of the base of the skull and neck regions where the cerebellum herniates through the foramen magnum by at least 3-5mm, pushing this component of the hindbrain downwards into the spinal cord, often accompanied by the development of a syrinx (Figure 6.1B2) (Milhorat *et al.* 1999). The syndrome was first described by Hans Chiari in the 1890s and the prevalence of the disorder is estimated to be up to 1 in 1000 people (Loukas *et al.* 2008; Labuda 2010). Chiari is broken into 4 subtypes, related to the severity of the deformation, with types I and II being predominant; in Chiari I/II the cerebellum herniation is often symptomatic and can be debilitating but is not associated with lethality (versus types III and IV where the malformation leads to mortality, often before or immediately after birth). The genetic basis for Chiari is unknown, although it is purported to be heritable and is suspected to be congenital (Speer *et al.* 2000). Chiari is diagnosed via MRI, usually in the third decade of life, following years of unattributed symptoms (personal communication, Conquer Chiari Annual Research Conference 2008) (Milhorat *et al.* 1999)). Symptoms of Chiari range from mild to severe

(described in detail, below) (Milhorat *et al.* 1999; Mueller and Oro 2004) and Chiari patients present with diverse phenotypes, complicating the prognostic and diagnostic criteria.

The Chiari malformations can be attributed to cell-differentiation defects. Chiari is hallmarked by improper ossification as a result of erroneous cell-fate decisions. The misappropriation of cells into certain fates is confined to specific areas, indicating an issue of regulation exclusive to subpopulations of cells forming the head and neck. Neural crest cells form connective tissue of all muscles innervated by cranial nerves (N. V, VII, IX, X, XI), the skeletal regions to which these muscle attach, the branchial skeleton, areas of the cranial base, the spinous processes of cervical vertebrae, and attachments of the pharyngeal constructors (Matsuoka *et al.* 2005). Cranial neural crest cells can differentiate into cartilage, endochondral bone, dermal bone, connective tissues, neurons and glia (Couly *et al.* 1993; Le Douarin *et al.* 1993; Kontges and Lumsden 1996; Le Douarin and Kalcheim 1999; Knecht and Bronner-Fraser 2002). Chiari phenotypes involve a range of the structures derived from the neural crest and, as such, Chiari is a candidate to be a neurocristopathy. Of note, many of these structures had previously been attributed to mesodermal origins and Chiari has previously been labelled a mesodermal or segmental defect (Mesiwala *et al.* 2001; Koyanagi and Houkin 2010). The aim of the current study was to further explore the contributions the neural crest to the areas affected in Chiari, which would support the classification of the disease as a neurocristopathy.

6.2.1 PONC expression in regions affected in Chiari I/II

Prior to undertaking new experimentation, it was necessary to conduct a detailed examination of the initial evidence supporting the role of the neural crest in generating the areas affected in Chiari I/II. Chiari is an extremely complex syndrome involving a multitude of seemingly incongruent symptoms. According to personal communications at the Conquer Chiari Annual Research Conference in November 2008, more than half of Chiari I/II patients are referred for psychological examination prior to their Chiari diagnosis as their differential diagnoses indicate a psychosomatic and not physiological issue (Milhorat *et al.* 1999). In light of the syndromic diversity among the patients, a comprehensive list of what phenotypic characteristics should be used as indicators for the malformation has been impossible to generate. One potential unifying component of the variegated symptoms is the embryological tissue of origin of the pathognomic deficiency resulting in the symptom. As such, initial analysis in the current study focused on compiling a list of the symptoms of Chiari I/II and the pathognomic deficiency that could be the aetiological cause, which was correlated with the results of previous lineage analyses to ascertain in how far the pathognomic deficiencies arise in neural crest-derived structures. Lineage analysis was undertaken using the *Wnt1*-Cre$^{+/-}$ strain of mice, in which a Cre-recombinase is combined with the *Wnt1* dorsal neural tube enhancer, such that the transgene is expressed in the neural crest precursor population and their resulting progeny (barring NC of rhombomere 1) (Jiang *et al.* 2000; Ferguson and Graham 2004; Matsuoka *et al.* 2005). *Wnt1*-Cre$^{+/-}$ founder mice are then combined with a Cre-reporter strain with transgenic floxed resistance-pA cassettes; the reporter strains in the current analyses included ROSA26LacZ$^{-/-}$ mice in which LacZ is under the control of the Rosa26 locus (Soriano 1999); and XZ-DR$^{-/-}$ mice with GFP under the control of the human Ubiquitin C minimal promoter (hUbC) (Zhang and Koentges, unpublished) (Schorpp *et al.* 1996; Lois *et al.* 2002).

The symptoms of Chiai I/II were compiled from primary literature on Chiari, medical resources and patient support websites (ChiariOne ; Milhorat *et al.* 1999; Speer *et al.* 2000; Mueller and Oro 2004; NINDS 2011) and included all symptoms involving the cranio-facial region. Symptoms were grouped into 6 categories: headaches (A), craniofacial anomalies (B), musculo-skeletal anomalies (C), pharyngeal/vocal impairments (excluding dysphagia) (D), dysphagia (E) and neurological abnormalities (F).

Symptoms of Category A include the characteristic Chiari I/II headaches which are often described as heavy, severe, suboccipital or posterior; the neural crest-derived components of the clivus, foramen magnum, cranial nerves and smooth muscles of cranial blood vessels may be contributing factors in these headaches (Table 6.1, Figure 6.1).

Category B includes the craniofacial anomalies leading to calvarial defects, foramen magnum malformations, Wormian bones, hypoplasia, and lambdoid sutures; neural crest was found to contribute in this category to the clivus, pharyngobasilar membrane attachments, occipital protuberance and nuchal ligament (Table 6.2, Figure 6.2).

The musculoskeletal anomalies described in Category C include cervical spina bifida occulta, ectopic ossification/cervical hypomobility and shoulder pain. These symptoms may arise due to malformations of neural crest-derived cervical spinous processes, the pre-vertebral ligaments, bones along the calvaria midline/tentorium and the connective tissue of the trapezius muscle (Table 6.3, Figure 6.3).

Category D includes symptoms related to pharyngeal/vocal impairments, including symptoms related to deficits in the extrinsic and intrinsic tongue musculature and connective tissue, all of neural crest origin, such as: displaced/deficient attachments, vocal impairments and laryngomalacia. The vocal impairments, mechanical dysphagia, laryngomalacia and additionally hoarseness can also be attributed to the PONC-derived larynx and pharynx muscles and attachments, and basihyoid and attachments (Table 6.4, Figure 6.4).

Dysphagia, described in Category E, is attributable to the neural crest derived pre-vertebral ligament (Table 6.5, Figure 6.5), as well as structures in Category D.

Finally, deficits of the cranial nerves may lead to several neurological problems (category F) in Chiari I/II, including impaired gag reflex, tremors, dysmetria, facial sensory loss, phototypic and visual sensory issues, and vocal cord paralysis (Table 6.6, Figure 6.6).

To date this is the first study that correlates the variegated multitude of symptoms associated with Chiari with the cellular origins of the effected structures leading to the phenotype, and supports a neurocristopathic origin of Chiari I/II.

6.2.2 Mutant analysis: Replicating the Chiari phenotype

The 2005 study reported in Matsuoka *et al.* revealed that some aspects of the Chiari phenotype were replicated in previously characterised mutant mice lacking genes involved in the ossification process (Matsuoka *et al.* 2005); most prominently, when the master bone-regulator, *Runx2*, is ablated, mice have deficiencies in the clivus, pharyngobasilar membrane attachment, bones along the calvarial midline, occipital protuberance, and nuchal ligament. Analysis of mutant strains provides powerful ad hoc evidence of the role of a relevant pathway in generating a phenotype. Our laboratory was interested in the potential role of the sonic hedgehog (SHH) signalling pathway in patterning the neural crest cells and obtained a smoothened mutant lacking the SHH ligand, Smo, specifically in neural crest cells (transgenic generated in laboratory of T. McMahon), which prohibited the activation of the SHH pathway in a lineage-confined manner. For the current study the effect of losing Smo was analysed with specific regard to replicating the Chiari phenotype.

The smoothened mutant lacks the attachment region of the pre-vertebral ligament in the cervical area, a phenotype shared by both Chiari and Klippel-Feil patients (Figure 6.7). However, the mutants did not display other

abnormalities associated with Chiari and exploring each individual pathway by generating a mutant strain was decided to be too laborious and unbiased for future work.

Table 6.1: Neural crest contributions to anatomical regions generating symptoms of category A

CATEGORY	PATHOGNOMIC DEFICIENCY	RESULTING SYMPTOM OF CHIARI I/II	NEURAL CREST-DERIVED ELEMENT
A	Clivus; size of the foramen magnum; length of cranial base	Headaches: heavy, severe, suboccipital, posterior	Clivus,cranial nerves, smooth muscles of cranial blood vessels
B	Craniofacial anomalies	Calvarial defects, dysplastic extended/constricted foramen magnum, platybasia, Wormian bones, hypoplasia, lambdoid suture/foramen	Clivus, pharyngobasilar membrane attachments, occipital protuberance, nuchal ligament
C	Musculo-skeletal anomalies	Cervical spina bifida occulta, ectopic ossification/cervical hypomobility, shoulder pain	Cervical spinous processes, pre-vertebral cervical ligament, bones along calvaria midline – tentorium, trapezius CT
D	Pharyngeal/Vocal Impairments	Displaced/deficient attachments, vocal impairments, laryngomalacia, gag reflex	Larynx & pharynx muscles, attachments, basihyoid and attachments
E	Dyspahgia	Swallowing difficulties	Prevertebral ligament
F	Neurological	Facial pain/numbness, syncope, aspiration sensory loss, apnea, impaired gag reflex, sensation defects	Cranial nerves, DRGs

A. HEADACHE

A1. *Wnt1-CrexROSALacZ*
NEURAL CREST

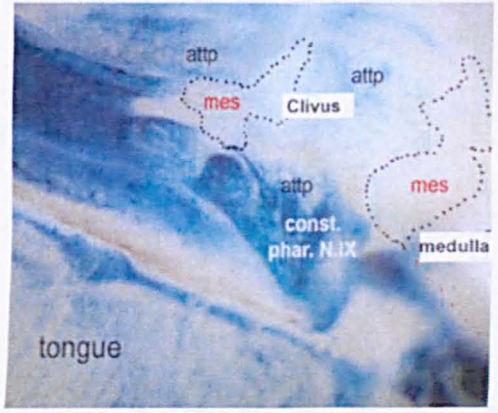

A2. MRI, CHIARI I PATIENT

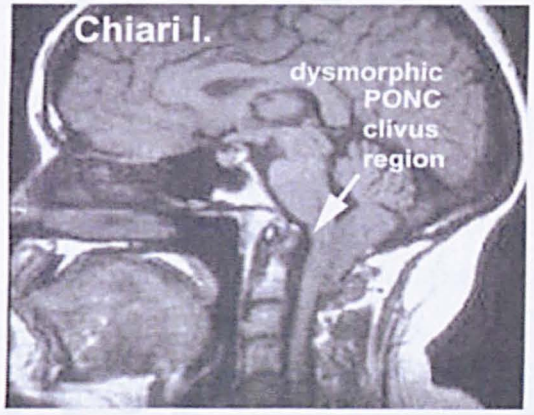

Figure 6.1: Category A

The symptoms of category A are a result of pathognomic deficiencies as outlined in the table above. Several of these structures have a neural crest component (**A1**) that leads to the physical deficiency in the Chiari malformation (**A2**)

A1-A2 after Matsuoka *et. al.2005*

Table 6.2: Neural crest contributions to anatomical regions generating symptoms of category B

CATEGORY	PATHOGNOMIC DEFICIENCY	RESULTING SYMPTOM OF CHIARI I/II	NEURAL CREST-DERIVED ELEMENT
A	Clivus; size of the foramen magnum; length of cranial base	Headaches: heavy, severe, suboccipital, posterior	Clivus,cranial nerves, smooth muscles of cranial blood vessels
B	Craniofacial anomalies	Calvarial defects, dysplastic extended/constricted foramen magnum, platybasia, Wormian bones, hypoplasia, lambdoid suture/foramen	Clivus, pharyngobasilar membrane attachments, occipital protuberance, nuchal ligament
C	Musculo-skeletal anomalies	Cervical spina bifida occulta, ectopic ossification/cervical hypomobility, shoulder pain	Cervical spinous processes, pre-vertebral cervical ligament, bones along calvaria midline – tentorium, trapezius CT
D	Pharyngeal/Vocal Impairments	Displaced/deficient attachments, vocal impairments, laryngomalacia, gag reflex	Larynx & pharynx muscles, attachments, basihyoid and attachments
E	Dyspahgia	Swallowing difficulties	Prevertebral ligament
F	Neurological	Facial pain/numbness, syncope, aspiration sensory loss, apnea, impaired gag reflex, sensation defects	Cranial nerves, DRGs

B. CRANIOFACIAL

B1. *Wnt1-CrexROSALacZ*
NEURAL CREST

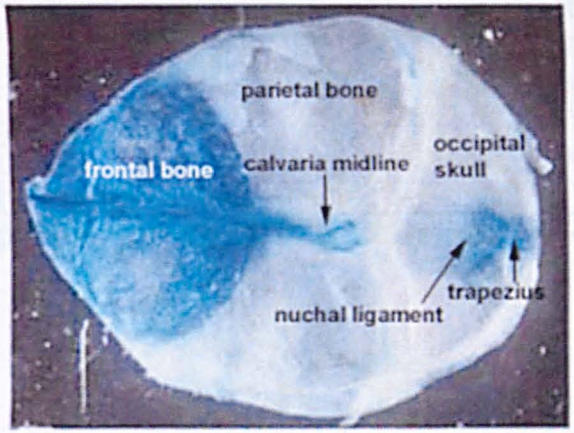

B2. ANATOMY

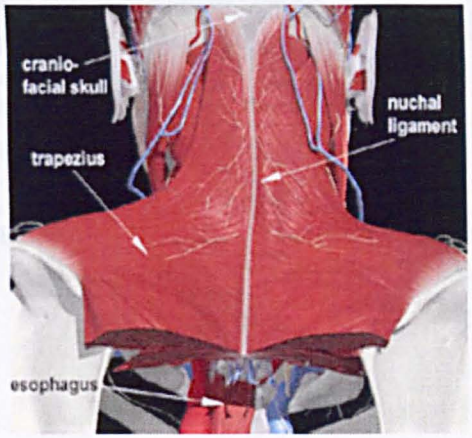

Figure 6.2: Category B

The symptoms of category B are a result of pathognomic deficiencies as outlined in the table above. The neural crest component of these structures and the mature anatomy in a non-affected condition are shown in **B1** and **B2**, respectively.

B1 after Matsuoka *et. al.2005*
B2 © 2003 Primal Pictures Ltd

Table 6.3: Neural crest contributions to anatomical regions generating symptoms of category C

CATEGORY	PATHOGNOMIC DEFICIENCY	RESULTING SYMPTOM OF CHIARI I/II	NEURAL CREST-DERIVED ELEMENT
A	Clivus; size of the foramen magnum; length of cranial base	Headaches: heavy, severe, suboccipital, posterior	Clivus,cranial nerves, smooth muscles of cranial blood vessels
B	Craniofacial anomalies	Calvarial defects, dysplastic extended/constricted foramen magnum, platybasia, Wormian bones, hypoplasia, lambdoid suture/foramen	Clivus, pharyngobasilar membrane attachments, occipital protuberance, nuchal ligament
C	Musculo-skeletal anomalies	Cervical spina bifida occulta, ectopic ossification/cervical hypomobility, shoulder pain	Cervical spinous processes, pre-vertebral cervical ligament, bones along calvaria midline – tentorium, trapezius CT
D	Pharyngeal/Vocal Impairments	Displaced/deficient attachments, vocal impairments, laryngomalacia, gag reflex	Larynx & pharynx muscles, attachments, basihyoid and attachments
E	Dyspahgia	Swallowing difficulties	Prevertebral ligament
F	Neurological	Facial pain/numbness, syncope, aspiration sensory loss, apnea, impaired gag reflex, sensation defects	Cranial nerves, DRGs

C. MUSCULO-SKELETAL

C1. *Wnt1-CrexROSALacZ*
NEURAL CREST

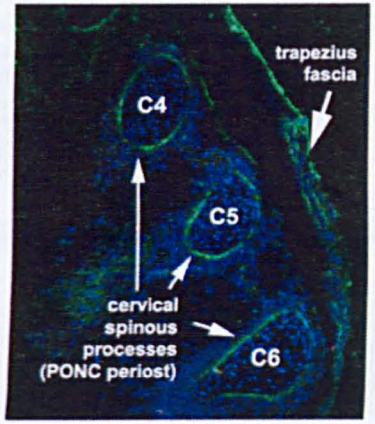

C2. ANATOMY

Figure 6.3: Category C

The symptoms of category B are a result of pathognomic deficiencies as outlined in the table above. The neural crest component of these structures and the mature anatomy in a non-affected condition are shown in **C1** and **C2**, respectively.

C1 after Matsuoka *et. al.2005*
C2 © 2003 Primal Pictures Ltd

Table 6.4: Neural crest contributions to anatomical regions generating symptoms of category D

CATEGORY	PATHOGNOMIC DEFICIENCY	RESULTING SYMPTOM OF CHIARI I/II	NEURAL CREST-DERIVED ELEMENT
A	Clivus; size of the foramen magnum; length of cranial base	Headaches: heavy, severe, suboccipital, posterior	Clivus,cranial nerves, smooth muscles of cranial blood vessels
B	Craniofacial anomalies	Calvarial defects, dysplastic extended/constricted foramen magnum, platybasia, Wormian bones, hypoplasia, lambdoid suture/foramen	Clivus, pharyngobasilar membrane attachments, occipital protuberance, nuchal ligament
C	Musculo-skeletal anomalies	Cervical spina bifida occulta, ectopic ossification/cervical hypomobility, shoulder pain	Cervical spinous processes, pre-vertebral cervical ligament, bones along calvaria midline – tentorium, trapezius CT
D	Pharyngeal/Vocal Impairments	Displaced/deficient attachments, vocal impairments, laryngomalacia, gag reflex	Larynx & pharynx muscles, attachments, basihyoid and attachments
E	Dyspahgia	Swallowing difficulties	Prevertebral ligament
F	Neurological	Facial pain/numbness, syncope, aspiration sensory loss, apnea, impaired gag reflex, sensation defects	Cranial nerves, DRGs

D. PHARYNGEAL / VOCAL

D1. *Wnt1-CrexROSALacZ*
NEURAL CREST

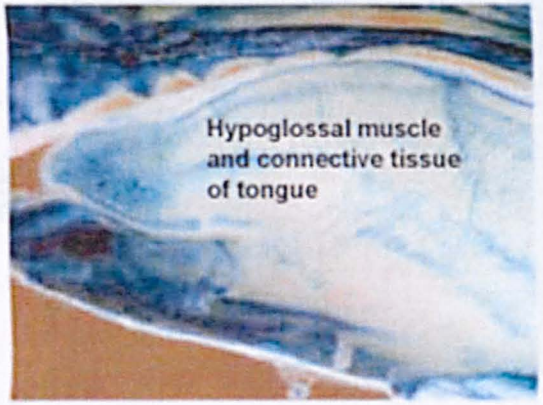

D2. ANATOMY

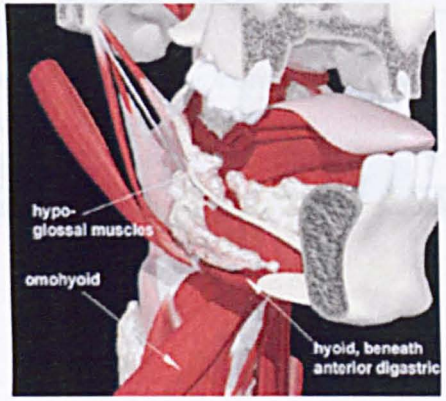

Figure 6.4: Category D

The symptoms of category B are a result of pathognomic deficiencies as outlined in the table above. The neural crest component of these structures and the mature anatomy in a non-affected condition are shown in **D1** and **D2**, respectively.

D1 after Matsuoka *et. al.2005*

Table 6.5: Neural crest contributions to anatomical regions generating symptoms of category D

CATEGORY	PATHOGNOMIC DEFICIENCY	RESULTING SYMPTOM OF CHIARI I/II	NEURAL CREST-DERIVED ELEMENT
A	Clivus; size of the foramen magnum; length of cranial base	Headaches: heavy, severe, suboccipital, posterior	Clivus,cranial nerves, smooth muscles of cranial blood vessels
B	Craniofacial anomalies	Calvarial defects, dysplastic extended/constricted foramen magnum, platybasia, Wormian bones, hypoplasia, lambdoid suture/foramen	Clivus, pharyngobasilar membrane attachments, occipital protuberance, nuchal ligament
C	Musculo-skeletal anomalies	Cervical spina bifida occulta, ectopic ossification/cervical hypomobility, shoulder pain	Cervical spinous processes, pre-vertebral cervical ligament, bones along calvaria midline – tentorium, trapezius CT
D	Pharyngeal/Vocal Impairments	Displaced/deficient attachments, vocal impairments, laryngomalacia, gag reflex	Larynx & pharynx muscles, attachments, basihyoid and attachments
E	Dyspahgia	Swallowing difficulties	Prevertebral ligament
F	Neurological	Facial pain/numbness, syncope, aspiration sensory loss, apnea, impaired gag reflex, sensation defects	Cranial nerves, DRGs

E. DYSPHAGIA

E1. *Wnt1-CrexROSALacZ*
NEURAL CREST

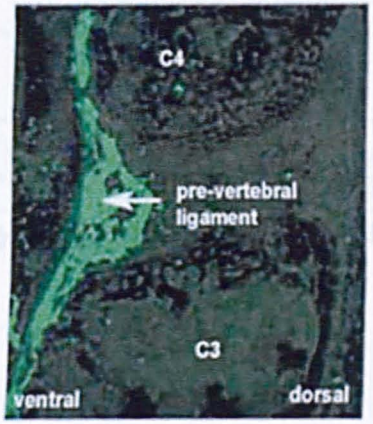

E2. ANATOMY

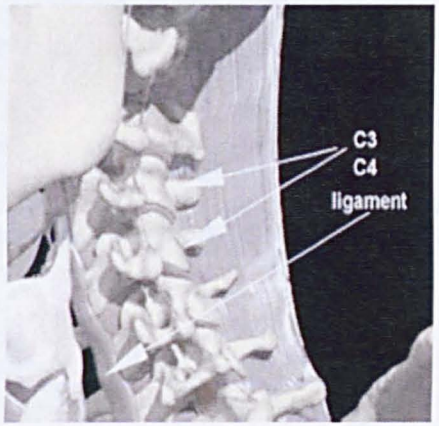

Figure 6.5: Category E

The symptoms of category B are a result of pathognomic deficiencies as outlined in the table above. The neural crest component of these structures and the mature anatomy in a non-affected condition are shown in **E1** and **E2**, respectively.

E1 after Matsuoka *et. al.2005*
E2 © 2003 Primal Pictures Ltd

Table 6.6: Neural crest contributions to anatomical regions generating symptoms of category F

CATEGORY	PATHOGNOMIC DEFICIENCY	RESULTING SYMPTOM OF CHIARI I/II	NEURAL CREST-DERIVED ELEMENT
A	Clivus; size of the foramen magnum; length of cranial base	Headaches: heavy, severe, suboccipital, posterior	Clivus,cranial nerves, smooth muscles of cranial blood vessels
B	Craniofacial anomalies	Calvarial defects, dysplastic extended/constricted foramen magnum, platybasia, Wormian bones, hypoplasia, lambdoid suture/foramen	Clivus, pharyngobasilar membrane attachments, occipital protuberance, nuchal ligament
C	Musculo-skeletal anomalies	Cervical spina bifida occulta, ectopic ossification/cervical hypomobility, shoulder pain	Cervical spinous processes, pre-vertebral cervical ligament, bones along calvaria midline – tentorium, trapezius CT
D	Pharyngeal/Vocal Impairments	Displaced/deficient attachments, vocal impairments, laryngomalacia, gag reflex	Larynx & pharynx muscles, attachments, basihyoid and attachments
E	Dyspahgia	Swallowing difficulties	Prevertebral ligament
F	Neurological	Facial pain/numbness, syncope, aspiration sensory loss, apnea, impaired gag reflex, sensation defects	Cranial nerves, DRGs

F1. *Wnt1-CrexROSALacZ,* NEURAL CREST,

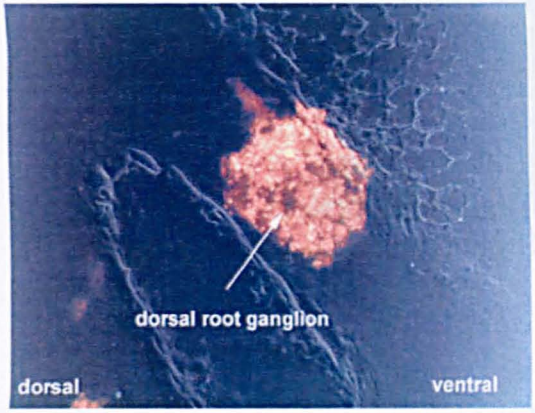

F2. ANATOMY

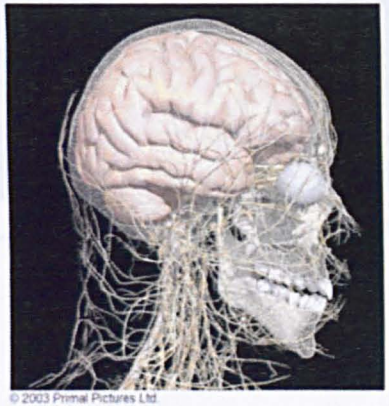

Figure 6.6: Category F

The symptoms of category B are a result of pathognomic deficiencies as outlined in the table above. The neural crest component of these structures and the mature anatomy in a non-affected condition are shown in **F1** and **F2**, respectively.

F1 Ryll & Koentges, unpublished
F2 © 2003 Primal Pictures Ltd

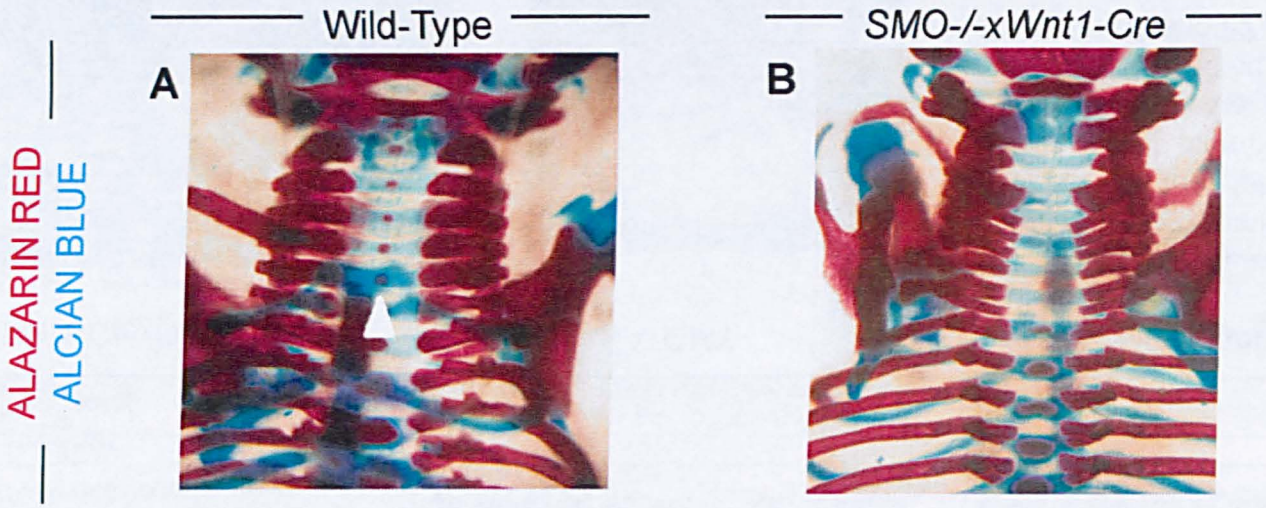

Figure 6.7: Pathognomic deficiency of the SMO$^{-/-}$; *Wnt1*-Cre$^{+/-}$ mice

Coronal view of whole mount alcian blue (blue), alizarin red (red) stained wild-type (A) and smoothened (SMO) ligand knockout transgenic mice at postnatal day 0 **(B).**

A. Wild-type animal in which the cartilage precursor to the cervical attachment of the prevertebral ligament is evident (above white arrowhead). This contrasts with **B** in which activation of the sonic hedgehog (SHH) pathway has been ablated in the neural crest cells of the transgenic animal lacking the SMO ligand. The attachment point of the pre-vertebral ligament is notably absent and ossification of the cranial base is slightly retarded. The SMO-knockout replicates the phenotype of Chiari and Klippel-Feil patients and indicates that the SHH pathway may play a role in generating the Chiari malformations.

* Transgenic knockout and histological preparation conducted by members of T. McMahon group; analysis by K. Jordan.

6.3 Conclusion

The accumulated evidence that symptoms of Chiari arise in neural crest derived structures, and ablation of certain pathways in the neural crest can replicate the Chiari phenotype, supports the hypothesis that Chiari is a neurocristopathy. In order to further explore the neural crest contribution to the Chiari phenotype, it was next necessary to more precisely elucidate the role of the neural crest in generating the structures of the cranial base associated with Chiari I/II.

6.4 Summary of Findings

- The diverse and seemingly incongruent symptoms of Chiari arise due to pathognomic defects affecting structures that are largely of neural crest origin;

- Neural crest being the common precursor to tissues affected in Chiari I/II is, to my knowledge, the first uniting feature to be identified among the majority of symptoms suffered by Chiari patients;

- The strong correlation between the symptoms and their structural origin supports Chiari as a neurocristopathy;

- Ablating the smoothened ligand in post-otic neural crest cells replicates the phenotype of Chiari and Klippel-Feil patients, who lack the attachment point of the pre-vertebral ligament; this indicates the sonic hedgehog pathway could play a role in developing the Chiari phenotype.

7. Homing into the anatomical defects of Chiari I/II

7.1 Introduction

Results of lineage labelling studies have mapped the cryptic boundaries of the neural crest in the neurocranium and cranio-cervical regions; many structures hitherto attributed to paraxial mesoderm have shown a dual origin (Figure 7.1), and neural crest forms the attachment regions connecting the head and shoulder girdle/neck vertebrae even in structures largely formed from somatic mesoderm (Figure 7.1). To refine the study of Chiari as a neurocristopathy, it was necessary to home into the anatomical location of the principle structural defect.

While many of the neural crest-derived structures associated with the symptoms of Chiari may be malformed in the given condition, the lack of congruence among them indicates no one is individually causative of the complaint. Additionally, the elusive nature of Chiari is such that diagnosis most commonly occurs in the third decade of life, indicating it as a late developmental defect reported to become symptomatic in the first decade of life in 37% of patients (Milhorat *et al.* 1999).

In his seminal work describing Chiari, Milhorat ascribed the chief anatomical defect of the Chiari syndrome to be a malformation of the posterior cranial fossa (PCF), the cup-like area in which the cerebellum sits, bounded by the tentorium, basiocciput, supraocciput and petrous ridges (Figure 7.2). While the brain of Chiari patients was found to be an average size, the PCF had a volumetric reduction (40%, on average) and cerebrospinal fluid volume was also diminished in 100% of the 364 patients assessed (Milhorat *et al.* 1999). Further morphometric studies attributed the small PCF to the length of the supraocciput and clivus (Koyanagi and Houkin 2010) and basioccipital hypoplasia (Noudel *et al.* 2009).

The ontogeny of the cranial base involves a significant amount of postnatal craniofacial growth in the structures contributing to cranial base angulation and the resulting morphology of the posterior cranial fossa (Coben 1998;

Jeffery and Spoor 2004; Jeffery and Spoor 2004). Detailed morphometric studies in humans and other primates have shown the clivus, which borders the PCF ventrally and whose angulation/retroflexion determines the size of the PCF overall, is a patchwork of three anlagen (the pre-, basisphenoid and basioccipital), separated from each other through synchondroses early in development. These synchondroses act as hinge-points during development that lead to a successive retroflexion of this bony base. Along the dorso-ventral axis, the closure of the growth plates of the sphenoid bone occurs at distinct developmental time-points (Figure 7.3). The spheno-ethmoid synchondrosis, between the ethmoid and presphenoid bones, undergoes juvenile closure; the mid-sphenoidal synchondrosis, separating the presphenoid and basisphenoid bones, has postnatal closure in the first decade of life; and finally the spheno-occipital synchondrosis, partitioning the basisphenoid and basioccipital bones, does not close until early adulthood. Any eccentric ossification in these areas would alter the length of the bone and the resulting posterior cranial fossa volume. Of particular significance for the overall size of the PCF is the spheno-occipital synchondrosis (SOS) ventrally and the supraoccipital/interparietal region dorsally (Jeffery and Spoor 2004; Jeffery and Spoor 2004). Premature closure (stenosis) of the SOS would block the necessary retroflexion and lengthening of the clivus and lead to platybasic (a flat skull base) condition characteristic of Chiari I (Noudel *et al.* 2009).

Given the age of onset of the symptoms and the time of diagnoses in Chiari patients, I re-examined the endochondral ossification process and the neural crest contribution at the cranial base around the spheno-occipital synchondrosis and the supra-occiput late in ontogeny, as the majority of fate maps utilised in the previous study (Chapter 6) were generated early in development before endochondral ossification is complete or utilising more imprecise methods, such as retroviral injections, that do not allow clean separation of label between neural crest and mesoderm (Couly *et al.* 1993; Le Douarin *et al.* 1993; Huang *et al.* 2000; Evans and Noden 2006).

An additional examination was conducted on a potential role of the neural crest in generating the suboccipital headaches, experienced by 81-98% of

Chiari patients (Milhorat *et al.* 1999; Mueller and Oro 2004). Headaches emerge when nociceptive neurons, located in the trigeminal and vagus ganglion that innervate the meninges (dura and arachnoids), sense increased vasodilation and intracranial pressure above a given threshold. Work by Strassman, Burstein and Levy, Goadsby and others have outlined the physiological basis of this pain system (the so-called trigeminocervical complex) and have defined the various fibre types involved (Strassman *et al.* 1996; Storer *et al.* 2001; Storer *et al.* 2003; Olesen 2006). These fibres are embedded inside the collagen matrix of the dura and arachnoids. Any physiological or genetic changes that affect the biomechanical properties of the system would mediate the stretching of the nociceptor terminals and could lead to headaches; these changes could include congenital increased intracranial pressure, different tissue composition and resulting compliance of venous drainage systems, or differences in the collagen composition (and associated proteins) of the meninges themselves.

The localized headaches in Chiari I/II could result from architectural differences among blood vessels of the brain that can skew fluid dynamics. Differences in blood vessel architecture may be attributed to the developmental origins of the cells providing the vasculature. Previous studies have shown that the vasculature of the brain is a complex patchwork of mesoderm and neural crest-derived cells that are discretely spatially organized, i.e. the meninges (and meningeal blood vessels) around particular brain regions are not mixed in origin (Etchevers *et al.* 2001); there is a spatial segregation in those meninges that are crest and those that derive from the mesoderm. The mechanisms of cellular development (i.e. how the vasculature forms the connective tissue walls of these blood vessels) has significant effects on vessel size and blood flow dynamics and may be determinants of suboccipital headaches. Mechanical properties of head vasculature are studied by others in the Chiari researcher community, using engineering and imaging tools (personal communication, Conquer Chiari Research Conference 2008), however no group, to date, has explored the implication that lineage differences relate to headaches in Chiari.

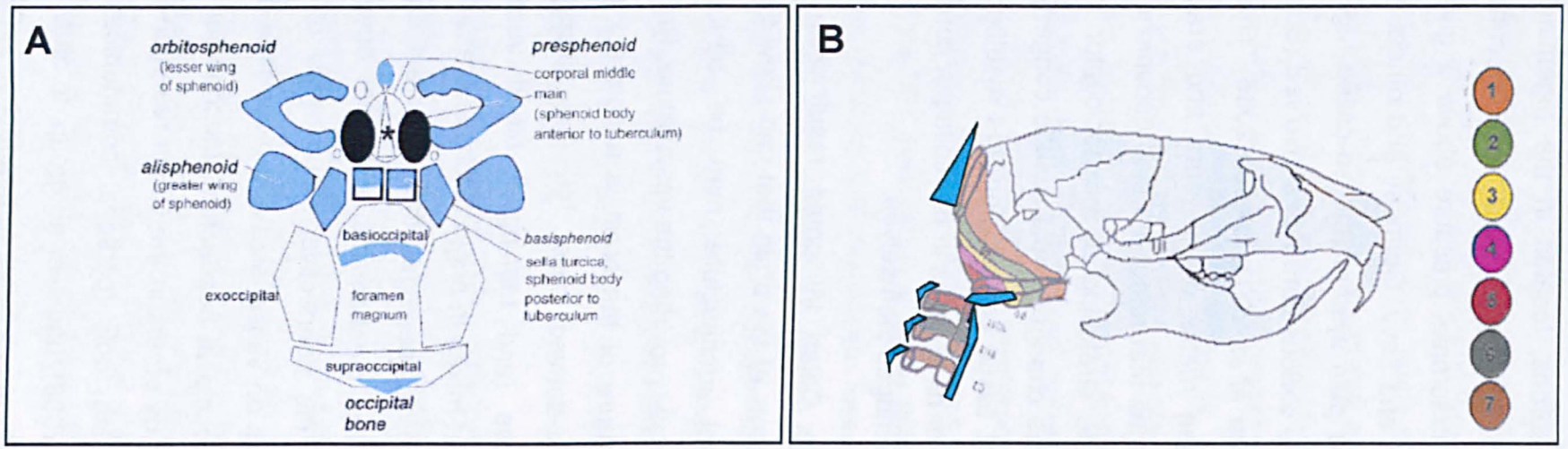

Figure 7.1: Neural crest contributions to the cranial base

A. Diagrammatic representation of the ossification centres of the cranial base (modified from Nemzek *et al.* 2000). Areas that are derived from the neural crest, as found in our fate-mapping studies, are indicated in blue. Notably, areas contributing to the Chiari phenotype arise from neural crest cells, including portions of the basioccipital and occipital bones, as well as components of the clivus.

B. Schematic illustration mapping the neural crest components of the cranial base and cervical regions (blue) to the areas previously mapped to be somitic mesoderm. The segmentation of the neurocranium aligns to the consecutive contributions of the somites, numbered from cranial to caudal 1-7. Modified from Huang *et al.* 2000.

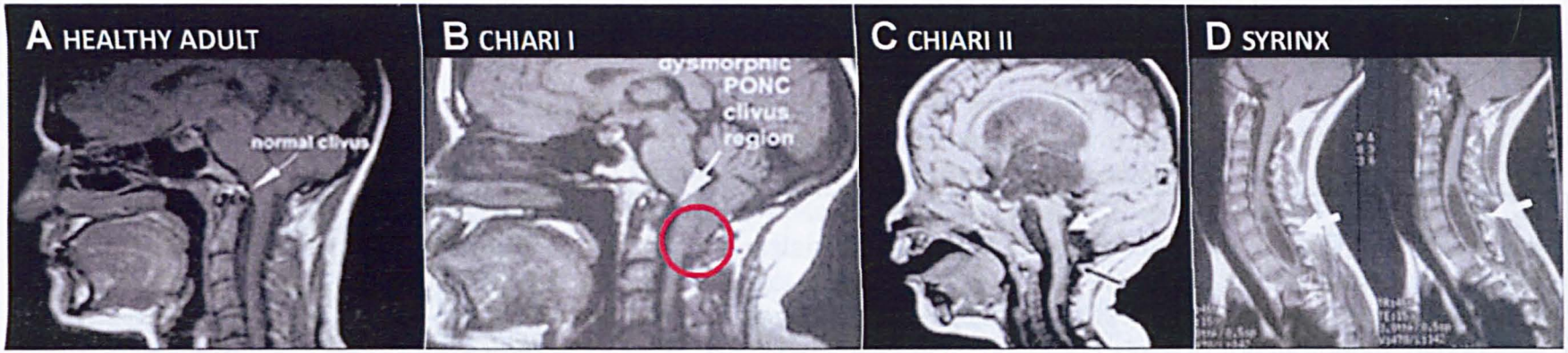

Figure 7.2: MRI of the Chiari malformations

The Chiai malformations are described clinically as any herniation of the cerebellum ≥ 3 mm below the foramen magnum, forcing that component of the brain into the spinal cord. Chiari is diagnosed by a sagittal T1-weighted MRI (Modified from Matsuoka *et al.* 2005).

A. Example MRI of a normal, healthy adult; this contrasts to **B**, where a dysmorphic clivus is visible and indicated with a white arrow.

In **B** the cerebellar herniation (often described as "peg-like") is visible (red circle). In a paediatric example of Chiari II (**C**) the clivus is almost totally absent (white arrow) and there is cerebellar retardation and pegs (black arrow).

The Chiari malformations often result in the development of a syrinx in the spinal cord, exemplified in **D**, where the left panel shows a moderate syrinx (white arrow), which enlarges with time (right panel, white arrow).

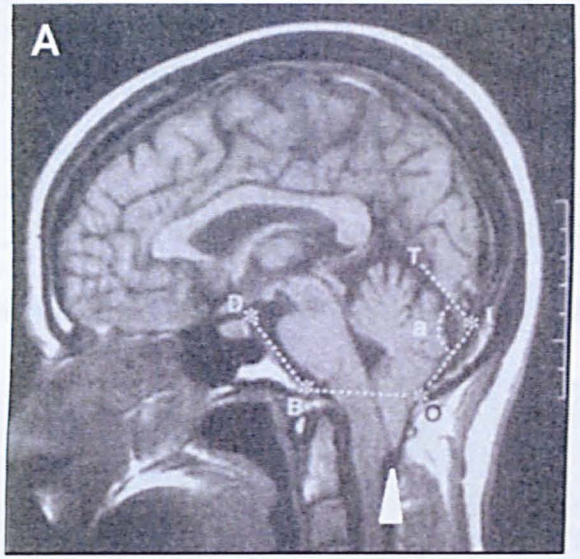
A
T
B
I
B
O

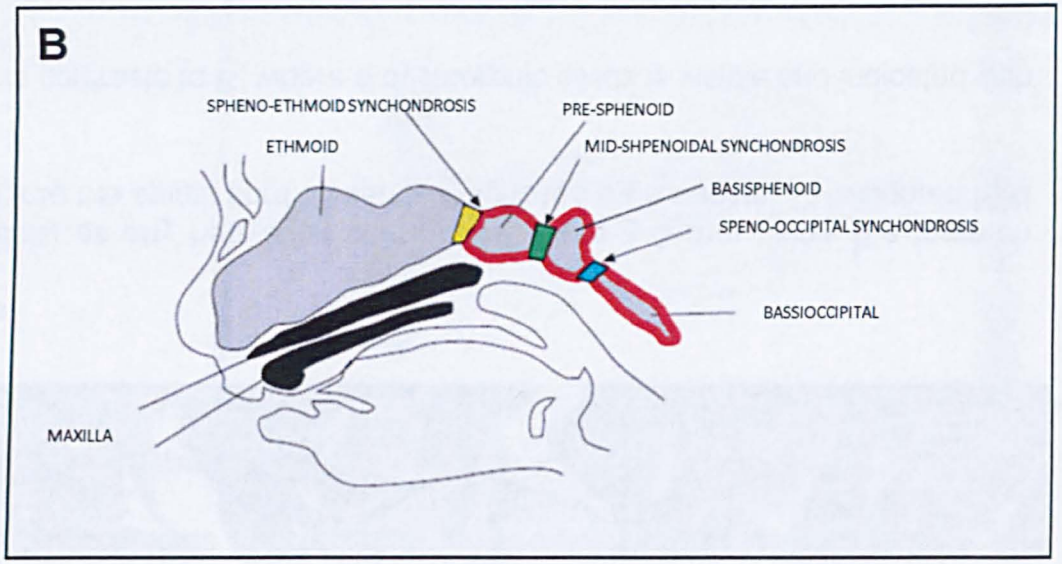
B
SPHENO-ETHMOID SYNCHONDROSIS
ETHMOID
PRE-SPHENOID
MID-SHPENOIDAL SYNCHONDROSIS
BASISPHENOID
SPENO-OCCIPITAL SYNCHONDROSIS
BASSIOCCIPITAL
MAXILLA

Figure 7.3: Homing into the primary anatomical defects of the Chiari malformations

A. The primary anatomical defect of Chiari I/II is a diminished volume of the posterior cranial fossa (PCF), leading to an overcrowding forcing the cerebellum to herniate through the foramen magnum. Measurements of the posterior cranial fossa (PCF) using T1-weighted sagittal MRI scans of a 44-year-old female patient with Chiari I. The PCF is the cup-like area housing the cerebellum, indicated with a white dotted line. The PCF is measured by examining the length of the clivus (D, dorsum sella, to B, basion), the distance across the foramen magnum (B to O, opisthion), the length of the supraocciput (from O to I, internal occipital protuberance) , and the slope of the tentorium (T) (as calculated by measuring the angle (a) formed by the tentorium and the supraocciput). Cerebellar herniation is evident, indicated with a white arrowhead. This patient had a short supracocciput, increased slope of the tentorium, hypoplasia of the clivus, and descent of the cerebellar tonsils 1.6 cm below the foramen magnum; all characteristic of Chiari I/II. Modified from Milhorat *et al.* 1999.

B. The volume of the PCF is partially determined by the angulation/retroflection of the clivus. The clivus is a patchwork of three anlagen (the pre and basisphenoids and the basioccipital), outlined in red. The anlagen are separated from each other through synchondroses acting as hinge-points during development that lead to a successive retroflexion and growth of this bony base. The spheno-ethmoid synchondrosis (gold box) undergoes juvenile closure; the mid-sphenoidal synchondrosis (green box) has postnatal closure in the first decade of life; and finally the spehno-occipital synchondrosis (blue box) does not close until adulthood. Any eccentric ossification in these areas would alter the length of the bone and the resulting posterior cranial fossa volume. Modified from Lieberman & McCarthy, 1998.

7.2.1 Late neural crest invasion into the cranial base

The current study utilised a newly developed transgenic reporter mouse strain (XZ-DR$^{-/-}$) which, when combined with *Wnt1*-Cre$^{+/-}$ mice confers labelling to all neural crest cells with GFP under the control of the hUbC minimal promoter, with the exception of neural crest from rhombomere 1 (which do not express the W*nt1* transgene); the GFP expression is strong enough to visualise *de novo* or in conjunction with an anti-GFP antibody. This study revealed a late re-invasion of neural crest into mesodermal areas, including a previously uncharacterised contribution to the vasculature of endochondral bones.

The clivus is a structure with dual neural crest and mesodermal origin; at E18.5 in the spheno-occipital synchondrosis anlage there is a large contribution of neural crest cells (Figure 7.4). The basisphenoid is of neural crest origin, while the basioccipital is somitic mesoderm. A late contribution of the neural crest was also observed in the occipital protuberance, supra-occiput, and the atlas (Figures 7.4-7.6).

A close examination revealed that at a time-point immediately preceding birth in murine development (E18.5), a considerable portion of the vascular endothelia inside the endochondral clivus is of neural crest origin (Figure 7.6). Neural crest also contributed to the endothelia of the atlas and the vasculature surrounding the cartilaginous tissues (Figure 7.6). This neural crest invasion is notably anatomically confined as the exoccipital condyle from the same section contains no neural crest contribution (Figure 7.7).

7.2.2 Neural crest contribution to cranial vasculature

Results of the study on the neural crest-derived vasculature of the cranial region (utilising the *Wnt1*-Cre$^{+/-}$ x XZ-DR$^{-/-}$ strain of mice) indicate the meninges of the cortex are neural crest in origin, while the meninx of the

cerebellum are unlabelled, presumably because the cerebellum derived from cells of rhombomere 1 (Figure 7.9). These results are in line with previous grafting studies showing the neural crest origins of forebrain meninges, while mesodermal cells comprise the midbrain and hindbrain meninx (Le Douarin and Kalcheim 1999). I observe that there are neural crest derived vessels in the cortex where both the pericyte and endothelia are of crest origins, as are the arachnoids (Figure 7.10). Arachnoids of the spinal cord were also found to be neural crest in work conducted on *Wnt1*-Cre$^{+/-}$ x ROSA26LacZ$^{-/-}$ mice, indicating a possible contribution of the neural crest to meninges of hindbrain.

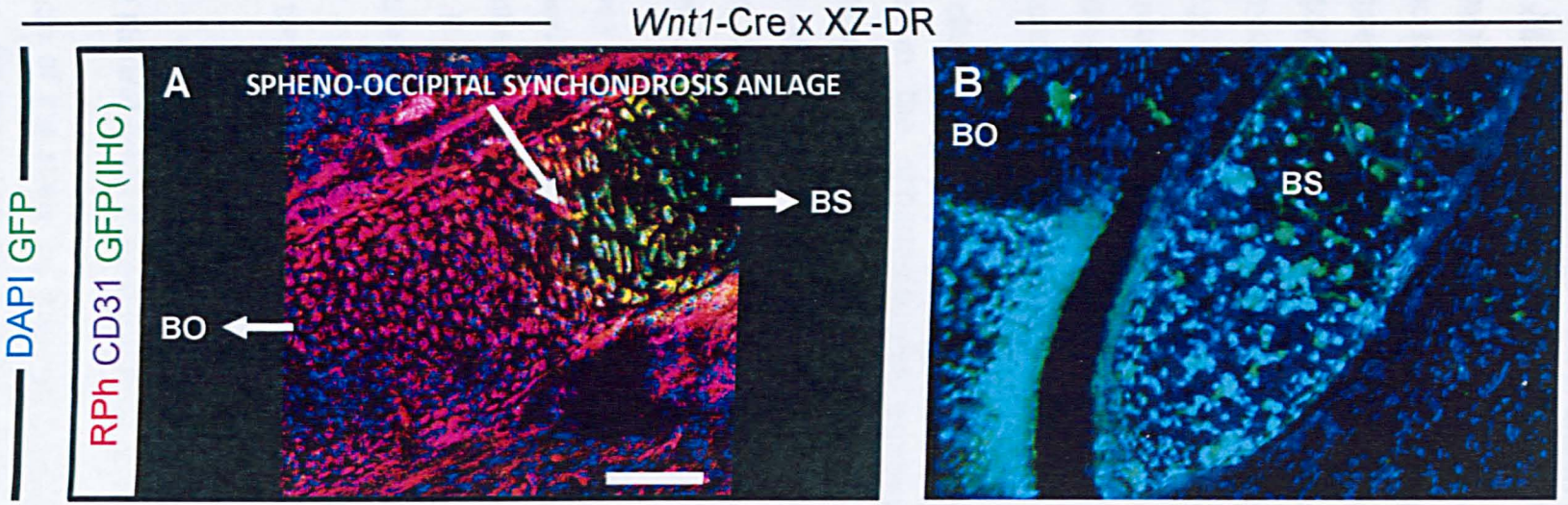

Figure 7.4: The dual neural crest and mesodermal origin of the mammalian clivus at E18.5

Sagittal section through the clivus immediately prior to birth at E18.5 after conception (positive vaginal plug is taken as E0); *Wnt1*-Cre$^{+/-}$ XZ-DR$^{-/-}$ mouse. **A.** IHC for GFP indicating the neural crest cells (green), CD31 (purple) and Rhodamine Phalloidin (red). **B.** *de novo* GFP expression under fluorescence on the Arcturus PixCell II LCM. Nuclear counterstain DAPI (blue, **A-B)**.

A-B. The spheno-occipital synchondrosis anlage (**SOS**) contains a large contribution of neural crest cells; the basisphenoid (**BS**) is neural crest while the basioccipital (**BO**) is mesodermal.

Scale bar indicates 50μm.

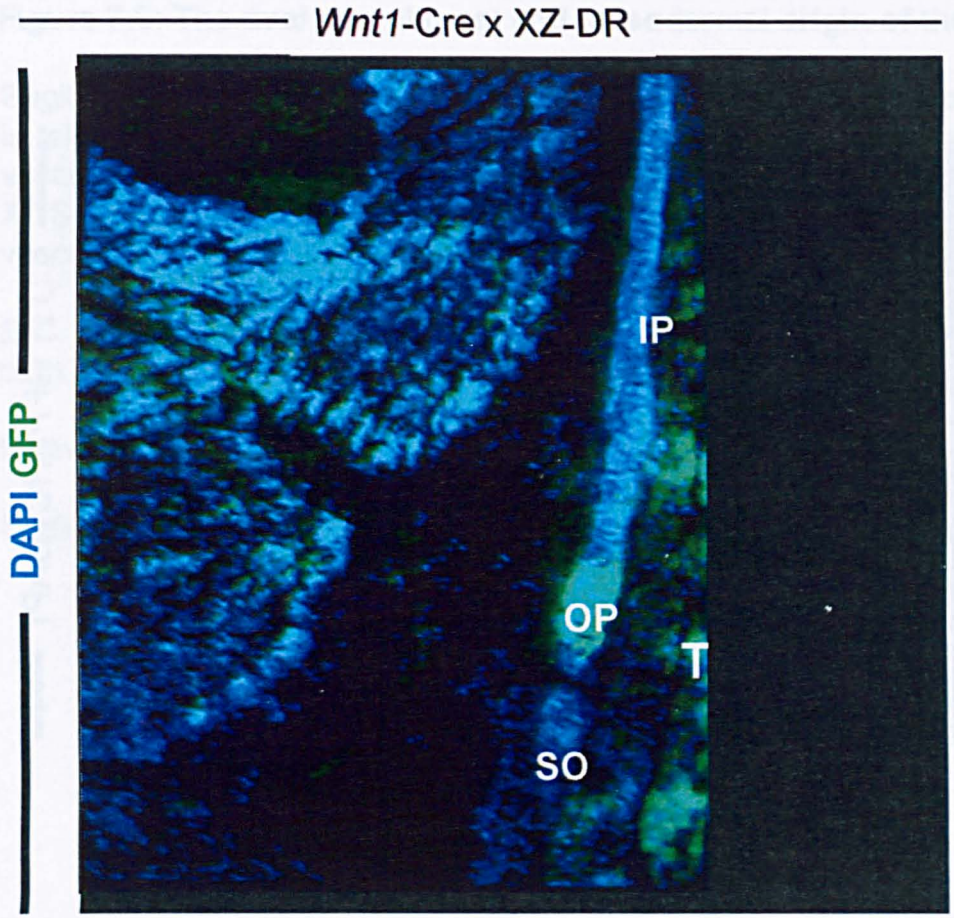

Figure 7.5: The dual neural crest and mesodermal origin of the mammalian cranial base at E18.5

Sagittal section through the cranial base immediately prior to birth at E18.5 after conception (positive vaginal plug is taken as E0); *Wnt*1-Cre$^{+/-}$ XZ-DR$^{-/-}$ mouse. *de novo* GFP expression under fluorescence on the PixCell II LCM. Nuclear counterstain DAPI (blue).

A late contribution of the neural crest is observed in the occipital protuberance, supra-occiput, and interparietal. The trapezius muscle is also neural crest in origin.

IP interparietal, **OP** occipital protuberance, **T** trapezius muscle, **SO** supraocciput

Acquired at 10x magnification.

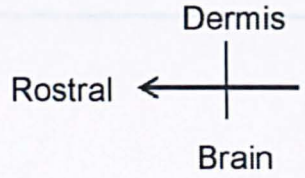

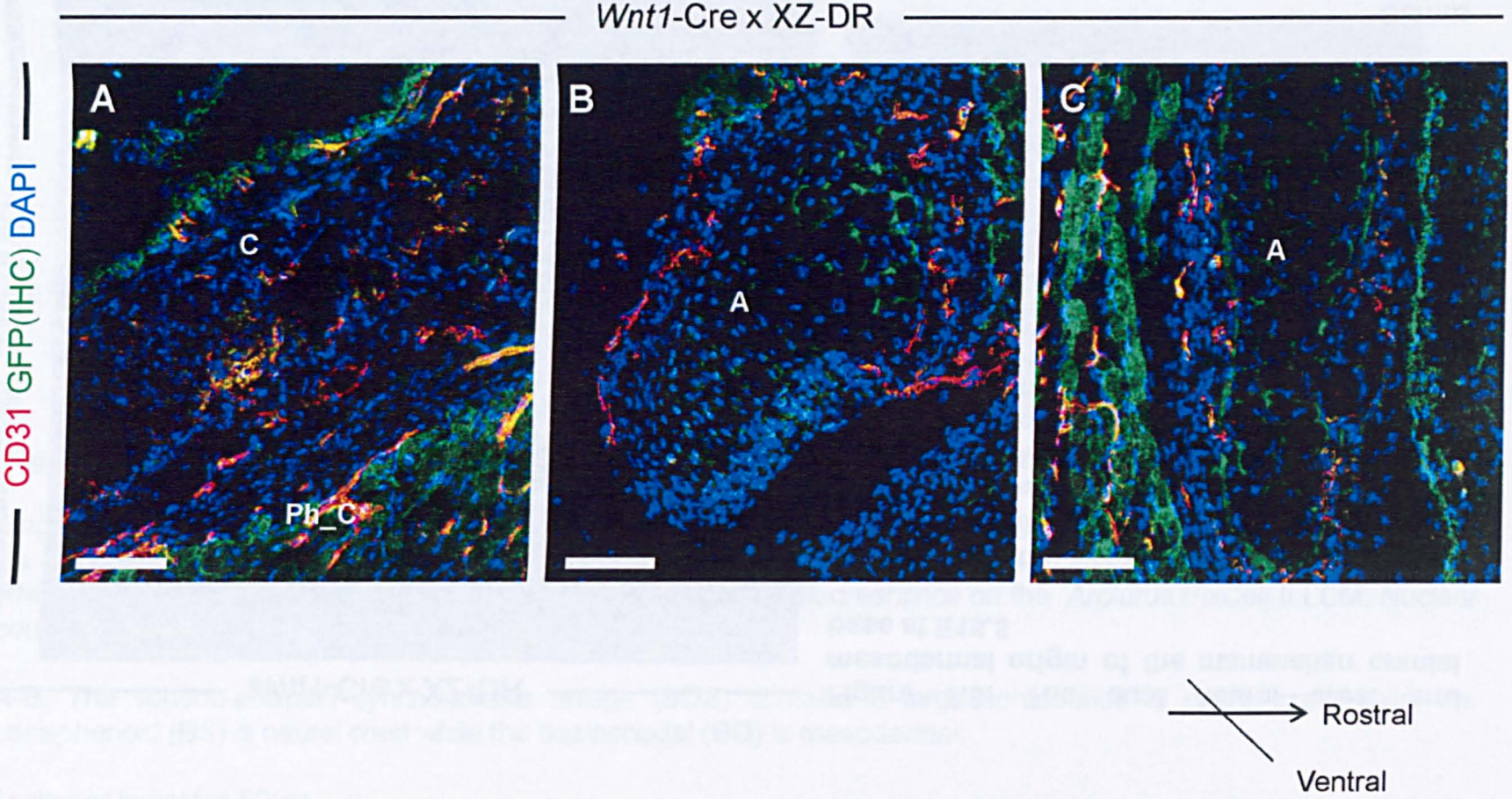
Wnt1-Cre x XZ-DR
CD31 GFP(IHC) DAPI
A
C
Ph_C
B
A
C
A
Rostral
Ventral

Figure 7.6: The dual neural crest and mesodermal origin of the cranial base vasculature at E18.5

Sagittal section through the clivus and atlas immediately prior to birth at E18.5 after conception (positive vaginal plug is taken as E0); *Wnt*1-Cre$^{+/-}$ XZ-DR$^{-/-}$ mouse. **A.** IHC for GFP indicating the neural crest cells (green), and CD31+ vasculature (red). Nucelar counterstain DAPI (blue, **A-B)**.
A. Some vasculature of the endochondral component of the clivus derives from the neural crest; as does the vasculature surrounding the forming bone and the pharyngeal constrictor muscles.

B-C. The atlas also contains neural crest-derived vasculature at the stage of murine development immediately prior to birth, at both it's ventral (**B**) and dorsal (**C**) margins.

C clivus, **Ph_C** pharyngeal constrictor muscles, **A** atlas

Scale bar indicates 50μm.

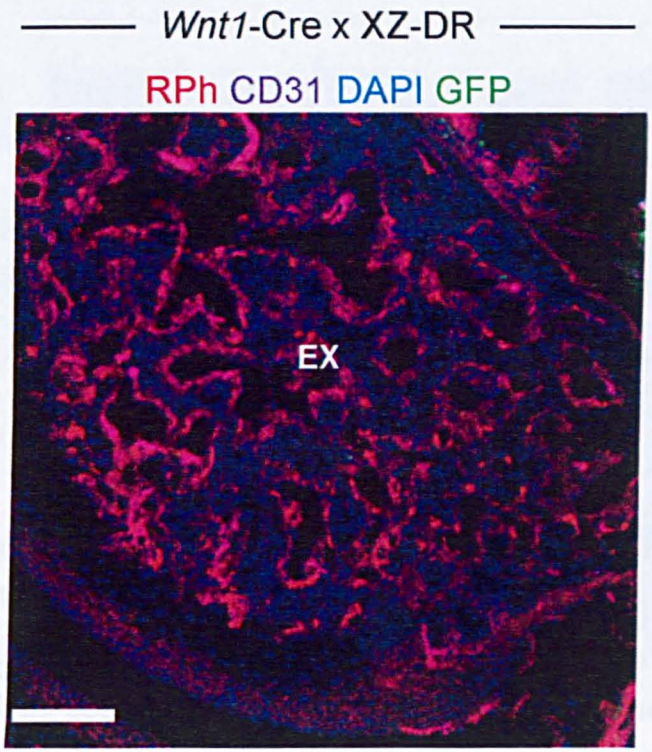

Figure 7.7: At E18.5 the murine exoccipital condyle is purely mesodermal

Sagittal section through the exoccipital condyle immediately prior to birth at E18.5 after conception (positive vaginal plug is taken as E0); *Wnt*1-Cre$^{+/-}$ XZ-DR$^{-/-}$ mouse. **A.** IHC* for GFP indicating the neural crest cells (green), Rhodamin Phalloidin (red) and CD31+ vasculature (purple). Nucelar counterstain DAPI (blue).

The vasculature of the exoccipital condyle, unlike other components of the cranial base from the same histological section, is purely mesodermal in origin. No neural crest cells are detected.

EX exoccipital condyle

Scale bar indicates 50μm.

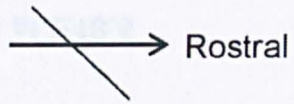

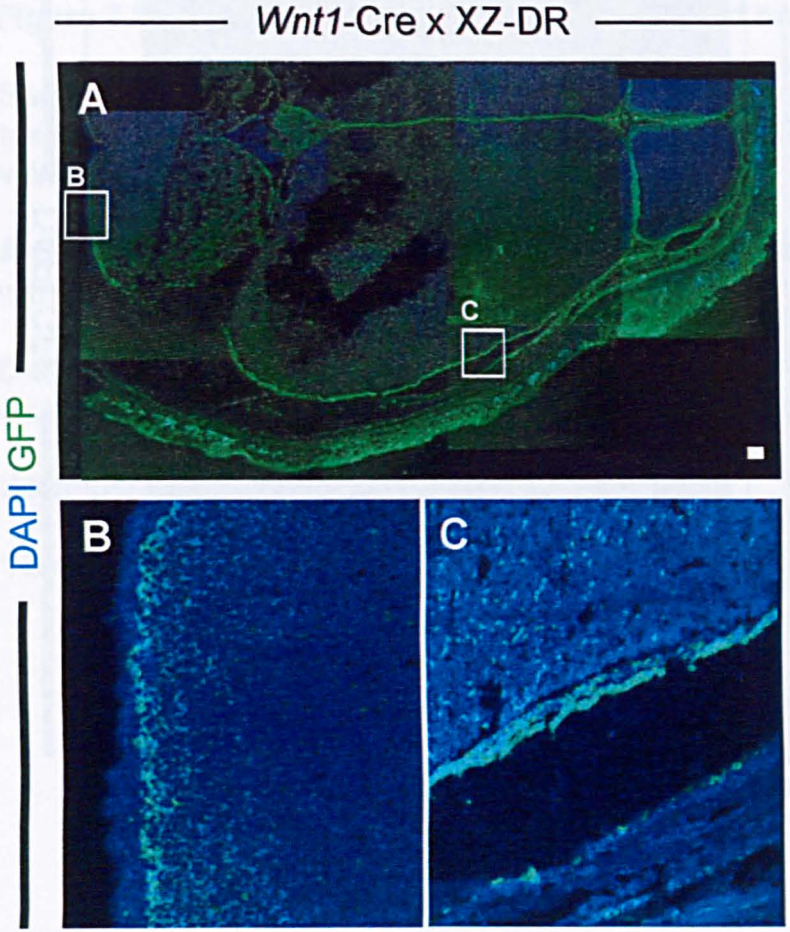

Figure 7.8: Neural crest contribution to the meninges

Transverse section through the murine cranium immediately prior to birth at E18.5 after conception (positive vaginal plug is taken as E0); *Wnt*1-Cre$^{+/-}$ XZ-DR$^{-/-}$ mouse. IHC for GFP indicating the neural crest cells (green); nuclear counterstain DAPI (blue, **B-C**).

A. Overview of the contribution of the neural crest to the murine cranium.

B. The meninges of the cerebellum are not labelled by the transgene, indicating either they are mesodermal or derive from the crest population of rhombomere 1, which does not express *wnt1*. Conversely, the arachnoids of the cortex are labelled (**C**).

Scale bar indicates 50μm.

* Stain and confocal by Dr X. Zhang, analysis by K. Jordan.

Lateral → Ventral

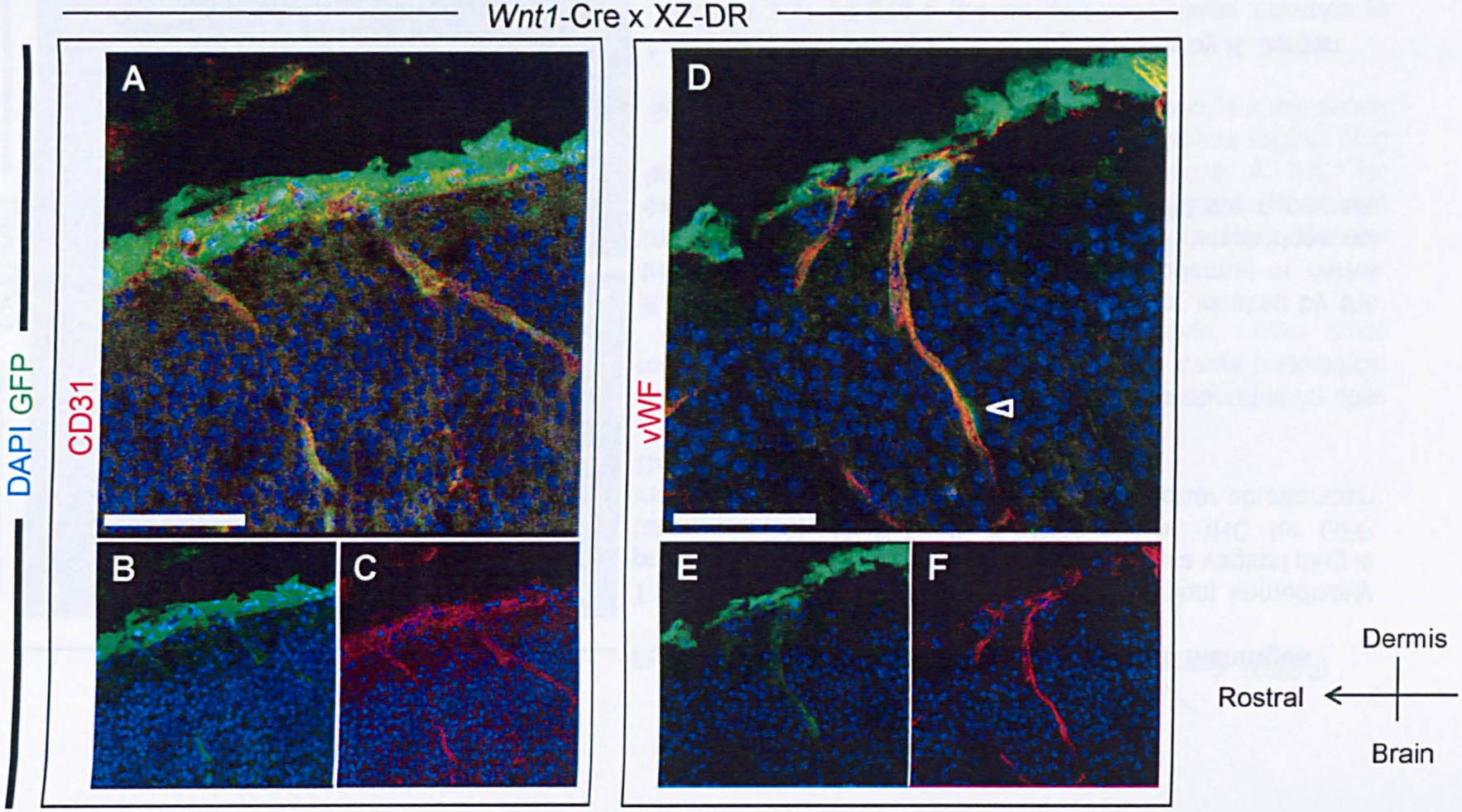
Wnt1-Cre x XZ-DR
DAPI GFP
CD31
vWF
A
B
C
D
E
F
Dermis
Rostral
Brain

Figure 7.9: Neural crest form the arachnoids and both the endothelia and pericytes of the cortex.

Sagittal section through the murine cortex immediately prior to birth at E18.5 after conception (positive vaginal plug is taken as E0); *Wnt*1-Cre$^{+/-}$ XZ-DR$^{-/-}$ mouse. IHC for GFP indicating the neural crest cells (green), CD31 (red, **A,C**) and vWF (red, **D,F**); nucelar counterstain DAPI (blue).

A-C. CD31/PECAM and GFP expression showing the meninx of the cortex are neural crest as is the vasculature within the cortex.

D-F. A second endothelial marker, von Willibrand factor, confirms the finding of neural crest-derived vasculature in the cortex and evidences both the endothelia (vWF+) and pericyte (vWF-, arrowhead) derive from the neural crest.

Scale bar indicates 50μm.

* Stain and analysis by K. Jordan, confocal by Dr X. Zhang.

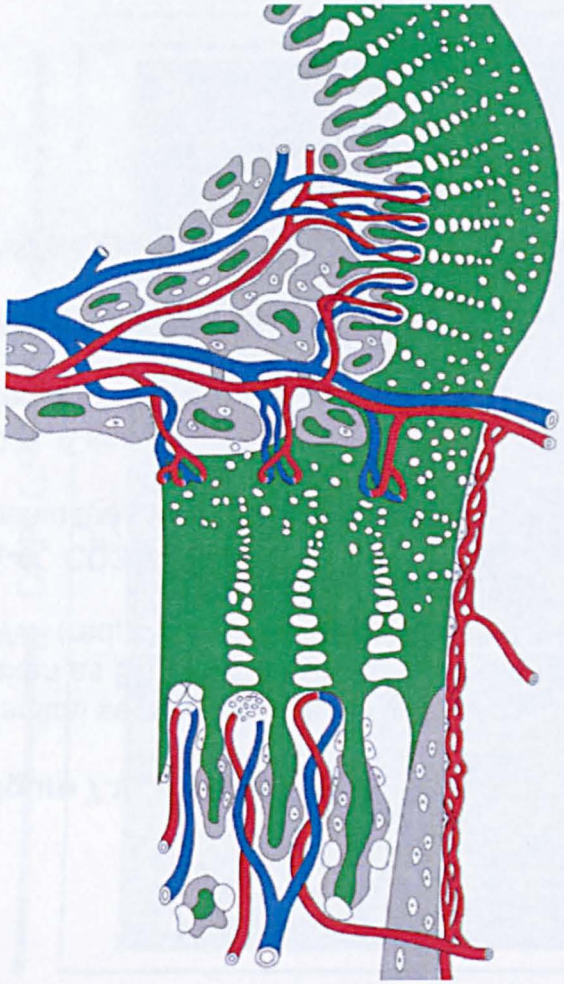

Figure 7.10 Endochondral ossification is dependent on vascular invasion of the cartilage template

Diagrammatic representation of endochondral bone development whereby a hyaline cartilage precursor is laid under a-vascular conditions (green). External to the cartilage the vascularised periosteum forms, contain osteoprogenitor cells and osteoblasts laying appositional matrix to stabilise the outside of the forming bone. At the centre of the bone (the primary ossification centre), chondrocytes grow and become hypertrophic and secrete vascular endothelial growth factor (VEGF) before they undergo apoptosis. The VEGF secretions recruit blood vessels from the periost, which grow into the spaces left by the apoptotic chondrocytes. The vasculature brings haemopoietic and osteoprogenitor cells to the bone cavity. Osteoblasts differentiate from the osteoprogenitors and osteoclasts from the bone marrow: these cells form the bone-proper.

Bone maturation is, therefore, contingent on chondrocyte hypertrophy and the ensuing vascularisation of the cartilage template.

7.3 Conclusion

Given the fundamental importance of vascularisation on endochondral development (Figure 7.8), the late invasion of neural crest vasculature to the cranial base is likely to be a key component of the bone maturation process. A deficiency in the late neural crest invasion could account for aberrant ossification and may link to the Chiari phenotype by affecting the height of the supraoccput/occipital protuberance (thus the tentorial angle), as well as the atlas/axis, accounting for the retroflexed odontoid process in Chiari I patients.

The contribution of the neural crest, mapped to the arachnoids, pericytes and endothelia of the cortex and medulla (Figure 7.11) could indicate that differences of compliance between these areas and the mesodermally-derived midbrain vasculature was a result of connective tissue defects among the neural crest vasculature.

The next phase of analysis focused on isolating single-cell precursors to the neural crest anlagen to the cranial skeleton and vasculature for whole transcriptome analysis.

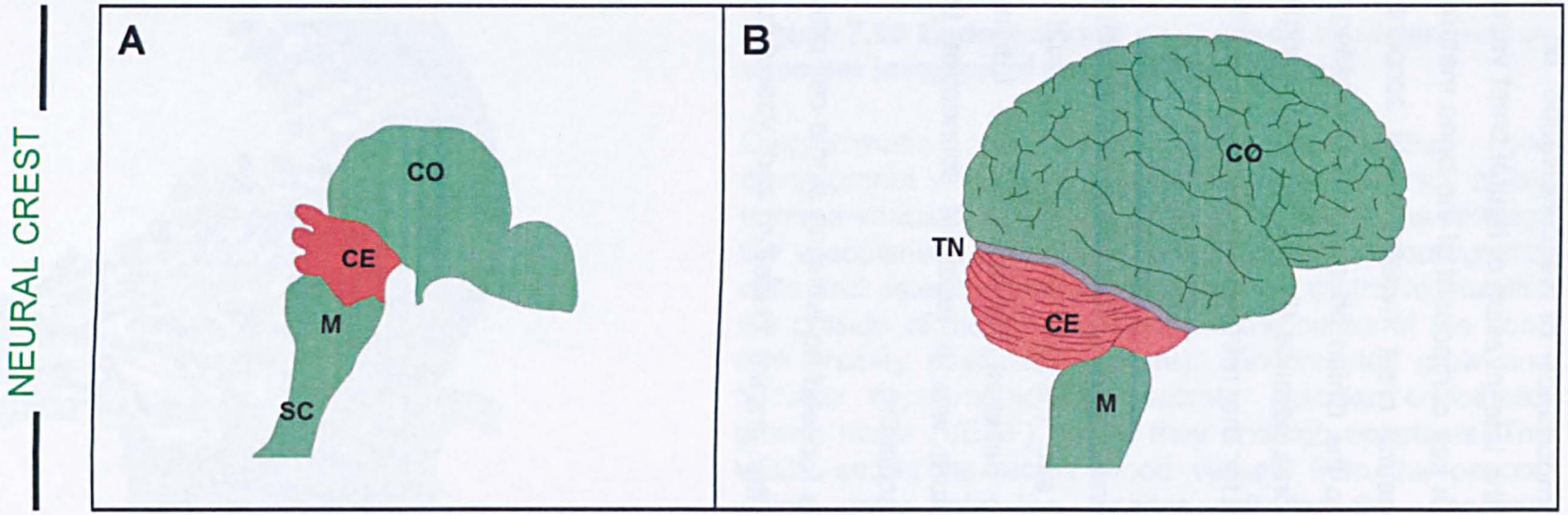

Figure 7.11: The neural crest and mesodermal contributions to the meninges and arachnoids of the human brain

Diagrammatic representation of the meninges that are neural crest (*Wnt1* expressing) (green) and those that do not express the *Wnt1* transgene (red) in the immature (**A**) and mature (**B**) conditions, as mapped to the areas corresponding to the results of the current study in murine brains. Neural crest forms the meninges of the cortex, medulla and spinal cord, while the cerebellar meninx derive from rhombomere 1 (which does not express *Wnt1*). The border of the tentorium is indicated in **B.**

CO cortex, **CE** cerebellum, **TN** tentorium, **M** medulla, **SC** spinal cord

7.4 Summary of findings

- The invasive neural crest makes a contribution to the occipital protuberance, supraocciput, atlas and clivus at late stages of murine prenatal development;

- The contribution of the neural crest to these structures implicates the neural crest in the maturation of the posterior cranial fossa, which is aberrantly formed in Chiari patients;

- At late stages of murine prenatal development, the vasculature of the endochondral bones of the cranial base comprises both neural crest and mesodermal cells;

- The neural crest contribution to cranial vasculature includes the arachnoids, pericytes and endothelia of forebrain (cortex) and some hindbrain structures (medulla), excluding the cerebellum.

8.1 Introduction

Gene expression profiling (via microarray analysis) of the early embryo during foetal development is a successful technique to interrogate the transcriptional networks underlying differentiation processes (Livesey *et al.* 2000). Interrogating the transcriptome of individual cells is a form of molecular analysis that probes the heterogeneity of developing tissues and can be used to explore regional differences among populations of cells (Tietjen *et al.* 2003). The current study aims to use single cell transcriptome analysis to explore the regulatory networks responsible for the differentiation of neural crest cells in the anlagen to structures affected in Chiari. The similarities and differences among the sub-populations of neural crest cells that give rise to various structures of the cranial base affected in Chiari I/II will be explored. Further analyses will be conducted on the transciptome of the neural crest-derived vasculature that may play a role in compliance issues in the Chiari malformations that result in the predominant symptom (sub-occipital headaches).

Laser capture microdissection (LCM) was used to isolate individual neural crest cells. The neural crest is genetically labeled and traced throughout the resulting anatomical structures derived from it using *Wnt1*-Cre$^{+/-}$ transgenic mice, in combination with two reporter strains (ROSA26LacZ$^{-/-}$ and XZ-DR$^{-/-}$) (Matsuoka *et al.* 2005). In *Wnt1*-Cre x ROSA26LacZ/XZ-DR mice, neural crest-derived cells can be identified via β-Galatosidase staining (ROSA26LacZ) on adjacent sections to those used for LCM and lineage identity of captured cells is confirmed using PCR for the transgene. In *Wnt1*-Cre$^{+/-}$ x XZ-DR$^{-/-}$ mice, neural crest cells can be visualised under fluorescent light during the isolation process on a PixCell II Laser Capture Dissection Microscope (Arcturus), allowing neural crest cells to be picked for analysis without contamination from mesodermal tissues. Notably, the technique allows the isolation of individual cells, however, in very dense cellular areas more than one cell may be picked at a time. Every attempt was made to be

diligent in assessing this and it was always noted when more than one cell was captured, although for the ease of nomenclature all samples were termed "single cell" samples.

I expression profiled single genetically-labeled neural crest cells from key regions affected in Chiari at crucial developmental time-points, namely at E9-10 after the cells have migrated into the branchial arches (to rule out genes associated with migration), at E13 when fate decisions are being made, and at E18.5 after the late invasion of neural crest cells identified in Chapter 7. Lineage labelled transgenic mice can also be utilised to isolate vasculature from the mesoderm in the cranio-facial region and to validate previous assertions that the vasculature is of a defined lineage-patchwork; expression profiles can also be generated for areas that are of NC (ex: internal carotid artery) versus mesodermal (ex: basilar artery) origin at embryonic stage E18.5. Previous studies have suggested that gene expression is more closely correlated with cell fate rather than lineage (Liu *et al.* 2009) and whole transcriptome analysis can be used to ascertain if this holds true for the vasculature of the cranial base. Furthermore, the transcriptome of the NC-derived meninges was investigated at E18. Unfortunately, the clean isolation of the neural crest-derived endothelia of endochondral bones (identified in Chapter 7) was beyond the limitations of the technique and the transcriptome of these cells could not be investigated during the current study.

8.2 Results: Single cell analysis of neural crest contributions to areas affected in Chiari I/II

The single-cell laser capture technique used for the study was pioneered by Koentges *et al.* and conditions for tissue preparation, single-cell collection, cDNA amplification, cDNA labelling and microarray hybridisation were optimised for this particular study (Technical Appendix 11.2).

8.2.1 Laser Capture Microdissection

The current study was designed to analyse the neural crest contributions to the structures affected in Chiari I/II that arise from both the early neural crest population and the late invading neural crest cells identified in our previous studies.

In early ontogeny I examine the genes being expressed at the time of cell-fate decisions (approximately E13) when erroneous expression could lead to the hypo or hyper-ossification experienced in Chiari I/II. The neural crest components of anlagen to structures that are affected in the majority of Chiari patients were isolated for analysis. Single cells were captured at E13 from the condensed mesenchyme anlagen to the neural crest clivus (basisphenoid and basiocciput) and pharyngeal constrictors (n=18) (annotated Cli/Ph or Cli_Ph), the pre-foramen magnum occipital region (n=21) (annotated FM), and the posterior cranial fossa (n = 26) (annotated PCF) (Figures 8.1-8.2 & Table 8.1). A total of 25 cells were also captured from branchial arches III & IV (annotated BA) at E9-10 to generate a list of genes expressed during and immediately after migration of post-otic neural crest cells into the branchial arches (Figure 8.3, Table 8.1). Seven controls from non-PONC cells were also captured at various time points (Table 8.1) (annotated control).

In late ontogeny, to further explore the transcriptome of neural crest-derived meninx, single cells from the neural crest derived meninges at E18.5 were also isolated (n = 8) (Figure, Table) (annotated meninges) (Figure 8.4, Table 8.1).

Previously reported regional differences in the lineage origins of cranio-facial vasculature were analysed in the current study at E18.5 and we find mosaic neural crest contribution to vasculature at the cranial base. At the axial level of the cochlea, neural crest and mesodermal vasculature developed in close spatial proximity and blood vessels were observed that appeared to have contributions from both (Figure 8.4). Single cells from the neural crest and mesodermal vasculature were subsequently isolated; neural crest n = 17 (annotated NC Vasc) and mesodermal n = 15 (annotated Meso Vasc) (Table 8.1).

8.2.2 Sample preparation prior to hybridisation to microarrays

For this pilot study, the experimental cohort was designed to include a minimum of three single cell samples from each experimental region, determined to be the minimum required for statistically significant analysis of gene expression between regions. Single cells from the regions of interest were captured in excess of this as in a previously published study only 10% of laser captured cells successfully passed quality controls and were hybridised to microarrays (Tietjen *et al.* 2003). The workflow was optimised (see Technical Appendix 11.2) and samples were subjected to rigorous quality controls prior to microarray analysis, including: confirmation of cDNA generation from total cellular RNA, analysis of successful re-amplificaiton of cDNA (including length of the product), confirmation of transgene and/or housekeeping gene expression via PCR or Southern hybridisation, and analysis of cDNA quality via Bioanalyzer and quantitative PCR (Figures 8.5-8.6). At various stages of quality controls the cohort of samples was narrowed down resulting in a total of 34 samples with sufficient quality to progress to microarrays, of which 26 were hybridised to arrays: E13 clivus/pharyngeal constrictors n = 2, E13 pre-foramen magnum occipital region n = 4, E13 pre-PCF n = 6 (of which loose mesenchyme outside the main condensation n = 3, annotated Loose PCF Mes), E9-10 branchial arch controls n = 3, E18.5 NC-meninges n = 4, E18.5 NC vasculature of cranial

base n = 3, and E18.5 mesodermal vasculature of cranial base n = 4. The microarrays were run in four rounds on three separate occasions.

8.2.3 Results from microarray analysis: Principle component analysis

Following hybridisation to microarrays (Affymetrix GeneChip Mouse 430 2.0), AffyBatch quality controls were performed (see Technical Appendix 11.2, Materials and Methods); the first cohort of samples (n = 12) all passed quality controls and were subjected to whole transcriptome principle component analysis (PCA). PCA is a statistical clustering technique that analyses the overall variance within the samples (in this case, differential gene expression) and subsequently groups those samples whose transcriptomes are more similar. Each principle component is a linear representation of the combination of overall gene expression patterns and each principle component represents variance among the expression pattern of the microarray, with the first two components accounting for the majority of the variance. When the first two principle components are plotted against one another, the whole transciptome clustering of the samples can be visualised.

Using PCA reveals that within the first cohort of samples, two discernable clusters are evident, one including the vasculature (meninges, NC-vasculature and mesodermal vasculature) and the other the non-vascular samples (Figure 8.7). The neural crest vasculature and meninges were more similar to the mesodermal-derived vasculature than they were to the neural crest precursors to the bones of the skull base, supporting the idea that cell fate more strongly correlates with gene expression than lineage. However; the two clusters also neatly divided the two time-points isolated (E13 versus E18.5), therefore, it cannot be ruled out that the clustering is due to two stages of terminal differentiation or developmental progression. Along the X-axis (representing principle component 1), the 3 sub-populations of neural crest cells from the E13 embryos (namely, the anlagen to the PCF, clivus/pharyngeal constrictors and foramen magnum) were more similar to each other than to the other sub-populations, potentially representing

regional variations in gene transcription in the developing cranial base. However, there were not enough replicates to confirm this with statistical significance. Among the vasculature samples, neither principle components 1 (X-axis) nor 2 (Y-axis) clustered the sub-populations of vasculature (namely meninges, NC vasculature and mesodermal vasculature).

The subsequent cohorts of samples included the final 14 microarrays. Post-hybridisation quality control analysis revealed 9 samples had a notably diminished overall intensity level (BA n = 3, meninges n = 2, NC-vasc n = 2, meso-vasc n = 2) as well as a borderline result from the Bioanalzer. The results from all of the cohorts were subjected to principle component analysis, which yielded absolutely no biologically meaningful clustering (Figure 8.8). When the 9 samples with poor intensity and Bioanlyzer quality were removed, the clusters were recapitulated with only one sample (#87, pre-foramen magnum) behaving as an outlier and clustering more closely to vasculature than the bone anlagen (Figure 8.9).

Within the PCA plot we noticed 4 samples were heavily clustered along the X and Y axes, including samples from 3 sub-populations of neural crest cells at E13 (sample 14 from the pre-foramen magnum, samples 31 and 33 from the loose PCF mesenchyme and sample 74 from the clivus/pharyngeal constrictors) (Figure 8.9). Sample 84 (also foramen magnum) was also closely aligned to this cluster. These samples had the commonality that they had the lowest percentages of genes which were positive for expression on the microarray, all under 4%. The reported array coverage in published studies of laser captured single cells has wide variation (Kamme *et al.* 2003; Seshi *et al.* 2003; Tietjen *et al.* 2003); within the literature, studies that are most analogous to our own in both the isolation method (namely, LCM from cryo-sectioned rodent tissues) and array platform (Affy GeneChip 430 2.0) report % present between 5.6%-13.9% (Kamme *et al.* 2003). These figures also match previous, unpublished, data from our own laboratory. During the optimisation stage of the current study (see Technical Appendix 11.2), it was noted that the array hybridised with a "blank" cell (a sample that had no cellular material added to the original cDNA generation step, and was

subsequently re-amplified) had 1% array coverage, while samples (n =4) that had failed pre-microarray quality controls (but were run for comparison), had an average coverage of 1.9% and samples that had passed pre-array controls but failed the control for array intensity (n = 9) had an average coverage of 3.7%. It was, therefore, decided to use 4% present as the threshold to include samples in gene expression analyses (Cli/Ph n = 1, PCF n = 3, PCF loose mes n = 1, FM n = 2, meninges n = 2, NC vasc n = 1, meso vasc n = 2).

Due to the diminished experimental cohort, after the exhaustive quality controls, differential gene expression analyses among the sub-populations of cells would not be statistically valid. Gene expression analyses of the single cells instead focused on elucidating the major pathways activated in the samples, especially those that discriminate between the vasculature and non-vasculature samples and/or may have relevance in generating the Chiari phenotype.

8.2.4 Results from microarrays: Single cell gene expression analyses

The axial origin of the cells was mapped by gene expression profiling of the Hox genes. The Hox signatures of the single cells analysed in the current study indicate the samples all arise from post-otic or cervical locations (Table 8.2). This is an important finding as past studies by J.L. Rinn *et al.* had demonstrated that even fibroblastic cells retain the HOX gene signature of their axial origin throughout development into the adult stage (Rinn *et al.* 2006; Rinn *et al.* 2008). As the cells in the current study express posterior signatures, it indicates they may have migrated from posterior locations into the cranial base.

Within the single cells analysed, genes in the latent transforming growth factor (TGF)-β (LTBP) family were found to be active in 80% of vascular samples as well as in the loose mesenchyme surrounding the pre-foramen magnum area (Table 8.3). LTBP genes were not expressed in any of the pre-skull base samples. The LTBP pathway is of interest as transgenic LTBP-3

knockout mice undergo premature stenosis of the basoccipital-basisphenoid synchrondroses (Figure 8.10). This phenotype is attributed to a precocious maturation of the tissue indicated by an over-extensive zone of hypertrophic chondrocytes, with vascularisation being the key committing step in chondrocyte hypertrophy (Dabovic *et al.* 2002; Dabovic *et al.* 2002). Interestingly, this indicates that the vascular invasion of the clivus (which was found to comprise both neural crest and mesodermal cells) could play a key role in the timing of the ossification of the synchondroses, leading to the angulation/retroflexion which determines the size of the PCF. If this is the case, the LTBP genes could be Chiari disease candidates, which could be screened for. Furthermore, it is intriguing to consider classifying Chiari as a vasculogenic disorder; although the bony structures of the cranial base are malformed in Chiari, this may be a result of aberrant vascular development hastening or delaying endochondral ossification.

Chiari has been postulated to be a connective tissue disorder as a link between inherited connective tissue diseases (namely, Ehlers-Danlos and related hereditary disorders of connective tissue) and Chiari was previously established (Milhorat *et al.* 2007); in a prospective study of 2,813 Chiari patients, 12.7% met the diagnostic criteria for hereditary connective tissue disorders (Milhorat *et al.* 2007). Examining connective-tissue related gene expression in the current study reveals extensive expression and an enrichment for collagens in the samples from both the vasculature and skull base anlagen (Table 8.4). As connective tissue related genes were expressed in all of the areas profiles, which are affected in Chiari I/II, the current data support Chiari as being a connective tissue disorder.

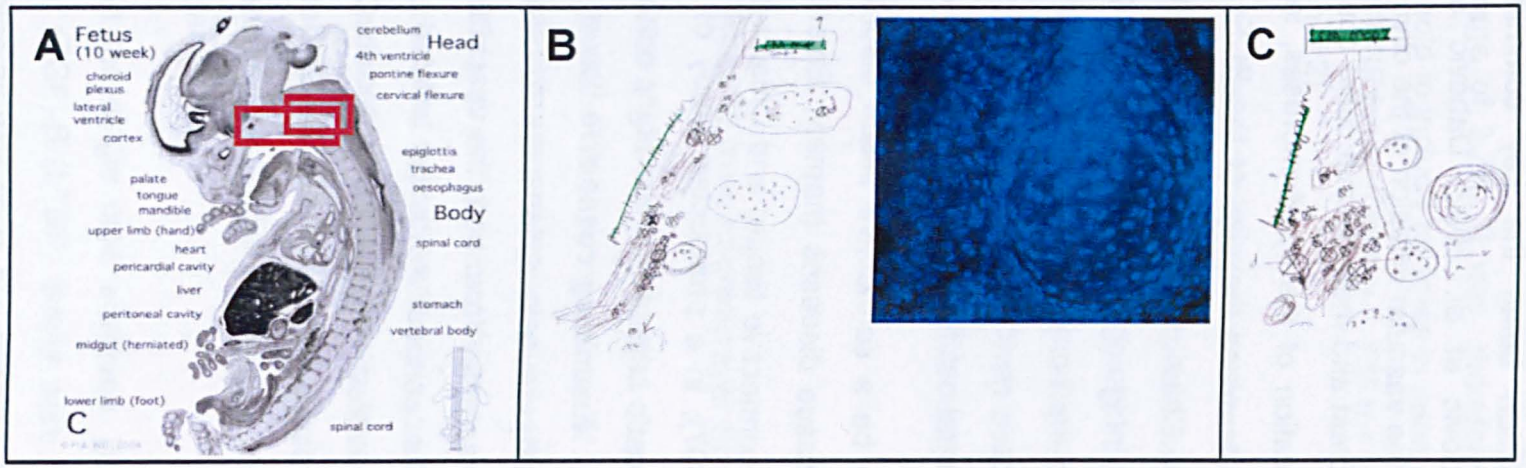

Figure 8.1: Laser capture microdissection maps for the single neural crest cells isolated at E13 from the anlagen to the clivus/pharyngeal constrictors and the foramen magnum

A. Human foetus** at 10 weeks of gestation; the areas analogous to those isolated for analysis in an E13 *Wnt1*-Cre$^{+/-}$ x ROSA26Lacz$^{-/-}$ mouse are highlighted in red boxes, comprising the condensed anlagen to the clivus/pharyngeal constrictor muscles and the neural crest components of the occipital region surrounding the foramen magnum.

B-C. Illustrative maps from laser capture microdissection* showing the exact locations of the single cell samples isolated for whole transcriptome analysis, as well as a 10X magnification image of the nuclear counterstain in the area of interest. Section orientation is indicated. The clivus/pharyngeal constrictor region is shown in **B**, while the future occipital area around the foramen magnum is shown in **C.**

**modified from M.A. Hill 2004; * Conditions for sample preparation, laser capture microdissection and subsequent whole transcriptome analysis are found in Materials and Methods.

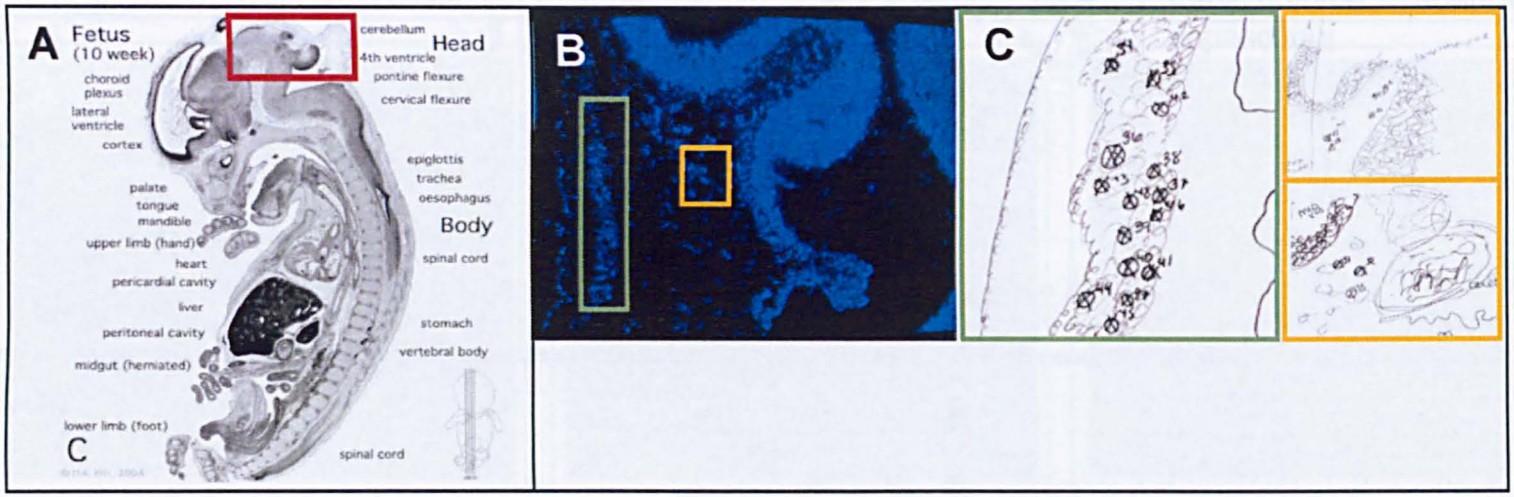

Figure 8.2: Laser capture microdissection maps for the single neural crest cells isolated at E13 from the anlagen to the posterior cranial fossa/tentorium

A. Human foetus** at 10 weeks of gestation; the area analogous to the one isolated for analysis in an E13 *Wnt1*-Cre$^{+/-}$ x ROSA26Lacz$^{-/-}$ mouse is highlighted (red box), comprising the future posterior cranial fossa (PCF)/tentorium.

B-C. Illustrative maps from laser capture microdissection* of the PCF/tentorium showing the exact locations of the single cell samples isolated for whole transcriptome analysis, as well as a 10X magnification image of the nuclear counterstain in the area of interest. Section orientation is indicated.

** Modified from M.A. Hill 2004; * Conditions for sample preparation, laser capture microdissection and subsequent whole transcriptome analysis are found in Materials and Methods.

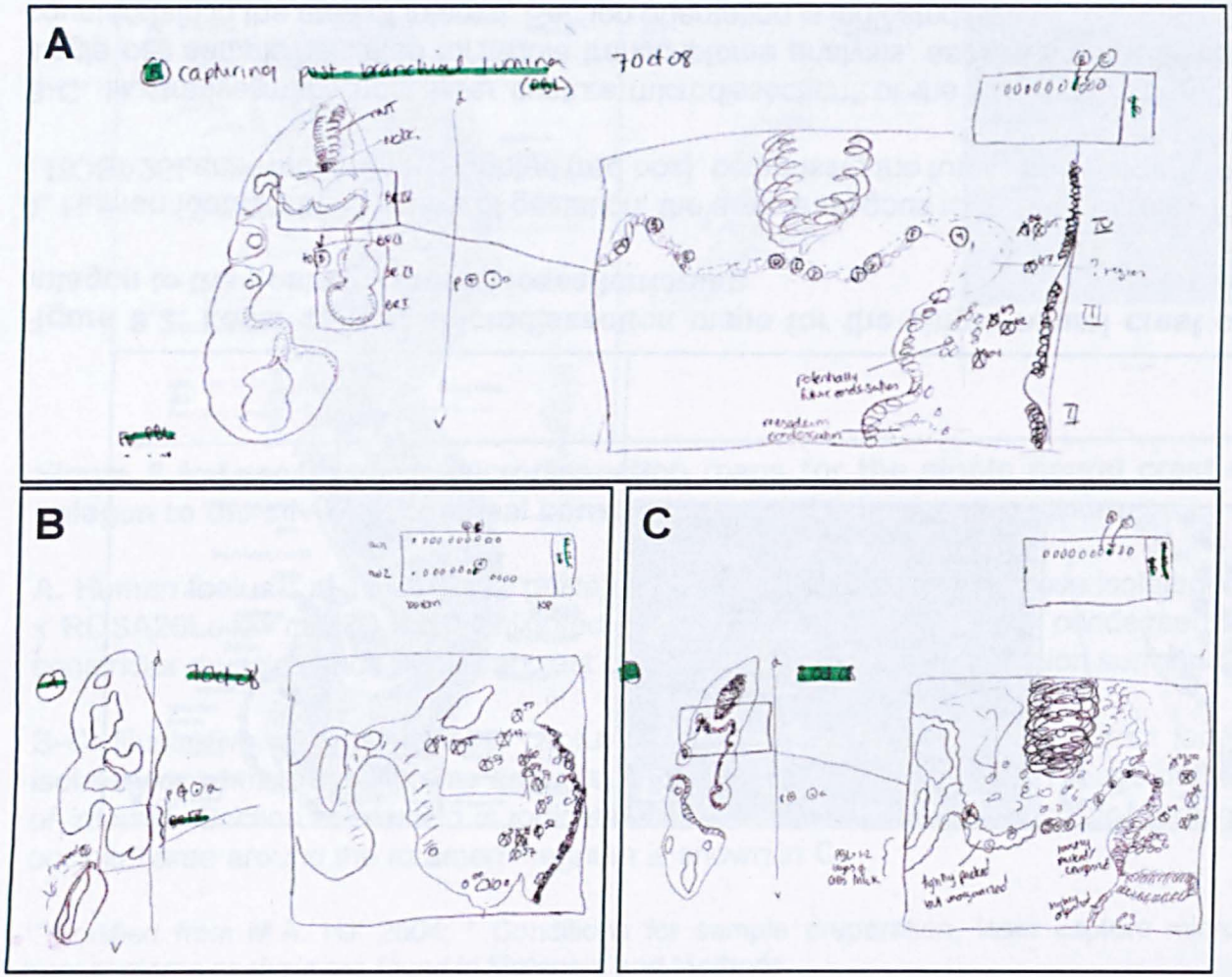

Figure 8.3: Laser capture microdissection maps for the single cells isolated at E9-10 from branchial arches III/IV and the post-branchial lumina

A-C. Illustrative maps from laser capture microdissection of branchial arches III & IV and the post-branchial lumina showing the exact locations of the single cell samples isolated for whole transcriptome analysis. Section orientation is indicated.

* Conditions for sample preparation, laser capture microdissection and subsequent whole transcriptome analysis are found in Materials and Methods.

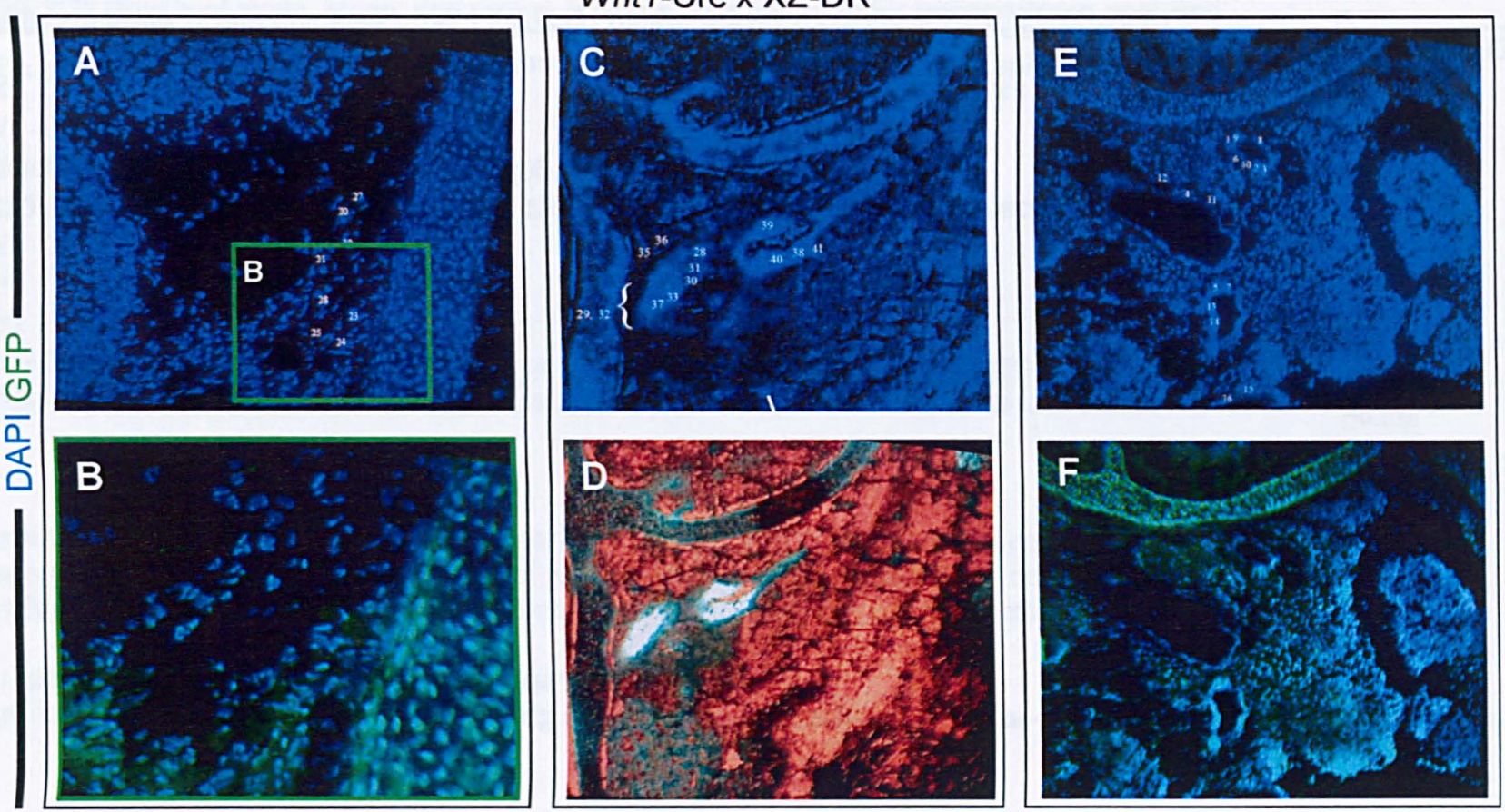
Wnt1-Cre x XZ-DR
DAPI GFP
A
B
C
D
E
F

Figure 8.4: Areas isolated for single cell transcriptome analysis of neural crest and mesodermal vasculature in the cranial base/meninges/arachnoids.

Sagittal sections of the neurocranium immediately prior to birth at E18.5 after conception (positive vaginal plug is taken as E0); *Wnt*1-Cre$^{+/-}$ XZ-DR$^{-/-}$ mouse. Images acquired with fluorescence on an Arcturus PixCell II LCM; GFP expression (*de* novo) indicating neural crest cells (green, **B, D, F**) and nuclear counterstain DAPI (blue, **A, C, D**).

A-B. Neural crest derived meninges/arachnoids at the tentorium are neural crest in origin; in **A** each number indicates the locations of the corresponding single cell sample.

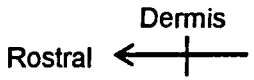

C-D. Neural crest-derived vasculature at the axial level of the cochlea; in **B** each number indicates the locations of the corresponding single cell sample.

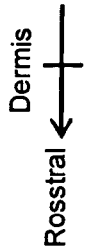

E-F. Heterogeneity of the origins of the vasculature of the cranial base; whereby samples were captured (white numbers in **E**) from both neural crest (green) and non-neural crest vasculature.

* Conditions for sample preparation, laser capture microdissection and subsequent whole transcriptome analysis are found in Materials and Methods.

Table 8.1: Details of strain, stage, and region of single cells captured for transcriptome analyses.

STRAIN	STAGE	REGION	SINGLE CELLS CAPTURED
Wnt1-CrexROSA28LacZ	E13	Clivus_Phayngeal Constrictors	18
Wnt1-CrexROSA28LacZ	E13	Foramen magnum	21
Wnt1-CrexROSA28LacZ	E13	Posterior cranial fossa	26
Wild-Type	E9-10	Branchial arches III/IV	25
Wnt1-CrexROSA28LacZ	E13	Control non-PONC cells	7
Wnt1-CrexXZ-DR	E18.5	NC-derived meninges	8
Wnt1-CrexXZ-DR	E18.5	NC-derived vasculature	17
Wnt1-CrexXZ-DR	E18.5	Mesoderm-derived vasculature	15

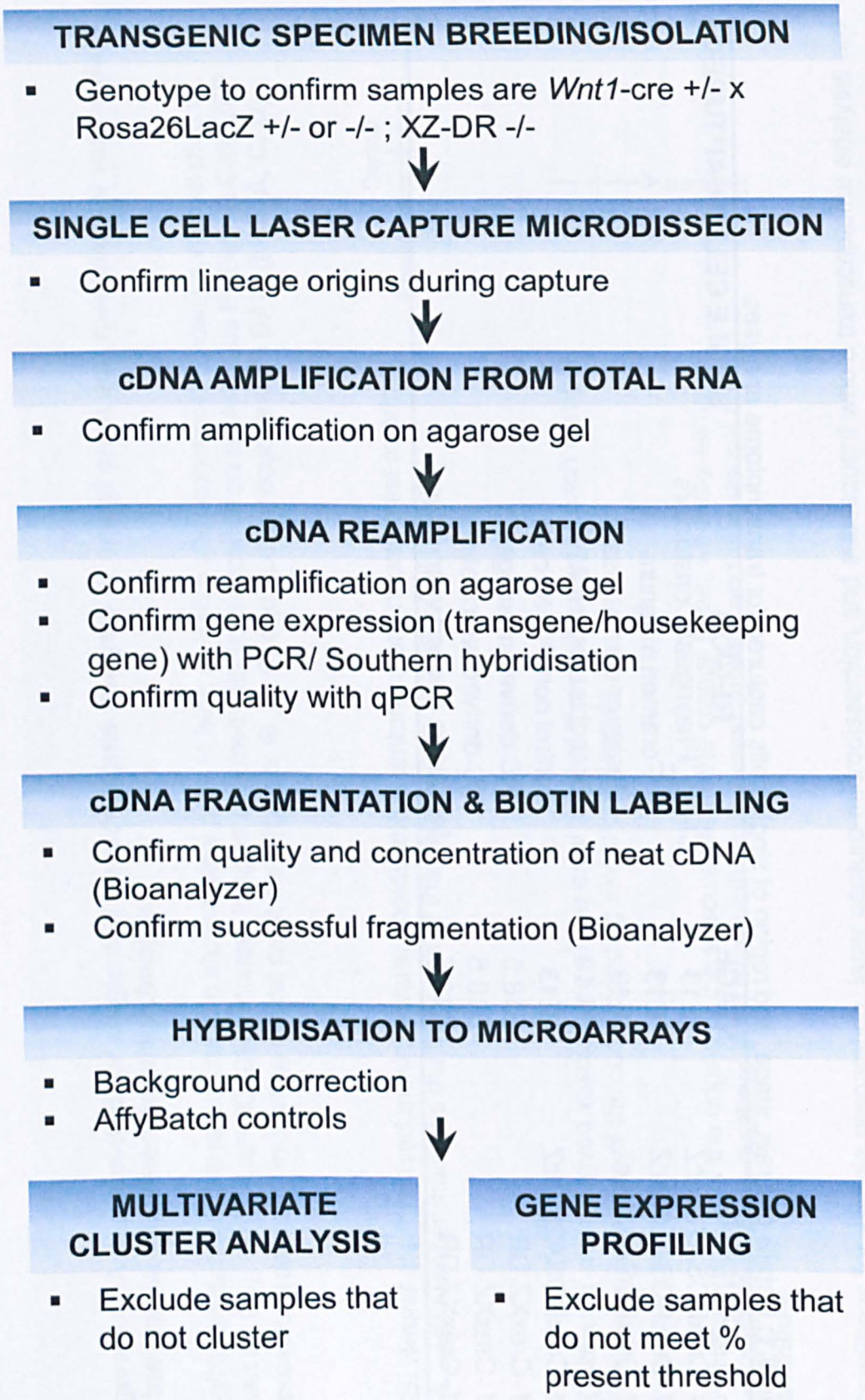

Figure 8.5: Optimised workflow for single cell transcriptome analysis

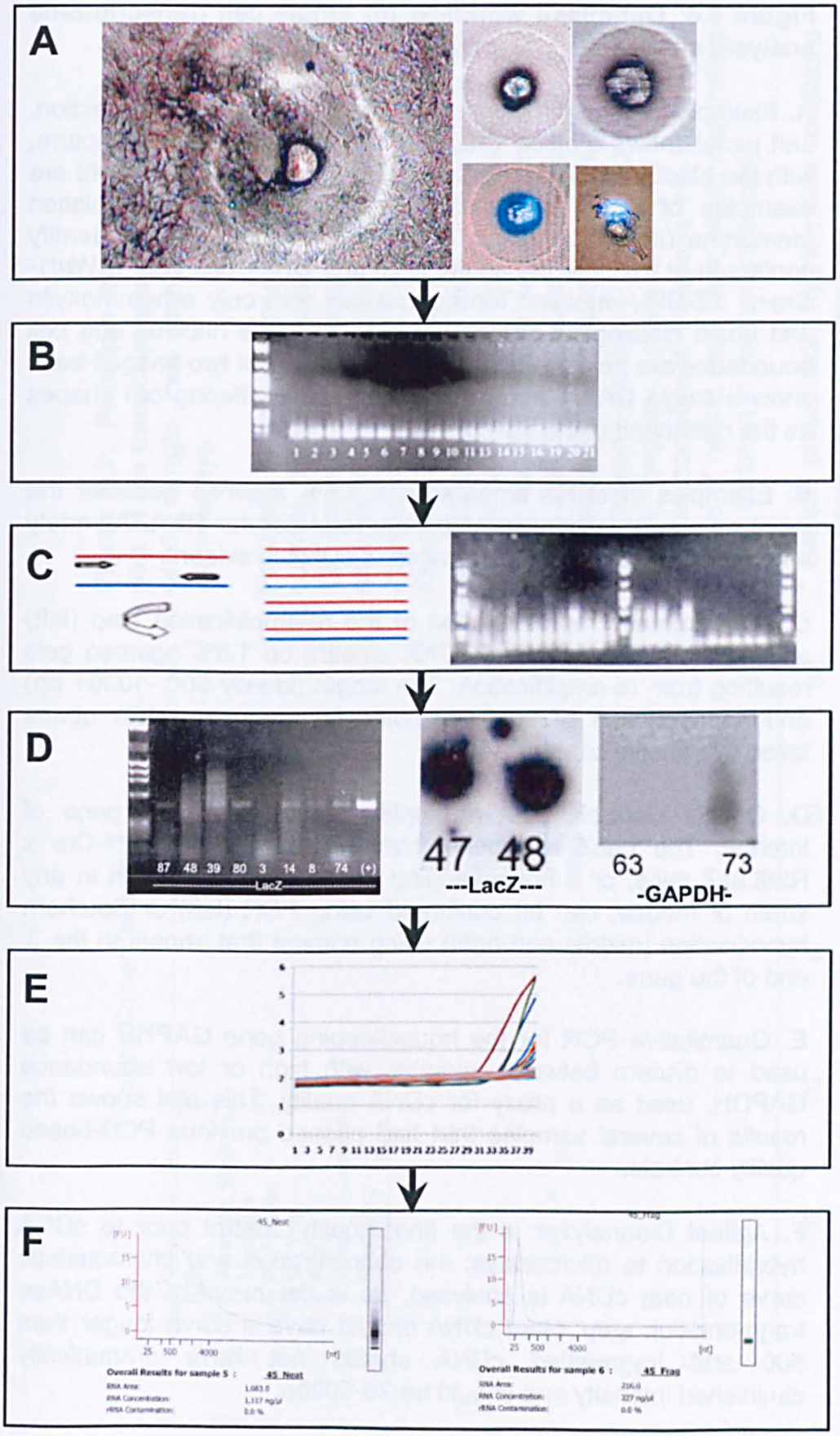
A
B
C
D
87 48 39 80 3 14 8 74 (+)
-LacZ-
47 48
---LacZ---
63 73
-GAPDH-
E
F
45_Neat
Overall Results for sample 5 : 45_Neat
45_Frag
Overall Results for sample 6 : 45_Frag

Figure 8.6: Optimised workflow for single cell transcriptome analysis studies

A. Example of samples isolated via laser capture microdissection. Left panel shows a blood vessel at 10X immediately post-capture, with the black rind indicating the region of capture. To the right are examples of single captured cells visualised on the isolation membrane (cap). Top left is a neural crest cell, lineage identify confirmed at the time of capture as it is a GFP+ cell from a *Wnt*1-Cre+/- XZ-DR-/- mouse. Top right, a cell with only a hematoxylin and eosin histological preparation, in which the nucleus and cell boundaries are hard to distinguish. Bottom set of two images each show a single DAPI+ nuclei but dramatically differing cell shapes as the right-hand cell is vascular.

B. Examples of cDNA smears on a 1.5% agarose gel after the initial reverse transcription step from total cellular RNA. A variety among the length and concentration of cDNA is evident.

C. Diagrammatic representation of the re-amplification step (left) accomplished via PCR and cDNA smears on 1.5% agarose gels resulting from re-amplification. The length (ideally 500 -1000+ bp) and concentration of some samples is adequate, while others failed this quality control.

D. Quality Controls post re-amplification: detecting a gene of interest. The LacZ transgene from single cells of *Wnt1*-Cre x R26LacZ mice, or a housekeeping gene such as GAPDH in any strain of mouse, can be confirmed using PCR (left) or Southern hybridisation (middle and right) using primers that anneal to the 3' end of the gene.

E. Quantitative PCR for the housekeeping gene GAPHD can be used to discern between samples with high or low abundance GAPDH, used as a proxy for cDNA quality. This plot shows the results of several samples that had passed previous PCR-based quality controls.

F. Agilent Bioanalyzer is the final quality control prior to cDNA hybridisation to microarrays: the concentration and characteristic curve of neat cDNA is analysed, as is the result of the DNAse fragmentation step. Neat cDNA should have a curve longer than 500 and fragmented cDNA should not have dramatically diminished intensity and should be 25-500bp.

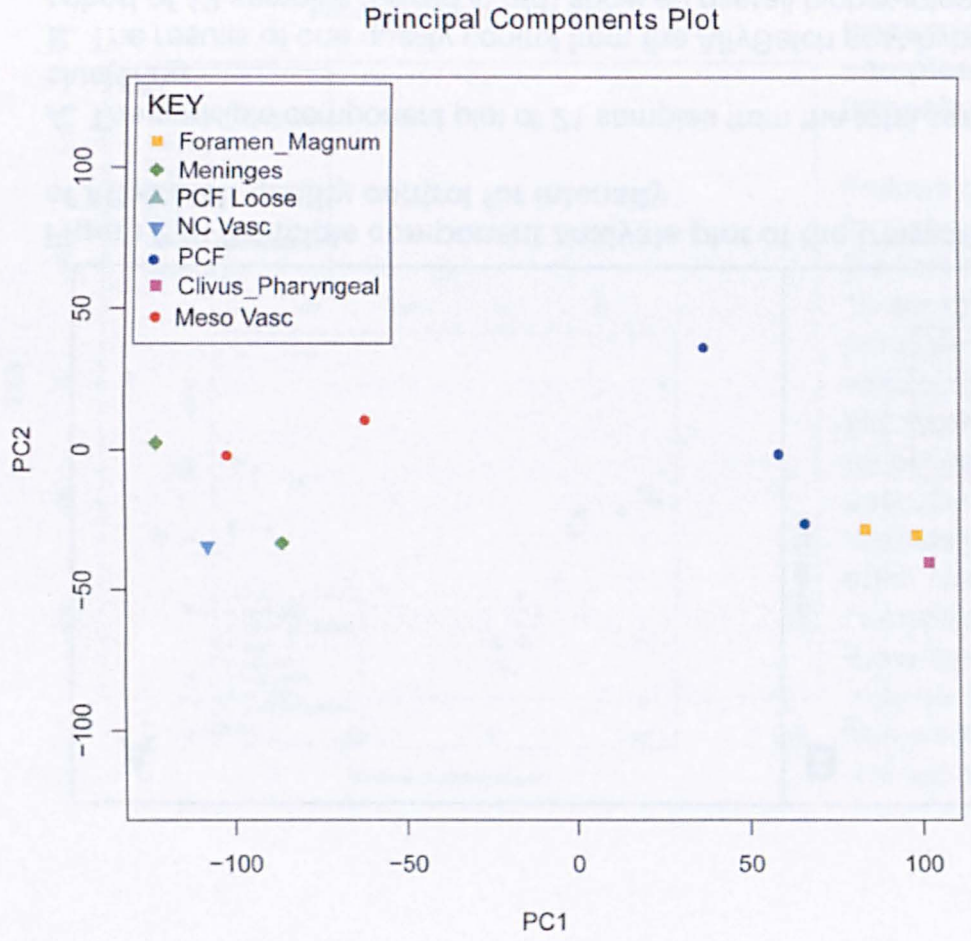

Figure 8.7: Principle component analysis plot of the transcriptomes of the first cohort of 12 single cell samples hybridised to microarrays

Following all pre- and post-hybridisation quality controls, the transcriptomes of the first cohort of 12 samples were subjected to clustering analysis. A plot of principle components 1 and 2 (accounting for 99% of the variability within the samples) clearly divides the samples into two sets along the X and Y axes. To the left are the vascular samples from the E18.5 mice; versus all the non-vasculature samples from the E13 mice are to the right. Interestingly, the transcriptomes of mesodermal versus neural crest derived vasculature do not segregate the lineage origins. Among the E13 samples, principle component 1 clusters the three sub-regions of neural crest cells, which may reflect region variation in the transcriptomes.

* Sample preparation, hybridisation conditions and descriptions of statistical analyses can be found in Materials and Methods.

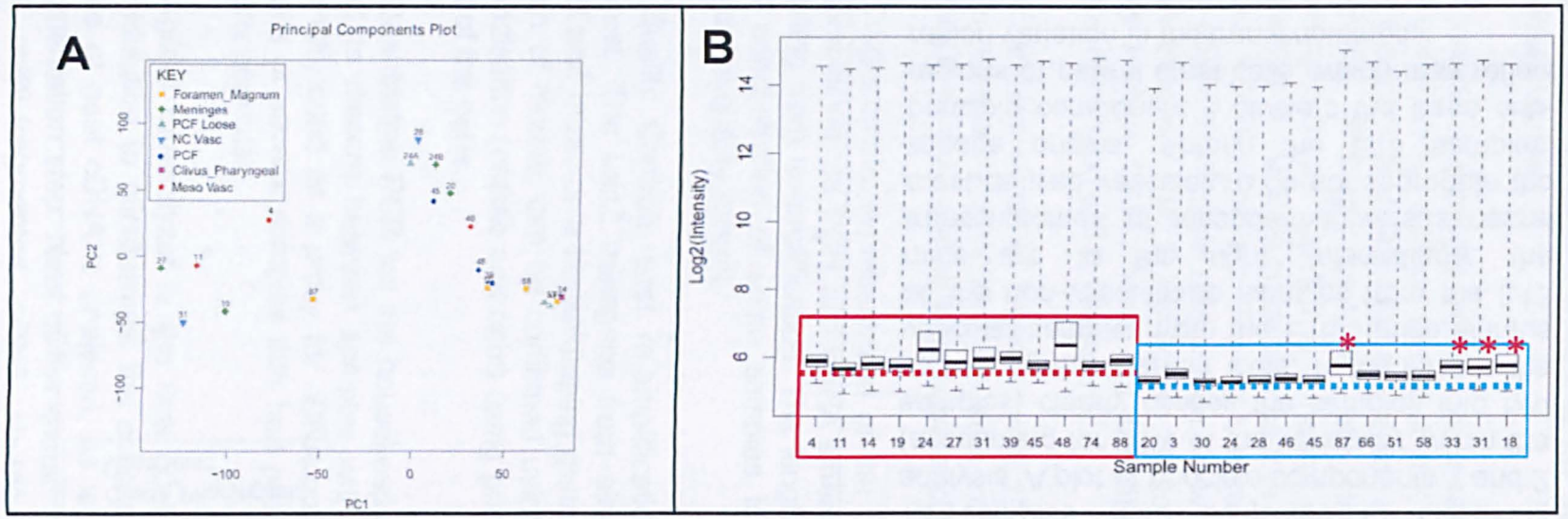

Figure 8.8: Principle component analysis plot of the transcriptomes of the total single cell cohort and results of *AffyBatch quality control for intensity*

A. The principle component plot of 21 samples from the total sample cohort which shows no discernible relevant clustering.
B. The results of one quality control from the AffyBatch post-hybridisation report: overall array intensity. The first cohort of 12 samples (boxed in red) show an overall higher intensity compared to the subsequent 14 samples analysed (boxed in blue). Lowest intensity among the first twelve samples indicated in red line, and is higher than the blue counterpart. Notably, 4 samples within the blue cohort had acceptable intensity (red *) and were included in further analyses.

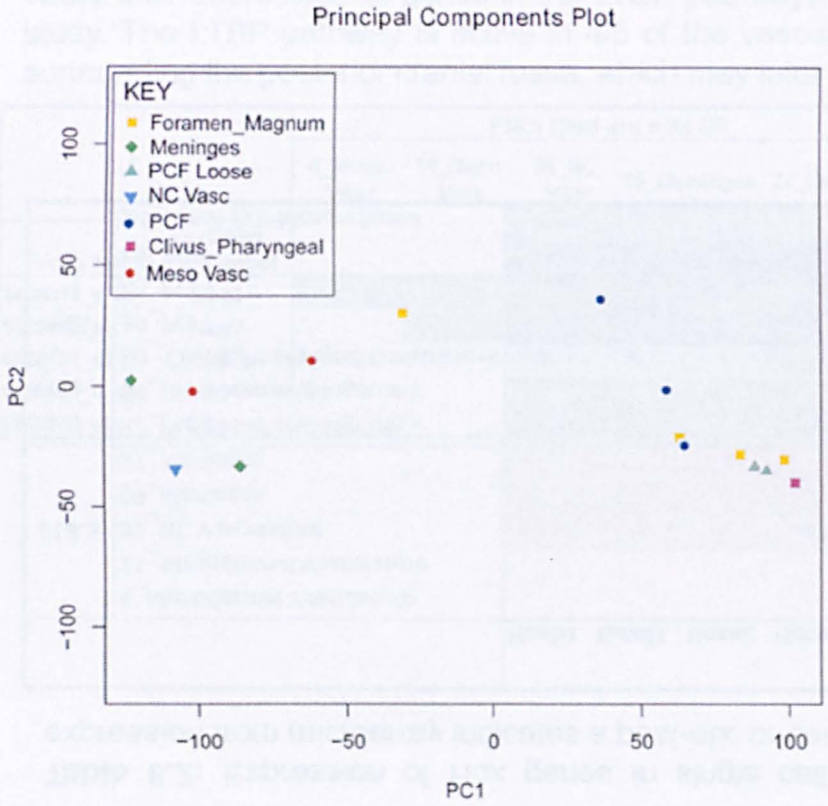

Figure 8.9: Principle component analysis plot of the transcriptomes of the first cohort of 12 single cell samples and 4 additional samples with acceptable intensity

Following all pre- and post-hybridisation quality controls, the four samples with acceptable overall intensity were added to the first cohort of 12 samples and the transcriptomes of the 16 samples were subjected to clustering analysis. A plot of principle components 1 and 2 (accounting for 99% of the variability within the samples) clearly divides the samples into two sets along the X and Y axes, with only sample 87 as an outlier (yellow box in left cluster). To the left are the vascular samples from the E18.5 mice; versus all the non-vasculature samples (bar #87) from the E13 mice are to the right. Notably, the samples to the bottom right most corner, comprising samples from 3 sub-regions of neural crest cells, have the lowest overall array coverage and this clustering may be due to that fact. For further analysis, only 12 sampled that successfully pass all QC and have %present > 4% were included in the analysis.

Table 8.2: Expression of Hox genes in single cell samples from the whole transcriptome analysis study. Hox expression from microarray indicates a post-otic or cervical origin of the samples.

		Hoxb1	Hoxd1	Hoxa2	Hoxa3	Hoxa4	Hoxb4	Hoxd4	Hoxc6	Hoxb6	Hoxb7	Hoxc8	Hoxd8	Hoxb9	Hoxc13
E18.5	4_Mesodermal Vasculature							x							
	11_Mesodermal Vasculature								x			x			
	31_NC Vasculature				x				x	x			x		
	19_Meninges				x	x									
	27_Meninges						x				x				x
E13	87_Pre-Foramen Magnum			x											x
	18_Pre-Foramen Magnum														
	80 _Clivus_Pharyngeal Constrictors	x	x												
	39_PCF	x													
	45_PCF														
	48_PCF								x		x				
	24_Loose PCF Mesenchyme						x								

Table 8.3: Expression of genes in the LTBP pathways in single cell samples from the whole transcriptome analysis study. The LTBP pathway is active in 4/5 of the vasculature samples and one sample from the loose condensation surrounding the posterior cranial fossa, which may later differentiate into vasculature. P, present; A, absent.

		E18.5 *Wnt1*-cre x XZ-DR					E13 *Wnt1*-cre x ROSA26LacZ						
Probe Set ID	Gene Symbol	4_Meso Vasc	11_Meso Vasc	31_NC Vasc	19_Meninges	27_Meninges	24_Loose PCF Mes	39_PCF	45_PCF	48_PCF	87_ForMag	18_ForMag	80 _Cli/Ph
1438312_s_at	Ltbp3	P	P	P	A	P	P	A	A	A	A	A	A
1418049_at	Ltbp3	A	P	A	A	P	A	A	A	A	A	A	A
1418061_at	Ltbp2	A	A	A	A	P	A	A	A	A	A	A	A
1436665_a_at	Ltbp4	A	A	A	A	A	A	A	A	A	A	A	A
1448870_at	Ltbp1	A	A	A	A	A	A	A	A	A	A	A	A

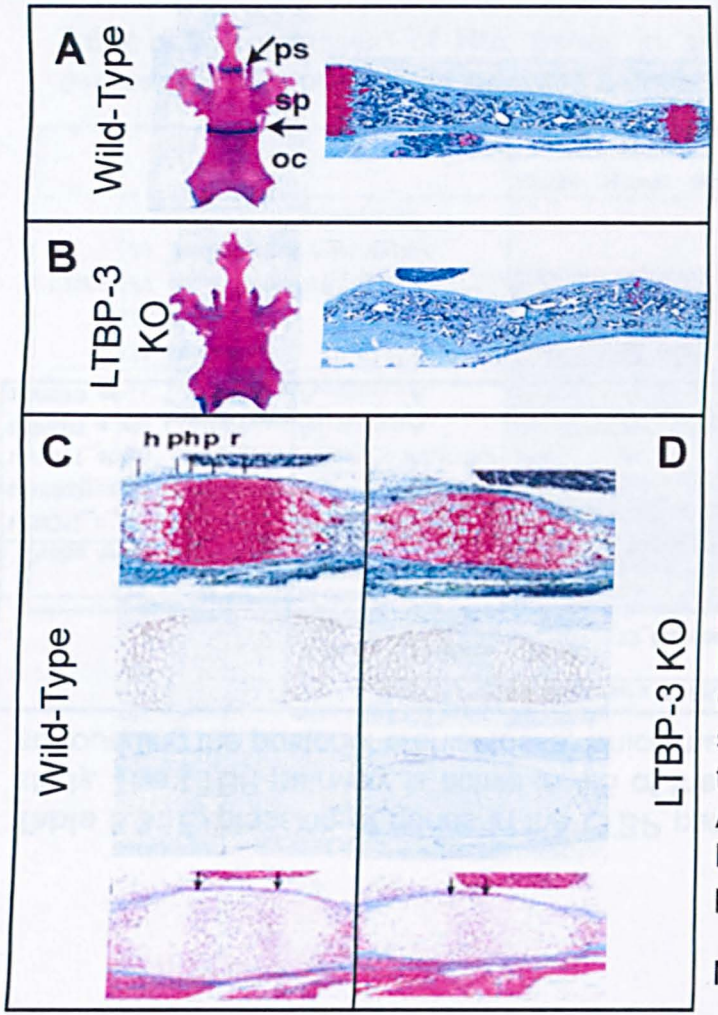

Figure 8.10: The effect of the LTBP pathway on the basoccipital-basisphenoid synchrondroses

Alcian blue (cartilage) and alizarin red (bone) histological preparations of wild-type (**A,C**) and LTBP-3 null mice (**B,D**). In **A-B** the left image is the cranial base of animals 3 weeks after birth, where LTBP-knockout mice show premature fusion of the synchondroses indicated in the wildtype between the occipital (oc), sphenoid (sp) and pre-sphenoid (ps) bones. The right images in **A-B** show sagittal sections through the clivus at 3 days after birth; the LTBP-3 knockout mutant (**B**) has abnormal ossification in the skull base, precocious ossification is indicated by an advanced zone of vascularised (hypertrophic) chondrocytes, and an abnormal, narrow synchondrosis.

C-D. Differences in the ossification of the wild-type and LTBP-3 mutant are evident at 1.5 days after birth. C & D top to bottom: hematoxylin, Safranin O and Fast green stain, immuno stain for Collagen X, immuno stain for Collagen II, and masson's trichrome staining for bone. The mutant has advanced bone fronts compared to the control, as well as a wider zone of hypertrophic chondrocytes. Arrows indicate fronts of basioccipital and basosphenoid bones. **h**, hypertrophic chondrocyte zone; **r**, resting chondrocyte zone; **p**, proliferating chondrocyte zone; **ph**, prehypertrophic chondrocyte zone.

Modified from *Dabovich et al.* 2002.

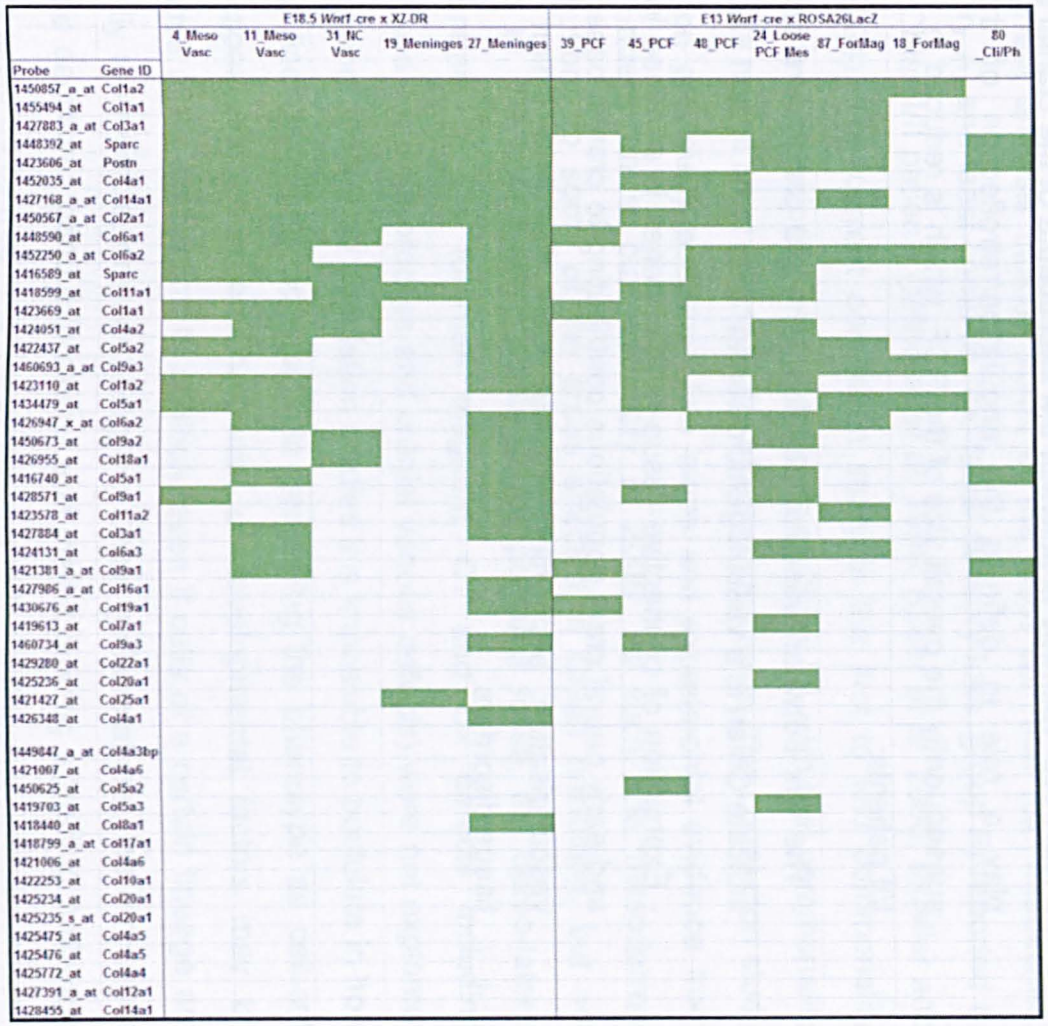

Table 8.4: Expression of collagens in the single cell samples from the transcriptome analysis study. All samples, regardless of lineage origin or fate are enriched for collagen expression. Present calls indicated with green box, absent in white.

8.3 Summary of findings

- Single cell laser capture microdissection followed by microarray analysis can be used to successfully probe cellular transcriptomes with the newly optimised protocol;

- Cell fate may correlate more significantly with gene expression than lineage;

- Whole transcriptome analyses cannot differentiate between neural crest and mesodermal-derived vasculature in the cranial base;

- Among the anlagen to the bone structures in the cranial base, whole transcriptome analyses may indicate there are regional differences among sub-populations of neural crest cells;

- The LTBP pathway is active in the vasculature of the cranial base and may play a role in defining the angulation/retroflection of the clivus and subsequently the overall size of the PCF, which is reduced in 100% of Chiari I/II patients;

- The link between vascular development and pre-mature ossification may indicate Chiari is a vasculogenic disorder;

- Expression of connective tissue-related genes is enriched in both the late and early neural crest populations contributing to cranial base formation and vascularisation, supporting previous work that links Chiari to connective tissue disorders.

9. Discussion & concluding remarks on Chiari as a neurocristopathy

9.1 Establishing Chiari as a neurocristopathy

Correlating the symptoms of Chiari with the pathognomic structure giving rise to them, and establishing if these structures are of neural crest origin was our first proxy for linking Chiari as a neurocristopathy. The symptoms included in the analysis were those associated with the pathognomic deficiencies most widely reported in Chiari, not based on actual symptom prevalence as absolute prevalence is hard to determine (given symptoms are self-reported by patients, the majority of Chiari patients are not included in large scale studies, and differences among the studies' methods may make comparisons among them difficult). As a result, the symptoms that fall within the current analysis include some of the most common (ex: headaches, category A) and least common (ex: facial sensory loss, group F) reported to effect Chiari I/II patients (Milhorat *et al.* 1999; Speer *et al.* 2000; Mueller and Oro 2004). The current correlation study is the first to find commonality among the vast majority of the symptoms of Chiari I/II, with that commonality being the neural crest origins of the affected structures. The correlation study relied on previously published fate maps and experimental evidence from work undertaken in our laboratory in 2005; as such, the mesodermal contributions to some of the areas affected in Chiari (including, but not limited to, the lateral components of the posterior fossa, the dorso-lateral components of the foramen magnum, C1 and C2 defects including retroflexed odontoid process and cranial venous defects) were not explored. Furthermore, based on correlation studies it is impossible to postulate in how far the lineage origins contribute to generating the phenotype as cell-cell interactions and other environmental or developmental factors may be causative of the complaint. In addition, even if cells of a certain lineage are primarily responsible for generating the Chiari malformations, the erroneous cell-fate decisions, gene expression and malfunctioning signalling pathways are not explored by mapping the symptoms to the pathognomic deficiencies.

One pathway that has developmental significance and may be involved in generating the Chiari phenotype was explored: the sonic hedgehog (SHH) pathway. A transgenic strain of mouse was obtained by our laboratory (gift of T. McMahon) in which the smoothened (SMO) receptor was ablated in a lineage-specific manner in neural crest cells. This transgenic mouse replicated one aspect of the Chiari phenotype, namely the loss of the attachment point of the pre-vertebral ligament. The fact that the other pathological features of Chiari were not recapitulated in the mutant indicates a variety of signalling pathways are likely to play a role in the Chiari I/II malformations. This complexity is reflected in the fact that no single gene has been linked to Chiari, which contrasts with several other cranio-facial anomalies that share some symptoms of Chiari, which can be mapped to mutations in a single gene, such as Apert's syndrome (FGFR2 mutations (Wilkie *et al.* 1995; Lomri *et al.* 1998)), Cleidocranial dysphagia (Runx2 mutations (Mundlos *et al.* 1997; Baumert *et al.* 2005)), Craniosynostosis (MSX2 mutations (Jabs *et al.* 1993)), Saethre-Chotzen syndrome (TWIST1 mutations (el Ghouzzi *et al.* 1997; Howard *et al.* 1997)), and Pfeiffer syndrome (FGFR1 or FGFR2 mutations (Muenke *et al.* 1994; Tartaglia *et al.* 1997)). Accepting that Chiari is likely to be a syndrome of compounding factors, further analyses focused on defining the precise anatomical defects of the malformations.

9.2 Homing in on the anatomical defects of Chiari I/II

To refine the current study of Chiari I/II and establish if it is, indeed, a neurocristopathy candidate, I examined the neural crest contribution to the precise anatomical defects primarily responsible for the characteristic cerebellar herniation in the syndrome. Previous studies have confirmed that the size of the brain is not accountable for the over-crowding resulting in the herniation, but rather this is the fault of a reduced overall volume (on average 40%) of the posterior cranial fossa (PCF) housing the cerebellum (Milhorat *et al.* 1999). Diminished PCF volume is attributed to length of the supraocciput and clivus (Koyanagi and Houkin 2010) and basioccipital hypoplasia (Noudel

et al. 2009). Therefore, the shortened cranial base and its reduced retroflection is likely caused by premature stenosis of the spheno-occipital synchondrosis, which usually closes after the first decade of life (from 9 years old onwards) and may explain the late onset of Chiari I/II. A key factor in establishing the timing and mechanics of endochondral ossification is the vasculogenesis of the anlagen. To our surprise, a late contribution of the neural crest to the vasculature of the endochondral areas of the cranial base affected in Chiari I/II has been observed. The neural crest derived vasculature was found in elements of the clivus, and also in the supraocciput (whose height is reduced in Chiari I and affects tentorial angle), the occipital protuberance, and the atlas/axis (which is responsible for the retroflexed odontoid process in Chiari I). Intriguingly, there was no neural crest contribution to the vasculature of the exoccipital condyle at the stage currently examined (E18.5). Our results may indicate that the primary anatomical defects of Chiari are caused by a hyper-ossification whereby the invasive neural crest contributes to precocious vascularisation of the endochondral bone resulting in early maturation of the bone leading to the phenotypical malformations. Alternatively, if vascular invasion is stunted a hypo-ossification phenotype would result. Because only a single time-point was sampled, it cannot be discerned if the neural crest vasculature arises from adjacent structures (which are of mixed neural crest and mesodermal origins) and develops concurrently with the mesodermal vasculature or are a late migrating population, although the lack of a neural crest contribution to the vasculature of these structures in previously published studies of earlier developmental stages indicates the latter possibility.

This finding is intriguing as it shows there is a striking similarity between the blood vessel supply in dermal bones (See Part I) and that of endochondral vasculature in the cranial base. As endochondral bone is phylogenetically younger than dermal bone, it is possible that programmes of vasculogenesis involving neural crest cells were co-opted in evolution into this new ossification process. Moreover, it acts as a cautionary tale regarding the time window of fate maps as it is likely that many more human diseases that have previously been characterized as mesodermal in origin might actually be

neurocristopathies due to the invasive nature of these populations. Notably neural crest cells appear to preferentially invade at points where they also act as attachment regions of musculature, i.e. at regions of pharyngeal constrictors (of the clivus region) and dorsally in the interparietal region surrounding the occipital protuberance that acts as attachment region of the trapezius (Matsuoka *et al.* 2005).

In addition to a reduced PCF volume, Chiari I/II is characterised by a reduction in volume and flow of cerebrospinal fluid. Results of our lineage analysis have revealed that neural crest-derived cells comprise the meninges of the cortex and medulla, as well as the arachnoids of these regions and the spinal cord. Conversely, the cerebellar meninx are mesodermal in origin. The finding that meninges of the cerebellum are not neural crest, but meninx of forebrain and hindbrain are, is at odds with previous findings of Etchevers and Couly. This warrants additional exploration into previously established fate maps, formulated in chick, which may not accurately reflect the lineage contributions to mammalian vasculature.

Neural crest cells are also found to contribute to the vasculature of the cortex, supplying both the endothelia and the pericytes of some vessels. The current study also confirmed that the vasculature of the cranial base is a mosaic of both neural crest and mesodermal origins. The neural crest meninges and vasculature, if aberrant in any way (ex: compliance, fluid skew, etc.) could be responsible for the sub-occipital headaches reportedly experienced by up to 98% of Chiari I/II patients (Mueller and Oro 2004). Conceptually, increased intracranial pressure (ICP) due to PCF over-crowding could also be a contributing factor to the headaches; however mechanical relief (via decompression surgery) does not always ameliorate the condition (personal communication, Conquer Chiari Research Conference 2008 & 2010). There is a highly variable response to decompression surgery, and continual headaches after surgery could result from an overabundance of pain receptors within the meninges involved in pain sensation and/or the mechanical composition and architecture of the meninges and cranial vasculature.

The discovery of the contribution of the neural crest to the vasculature of the cranial base further indicates Chiari I/II could be a neurocristopathy and may even be a vasculogenic disorder. However, these studies do not shed light on the exact gene expression and pathways involved in generating the cranial base and to explore this, the transcriptomes of the anlagen to the structures affected in Chiari I/II were probed.

9.3 Single-cell transcriptome analysis

Single-cell transcriptome analyses were conducted on the neural crest cells in areas affected in the Chiari I/II malformations at the time of cell-fate decisions (E13 in the mouse) including: anlagen to the clivus/pharyngeal constrictors, the mesenchymal condensation precursors to the posterior cranial fossa and the foramen magnum. Additional transcriptome analyses included the E18.5 neural crest meninges and the mature vasculature in the cranial base to determine if there are differences in the transcriptomes of neural crest versus mesodermal vasculature.

The protocol used was generated in a 2003 study by Tietjen *et al.* and required extensive optimisation for use in the current analyses (see Technical Appendix 11.2). While I am confident the optimised protocol is now sufficient for studies of this nature (and produces similar array coverage to previously published studies (Kamme *et al.* 2003; Tietjen *et al.* 2003)), following the optimisation and inclusion of new quality controls there were not enough samples in each experimental group to generate statistically significant differential gene expression profiles. The data generated in the current study was, instead, used to explore crucial pathways expressed in the majority of samples that may be linked to Chiari. Differential analysis confirmed the cells from E18.5 were all vascular in nature and some cells from the PCF anlagen and one sample from the Clivus_Pharyngeal Constrictor region may also have been vascular precursors (see Technical Appendix 11.2). Clustering analysis indicated that the transcriptomes of the vasculature samples are more similar to one another than they are to the cells from the mesenchymal condensations; although this may also reflect

the cells from E13 being less terminally differentiated than the vasculature samples. The clustering analysis was not biased by array coverage or hybridisation efficiency as the final quality controls removed samples that may have had low array intensity biases, low gene expression or poor array coverage (under 4% present hits) (see Technical Appendix 11.2). The principle component clustering in the final 12 samples, therefore, likely reflects genuine differences in the transcriptomes of the single cells profiled.

The majority of the E18.5 vasculature (4/5 samples) expressed genes in the LTBP pathway; this was true for samples from the meninges, neural crest vasculature and mesodermal vasculature. The LTBP pathway was also active in a cell captured in the loose mesenchyme surrounding the cerebellum at E13, which could indicate this cell had a vascular fate. The LTBP pathway was not active in the bone-precursor cells from E13, which is unsurprising as the LTBP pathway plays a role in endochondral bone maturation mediated by vascular invasion and chondrocyte hypertrophy.

Interestingly, all the cells profiled (from all regions and time-points) were enriched for expression of a multitude of collagens. This correlates with previous assertions that Chiari links to connective tissue disorders (Milhorat *et al.* 2007). Given the importance of collagens in providing structural support and scaffolding for bone development, it is likely that connective tissue defects could play a role in the hyper and hypo-ossification in Chiari I/II, as well as in compliance issues of the vasculature.

Future studies that introduce additional samples into the experimental cohort would lead to the ability to generate statistically significant gene expression profiles of the regions of interest. Notably, in light of the concurrent study on dermal bone development, described in Part I, it would be prudent in the future to further refine the regions from which cells are isolated as mesenchymal condensations and bone formation may be more complex than previously anticipated.

9.4 Conclusion and future perspective

Results presented here support classifying Chiari as a neurocristopathy and confirm the areas involved, both skeletal and vasculature, are neural crest in origin. Several anatomical regions previously thought to be void of neural crest have been shown to be of mixed neural crest and mesodermal origins and many include a late invasion of neural crest vasculature. The defects giving rise to Chiari I/II are likely to occur in only subsets of cell populations, given that the vast majority of the neural crest derived tissues (and the adjacent mesoderm) are unaffected. In fact, a unifying component of the Chiari malformation is it seems to primarily involve tissues of mixed origins and/or those whose lineage is still being elucidated. At this stage it is impossible for us to postulate which is more important: the initial cell fate decisions of the neural crest cells in the regions affected, or the contributions of the newly-identified late invasion of the neural crest. The invasive neural crest may be responsible for the maturation of the bones at the cranial base, but in order to elucidate how this process occurs a further time-course analysis of cranial base vascularisation is warranted. Additionally, single-cell analysis of the neural crest vasculature in the endochondral bones of the cranial base is feasible if cell isolation is accomplished via dissociation rather than laser capture. Dissociation of tissues to isolate cells may also be less disruptive to RNA than the laser capture process.

Finally, while there are no mouse models of Chiari I/II, Marin-Padilla and colleagues demonstrated that retisnoic acid (RA) shock (via injecion of high doses of vitamin A) at day E8 in hamster gestation resulted in offspring with Chiari-like phenotypes, including: cerebellar herniation, a flattened cranial base, a shortened basioccipital, problems with the odontoid process and what today would be called tethered cord syndrome (Marin-Padilla and Marin-Padilla 1981). Further studies in mice have revealed that RA shock to E8.5-9.5 mice will result in the same syndromic features (Kessel 1992). Retinoic acid signalling is, therefore, likely to play a part in developing the Chiari phenotype and RA shock and the resulting retention of Froriep's ganglion (with their high volume of nociceptive neurons) may be responsible for the hypersensitivity and chronic headaches of Chiari patients (Goldstein *et al.* 1996; Fanarraga *et al.* 1997). A cursory examination of the single cell

samples from our transcriptome analysis reveals that 11/12 of the final samples in the experimental cohort express genes associated with retinoic acid signalling (Table 9.1). Future work correlating the teratogenic action of RA with the development of the Chiari phenotype in mice (via RA shock at defined developmental time-points and a time-course analysis of the malformation development) could elucidate the roll of retinoic acid signalling in the Chiari malformations and may also clarify if early cell fate decisions or late NC invasion is more important to developing the phenotype.

Table 9.1: Expression of genes associated with retinoic acid signalling in the single cell transcriptome analysis study. P, present; A, absent.

	E18.5 *Wnt1*-cre x XZ-DR					E13 *Wnt1*-cre x ROSA26LacZ						
	4_Meso Vasc	11_Meso Vasc	31_NC Vasc	19_Meninges	27_Meninges	39_PCF	45_PCF	48_PCF	24_Loose PCF Mes	87_ForMag	18_ForMag	80_Cli/Ph
Gene ID												
Rbp1	P	P	P	P	P	A	A	A	P	P	A	P
Aldh2	A	A	A	A	A	A	A	A	A	A	A	A
Crabp1	A	A	A	A	A	A	A	A	P	A	A	A
Rxra	A	A	A	A	A	A	A	A	P	A	A	M
Rxrb	P	A	A	A	A	A	P	A	A	A	A	A
Rarres2	A	P	A	A	P	A	A	A	A	A	A	A
Parp1	A	A	P	A	A	A	A	A	M	A	A	A
Parp2	A	A	P	A	A	A	P	A	A	A	A	A
Parp3	P	P	A	A	A	A	A	A	P	A	A	A
Parp4	A	A	A	A	A	P	A	A	A	A	A	A
Parp9	A	A	A	A	A	A	A	A	A	A	P	A
Parp14	A	A	A	A	A	A	A	A	A	A	A	P

10.1 General Molecular Biology

10.1.1 Genomic DNA Preparation: Genomic DNA (gDNA) for polymerase chain reactions (PCR) was purified from cells (~5 x 10^6 cells) and tissues (maximum 25 mg) using a DNeasy Blood & Tissue Kit (Qiagen) according to the manufacturer's instructions with no modifications. gDNA was eluted in 30-50 µL under low salt conditions and sample concentrations were measured using a NanoDrop ND-1000 Spectrophotometer, operated by ND-1000 V3.6.0 software.

10.1.2 Standard PCR (template <2 kb): All probes and amplifications of target DNA/cDNA described herein were amplified via gradient PCR in a Mastercycler Gradient PCR machine (Eppendorf) using a final volume of 20 µL, comprising 25 ng/µL genomic DNA or 10 pg/µL plasmid DNA combined with a master mix of: 0.125 U/µL AmpliTaq® DNA Polymerase, 1x PCR Buffer II, 2.5 mM $MgCl_2$ (Applied Biosystems), 0.5 mM dNTP (Roche), 0.5 µM primers. Reactions containing gDNA were supplemented with 10% DMSO (Sigma). Thin-walled 0.2 mL tube trips (Helena Biosciences) were used for all PCR reactions.

Standard PCR protocol was as follows: initial denaturing at 94°C for 2 min, followed by 30 cycles of [30 sec denaturation at 94°C, 30 sec of annealing at 60°C +/- 10-15°C, 1 min per kb extension at 72°C] and a final extension of 10 min at 72°C, followed by a 4°C hold until analysis.

Note: Annealing temperatures were modified if the optimal primer annealing temperature, as defined by Primer-Blast, is beyond the 59-61°C range.

10.1.3 Visualising DNA, RNA and cDNA: All PCR products, plasmid digests and DNA smears were visualised on 0.8-2% agarose gels (Helena

Biosciences or SeaKem) in 1xTAE supplemented with 6% Ethidiumbromide (Sigma) via the addition of 1xDNA loading dye. Gels were run at 80-100V in a horizontal gel electrophoresis system (VWR International).

Fragments requiring purification were run on 0.8-1.5% high quality agarose (Seakam) gels, also in 1xTAE and 6% Ethidiumbromide, run at 80V until proper separation was achieved.

10.1.4 Gel Extraction: DNA fragments were isolated from high quality SeaKem GTG Agarose gels using a scalpel under UV Light on a High Performance UV TransIlluminator. The fragment was purified using a QIAquick Gel Extraction Kit (Qiagen) according to the manufacturer's instructions with no modifications.

10.1.5 Ladder Marker: Sizing of nucleotide fragments was based on a ladder marker with the final concentration 0.2 mg/mL λ*HindIII* DNA (Fermentas) and φ174*Bsu*R1 DNA (Fermentas) as illustrated below:

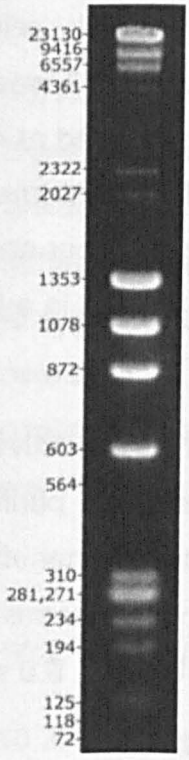

10.1.6 Sequence Alignment, Visualisation and Annotation: Comparative sequence alignments were performed using MegAlign from the Lasergene® software package (DNAstar). Sequence visualisation and annotation were performed using SeqBuilder (DNAstar).

10.1.7 Primer Design: Primers were designed using Primer-BLAST software (NCBI), with *mus musculus* as the reference species. Input sequences were entered as FASTA files, optimal product size was chosen, and melting temperatures were set (minimum 57°C, optimal 60°C, maximum 63°C). The program automatically generates the most common binding from BLAST results and primers were selected such that they were exclusive to the target of interest and would not yield ulterior products (especially when being used with genomic DNA).

10.1.8 Plasmid Propagation

10.1.8a Plasmid Propagation: Re-growth of plasmids was achieved in chemically competent One Shot ® TOP10 E.Coli cells (Invitrogen C4040-10). Tranformations were performed with the following protocol: cells were thawed from -80°C on ice for 20 min then 2-3 µL of plasmid DNA was added, cells were returned to ice for a further 20 min then heat shocked at 42°C for 30 sec, 200 µL SOC was added and cells were immediately returned to ice for a minimum of 5 min. Cells were shaken horizontally for 1 hour and plated on LB/Amp selective plates. Colonies formed overnight at 37°C in a bacterial incubator (Sanyo).

Single colonies were isolated and grown in 4-6 mL of LB selective media, incubated at 37°C overnight with shaking. Plasmids were purified with Qiagen Miniprep kits (Qiagen, 27106) according to the manufacturer's protocol and the concentration of the isolated plasmid was determined on a NanoDrop ND-1000 Spectrophotometer operating ND-1000 V3. 6.0 software.

10.1.8b Modifications for TOPO Plasmids were as follows: the cloning reaction consisted of 2 µL PCR fragment (50-100 ng DNA), 1 µL TOPO vector, 1 µL salt solution (1.2M NaCl, 0.06M $MgCL_2$), and 2 µL dH2O; this was mixed gently and incubated for 5-15 min (depending on the length of the insert) at 37°C. The transformed cells were plated onto LB-AMP plates augmented with 100 µL of 20 mg/mL X-gal (plated 30 min prior to the addition of cells). Successful TOPO transformations resulted in white colonies used for further analysis.

10.1.9 Sequencing Plasmids: Sequencing was performed at Warwick University by the Molecular Biology Service of the School of Life Sciences. Typically 200 – 500 ng of DNA was combined with 5.5 pmol of a single sequencing primer (see below) and brought to a total volume of 10 µL using dH2O. Samples were run on a 3130x Genetic Analyser (Applied Biosystems) operating BigDye Terminator Version 3.1.

Sequencing Primers, Name 5'-3'
M13Fwd: tgtaaaacgacggccagt
M13Rev: caggaaacagctatgacc

10.1.10 Restriction Digests: Restriction enzyme mediated plasmid digestions were achieved using enzymes purchased from New England Biolabs. Standard digests consisted of: 3 µg DNA plasmid, 3 µl restriction buffer (as recommended by manufacturer), 1.5 µL restriction enzyme, dH20 to a total volume of 30 µL. Reactions were incubated in a bacterial incubator overnight at 37C°. The digestion (complete and not over-fragmented) was confirmed using gel electrophoresis (section 10.1.3). Linearised plasmids were then column purified (QIAquick PCR Purification Kit).

10.2. Animal Work

10.2.1 Supply & Husbandry: Transgenic (*Wnt1*-Cre, ROSAEYFP, ROSALacZ, Hand2, XZ-DR) and wild-type (SV129/B6 background) mice

were housed/maintained by the BSU facilities at Warwick University. Transgenic and wild type mice were obtained from projects with authority to breed animals of that type and to provide them for use on other projects in accordance with current legislation in the UK (Animals Scientific Procedures Act 1986). Embryos isolated for analysis at the stages indicated were collected after timed matings in which the date of a positive plug was taken as E0. Genetically modified strains are established lines; no transgenic lines were generated as part of this study. Transgenic alleles are designated with a "-"; conversely, wildtype alleles are designated by "+".

10.2.2 Generation of Transgenic Animals

10.2.2.1 Generation of transegenic animals, *Wnt1*-Cre x ROSA26LacZ: Neural crest cells were permanently labelled utilising the well-characterised *Wnt-1* dorsal neural tube enhancer region (Rowitch 1998). The *Wnt-1* enhancer confers transgene expression on the entire dorsal neural tube neural crest precursor population, and their subsequent progeny (with the exception of NC-cells from rhombomere I, McMahon & Koentges, unpublished). *Wnt1*-Cre mice were crossed with Cre-reporter mice carrying transgenic floxed resistance-pA cassettes in front of LacZ under the control of ROSA26; this combination yields offspring in which the floxed cassettes are subject to Cre-mediated excision. The neural crest cells of these *Wnt1*-Cre x R26-LacZ offspring can be visualised with either X-gal staining (LacZ), or labelled with an anti-βGal/LacZ antibody. *Wnt1*-Cre mice were obtained from the Jackson Laboratory (USA) and crossed with the ROSA26 reporter mice also obtained from Jackson Laboratory (USA).

10.2.2.2 Generation of transgenic animals, *Hand2*-Cre x ROSA26LacZ: *Hand2*-Cre mice express Cre-recombinase under the control of a 7kb upstream region of Hand2 (Ruest *et al.* 2003). Specimen and live mice were provided by D. Clouthier. *Hand2*-Cre mice were crossed with ROSALacz mice to generate the *Hand2*-Cre x ROSA26LacZ line. Cells in which Cre-

mediated excision has taken place can be labelled with an anti-β-Gal antibody for visualisation.

10.2.2.3 Generation of conditional knockout, *Hand2*$^{fl/fl}$ x *Wnt1*-Cre-R26Lacz, bred and maintained by H. Yanigasawa at the University of Texas (Dallas): Hand2 was specifically deleted in neural crest cells using the following method: briefly, loxP sites were inserted into the Hand2 allele flanking exon 1 in the 5' UTR (Hendershot *et al.* 2007). *Hand2*$^{fl/fl}$ mice display a normal phenotype and have normal Hand2 expression, validated by qRT-PCR (Hendershot *et al.* 2008). Excision of Hand2 and visualisation of the cells in which the excision has taken place, is achieved by crossing the *Hand*$^{2fl/fl}$ mice with hemizygous *Wnt1*-Cre and homozygous ROSA26LacZ mice. Specimen (torso) and slides (cranio-facial) of *Hand2*$^{fl/fl}$ x *Wnt1*-Cre$^{+/-}$ x R26Lacz$^{+/-}$ mice were provided by H. Yanigasawa and D. Clouthier.

10.2.2.4 Generation of targeted deletion of Hand2 BA enhancer, bred and maintained by D. Clouthier at the University of Colorado: Hand2 expression in the branchial arches requires the Endothelin-1 (ET-1) enhancer. This 208 bp enhancer was deleted using homologous recombination (Yanigasawa *et al.* 2003). The enhancer lies within a 754 bp *XHOI-BamHI* fragment, which was replaced with a loxP-flanked *neo* cassette. Cre-mediated excision results in *BAenh*$^{-/-}$ mice. Specimens provided by D. Clouthier.

10.2.2.5 Generation of XZ-DR, bred and maintained by X. Zhang, University of Warwick. The XZ-DR transgenic is a Cre-reporter strain of mice generated by Dr Xintao Zhang. XZ-DR mice carry transgenic floxed resistance-pA cassettes in front of GFP under the control of the Ubiquitin C promoter. *Wnt1-Cre* mice were crossed with the XZ-DR-reporter yielding offspring in which the floxed cassettes are subject to Cre-mediated excision. The neural crest cells of these *Wnt1*-Cre x XZ-DR offspring are permanently labelled

and can be directly visualised under fluorescence or by labelling with an anti-GFP antibody. Specimen that had been isolated, and embedded fresh (no fixation treatment) were provided by X. Zhang.

10.2.3 Genotyping: Genotyping of transgenic animals was performed using PCR on tissue isolated via genomic DNA isolation (see 10.1.1 above) of embryonic limbs and/or tails, or via HotSHOT genomic DNA extraction (see 10.2.3.1 below) from ear punches or embryonic materials. PCRs were performed using specific primers and protocols, as described below.

10.2.3.1a HotSHOT Genomic DNA Extraction: Genomic DNA was isolated from single ear punches as follows (Truett *et al.* 2000): 75 µL of alkaline HotSHOTreagent (25 mM NaOH, 0.2 mM Disodium EDTA, pH12) is added directly to the tissue and incubated at 95°C for 10-60 min with occasional vortexing, until the tissue is dissociated; 75 µL of Neutralising reagent (40 mM Tris-HCL (Sigma), pH 5) is added directly to the sample and temperature is reduced to 4°C for 1 hour. This preparation was then stored at -20°C until it was used directly for PCR reactions (1-5 µL per 20 µL reaction).

10.2.3.1b HotSHOT Genomic DNA Extraction From Embryonic Materials: Genomic DNA isolated from embryonic materials (including limbs and tails of embryonic mice from stages E10-E18) were performed as above with the following modifications: 75-200 µL of HotSHOT reagent is added to the tissue (as appropriate for the tissue volume); tissue is boiled or heated at 95°C for >1 hour until the majority of the tissue has dissolved; 1 volume of neutralising reagent is added and the solution is chilled at 4°C for 1 hour. DNA is precipitated from the solution as follows: 1/10 volume 5 M NaCl was added to equalize ionic concentrations; 2 x 100% EtOH (chilled to -20°C) was added and the solution was mixed thoroughly; the mixture was incubated at -20°C for at least one hour then centrifuged at 13,200 rpm for 15-20 min; the supernatant was discarded and the pellet was washed with

200 µL 70% EtOH at -20°C then centrifuged for a further 5 min; the supernatant was discarded and the pellet was air dried in an extraction hood until the pellet was dry and clear; the pellet was resuspended in the desired volume (up to 50 µL) of dH20 (Ultrapure™/GIBCO).

10.2.3.2 PCR for Genotyping: PCR reactions for genotyping were set up as follows in 20 µL total volume: 3-5 µL gDNA isolated using HotSHOT or 250-500 ng gDNA isolated from 1.1; 0.5 mM dNTP (Roche), 0.5 µM Primers; 2.5 mM $MgCL_2$; 1 x PCR Buffer II; 0.125 U/L Amplitaq®; 10% DMSO (Sigma); brought to 20 µL volume using DNAse/RNAse free distilled water (Ultrapure™/GIBCO). Protocol for PCR was as follows: initial denaturation 20 sec at 94°C, N cycles of [denaturation 30 sec at 94°C, annealing 30 sec at X°C [see table below], extension 30 sec at 72°C], followed by a final extension of 10 min at 72°C and a 4°C hold until PCR products are analysed on a 0.8-2% Agarose + 6% Ethidiumbromide gel. All primers for individual genotyping reactions, N number of cycles and annealing temperature X are listed below:

Transgenic Allele	**Primer (Name: 5'-3')**	**X Annealing Temperature**
Wnt1-Cre	IMR0015: CAAATGTTGCTTGTCTGGTG IMR0016: GTCAGTCGAGTGCACAGTTT IMR1398: CCTCTATCGAACAAGCATGCG IMR1399: GCCAATCTATCTGTGACGGC	61°C
Rosa26LacZ	Sor1: AAAGTCGCTCTGAGTTGTTAT Sor2: GCGAAGAGTTTGTCCTCAACC Sor3: GGAGCGGGAGAAATGGATATG	61°C
Rosa26EYFP	Sor1: AAAGTCGCTCTGAGTTGTTAT Sor3: GGAGCGGGAGAAATGGATATG IMR4982: AAGACCGCGAAGAGTTTGTC	68°C

Hand2-Cre	TWCre1: GCTGGTTAGCACCGCAGGTGTAGAG TWCre3:CGCCATCTTCCAGCAGGCGCACC	68°C

Expected Fragment Sizes

Strain	Transgene	Wildtype Allele	Reference
Wnt1-Cre	322 bp	200 bp	Jackson Labs
Rosa26LacZ	~300 bp (Sor1,Sor2)	603 bp (Sor1,Sor3)	Soriano 1999
Rosa26EYFP	320 bp (Sor1,IMR4981)	603 bp (Sor1,Sor3)	Jackson Labs
Hand2-Cre	500 bp		D. Clouthier

10.2.4 Project Licence, *Analysis of the kinetics of dermal bone mineralisation:* Experiments for labelling mineralised bone matrix were undertaken under a new project licence (Home Office reference PPL70/7118) held by K. Jordan. The licence contains one protocol, "Injection of labelling agents," see Section 10.2.4.1 below for details.

10.2.4.1 Injection of Labelling Agents: Animals obtained by continued use were used to map a time-course of bone mineralisation and to track newly synthesised cells within the bone. Concentrations of labelling agents were chosen such that the labelling was expected to be conferred to the dam and her offspring, without any pharmacological side effects (see below).

10.2.4.1a Route: Labelling agents were administered via intraparitoneal injection to mouse dams. Dosages were sufficient to confer the agents to the foetuses to achieve embryonic labelling.

Labelling Agent	Dosage	Reference
Calcein	10 mg/kh	Sun *et al.* 1992
Doxycycline	50 mg/kg	Pautke *et al.* 2005
Xylenol orange	90 mg/kg	Sun *et al.* 1992

10.2.4.1b Labelling Agents and Dosages: Mineralised bone was permanently labelled at 2-3 time-points between E11 and P0 with non-harmful fluorescent dyes including fluorochromes and tetracyclines. Labelling agents were chosen that could be visualised without any treatment to enhance signal in emission areas with non-overlapping spectra such that they could be concomitantly analysed. Dosages were established from literature values, as below, and were prepared in Phosphate Buffered Saline (PBS, 137 mM NaCl, 2.7 mM KCl, 8 mM Na_2HPO_4, 1.4 mM KH_2PO_4, pH 7.4) and sterilised prior to administration.

10.2.4.1c Collection of Specimen and Subsequent Analysis: Specimen subjected to the protocol were terminated via an appropriate Schedule 1 method and the tissues were harvested (no sooner than 3 days after the last injection). Samples were fixed in fresh 4% PFA overnight, embedded in OCT (Optimal Cutting Temperature) media (TissueTek, VWR) and stored at -80°C until cryostectioning. Cryosectioning was performed on OTF 5000 Cyrostat (Bright, UK) at a thickness of 15-17 µM. Samples were counterstained with 1:1000 DAPI (Invitrogen) and 1:100 Rhodamine-Phalloidin-555 (Invitrogen) and Image Acquisition and Analysis were conducted as per details below (see Sections 10.4.4 & 10.4.5).

** **4% PFA Preparation:** 500 mL of 4% PFA stock was prepared as follows: 20 g of PFA was diluted in dH2O, 3-4 drops of 10 N NaOH was added and the solution was heated to 65°C. PBS (tablet form, Sigma) was added to obtain a 1 x PBS solution and the solution was chilled on ice. The pH was confirmed (~7.5) and the solution was aliquoted and maintained at -20°C. Prior to use aliquots were thawed at a temperature not exceeding 37°C.

10.3. Single-Cell Laser Capture Microscopy

10.3.1 Sample Preparation: Embryos from wildtype (SV129/B6), *Wnt1*-Cre +/- x Rosa26LacZ -/- and *Wnt1*-Cre +/- x XZ-DR -/- crosses were isolated at the following time-points after timed-matings: E9.5-10 (SV129/B6), E13 (*Wnt1*-Cre x LacZ), and E18-19 (*Wnt1*-Cre x XZ-DR). Pregnant dams were terminated via Schedule 1 (cervical dislocation) and embryos were dissected from the uterus and placed in ice-cold PBS, their tails were removed for genotyping (see Section 10.2.3) and the embryos were embedded (fresh, no fixation) in the sagittal or coronal orientation in OCT (optimal cutting temperature) mounting media (TissueTek, VWR). Samples were stored at -80°C until such time as they were cryosectioned on an OTF 5000 Cyrostat (Bright, UK) at a thickness of 7 µm onto charged (for immunohistochemistry) or non-charged slides (for laser capture microdissection) (both Superfrost, VWR).

10.3.1.1 Staining Cryosections for Laser Capture Microdissection: Sections for laser capture dissection were stained using the following protocols at room temperature in an extraction hood using fresh reagents in coplin jars. SV129/B6 & *Wnt1*-Cre x LacZ: 70% EtOH 2 min, dH2O rinse, Mayer's Hematoxylin (Sigma) 2 min, dH2O rinse, Scott's Tap Water Substitute (Bluing Reagent) (Sigma) 1 min, 70% EtOH 10 sec, 95% EtOH 10 sec, Eosin Y (Sigma) 20 sec, 95% EtOH 30 sec, 95% EtOH 30 sec, 100% EtOH 1 min (Sigma), 100% EtOH 1 min, Xylene (Sigma) 5 min, Xylene 5 min, air dry 15 min.

XZ-DR: 70% EtOH + 5:1000 DAPI (Invitrogen) 2 min, 95% EtOH 10 sec, 95% EtOH 30 sec, 100% EtOH 1 min, 100% EtOH 1 min, Xylene 5 min, Xylene 5 min, air dry 2 min.

10.3.2 β-Galactagosidase Staining: β-Gal staining of *Wnt1*-Cre x ROSA26LacZ permanently labels all cells in which the Cre-mediated excision has taken place; thereby allowing visualisation of all post-otic neural crest cells and their progeny.

10.3.2.1 Whole Mount β-Gal Staining: Wnt1-Cre+/- x Rosa26LacZ-/- embryos were fixed in freshly prepared 4% buffered PFA on ice for 30 min with shaking, then rinsed twice with PBS. Next the sample was washed for 5 mins at room temperature on a nutator with Solution A (0.1M Phosphate Buffer pH7.4 (Sigma), 2 mM $MgCl_2$ (Sigma), 5 mM EDTA (Sigma)); fresh solution A was then added for a further 25 min. The sample was then shaken for 10 min at room temperature in Solution B (0.1 M Phosphate Buffer pH7.4 (Sigma), 2 mM $MgCl_2$ (Sigma), 0.01% Sodium Desoxyxholate in dH2O (Sigma/GIBCO), 0.02% Nonidet (Sigma). Fresh, pre-warmed Solution B was then added for a further 10 min at 37°C. Solution B was then replaced with freshly prepared Solution C (Solution B supplemented with 5 mM Ferrocyanide ($K_4Fe(CN_6)$) , 5 mM Ferricyanide ($K_3Fe(CN_6)$) and 1 mg/mL X-Gal) and the sample was incubated overnight at 37°C in the dark. The following day, embryos were washed 2 x 10 min with Solution B, pre-warmed to 37°C, then post-fixed in 4% PFA for further storage.

10.3.2.2 Cryosection β-Gal Staining: Cryosections of fresh (un-fixed) sections were fixed in fresh 4% PFA for 10 min at room temperature, rinsed three times with PBS, then subjected to the following serial solutions: Solution A for 2 x 10 min at room temperature; Solution B for 20 min at room temperature; pre-warmed Solution B for 10 min at 37°C; Solution C overnight in the dark at 37°C. The following morning slides were washed in pre-warmed Solution B, 2 x 10 min at 37°C. Slides where rinsed 2 x PBS, post-fixed in 4% PFA for ten minutes, rinsed 2 x PBS and counterstained. Counterstaining consisted of: 2 min in Mayer's Hematoxylin (Sigma), 2 min in Scott's Tap Water Substitute (Bluing Reagent) (Sigma) and mounted in Clarion (Sigma) or Mouwiol aqueous mounting medium.

Embryos and sections that were stained with β-Gal were used for reference of the cellular origins of structures being subjected to LCM and for correlating pathognomic deficiencies with symptoms of Chiari (see below).

10.3.3 Laser Capture Microdissection (LCM): Cells were captured from slides prepared as above using a PixCell II Laser Capture Microdissection microscope as described by the manufacturer; cells were captured onto clean caps from Molecular Devices. Cells were captured using the minimum power and duration necessary to isolate the cells; if necessary (for unusually thick or re-hydrated tissues) modifications from the standard were applied for optimal capturing. The amount of cells per capture was estimated from visualising the cells on the cap (H&E and/or DAPI stain) and the regions being captured were photographically documented.

10.3.4 cDNA Generation (modified from Tiejen *et al.* 2003): Post-capture, a microneedle in an RNAase-free environment was used to seed individually captured cells into thin-walled PCR tubes (Perkin-Elmer) containing 4 µl of ice cold lysis buffer (containing Nonidet P40 (USB), MMLV 1st strand buffer (Fisher), RNAase inhibitor (Applied Bioscience), 50 OD/mL pd(T)24 (Operon) and 12.5 mM each of dATP, dCTP, dGTP, and dTTP (all Fisher)). Cells were lysed at 65°C for 1 min followed by a 5 min room temperature incubation to anneal oligo-dT to RNA. First-strand cDNA synthesis was initiated by adding 6:1 (vol:vol) MMLV (200 U/µL) and AMV (15 U/µL) reverse transcriptases (both Invitrogen) followed by 37°C incubation for 15 min then heat inactivation at 65°C for 10 min. poly(A) was added to the first-strand cDNA product via a tailing buffer (100 U Terminal Transferase (Roche) & TdT buffer (Invitrogen), plus dATP) at 37°C for 15 min, followed by 10 min heat inactivation at 65°C. PCR buffer was then added to sample (containing 2.5 mM MgCl2, 100 µg/mL BSA, 1 mM dNTPs, 0.05% Triton, 5 µG AL1 primer (see table below for sequence) as well as 14 U AmpliTaq (Invitrogen)). PCR amplification was then performed as: 25 cycles of [1 min at 94°C, 2 min at 42°C, 6 min at 72°C with 10 s extension per cycle]. An additional 5 U of Taq

polymerase was added before performing 25 additional PCR cycles (no extension time between cycles). Following first-strand synthesis, 10 uL of cDNA was run on a 1.5% agarose gel for 70 minutes at 80V to visualise the smear of DNA from 0.4 - 1.2 kB, confirming the success of the reaction.

Initial cDNA amplification yields approx 10–20 µg of cDNA from RNA of individual cells; re-amplification of 2.5-5 µL of each PCR-purified cDNA product is then undertaken (reaction contains 1-5 µL original cDNA plus 100 µL PCR mix: 2.5 mM $MgCl_2$, 0.2 mM dNTPs, 5 U AmpliTaq, and 5 µg AL1 primer) with 30 cycles of [1 min 30 sec at 94°C, 2 min at 42°C, 3 min at 72°C]. Samples are run in triplicate and the PCR product is purified (Qiagen kit according to manufacturer's instructions), eluted in 30 µL and pooled. cDNA concentration is measured using a NanoDrop Spectrophotometer; typical yield from the reamplification reaction is 30 µg.

OLIGOS (from MWGEurofins/Operon)

AL1 primer: ATT GGA TCC AGG CCG CTC TGG ACA AAA TAT GAA TTC (T)24 (0.2 umol scale)

Oligo dT24 (0.2 umol scale)

10.3.5 Southern Hybridisation: Quality of cDNA was checked by Southern blot. 10 µL aliquots of cDNA, ladder marker and a positive control plasmid were run on 2% agarose gels for 2 hours at 80V. The gel was depurinated in a 0.2 N HCL solution for 25-30 mins, denatured in a 0.5 M NaOH + 1.5 M NaCL solution for 25 mins, and neutralised in 1. 5M NaCL+ 0.5 M Tris pH7.5 solution for 25 mins. The gel was blotted on a pre-wet nylon transfer membrane (Hybond N+, Amersham) for 2 hours at constant pressure in a posiblotter (Stratagene). cDNA was UV crosslinked onto the membrane and cDNA transfer was confirmed under UV-light.

The blot was and hybridized with DNA probes for the transgene of interest (LacZ), as well as the ubiquitously expressed gene GAPDH.

10.3.5.1 Generation of Probes for Southern Hybridisation: Probes were designed to correspond to the 3' region of the gene in question, in line with the 3' bias of the cDNA. The probe was generated using 5-9 µL of gel purified DNA fragment (details of plasmids and restriction digest (all New England Biolabs) in table below) brought to a volume of 24 µL using dH2O; 10 µL of random oligonucleotide primers were added to the fragment and boiled for 5 min then put on ice for 3-5 min; following chilling, 10 µL of 5X Primer buffer was added and the solution was moved to the radioactivity suite.

In the radioactivity suite, ~250 ng of cDNA was radioactively labelled with 50 µCi of αP^{32} dCTP via Klenow extension with Klenow enzyme (5 U/µL) (Roche). The probe-solution was incubated for 15 min at 37°C, purified on a NucTrap column (pre-wet with 80 µL of 1xSTE solution) in a BETASheild Push column device, and collected in a 1.5 mL Eppendorf tube. Probe labelling efficiency was measured using 1 µL of labelled probe in 7 mL Ecoscint scintillation fluid on a Beckman counter. Probe labelling was considered a success with a count >250,000 cpm. Hybridisation (BUCK) Buffer was generated using Na_2HPO_4, 20% SDS, BSA and dH2O, to which boiled herring sperm DNA (Promega) was added 1:100. The nylon blot was pre-hybridised in native BUCK Buffer (no hot probe) for 30-60 min, after which the probe was boiled for 2-5 min and added to the Hyb solution in a final concentration of $1\text{-}2x10^6$ cpm/mL. The membrane was hybridised with the hot probe overnight at normal stringency conditions (60°C). The next morning the nylon membrane was washed 2 x 20 min with the wash solution (0.5% SDS, 0.05xSSC in dH2O) at the hybridisation temperature. The membrane was stored on x-ray film (Kodak Fujifilm) and was exposed for one night to one week in an x-ray cassette at -80°C, after which the film was developed.

Gene	Primers, Name: 5' - 3'	Plasmid	RE for Digest
LacZ	1(Fwd):TTCAACATCAGCCGCTACAG 4(Rev):GCGGTTGGAATAATAGCGAG	P128, pCRII TOPO	EcoRI

GAPDH	N/A	pCRII TOPO, Gift from K. Vance	EcoRI

10.3.6 PCR: The presence of several genes in the cDNA was confirmed via PCR, conducted as in Section 10.1.2. Primers were designed as in Section 1.7. Genes and their primers are detailed below.

Gene	Forward, Name: 5'-3'	Reverse, Name: 5'-3'
LacZ	1:TTCAACATCAGCCGCTACAG	2: TTTCCTTACGCGAAATAC GG
	3:TTCAACATCAGCCGCTACAG	4:GCGGTTGGAATAATAGCGAG
	6:CCAGCTGGCAGTTCAGGCC AATCC	7:AACGATCGCCAGTTCTGTAT GAACG
Twist	1:GCTGAGCAAGATTCAGACCC	2:TTCTTCGTCAAAAAGTGGGG
	3:AATTCACAAGAATCAGGGCG	4:CAGTTTGATCCCAGCGTTTT
Tlx	1:GTGACACCAGGAGGGACAGT	2:ACTCCACCAAAATCACCAGC
GAPDH	Fwd: CTTCACCACCATGGAGAAGGCC	Rev: GTGAGGGAGATGCTCAG TGTTG

10.3.7 qPCR: To evaluate the internal control, GAPDH, qPCR was carried out on an ABI PRISM 7000 Sequence Detection System, operating ABI Prism 7000 software (both Applied Biosystems). PCR reactions consisted of: 1x TaqMan Gene Expression Master Mix (Applied Biosystems), 1x mouse GAPD (GAPDH) Endogenous Control (FAM/MGB Probe, Non-Primer Limited), 2 µL reamplified cDNA, in a total volume of 20 µL. To generate standard curves that cover the same range of amplification as the laser captured samples, serial dilutions of a single, well-characterised sample were analysed, as well as an RT-negative control. All reactions were performed in triplicate. Results were analysed using Microsoft Excel (Microsoft).

10.3.8 Tissue Culture (to isolate control cDNA): All cell culture experiments were carried out using aseptic technique in a Class II Microbiological Safety Cabinet (Walker Safety Cabinets Ltd.). Commercially procured cell lines were maintained in their optimal media supplemented with fetal bovine serum (FBS) at 37°C in a 5% CO_2 humidified Galaxy R Incubator (Wolf Laboratories). Once confluent or at their desired time-point, cells were

washed twice with phosphate buffered saline (PBS) and trypsinised with 1x 0.05% trypsin-EDTA. Cells were incubated at 37°C until rounded and detached then resuspended in 10mL growth medium. Cells suspension was then transferred to a sterile 50mL falcon tube and cells were pelleted at 1000 rpm for 4 min at 21°C. At this point the cell pellet was used to harvest RNA and reverse transcribe cDNA (see 10.5.4.1 below), or for cell passage as follows. For passaging, the cell pellet was re-suspended in growth medium and cultured at an appropriate dilution. Cells for image analysis were grown on fresh, charged slides (VWR); once cells reached their harvest time they were washed twice with PBS and stained using the protocols for immunohistochemistry (see 10.4.2 below).

10.3.8.1 RNA Isolation from Cultured Cells: RNA was isolated from cell lines (approximately $1x10^7$ cells/isolation) using an RNeasy mini kit (Qiagen) according to the manufacturer's instructions, with no modifications. Total RNA was eluted using RNAse/DNAse free water in a volume of 30 µL and concentration was determined using a nanodrop (Section 1.1). RNA was stored at -80°C.

10.3.8.2 cDNA Generation: First strand cDNA was synthesised from total cellular RNA using the SuperScript III First-Strand Synthesis Systems for RT-PCR kit (Invitrogen), according to manufacturer's protocol with no modifications.

10.3.9 Bioanalysis: Prior to microarray analysis, cDNA quality was analysed using a 2100 Bioanalyzer (Agilent Technologies). Samples of whole, unfragmented cDNA, as well as fragmented samples (prior to addition of Biotin) were measured. Samples were prepared with an RNA kit and the output consisted of the fluorescent intensity, the running time, RNA (cDNA) area and RNA (cDNA) concentration. Bioanalyzer traces were used to qualitatively characterise the neat (whole, unfragmented) sample, to quantify the concentration of cDNA hybridised to the microarray chip, and to assess the result of the fragmentation.

10.3.10 Microarray Hybridisation

10.3.10.1 cDNA Fragmentation: Prior to microarray analysis, cells that have passed quality controls (Southern hybridisation, PCR and/or RT-PCR, Bioanalyzer) are fragmented as follows: 15-20 µg of re-amplified, purified cDNA is combined with 10X One-Phor-All Buffer (Amersham) and ~1 U of RQ1 DNAse (Promega) in a total volume of 60 µL. Samples are incubated at 37°C for 13 minutes then heat inactivated at 99°C for 15 minutes, after which 1.5 µL is taken for bioanalysis (see Section 10.3.9).

10.3.10.2 Biotin Labelling: Using the entire 58.5 µL fragmented sample, biotin end-labelling is achieved by adding 1.0 mM Biotin-N6_ddATP (Perkin Elmer), and ~20 U Terminal Transferase (Invitrogen). The sample is incubated at 37°C for 90 minutes then heat inactivated at 65°C for 15 minutes and stored at 4°C until hybridisation to microarray.

10.3.10.3 Hybridisation: Biotin labelled samples were hybridized to Affymetrix Gene Chip 430 v2.0a microarrays due to the comprehensive nature of the chips which house 39,000 transcripts per array. Hybridisation by the Warwick University Molecular Biological Services Unit followed the standard Affymetrix protocol for Eukaryotic Target Hybridisation.

Hybridisation cocktail consisted of: 58.5 µL cDNA (containing approximately 15-20 µg), 3.3 µL Control Oligonucleotides (B2), 10 µL 20x Eukaryotic Hybridisation Controls (bioB, bioC, bioD, cre), 100 µL 2x Hybridisation Buffer, 2 µL Herring Sperm DNA (10 mg/mL), 2 µL BSA, 20 µL DMSO (Sigma), and dH2O (Ultrapure™/GIBCO) to a total volume off 200 µL, of which 130 µL is used for hybridisation.

The hybridisation protocol was as follows: arrays were warmed to room temperature and the hybridisation cocktail was heated to 99°C for 5 min followed by 45°C for 5 min then spun at 13,000 rpm for 5 minutes to remove

insoluble materials; the array was wet with 1xhybridisation buffer and incubated for 10 min at 45°C with rotation, then buffer is removed from the array and the hybridisation cocktail is added. Hybridisation takes place overnight at 45°C for 16 hours, rotating at 50 rpm. The next day the sample is pulled off the array and the array is washed twice according to the standard Affymetrix protocol.

10.3.11 Microarray Analysis (Statistical): Prior to gene expression analysis, background corrections on the arrays were performed using the GeneChip Robust Multiarray Average package (GCRMA; http://www.bioconductor.org/packages/2.2/bioc/html/gcrma.html), which removes any bias created due to the nucleotide content of the probes (Naef and Magnasco, 2003). AffyBatch Quality controls were run on all the arrays to assess the overall array intensity, density, 3'/5' ratios, and the presence of negative and positive border elements; further analyses were also conducted to assess RNA degradation. Dr Sascha Ott (Warwick University) developed small R functions based on the tools of the Bioconductor package (http://www.bioconductor.org/; Gentleman *et al.,* 2004) for principle component analyses, gene expression analyses, analyses of overlap and differential expression between arrays.

10.3.12 Correlating pathognomic deficiency with symptom: Symptoms of Chiari were compiled via a primary literature search (see Bibliography) and medical resource and patient support websites including: www.conquerchiari.org/index.htm, http://chiarione.org/symptoms.html, http://www.ninds.nih.gov/disorders/chiari/detail_chiari.htm. Aetiology of structures involved in these symptoms was derived primarily from Matsuoka *et al.* 2005, Le Dourain & Kalchiem 1999, and from lineage labelling experiments in this study (see Section 10.3.2 β-Galactagosidase staining above).

10.4. Analysis of Dermal Bone Development

10.4.1 Sample Preparation

10.4.1.1 Samples for Immunohistochemistry: Samples were prepared as in Section 10.3.1, with the following modifications: specimen from embryonic stage E16 onwards were fixed overnight in fresh 4% PFA at 4°C, with the exception of samples from the *Wnt1*-Cre x DR-XZ cross. All specimen for immunohistochemistry from embryonic stage E16 onwards were cut to a thickness of 12-17 µm onto charged slides.

10.4.1.2 Flat-Mount Bone Preparation: The murine frontal bone from one wild-type mouse at post-natal stage P2 was flat-mounted onto a slide as follows. The specimen was culled via cervical dislocation (Schedule 1) and fixed in 4% PFA at 4°C for one week. Following fixation the specimen was decapitated, the dermis was removed and the frontal bone was isolated together with the parietal and part of the nasal bones to ensure the frontal bone was undisturbed. The brain and meninges were dissected out and the sample was treated with permabilisation (0.1% Triton) and counterstaining (1:10,000 DAPI) overnight at 4°C. The following morning sample was rinsed 3 times with cold PBS. The frontal eminence was separated along the frontal suture and the pars orbitalis removed to obtain a flat surface and mounted onto a charged slide into two orientations (one lobe with L1 up and the other with L3 up). The bone was mounted with mouwiol and the slide was sealed with vacuum grease. The slide was imaged as described in Section 10.4.4.

10.4.2 Immunohistochemistry: Multiplex immunohistochemistry was performed on sections of embryos from all crosses listed above (Section 10.2.2), prepared as described in Section 10.2.4.1. Slides were defrosted at room temperature for 5 min, fixed in 4% paraformaldehyde for 15 min at room temperature, rinsed 3 x in PBS and blocked with permabilisation for 1 hour at room temperature. Blocking Solutions are listed below, with 20% Roche Western Block Solution (WBS) (Roche) + 0.1% Triton used as the default. Following blocking, primary antibodies were incubated at 4°C overnight in the Blocking Solution. The next morning samples were washed for 1-2 hours(s) with the Wash Solution associated with the given Blocking

Solution (see table below), with changes every 5-15 min. Secondary and conjugated antibodies were then incubated for 1 hr at room temperature in the Blocking Solution, followed by 1-2 hour(s) of washes (with frequent changes) and a PBS rinse. Slides with tyramide amplification (β-Galactogosidase (AbCam) and Hand2 (R&D) antibodies) had the following additional steps: quenching of endogenous peroxidases with 0.3% H2O2 during blocking; tyramide amplification (Perkin Emler Kit) with 5 µl conjugated (FITC, Cy3 or Cy5) tyramide in 500 µL Ampli-Buffer for 10-15 min; stopping of amplification reaction with 4% PFA or 0.01 N HCl for 10 min and 3 x PBS rinse. All slides were counterstained with DAPI (Invitrogen), administered either at 1:1000 for 5 min, or 1:2000 for 20 min with Rhodamine Phalloidin (Chemicon 1:250). Slides were then rinsed a final time in PBS and mounted in Mouwiol + DABCO. Slides were cover-slipped and sealed with nail varnish. Details of antibodies used can be found below.

** **Mouwiol Preparation:** The following are combined: 6 g Glycerol (Sigma), 2.4 g Mouwiol 4-99 (Calbiochem), 6 mL dH2O, 12 mL 0.2M Tris Buffer pH8.5. The solution is mixed slowly for >3 hr after which 12 mL 0.2 M Tris Buffer pH8.5 is added and the mixture is stirred overnight on a warm plate. The following morning the Mouwiol is incubated for 10 min at 55°C, centrifuged at 5000 g for 15 min or until supernatant is clear. Supernatant was removed and 2.5% w/v DABCO (1,4-diazobicyclo-[2,2,2]-octane, Sigma) was added to prevent fading. Mouwiol aliquots were stored at -20°C until use, at which point the temperature was raised to 37°C. For all mountings, 30 µL of Mouwiol are used.

Blocking Solution	Wash Solution
20% Fetal Bovine Solution (FBS) (Sigma) in PBS + 0.1% Triton (Sigma)	2% FBS/PBS
20% Roche Western Blocking Solution (WBS) (Roche) in PBS + 0.1% Triton	2% WBS/PBS
Superbloc (3 part Maleic Acid Buffer MAB, 1 part FBS, 1 part WBS) + 0.1% Trition	TBST + 1xWBS

* Slides undergoing tyramide amplification had 0.3% fresh Hydrogen

Peroxide (H2O2) added to the blocking solution

PRIMARY ANTIBODIES

Protein	Host	Working Dilution	Company	Reference
α-SMA-FITC conjugated	Mouse, IgG2a	1:200	AbCam	ab8211
α-SMA-cy3 conjugated	Mouse, IgG2a	1:200	Sigma	C6198
β-Catenin	Mouse, IgG1k	1:100	Millipore	05-665
β-Catenin	Mouse, IgG1	1:100	BD	610153
β-Galactagosidase	Chicken, IgGY	1:500+Amp1: 1500	AbCam	ab9361
CD31 (PECAM)	Rabbit, IgG	1:20	AbCam	ab28364
Collagen I	Mouse, IgG1	1:200	AbCam	ab6308
Collagen I	Rabbit, IgG	1:100	AbCam	ab21286
Collagen I	Rabbit, IgG	1:100	AbCam	ab59435
Collagen II	Goat, polyclonal	1:100	AbCam	ab24128
Col14A1 (Undulin)	Mouse, IgG1k	1:250	Stratech	H0000737-M01
CRABP1	Mouse, IgG2b	1:100	AbCam	ab2816
Decorin	Mouse, IgG2b	1:200	AbCam	ab54728
Fibronectin	Rabbit, IgG	1:100	Sigma	F3648
GFP	Chicken, IgGY	1:400	AbCam	ab13970
Hand2	Goat, polyclonal	1:50+Amp1:1 500	R&D	AF3876
MMP9	Mouse, IgG1	1:200	AbCam	ab58803
MMP9	Rabbit, IgG	1:200	AbCam	ab38898
MMP13 (VIIIA2)	Mouse, IgG1	1:100	AbCam	ab52128
MMP13 (Hinge-Region)	Rabbit, IgG	1:100	AbCam	ab39012
Notch (activated)	Rabbit, IgG	1:100	AbCam	ab8925
Osteocalcin	Mouse, IgG1	1:100	Stratech	NB600-1528
Osteopontin	Rabbit, IgG	1:100	AbCam	ab63856
Periostin (POSTN)	Rabbit, IgG	1:100	AbCam	ab14041
Runx2	Mouse, IgG2a	1:200	AbCam	ab76956
von Willibrand Factor	Sheep, polyclonal	1:500	AbCam	ab11713
Wnt5a	Rabbit, IgG	1:100	AbCam	ab72581

SECONDARY ANTIBODIES & COUNTERSTAINS

Antibody	Working Dilution	Company

DAPI	1:1000	Invitrogen
Rhodamine Phalloidin (F-Actin)	1:250	Chemicon
Rhodamine Phalloidin-555 (F-Actin)	1:100	Universal Bio
goat anti-Rabbit AlexaFluor 546	1:200	Invitrogen
donkey anti-Rabbit AlexaFluor 555	1:200	Invitrogen
donkey anti-Rabbit AlexaFluor 488	1:200	Invitrogen
donkey anti-Rabbit AlexaFluor 594	1:200	Invitrogen
donkey anti-Rabbit AlexaFluor 647	1:200	Invitrogen
donkey anti-goat AlexaFluor 594	1:200	Invitrogen
donkey anti-goat AlexaFluor 488	1:200	Invitrogen
donkey anti-goat AlexaFluor 555	1:200	Invitrogen
donkey anti-goat AlexaFluor 647	1:200	Invitrogen
donkey anti-sheep AlexaFluor 488	1:200	Invitrogen
donkey anti-sheep AlexaFluor 546	1:200	Invitrogen
donkey anti-sheep AlexaFluor 647	1:200	Invitrogen
goat anti-chicken AlexaFluor 488	1:200	Invitrogen
goat anti-chicken AlexaFluor 647	1:200	Invitrogen
goat anti-mouse IgG1 AlexaFluor 488	1:200	Invitrogen
goat anti-mouse IgG1 AlexaFluor 555	1:200	Invitrogen
goat anti-mouse IgG2a AlexaFluor 488	1:200	Invitrogen
goat anti-mouse IgG2a AlexaFluor 555	1:200	Invitrogen
donkey anti-mouse IgG AlexaFluor 488	1:200	Invitrogen
donkey anti-mouse IgG AlexaFluor 555	1:200	Invitrogen
donkey anti-mouse IgG AlexaFluor 647	1:200	Invitrogen

10.4.2.1 Matrix Labelling: In some instances, prior to slide mounting (following the immunological staining or in its absence), mineral matrix of bone was stained with a labelling agent, either: Calcein, Xylenol Orange, Doxycyline, Calcein Blue, or Alazarin Complexone (All Sigma). Labelling agents were made into solution with PBS, with 5 mg/50mL an effective concentration of all agents to allow visualisation of labelling (for spectral acquisition see Section 10.4.4.1). Slides were dipped in the labelling reagent

for 10 sec – 45 sec (concentration and agent dependent), rinsed several times with PBS then mounted as described above (Section 10.4.2).

10.4.3 *In Situ* Hybridisation: to detect mRNA from transcribed genes.

10.4.3.1 Generation of Antisense RNA Probes for ISH: Plasmids for generating RNA probes for *in situ* hybridisation were generated either via: a) PCR (as described in Section 10.1.2) of mouse genomic DNA, sub-cloned into pCRII TOPO and fully sequenced (Section 10.1.8b), or; b) regrowth of a clone from the NIA15K collection (as described in Section 10.1.8a). 5 µg of plasmid were linearised overnight (as described in Section 10.1.10) with a 5' overhang and purified with QIAquick PCR Purification Kit (Qiagen) according to manufacturer's protocols, eluted in a final volume of 50 µL in Ultrapure® dH2O (GIBCO).

RNA probes were synthesised from linearised plasmids using RNA polymerase T7 or SP6 (Roche Diagnostics) in a 2 hour synthesis reaction (37°C) containing: 1 x DIG or Fluorescein RNA labelling mix, 1 x Transcription Buffer (Roche), 0.1M DTT (Invitrogen), 1 U/µL RNAse inhibitor (Promega), in a total reaction volume of 20 µL. Synthesis was confirmed by running 1 µL of reaction mix on a 1% Agarose Gel. RNA was precipitated for 1 hr – overnight at -20°C after the addition of 2.5 µL 4M LiCl and 60 µL 100% EtOH. RNA was pelleted (centrifugation at 13,200 rpm for 20 min at 4°C) and the pellet was washed with 70% EtOH, centrifuged for 5 min (13,200 rpm, 4°C) with the supernatant discarded, then air dried in an extractor hood until clear and re-suspended in 50 µL Ultrapure® dH2O (GIBCO).

Gene	Plasmid	RE	Polymerse	Detects Last	Note
Hand2	pBR43	BamHI	T7	Exon	Performed by B. Ryll
Runx2 Type II	pKJR2II	SpeI	T7	Intron1	Fail
Runx2 TypeI/II	pKJR2I_II	XhoI	SP6	Intron2	Fail

10.4.3.2. Fluorescent RNA ISH on Mouse Cryosections:

Day 1: Acetylation, Pre-Hybridisation and Hybridisation: Single and double fluorescent RNA ISH was carried out using a protocol designed and optimised by X. Zhang, modified from Scharen-Wiemers and Gerfin-Moser. Cryosections were prepared as in Section 10.3.1. Sections were defrosted, fixed in fresh 4% buffered PFA for 15 minutes and rinsed 3 x in PBS (3 min each) then incubated in Acetylation Solution (0.1M TEA, 0.02M NaOH, 0.75mL Acetic Anhydride) for 10 min at room temperature. Sections were next washed 3 x in PBS and incubated for 2 hours at room temperature with Hybridisation Buffer (50% Formamide, 5x SSC [from stock 20xSSC = 3.0 M NaCL, 0.3 M Sodium Citrate], 5 x Denhardts [from stock 50xDenhardt's = 1%w/v Ficoll400, 1% Polyvinylpyrrolidone (PVP), 1%BSA], 0.25 mg/mL Baker's yeast tRNA, 0.5 µg/mL Herring Sperm DNA). The DIG, DNP or FITC-labelled RNA ISH probe (200-400 ng/mL per target gene) was boiled for 5 min, placed on ice, then added to the Hydybridisation Buffer. The sections were hybridised with 100-200 µL Hyb Buffer (containing probe), coverslipped and placed in a humidified chamber (5xSSC, 50% Formamide) overnight at 68-72°C. Separate chambers were used for slides with different probes to avoid cross-contamination.

Day 2: Post-Hybridisation Washes & Immunological Staining: Coverslips were removed in pre-heated (hybridisation temperature) 5xSSC. Slides were washed 2 x 30 min in pre-heated (hybridisation temperature) 0.2xSSC, then 5 min 0.2xSSC at room temperature. Immunological staining was conducted as follows: slides were incubated for 5 min in Solution B1 (0.15 M NaCl, 0.1 M Tris pH7.5) then blocked for 1-2 hours with B2 (B1 supplemented with 10% Fetal Bovine Serum (FBS) (Invitrogen)). Slides were next labelled by incubating them with 500 µL B2 + antibody (1:30,000 Anti-Fluorescin-POD (Jackson), 1:4,000 anti-DIG-POD (Roche) or 1:,1000 anti-DNP-POD (Perkin Elmer)) at 4°C, overnight in a humidified chamber. The next morning slides are rinsed 3 x 5 min with PBS.

Day 3- end:

Single Fluorescent ISH: Slides were washed 3 x 30 min at room temperature with B1. Tyramide amplification was achieved using 3.2 µL FITC/Cy3/Cy5 conjugated Tyramide in 200 µL 1xPlus Amplification Solution (Perkin Elmer); amplification was conducted at room temperature for a probe-dependent time ranging from 30 min – 2 hours. POD activity was then quenched with 0.01N HCL for 10 min, room temperature (dark). Slides were washed a further 3 x 3 min with B1*. Slides were counterstained for 5 min with 1:1000 DAPI ($7x10^{-4}$M, Invitrogen) in Utrapure® dH20 (GIBCO), washed 3 x dH2O and mounted with Mouwiol and sealed with nail varnish.

* For Double ISH, move to 'Double Fluorescent ISH' at this point.

Double Fluorescent ISH: Double ISH were performed as above and Day 2 is repeated using a second antibody (1:30,000 Anti-Fluorescin-POD (Jackson), 1:4,000 anti-DIG-POD (Roche) or 1:,1000 anti-DNP-POD (Perkin Elmer)). Probes are typically developed in the following order: FITC, then Cy3, then Cy5.

Brightfield ISH on Mouse Cryosections: Protocol is the same as above with the following modifications: Day 2 Immunological Staining (overnight 4°C) was achieved with B2 Solution containing 1/2000 anti-DIG-AP (Roche Diagnostics). On Day 3 the slides were washed 3 x 30 min at room temperature with B1 then 5 min with B3 (0.1Tis pH9.5, 0.1M NaCl and 50mM $MgCl_2$). A development step is then completed with B3 supplemented with 6.75 U/mL NBT and 3.5 U/mL BCIP substrates (both Roche), in the dark for 3 hrs to overnight. Development is quenched by washing the slides in B3 for 10 min, then a PBS wash for 10 min, at room temperature. Sides were then mounted with Mouwiol.

10.4.4 Image Acquisition: Confocal microscopy was performed at Warwick University using Leica TCS SP2 and SP5 systems using 10x, 20x, 40x, 63x,

and 100x lenses. Alexa Fluor 488 was excited at 488 nm and emission was measured around 500 nm on the FITC channel; Alexa Fluors 546, 555, RPh and Cy dye 3 were excited at 543 nm and emission measured around 555 nm (TRITC channel). Alexa Fluor 647 and Cy dye 5 were excited at 633 nm and emission measured around 655 nm. DAPI stain was excited at 364 nm and emission measured around 400 nm. Reflectance images were acquired by exciting with the 488 laser and collecting using PMT. The measurement range was optimised to guarantee no overlap or bleed-through between the channels. All image acquisition occurred in the x, y and z-planes, resulting in a z-series. The average z-series comprised a step size of ~0.4-0.9 µm and the entire depth of the section was imaged. Brightfield images were acquired at Warwick University under a dissecting microscope, in a single optical plane.

10.4.4.1 Image Acquisition: Matrix Labelling

Samples that had been subjected to mineralised matrix labelling were imaged with the following parameters to ensure no spectral overlap occurred.

Labelling Agent	Excitation/Emission	SP5 Laser	SP2 Laser	Overlaps:
Alizarin complexone	530-580 / 624-645	DPSS 561	HeNe 1.5 mW (543)	
Calcein	495 / 517	Ar 100 mW (488)	Ar 100 mW (488)	FITC
Calcein blue	373 / 420-440:	Diode 20 mW (DAPI)	Diode 20 mW (DAPI)	DAPI
Doxycycline	390-425 / 520-560	Diode 20 mW (DAPI)	Diode 20 mW (DAPI)	RPh
Xylenol orange	440/570 / 610: 555	DPSS 561	HeNe 1.5 mW (543)	

10.4.5 Image Analysis

10.4.5.1 Image Analysis, 2D: 2D image reconstructions were completed using LeicaLiteAS and Adobe Photoshop softwares. Images were either of individual optical sections from a z-series, or collapsed maximal or average projections of z-series. Image files from the confocal were converted into

colour and channels were superimposed. Adjustments for brightness and contrast were made, in a linear fashion to the entire image, as needed.

10.4.5.2 Image Analysis, 3D: All 3D reconstructions of z-series were created using the freeware BioImageXD developed by the Universities of Jyväskylä and Turku in Finland and the Max Planck Institute of Germany: World Wide Web http://www.bioimagexd.net.

11. Technical Appendices

11.1 Technical Appendix: Determining the emission spectra of in vivo labels for the biomineralised matrix

Prior to *in vivo* experimentation, described in Chapter 3.3, the emission spectra, as visible on a Leica SP2 confocal microscope, was determined for each of the potential labelling agents that could be used in the study. A total of nine chelating agents were successfully used in previously published studies of *in vivo* analyses of endochondral biomineralisation: alazarin complexone, BAPTA, calcein, calcein blue, doxycycline, rolitetracycline and tetracycline hydrochloride (published dosages, and the expected excitation/emission spectra of each are found in Table 11.1.1). For the purpose of the current study, I chose to focus on four of these labelling agents: alizarin complexone, calcein, xylenol organe and doyxcyline. To confirm it is possible to image the labelling agents without overlap, previously untreated slides from wild-type mice were subjected to histological addition of each agent (at *in vivo* concentrations) and imaged. The resulting wavelength (λ) range of the emission spectra, when excited with various wavelength lasers, was documented and extensive overlap was seen between the four compounds. The total detectable emission spectra for each compound is shown in Figure 11.1.1, with the optimal range indicated with a bold bar. For each agent, the optimal detection range (as well as the total range in which the dye is visible) was determined on the laser that corresponded to the recommended excitation range, as published. Once the optimal wavelength range for detecting the labelling agent (denoted OPT) was determined, I measured the bleed-through to other channels, as well as the emission detected in the OPT range when the agent was excited by the other lasers on the SP2 confocal microscope. The resulting images of these investigations (with the compound, excitation laser and wavelength detected) are presented in Figures 11.1.2 to 11.1.7.

Labeling Agent	Excitation/Emission	SP5 Laser	SP2 Laser	Dosage	Method	Reference
Alizarin complexone	530-580 / 624-645	DPSS 561	HeNe 1.5mW (543)	25 mg/kg	IP	Sun et. al. 1992
Alizarin complexone	530-580 / 624-645	DPSS 561	HeNe 1.5mW (543)	30 mg/kg	SC*	Pautke et. al. 2005
BAPTA	200-325 / 410-550	Diode 20mW (DAPI)	Diode 20mW (DAPI)	75 mg/kg	SC*	Pautke et. al. 2005
BrdU (5-bromo-2'-deouxyridine)				20 mg/kg	IP	Lana-Elola et. al.2007
Calcein	495 / 517	Ar 100mW (488)	Ar 100mW (488)	10 mg/kh	IP	Sun et. al. 1992
Calcein	495 / 517	Ar 100mW (488)	Ar 100mW (488)	30 mg/kg	SC*	Pautke et. al. 2005
Calcein blue	373 / 420-440:	Diode 20mW (DAPI)	Diode 20mW (DAPI)	15 mg/kg	SC*	Pautke et. al. 2005
Doxycycline	390-425 / 520-560	Diode 20mW (DAPI)	Diode 20mW (DAPI)	50 mg/kg	SC*	Pautke et. al. 2005
Hematoporphyrin	530-560 / 580: 555	DPSS 561	HeNe 1.5mW (543)	300 mg/kg	SC*	Pautke et. al. 2005
Rolitetracycline	390-425 / 520-560	Diode 20mW (DAPI)	Diode 20mW (DAPI)	25 mg/kg	SC*	Pautke et. al. 2005
Tetracycline hydrochloride				30 mg/kg	IP	Sun et. al. 1992
Xylenol orange	440/570 / 610: 555	DPSS 561	HeNe 1.5mW (543)	90 mg/kg	IP	Sun et. al. 1992
Xylenol orange	440/570 / 610: 555	DPSS 561	HeNe 1.5mW (543)	90 mg/kg	SC*	Pautke et. al. 2005

* Subcutaneous following surgical procedure to damage the bone

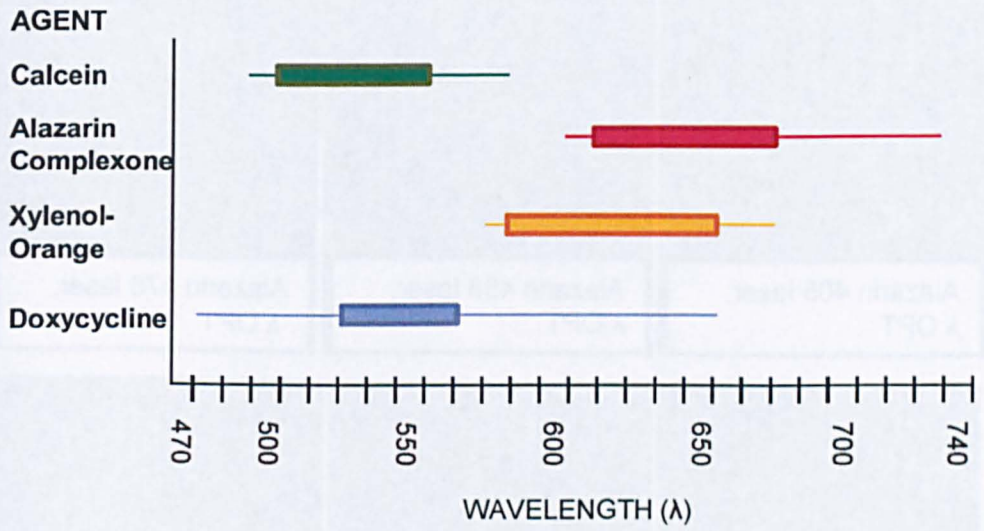

Figure 11.1.1: The emission wavelengths of 4 chelating agents as determined experimentally

The recommended *in vivo* dosage was histolgically added to sections of wild-type, newborn mice. Maximal range indicated by line, OPT (optimal range for detection) indicated by bar. Emission spectra is significantly wider than reported in the literature.

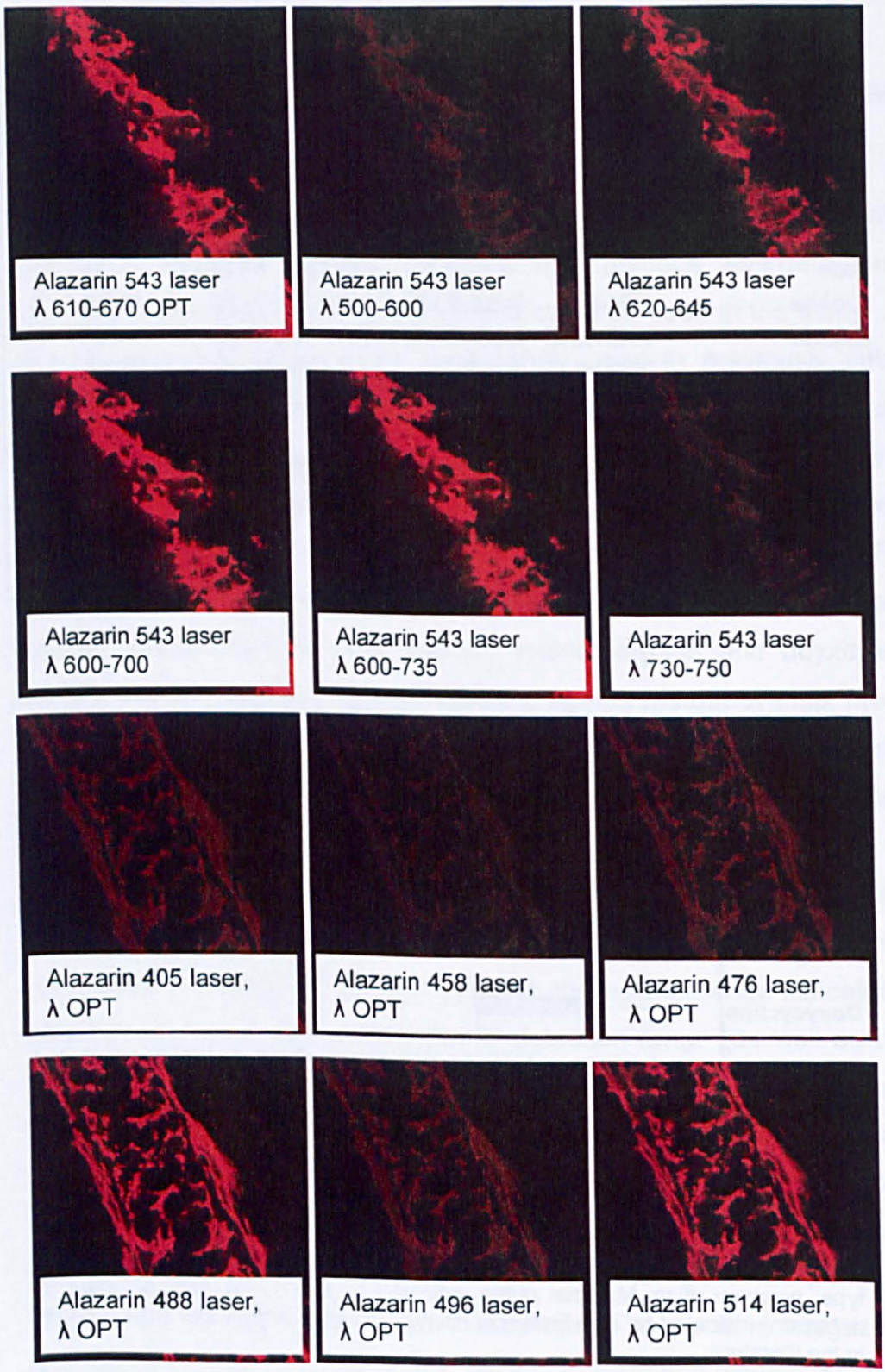

Figure 11.1.2: Emission spectra of alazarin complexone

Figure 11.1.3: Emission spectra of alazarin complexone continued

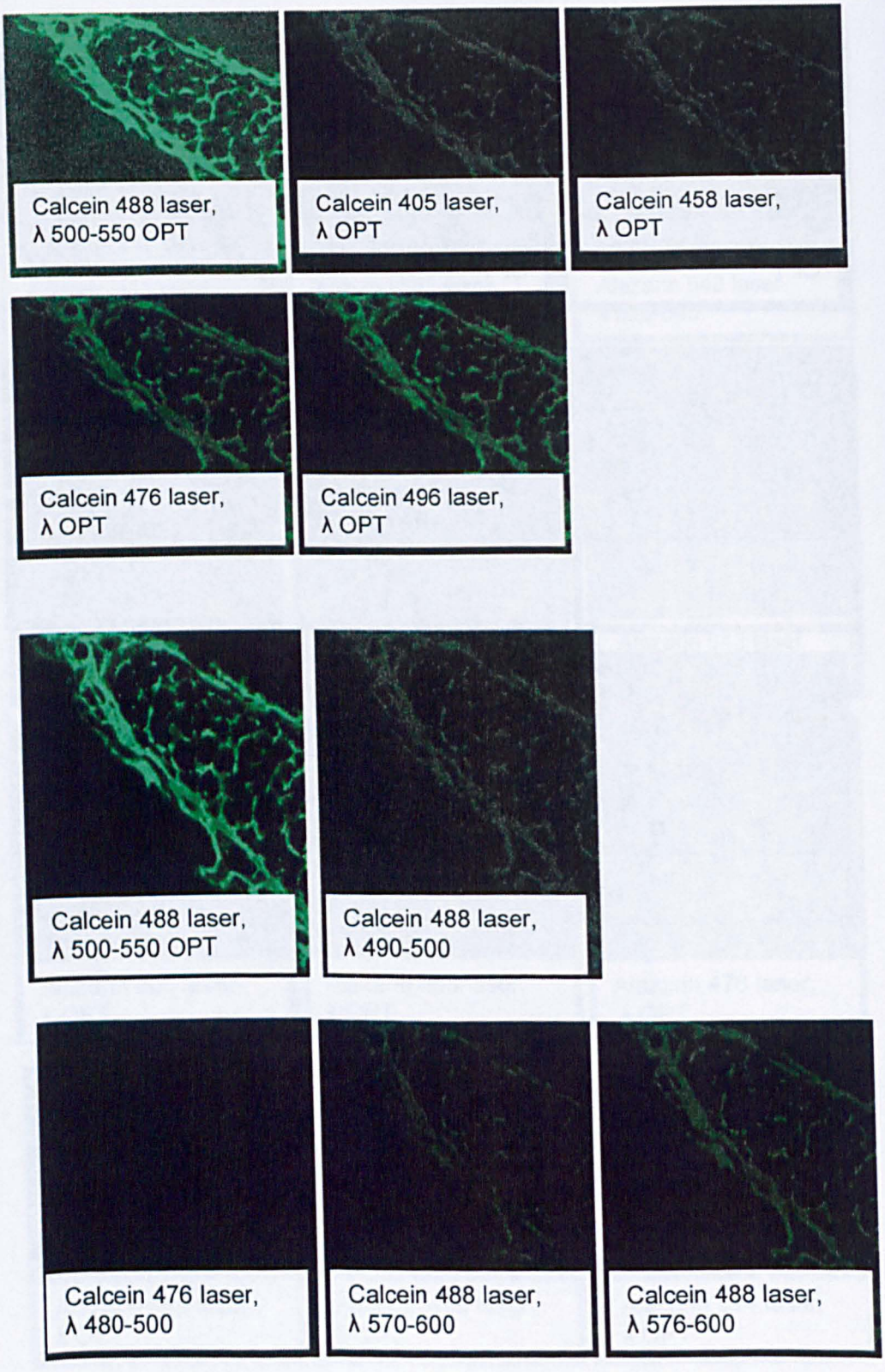

Figure 11.1.4: Emission spectra of calcein

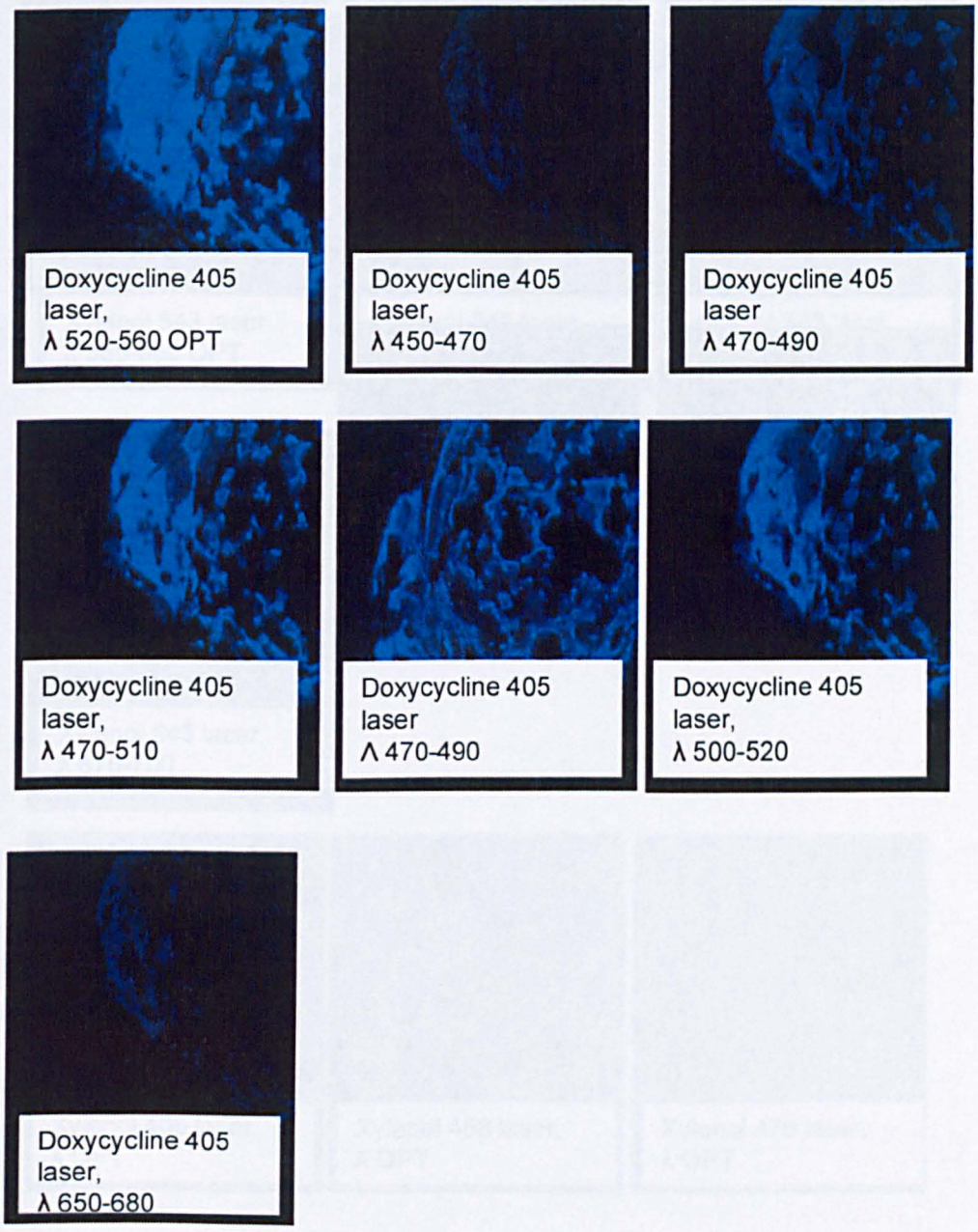

Figure 11.1.5: Emission spectra of doxycycline

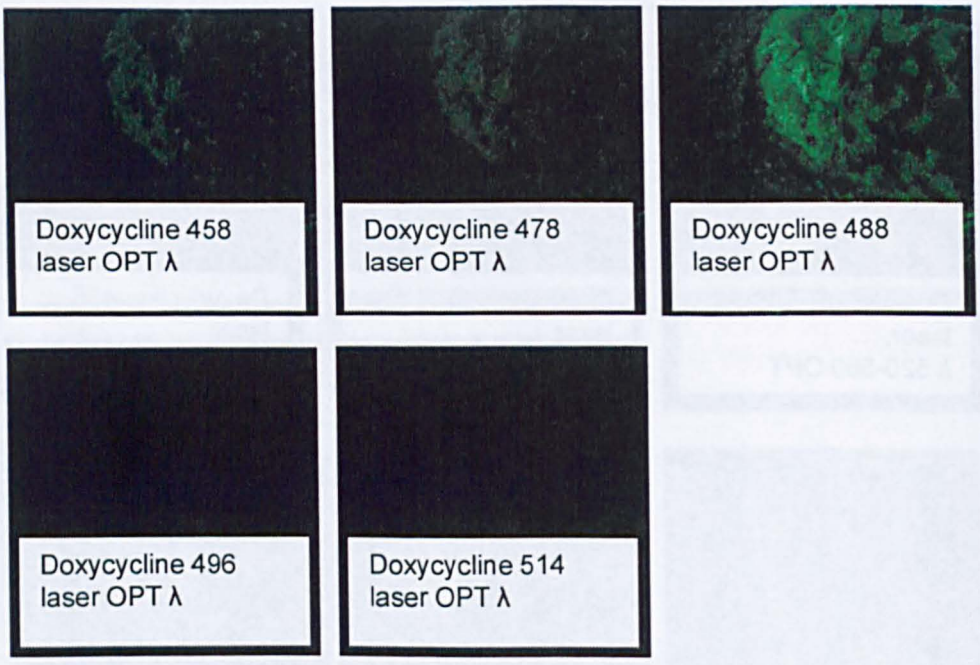

Figure 11.1.6: Emission spectra of doxycycline continued

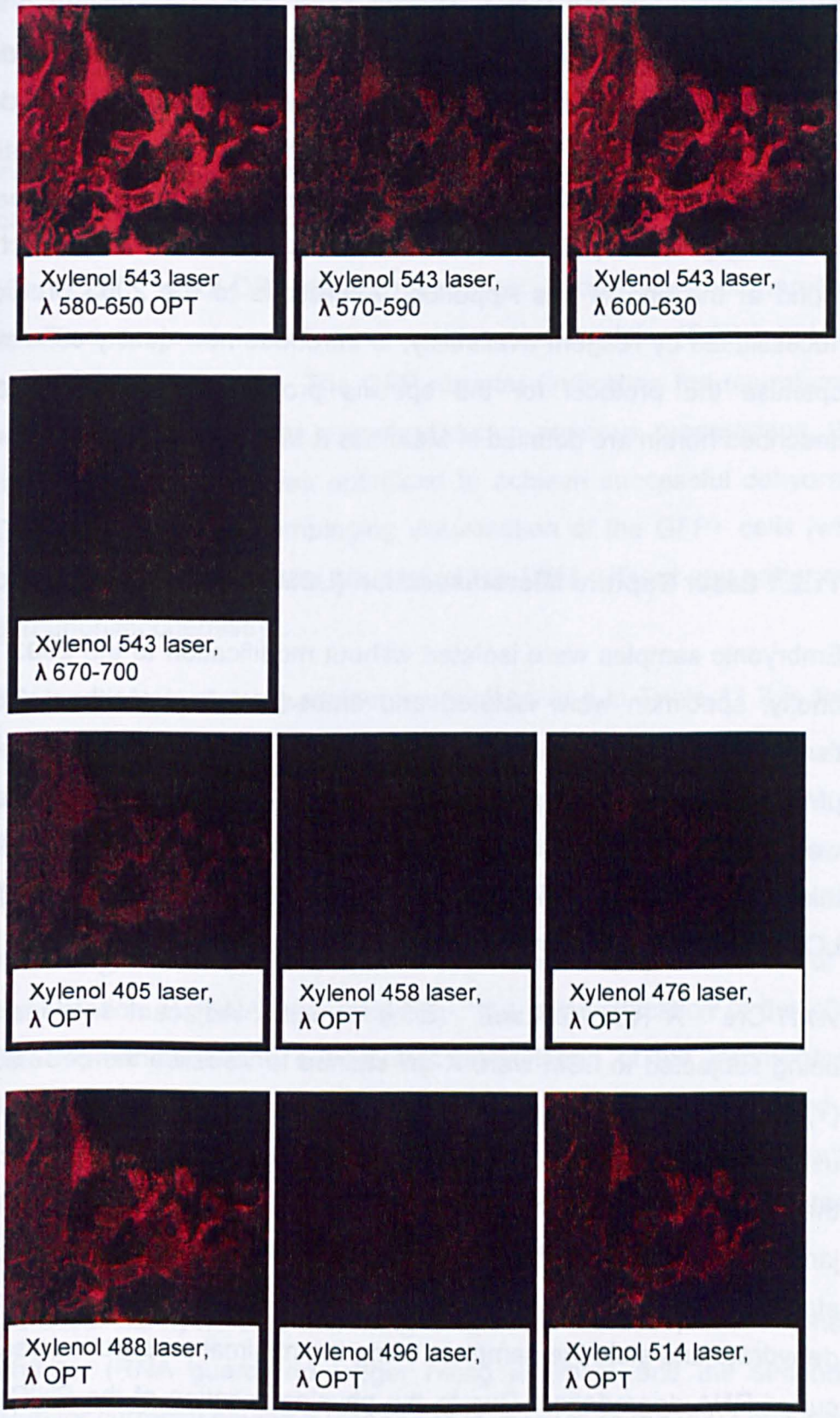

Figure 11.1.7: Emission spectra of xylenol orange

11.2 Technical Appendix: Optimising the single cell transcriptome analysis protocol

The protocol used for the single cell transcriptome analysis study described in Chapter 8 was modified from one pioneered by Koentges *et al.* described in Tietjen *et al.* 2003. This technical appendix details the modifications and optimisations to the 2003 protocol that were conducted to yield the current laboratory protocol (referred to herein as "Updated Protocol"), which can be found at the end of this Appendix. Alterations to the 2003 protocol were necessitated by reagent availability, to introduce new quality controls and to optimise the protocol for the specific project at hand. All procedures described herein are detailed in Materials & Methods, Chapter 10.

11.2.1 Laser Capture Microdissection (LCM)

Embryonic samples were isolated without modification to the 2003 protocol, briefly: specimen were isolated and embedded fresh (without fixation) in tissue tek mounting media before being cryo-sectioned at a thickness of 7-10 µM onto alternating charged (for LCM) or non-charged (for IHC) slides, which were kept at -80°C until they were used for laser capture microdissection (for this study, a period of no more than a few days). Slides were prepared for LCM as follows, according to the genetic background of the sample:

Wnt1-Cre$^{+/-}$ X ROSA26LacZ$^{-/-}$ (E13) samples: Adjacent sections to those being subjected to LCM were X-gal stained to visualise the β-Galactosidase (+) cells, indicating their neural crest origin. Samples for LCM were prepared using a standard histopathological hematoxylin and eosin stain to visualise the nuclear and cytoplasmic boundaries. All stains were performed in coplin jars that had been cleaned to be RNAse/DNAse free. Optimisation of the staining protocol was necessary as the objective was to completely dehydrate and stain the samples, using the minimal preparation necessary to curtail RNA degradation. Due to the physical location of the PixlCell II LCM microscope (in a room that also contains a live-cell imaging system that involves fluid injection and yields a high humidity), the slides were re-hydrate

quickly, which prohibited successful laser capturing. As such, the duration of the dehydration steps were increased and the air-drying decreased and individual slides would be subjected to capturing for no more than 1 hour or until capturing became confounded by tissue rehydration.

Wild-type (E9-10), non-transgenic samples: prepared as above with the omission of the parallel β-gal staining.

Wnt1-Cre$^{+/-}$ x XZ-DR$^{-/-}$ (E18.5) samples: Slides were prepared using a modified protocol including a nuclear counterstain (DAPI) but no other histological preparation. The GFP reporter (indicating the neural crest cells) was a soluble molecule, quenched during aqueous preparations, therefore, the staining protocol was optimised to achieve successful dehydration and DAPI staining without impinging visualisation of the GFP+ cells (which was possible in the fluorescent channel of the LCM without any enhancement or immunohistochemistry).

The successful staining protocols are described in Table 11.2.1; for images from LCM see Chapter 8.

11.2.2 Modifications resulting from enzyme availability

The single cell transcriptome study relies on the successful reverse transcription of cDNA from total RNA, the re-amplification of the cDNA, and the fragmentation and subsequent biotinylation of the fragmented cDNA; these steps are all mediated by enzymes, some of which had become unavailable or were altered (yielding new cloned or recombinant forms) in the interim between the 2003 protocol being generated and the current study. Specifically, the updated protocol contains modifications in:

- the cellular lysis step following single cell isolation, due to one RNAse inhibitor (RNA guard) no longer being available and the second RNAse inhibitor currently having a higher activity level than the 2003 enzyme;

- the initial RNA reverse transcription to cDNA step to account for a new AML reverse transcriptase having a higher activity level than the 2003 enzyme;

- the fragmentation step as strict adherence to the old protocol generated overly-fragmented cDNA (less than 25-mer fragments that could not be expected to anneal to the 25 bp probes of the microarray, or >500-mer fragments that could also have difficulty annealing), despite the activity level of the enzyme not changing between 2003 and the current study.

The modifications to the protocol ensure the same number of enzymatic units mediate each step of the updated protocol as they did in the 2003 protocol.

The enzymes used in the 2003 and updated protocols are described in Table 11.2.2.

11.2.3 Quality controls

The 2003 protocol recommends using Southern hybridisations as a control for the cDNA quality and to confirm the cellular identity of the single cells captured (which can also be checked via PCR). The updated protocol has modified the quality controls as follows:

- The lineage origins of the cells are confirmed in samples from *Wnt1*-Cre$^{+/-}$ x R26LacZ$^{-/-}$ mice by PCR for the LacZ transgene after the reamplification of the cDNA; while lineage of the cells in samples from *Wnt1*-Cre$^{+/-}$ x XZ-DR$^{-/-}$ samples is confirmed at the time of capture by visualising the captured cell on the cap using fluorescence (GFP+ neural crest cells are green) (For images see Chapter 8).

- The presence of the housekeeping gene GAPDH is confirmed with PCR after the reamplification of the cDNA (For images see Chapter 8).

- After both the initial cDNA transcription and subsequent reamplification, an aliquot of the sample is run on an agarose gel to confirm the length of the product and the relative concentration of cDNA (For images see Chapter 8). Notably, there is no strict criteria for what is considered "good" but a successful experiment should yield several micrograms of cDNA around 1000 bp in length (which is 3' biased due to the nature of the reverse transcription).

- Southern hybridisations are no longer used as a primary quality control as the cDNA quality is assessed with a Bioanalyzer (see below) and the lineage origin confirmed as above. Southern hybridisations were deemed, therefore, to be an unnecessary and time-consuming use of the very limited sample material.

- The quality and concentration of the neat (unfragmented) cDNA was confirmed on an Agilent 2100 Bioanalyzer (Figure 11.2.1). Bioanalysis was also used to check the successful fragmentation of the cDNA prior to hybridisation to microarrays (Figure 11.2.1). The Genomics Facility of Warwick University's School of Life Sciences conducted the bionanalysis of the single cell cDNA, a quality control that was used by the Genomics Facility in studies conducted by other laboratories using cDNA or RNA from pools of cells. Bioanlysis of cDNA from single cells had not previously been examined at the on-site facility and results were loosely comparable to results from pools of cells, although it required trial and error was used to determine what was a "good" result. Specifically, a good sample was one that had a nice curve of cDNA with a long migration time (indicating cDNA length) and a high concentration. Samples whose neat cDNA was more of a peak than a curve and had short migration time were considered to be poor quality.

- Quantitative PCR (qPCR) of the GAPDH housekeeping gene was also used to analyse the overall quality of the cDNA. Standard curves were generated from serial dilutions (2.5 nanograms/μL to .25 picograms/μL) of cDNA generated from whole RNA of the mouse osteoblastic cell line MC3T3-E1. As a second control, high quality reamplified cDNA from a different study (conducted by Dr Keith Vance (KV), unpublished), generated using the 2003 protocol, was concurrently analysed. Results indicate that all the samples generated in the current study using the updated protocol have GAPDH in a low abundance (in amounts between the 2.5 picogram/μL and 0.25 picogram/μL controls from MC3T3-E1 cells); however, the curves generated are, for the most part, comparable or more robust than those from the KV sample. The KV sample (which yielded 12.3% present calls when hybridised to microarrays concurrently with samples from the present study) may have experienced degradation in the 4 year gap between its amplification and

qPCR analysis; alternatively, the majority of the samples isolated in the current study can be considered to be of equal or higher quality than the KV control sample. Notably, the curves did not start to spike until many cycles into the qPCR (approximately 35/40) and the results are not used for any quantification purposes, merely to discriminate the quality between the various samples. As such, there is a clear distinction between the samples that have superior versus inferior curves (Figure 11.2.2).

11.2.4 Validating microarray results: AffyBatch Report

A total of 26 samples sufficiently passed quality controls prior to hybridisation and were selected for further analysis. As a means of comparison I also hybridised some samples that had failed the Bioanalyzer quality controls (being over-fragmented n = 2, poorly-fragmented n = 2) and a blank sample (no cell material added to initial cDNA reverse transcription step, blank was subsequently re-amplified, n = 1) to confirm the protocol had successfully discriminated between samples that would produce good quality microarray results and those that would not.

Prior to gene expression analysis, background corrections on the arrays were performed using the GeneChip Robust Multiarray Average package (GCRMA; http://www.bioconductor.org/packages/2.2/bioc/html/gcrma.html), which removes any bias created due to the nucleotide content of the probes (Naef and Magnasco, 2003). AffyBatch Quality controls (Bioconductor) were run on all the arrays to assess the overall array intensity, 3'/5' ratios of housekeeping genes, and the presence of negative and positive border elements. Because the QC report was designed to analyse standard microarray experiments of cDNA/RNA from pools of cells, the report was used largely to inter-compare the single cell samples to each other.

The QC report indicated that the overall intensity of the majority of the arrays was acceptable and even comparable to the QC report standard generated for pools of cells (QC standard mean intensity = 6-8; single cell sample mean intensity = ~6); the Bioanalyzer-failed arrays had a reduced intensity as did

several arrays that had been deemed "borderline" based on Bioanalyzer results as they had a sharp peak of cDNA, where "good" samples had a characteristic curve. For the purposes of gene expression analyses, the microarrays with diminished brightness and questionable Bioanalyzer results were removed from the analysis (See Chapter 8). This highlighted the importance of being strict with the Bioanalyzer controls, as neat cDNA quality directly correlated with samples having poor overall intensity and low array coverage.

The 3' to 5' ratio of the housekeeping genes GAPDH and β-Actin were, for the most part, beyond the range recommended by the QC standard (GAPDH recommended ratio of 1, β-Actin recommended ratio under 3). As the recommended range of ratios is between 1 and 3, the QC report only indicates if a ratio is within a good range (-3 to 3), in a borderline range (>3 or <-3) or significantly outside of this; no absolutely values are given (Table 11.2.3). Among our 26 "good" samples, for β-Actin, 12/26 (46%) were within the good to borderline range, 10/26 (39%) were significantly beyond the -3 to 3 boundaries and 4/26 (15%) had ratios that were not computed (presumably due to missing probe values); comparatively 4/5 control (Bioanalyzer-failed) samples (80%) were within the good to borderline range. For GAPDH, 11/26 (42%) of the "good" samples were within the plotted range, 8/26 (31%) were outside the recommended range and 7/26 (27%) had uncomputed ratios. Comparatively, 100% of the "bad" arrays had GAPDH 3' to 5' ratios that were within the acceptable range. The discrepancy whereby poor quality samples gave ostensibly better 3' to 5' ratios than "good" samples is accounted for by the fact the QC report scales the intensities to determine the ratio; even though the intensity of the overall "bad" arrays was diminished, scaling the intensity to calculate the ratios would indicate a hit for a housekeeping gene that might not actually be above background. I confirmed this by examining the present hits on the "bad" arrays, where I found that of the 3 probes for GAPDH and 3 probes for β-Actin, only 1 sample (of the 5) had a single β-Actin hit, while 2 samples had a single GAPDH hit. Contrasting this, 20 of the 26 "good" samples had at least 1 present hit for β-Actin (of which 10 had 2/3 present calls) and 19/26 "good" samples had at least 1 present hit for

GAPDH (2/26 had triple hits, and 7/26 had double hits) (Table 11.2.4). Additionally, the overall intensity of the housekeeping genes was significantly higher in the "good" arrays compared to the 3 present hits in the Bioanalyzer-failed samples.

The 3' to 5' ratios being beyond the recommended limits of the QC standard in the "good" samples was unsurprising given the 3' bias of the cDNA generated in the current protocol and short length of the cDNA transcripts generated in the initial reverse transcription step (approximated to be between 500-1000 bp). As a comparison, a published report of single cell transcriptome analyses from laser captured samples hybridised to microarrays indicate a GAPDH 3' to 5' ratio of a mean 6.76 and β-Actin 3' to 5' ratio of a mean 57.92; comparatively, in the same report, unfractionated pooled cells that were isolated and also hybridised to microarrays had 3' to 5' ratios of 0.89 and 1.44 for GAPDH and β-Actin, respectively (Seshi *et al.* 2003). These results indicate the ratios in the current study are not beyond the acceptable limit for published studies.

The aspects of the QC report relating to the intensity across the arrays (as determined by examining the positive and negative border elements) were not deemed to be useful in the current study as the low percentage of present hits may be perceived by the software to be a bias in the hybridisation. A cursory examination does show, however, that among all the "good" arrays, the intensities cluster toward the middle of the plot (indicating unbiased hybridisation), while in the Bioanalyzer-failed and blank sample the intensities cluster in a corner of the plot (Figure 11.2.3).

In addition to the AffyBatch QC report, further analyses were also conducted to assess RNA degradation. RNA degradation analysis compares the intensity of 3' versus 5' probes among genes described as present in the array. Little RNA degradation will yield a straight line, while extensive RNA degradation will have a sloped line. Reassuringly, the plots for the "good" samples indicate very little RNA degradation (Figure 11.2.4); although the validity of using this control for QC in reamplified cDNA from single cells has not been examined in published reports.

11.2.5 Validity controls from previously published reports

Following AffyBatch quality controls and RNA degradation analysis, the microarrays were subjected to further quality controls in line with quality controls reported in previous studies, see below (Kamme *et al.* 2003; Seshi *et al.* 2003; Tietjen *et al.* 2003; Esumi *et al.* 2008).

11.2.5.1 Representation of transcriptome complexity

Following AffyBatch QC, 9 samples were removed from further analysis due to an overall diminished brightness of the arrays combined with the borderline/questionable Bioanalyzer result from those samples. Among the remaining 17 samples, array coverage ranged from 1.7-14.9% present, with a mean coverage of 5.8%; among the blank array and the four control "bad" Bioanlyzer-failed samples, array coverage ranged from 1% (blank) to 2.6%, with a mean coverage of 1.9%. For comparison sake, among the 9 arrays removed for having questionable Bioanalyzer quality and low intensity as indicated by the AffyBatch QC report, the range of coverage was 1.7-5%, with a mean of 3.7% (Table 11.2.5).

Previous studies analogous to our own, using microarrays to interrogate the transcriptome of LCM-isolated single cells from rodent tissues, reported array coverage ranging from 5.6%-13.9%. Other published studies using dissociation as a means to isolate single cells report higher array coverage, and one study reported extremely high array coverage from LCM dissected single cells (28-41% present, mean 36%), however, this was on a custom designed array which would be expected to have more bias toward genes that are predicted to be expressed in the cell type studied (Seshi *et al.* 2003). Notably, I was unable to determine how many genes are "expected" to be expressed in any given single cell, as this value would vary based on the cell type, stage in the cell cycle, and innumerable other factors.

I, therefore, decided to use 4% as the cut off to include arrays for further analyses, which further reduced the experimental cohort by 5 arrays to 12, with % present ranging from 4-14.9% and a mean % present of 9.1%.

The technique described herein for isolating single cells is robust enough to capture single cells; however, in highly dense areas, some cellular material from adjacent cells might also be captured. Furthermore, the thickness of the sections were designed to ensure only a single cell plane, however there were inevitably times when the capture was not a clean single cell. I was diligent in recording this and quantifying the exact number of cells captured (as indicated by both the nuclear stain and the margins of cells on the histopathological presentation) and as a default I indicated a 2-cell capture unless an absolute clean margin around the entire cell was visible. I observed also that published reports of single cell LCM studies that display their captures in figures are analogous to my own and most appear to have more than one cell; I accept that "single cell" has become nomenclature for a tiny volume of no more than a few cells. I was anxious to examine the effect of increased cell volume on the final data output. While the technique should not be biased toward samples that have more than one cell, I correlated the number of cells captured with the array coverage in the final cohort of 12 arrays and found no relationship between them (R^2 = 0.0931) (Figure 11.2.5). I also confirmed that the amount of cDNA hybridised to the array did not correlate with the array coverage; this was true using the [hybridised] as either the concentrations of the neat cDNA (R^2 = 0.0006) or the fragmented cDNA (R^2 = 0.1124), as determined by the Bioanalyzer (Figure 11.2.5). When I included the total cohort of the initial 26 samples, including those that had been excluded due to poor intensity/Bioanalyzer results, there was still no relationship between cell number and array coverage (R^2 = 0.0289), neat cDNA concentration (R^2 = 0.0304) or fragmented cDNA concentration (R^2 = 0.1741) (Figure 11.2.6).

11.2.5.2 Clustering analyses

Clustering analyses can be used to group cells based on whole-transcriptome expression profiles (Kamme *et al.* 2003); the expectation is that cells of a similar type should cluster more closely to one another than to cells of another type. I use principle component analysis (PCA), conducted by Dr Sascha Ott, as my clustering method (see Chapter 8) and find that the neural crest cells giving rise to non-vascular structures cluster more closely to each other than to vasculature cells; and PCA could not discriminate between neural crest versus mesodermal vasculature (Figure 11.2.7). Notably, the clusters could also be seen to represent stages of differentiation, as samples from E13 were more closely aligned to each other than those from E18.5, with the exception of sample 87.

The microarrays were run in two main batches and when the samples are analysed with PCA, the first cohort clusters nicely, while the other (containing the 9 samples with diminished intensity –circled in red-) did not (Figure 11.2.7). To confirm that the arrays with overall intensity did not cluster well, and the lack of clustering was not an artefact of including samples with extremely low array coverage, PCA was run on all samples with % present >2.5%; and the clusters were not recapitulated.

I, therefore, conclude that the PCA confirmed the arrays with low intensity and low % present had transcriptomes unlike biologically similar and adjacent cells (Figure 11.2.8).

I could not determine, using PCA, to what extent the clusters were biologically relevant, however, they were a useful tool to confirm the transcriptomes of the E13 analgen to structures affected in Chiari were dissimilar to the transcriptomes of terminally differentiated vasculature of the cranial base in E18.5 specimen.

11.2.5.3 Hybridisation efficiency

Studies of single cell transcriptomes often use analysis of well-characterised genes, specific to the cell-type of interest, to confirm the capture and validate the microarrays (Kamme *et al.* 2003; Seshi *et al.* 2003; Tietjen *et al.* 2003;

Esumi *et al.* 2008). I confirmed the lineage of the capture as described above, as well as using PCR to detect the presence of the LacZ transgene in the E13 samples and the GAPDH housekeeping gene in the 18.5 samples. The samples from neural crest cells in the E13 specimen were from condensed mesenchymal anlagen to structures affected in Chiari, the majority of which were precursors to bony structures. I was hesitant to confirm the fate of cells from these regions with genes expected to be expressed given the study of dermal bone development described in Part I indicated that gene expression in bone development is complex; furthermore, the condensed mesenchymal precursors to the bone structures would be expected to contain both vascular and osteoblastic lineages and may be at various stages of terminal differentiation. We did, however, examine the expression of some markers associated with certain cell fates and confirmed the samples from the E18.5 vasculature expressed vasculogenic markers, as well as various collagens and adhesion molecules and some muscle/fibroblastic markers- presumably confirming these are endothelia and/or pericytes (Table 11.2.6). Among the E13 samples, those from the anlagen to the posterior cranial fossa/tentorium had similar profiles (among the limited genes examined) to both the E18.5 vascular samples and the condensed mesenchyme from the other sub-populations of E13 neural crest cells (Table 11.2.6). This explains why the PCF samples cluster closely to the other E13 sub-populations, but on the perimeter of the cluster toward the E18.5 samples. Additionally, samples 87, from the clivus/pharyngeal constrictor region, has a similar profile to the vascular cells from the E18.5 samples (confirmed with cluster analysis), indicating it may be a precursor to the vasculature in the mesenchymal condensation at the cranial base/pharyngeal interface. Examining this limited cohort of markers further emphasized how diverse the expression profiles of the cells were and reiterated that many markers are not confined to being expressed by cells of a single fate; a future study, to increase the experimental cohort and produce statistically significant expression profiles from the various regions explored in this pilot study is warranted.

In studies categorising differential gene expression between groups of cells, the ultimate confirmation of the present calls on microarrays includes either quantitative real-time PCR (qRT-PCR) or *in situ* analysis of the mRNA expression in the adjacent tissues to those captured. In the current study, differential analysis between groups was prohibited by the low number of samples from each group in the 12 microarrays that ultimately passed all quality controls. Any differential expression would be statistically invalid as there were not three replicates in each group. As such confirmation of gene expression with *in situ* is planned once future studies increase the cohort.

11.2.5.4 Further controls

In the current study, the abundance of the transcripts of expressed genes was not examined; the study was binary in nature and the microarrays were not used to quantify gene expression levels. This obliterated the need for quality controls relating to confirming the accuracy of in how far the cDNA represented the distribution of RNA (ex: qRT-PCR, spiking in RNAs, dilution experiments).

There were, however, two controls not included in the current study that would be recommended in future studies: reproducibility of the arrays (cDNA from the same cell hybridised in duplicate) and controls for the labelling efficiency in the biotinylation step.

A reproducibility analysis was conducted early in the study, prior to optimisation of the fragmentation step, in sample #8, which was found to be over-fragmented based on Bioanalyzer results. Among the three replicates, only 30-40% of the present hits were shared between all three arrays (depending on the overall % present), 10-15% were shared between any two of the arrays, and 47-51% were unique present calls among one of the replicates. Comparing the three replicates of sample 8 to the blank sample, run in the same batch, revealed 93% of the present calls in the blank were not shared with any of the replicates of sample 8. This indicated that the three repeats were not reproducible, but most probably contained "real" hits,

but the over-fragmentation had indiscriminately split the cDNA such that only 2-2.6% of the genes on the array were indicated to be expressed (compared to the 1% array coverage of the blank sample). Low expression levels in the arrays could also be attributed to incomplete biotin labelling, such that there was no "tag" on the cDNA annealed to probes that would allow the scan to detect the hybridisation. In the future, controls for labelling would be recommended and optimisations undertaken as necessary; issues of labelling were not raised in the Tietjen *et al.* 2003 protocol, and the terminal transferase enzyme conferring the biotin label has not been altered (cloned, recombined, altered activity level, etc) since the 2003 study. However, the finding that the fragmentation needed optimisation despite no discernible changes to the RQ1 DNAse enzyme supports the idea that all steps involving enzymatic reactions should be checked with a quality control and not assumed to be successful.

11.2.6 Discussion

The aim of the optimisation to the 2003 protocol was to create a workflow that would enable me to explore the transcriptomes of single cells isolated by laser capture microdissection. An ideal workflow would be able to distinguish between samples that would generate good data, from those whose poor quality is prohibitive to further analyses. We hybridised 26 "good" samples that had passed pre-microarray quality controls and an additional 5 "bad" samples, which had failed QC or were blank. The final experimental cohort, following the post-hybridisation controls, included only 12 samples, or 46% of the original 26 (excluding 56%). It is impossible for us to know how this compares to published studies as the process of optimisation is never included in the final literature report. Crucially, in hindsight I should not have hybridised 9 of the arrays with questionable bioanalyser results, which would have reduced the % of arrays excluded from the final cohort to the 30% with extremely low array coverage. Although the samples with low % present may be perfectly valid, and represent more quiescent cells, I chose to err on the

side of caution and not include samples with less than 4% coverage in analyses for the study.

Within the 12 final samples, those that were captured from E13 samples (n = 7) had a % present range on the array of 4-8.9% with an average of 6.6%; the E18.5 samples (n =5) have a % present range from 7.5-14.9%, with an average of 10.7%. I attribute this difference to the fact that the E13 samples were the first to be captured and used to optimise the protocol, and the E18.5 samples were isolated at a later date under the most optimised conditions, with minimal time for degradation prior to hybridisation. If this is the case, future studies should expect to yield similar results to the E18.5 samples using the optimised protocol. Alternatively, the cells at E13 may have less genes being expressed due to the stage of cell differentiation or the nature of the tissues from which they were isolated.

Overall, I am satisfied that the current updated protocol can be used to successfully conduct single cell transcriptome analyses, provided strict adherence to quality controls is followed. Further optimisations to confirm reproducibility and biotin labelling efficiency will further enhance the current protocol.

Table 11.2.1: Histological preparations for tissues subjected to laser capture microdissection (LCM). Protocols were optimised according to genotype to identify cell lineage and morphology, thoroughly dehydrate the tissue and minimise RNA degradation.

2003 PROTOCOL		UPDATED: *Wnt1*-Cre x R26LacZ		UPDATED: *Wnt1*-Cre x XZ-DR	
70% EtOH	30 Sec	70% EtOH	2 minutes	70% EtOH + 5/1000 DAPI	2 minutes
H2O	5 sec	H2O	5 sec	95% EtOh	10 sec
Mayer's Hematoxylin	1 minute	Mayer's Hematoxylin	2 minutes	95% EtOh	30 sec
H2O	5 sec	H2O	5 sec	100% EtOH	1 minute
Bluing Reagent	1 minute	Bluing Reagent	1 minute	100% EtOH	1 minute
7-% EtOh	10 sec	7-% EtOh	10 sec	Xylene	5 minutes
95% EtOH	10 sec	95% EtOH	10 sec	Xylene	5 minutes
Eosin Y	20 sec	Eosin Y	20 sec	Air Dry	2 minutes
95% EtOh	30 sec	95% EtOh	30 sec		
95% EtOh	30 sec	95% EtOh	30 sec		
100% EtOH	1 minute	100% EtOH	1 minute		
100% EtOH	1 minute	100% EtOH	1 minute		
Xylene	5 minutes	Xylene	5 minutes		
Xylene	5 minutes	Xylene	5 minutes		
Air Dry	15 minutes	Air Dry	2 minutes		

Table 11.2.2: Enzymes used in the single cell transcriptome analyses. Enzymes with modifications (due to availability, activity, properties, etc.) between the 2003 and updated protocol are indicated in red.

2003 PROTOCOL				UPDATED PROTOCOL			
Enzyme	Activity	Company	Catalog #	Enzyme	Activity	Company	Catalog #
RNA Guard	35,700 U/mL	Amersham Pharmacia	27091501	No replacement product			
Prime RNAse inhibitor	30 U/µL	Brinkman Eppendorf	32005.357	RNAse inhibitor (cloned)	40 U/µL	Applied Biosystems	AM2682
MMLV reverse transcriptase + buffer	200 U/µL	Invitrogen	28025-013	MMLV reverse transcriptase + buffer	200 U/µL	Fisher UK	BPE32085
AMV reverse transcriptase	1-5U/µL	Invitrogen	18020-024	AMV reverse transcriptase (cloned)	15U/µL	Fisher UK	12328-019
Terminal transferase (recombinant)	400 U/µL	Roche	03-3333-566	Terminal transferase (recombinant)	400 U/µL	Roche	03-3333-566
RNAse free DNAse, RQ1	1 U/µL	Promega	M6101	RNAse free DNAse, RQ1	1 U/µL	Promega	M6101
Terminal transferase	15 U/µL	Invitrogen	10533-016	Terminal transferase	15 U/µL	Invitrogen	10533-016

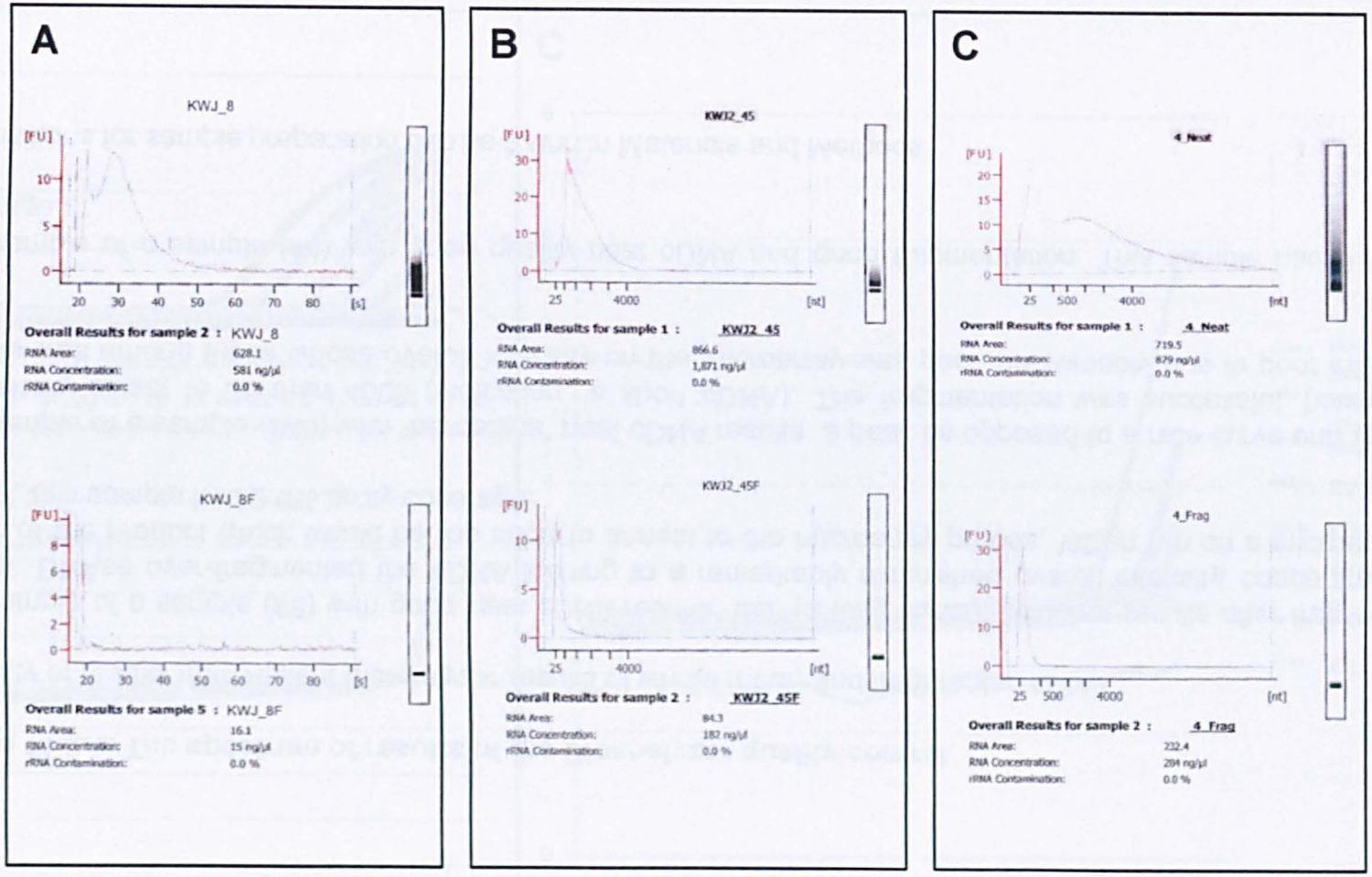
A
KWJ_8
[FU]
10
5
0
20 30 40 50 60 70 80 [s]
Overall Results for sample 2 : KWJ_8
RNA Area: 628.1
RNA Concentration: 581 ng/µl
rRNA Contamination: 0.0 %
KWJ_8F
[FU]
8
6
4
2
0
20 30 40 50 60 70 80 [s]
Overall Results for sample 5 : KWJ_8F
RNA Area: 16.1
RNA Concentration: 15 ng/µl
rRNA Contamination: 0.0 %
B
KWJ2_45
[FU]
30
20
10
0
25 4000 [nt]
Overall Results for sample 1 : KWJ2_45
RNA Area: 866.6
RNA Concentration: 1,871 ng/µl
rRNA Contamination: 0.0 %
KWJ2_45F
[FU]
10
5
0
25 4000 [nt]
Overall Results for sample 2 : KWJ2_45F
RNA Area: 84.3
RNA Concentration: 182 ng/µl
rRNA Contamination: 0.0 %
C
4_Neat
[FU]
20
15
10
5
0
25 500 4000 [nt]
Overall Results for sample 1 : 4_Neat
RNA Area: 719.5
RNA Concentration: 879 ng/µl
rRNA Contamination: 0.0 %
4_Frag
[FU]
30
20
10
0
25 500 4000 [nt]
Overall Results for sample 2 : 4_Frag
RNA Area: 232.4
RNA Concentration: 284 ng/µl
rRNA Contamination: 0.0 %

Figure 11.2.1: The spectrum of results of the Bioanalyzer quality control

A variety of results from Agilent Bioanalyzer results of whole (neat) and fragmented cDNA.

A. Example of a sample (#8) with good neat cDNA results, top, (a long curve), but poor results after fragmentation, bottom. DNAse over-fragmented the cDNA leading to a remarkably diminished overall intensity, concentration and length of the product which would be too short to anneal to the microarray probes. When run on a microarray as a control, this sample had 2.6% array coverage.

B. Example of a sample (#45) with "borderline" neat cDNA results: a peak as opposed to a nice curve and the height of intensity closer to 25 than 4000 (indicating a short cDNA). The fragmentation was successful, however, this sample was among those whose overall intensity on the microarray was poor, presumably due to poor initial cDNA quality.

C. Example of a sample (#4) with good quality neat cDNA and good fragmentation. This sample had 9.7% array coverage.

* Conditions for sample preparation can be found in Materials and Methods.

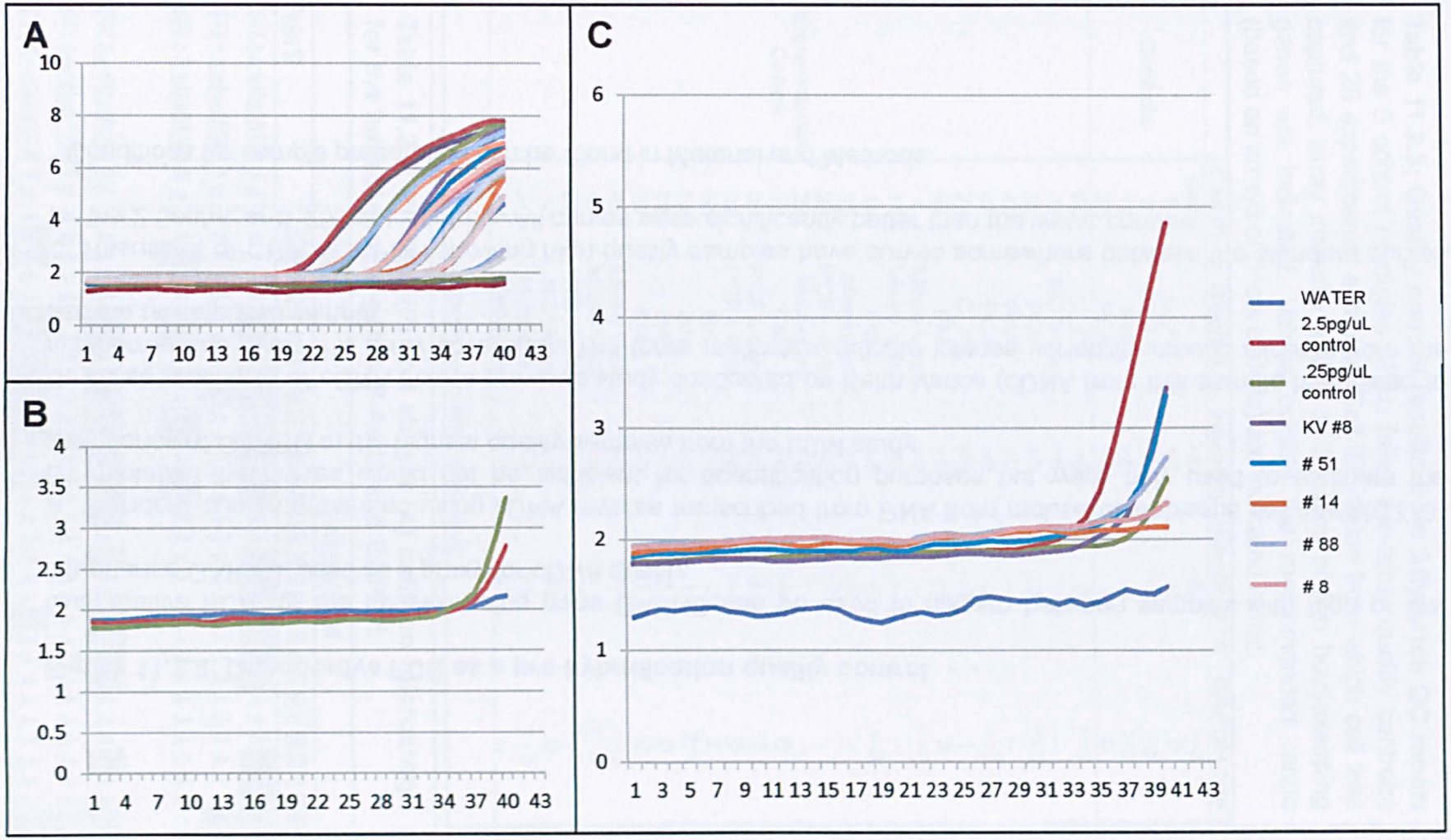
A
10
8
6
4
2
0
1 4 7 10 13 16 19 22 25 28 31 34 37 40 43
B
4
3.5
3
2.5
2
1.5
1
0.5
0
1 4 7 10 13 16 19 22 25 28 31 34 37 40 43
C
6
5
4
3
2
1
0
1 3 5 7 9 11 13 15 17 19 21 23 25 27 29 31 33 35 37 39 41 43
WATER
2.5pg/uL control
.25pg/uL control
KV #8
51
14
88
8

Figure 11.2.2: Quantitative PCR as a pre-hybridisation quality control

Quantitative PCR for the housekeeping gene GAPHD can be used to discern between samples with high or low abundance GAPDH, used as a proxy for cDNA quality.

A. Standard curves generated using cDNA reverse transcribed from RNA from mouse osteoblastic cell line MC3T3-E1. Notably, the curves would not be sufficient for quantification purposes but were only used to estimate the abundance of GAPDH in the highest quality samples from the LCM study.

B. Three replicates of cDNA from a previous study conducted by Keith Vance (cDNA from this sample hybridised to microarray had over 11% array coverage). The three replicates indicate intense variability among aliquots from the sample re-amplified sample.

C. Results of qPCR for GAPDH showing high quality samples have curves somewhere between the standard curves for the 2.5pg/μL and .25pg/μL controls. All curves were significantly better than the water control.

* Conditions for sample preparation can be found in Material and Methods.

Table 11.2.3: Quality control results from AffyBatch QC report for the 5 control (samples which failed pre-array quality controls) and 26 experimental samples. Cell ID, region from which cell was captured, array intensity and 3' to 5' ratios of two housekeeping genes are indicated. Values outside the recommended range (based on arrays of pools of cells) are indicated in red.

	Cell ID	Region	Intensity	β-Actin 3'/ 5'	GAPDH 3'/5'
Controls	blank	--	<6	-2.5	<-3
	8	C_Ph	<6	>3	2
	8	C_Ph	<6	>>3	>3
	14	FM	>6	-1	>3
	33	PCF	<6	1	0
Experimental Cohort	80	C_Ph	>6	3	>>3
	31	NC Vasc	>6	>>3	--
	39	PCF	>6	3	>>3
	45	PCF	<6	--	--
	48	PCF	>6	2	>>3
	74	C_Ph	<6	-1	1
	88	FM	>6	-1	3
	4	Meso Vasc	>6	--	>>3
	11	Meso Vasc	<6	--	--
	14	FM	>6	1	<-3
	19	Meninges	>6	>>3	--
	24	PCF Loose	>6	>>3	--
	27	Meninges	>6	--	--
	18	FM	>6	>>3	0
	31	PCF Loose	>6	2.5	3
	33	PCF Loose	>6	>>3	3
	51	BA	<<6	-3	2
	58	BA	<<6	-1.5	2.5
	66	BA	<<6	-1.5	0
	87	FM	>6	-1.5	0
	45	Meso Vasc	<<6	>>3	>>3
	46	Meso Vasc	<<6	>>3	>>3
	28	NC Vasc	<<6	2	>>3
	30	NC Vasc	<<6	>>3	0
	20	Meninges	<<6	>>3	>>3
	24	Meninges	<<6	>>3	--

=outside recommended limit

Table 11.2.4: Present (P) and absent (A) calls on microarrays for the housekeeping genes β-Actin and GAPDH.

	Control					Experimental Cohort																									
Probe ID	--	8A	8B	14	33	4	11	14	19	24	27	31	39	45	48	74	88	20	30	24	28	46	45	87	66	51	58	33	31	18	80
AFFX-b-ActinMur/M12481_3_at	A	A	A	A	A	P	P	A	P	P	P	P	P	P	P	A	A	P	P	P	P	P	P	P	A	A	A	P	P	P	P
AFFX-b-ActinMur/M12481_5_at	A	A	A	A	A	A	A	A	A	P	A	A	A	A	A	A	A	A	A	A	A	A	A	A	A	A	A	A	A	A	M
AFFX-b-ActinMur/M12481_M_at	A	A	P	A	A	P	P	A	P	A	P	P	A	P	P	A	A	A	A	A	A	P	A	A	A	A	A	A	A	A	A
AFFX-GapdhMur/M32599_3_at	A	A	A	A	A	P	P	A	P	P	P	P	P	P	P	P	A	P	A	P	P	P	P	P	A	A	A	P	A	A	P
AFFX-GapdhMur/M32599_5_at	A	A	A	A	A	A	A	A	A	A	A	M	A	A	A	A	A	A	A	A	A	A	A	A	A	A	A	A	A	A	P
AFFX-GapdhMur/M32599_M_at	A	P	P	A	A	P	P	P	P	P	P	P	A	P	A	A	A	A	A	A	A	P	A	A	A	A	A	A	A	A	P

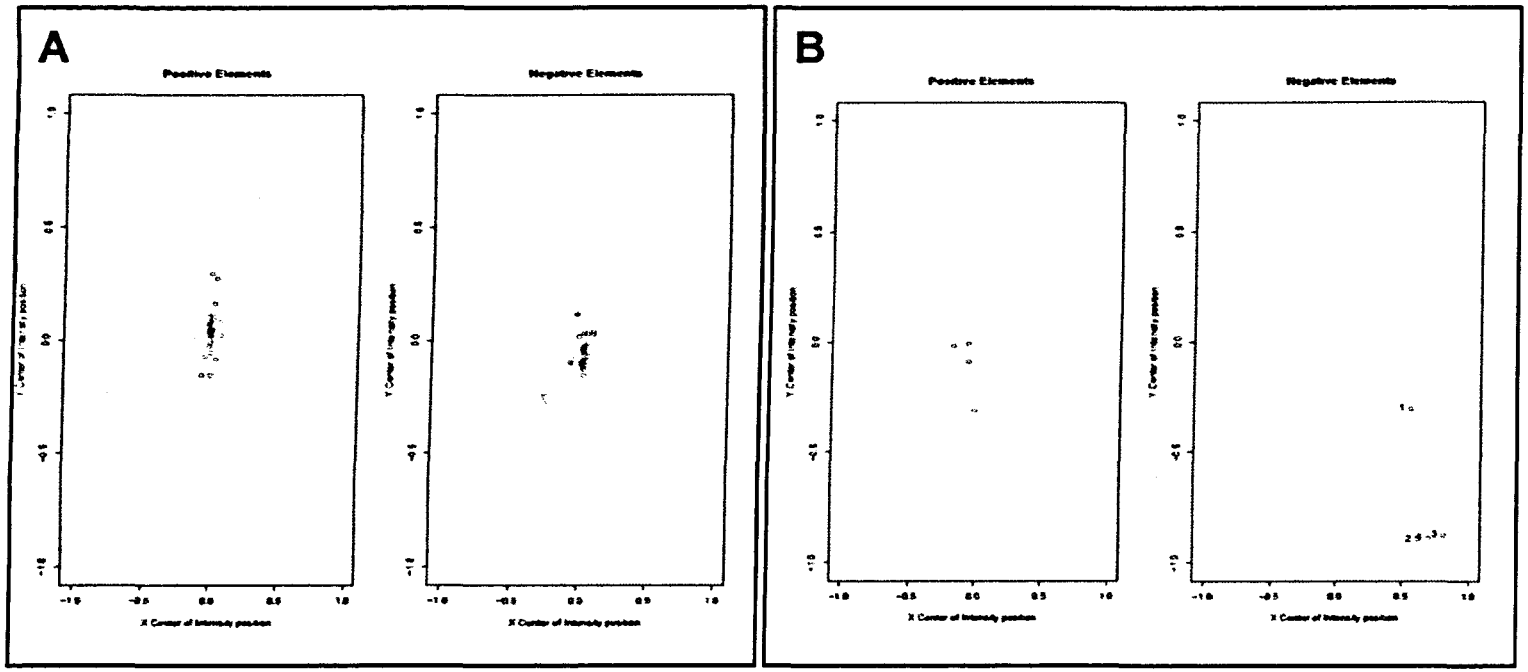

Figure 11.2.3: Results of AffyBatch quality controls for border element clustering

The results of the clustering of the positive and negative border elements for the "good" microarrays (**A**) versus the "bad" Bioanalyzer-failed control microarrays (**B**) demonstrates the poor clustering among the controls.

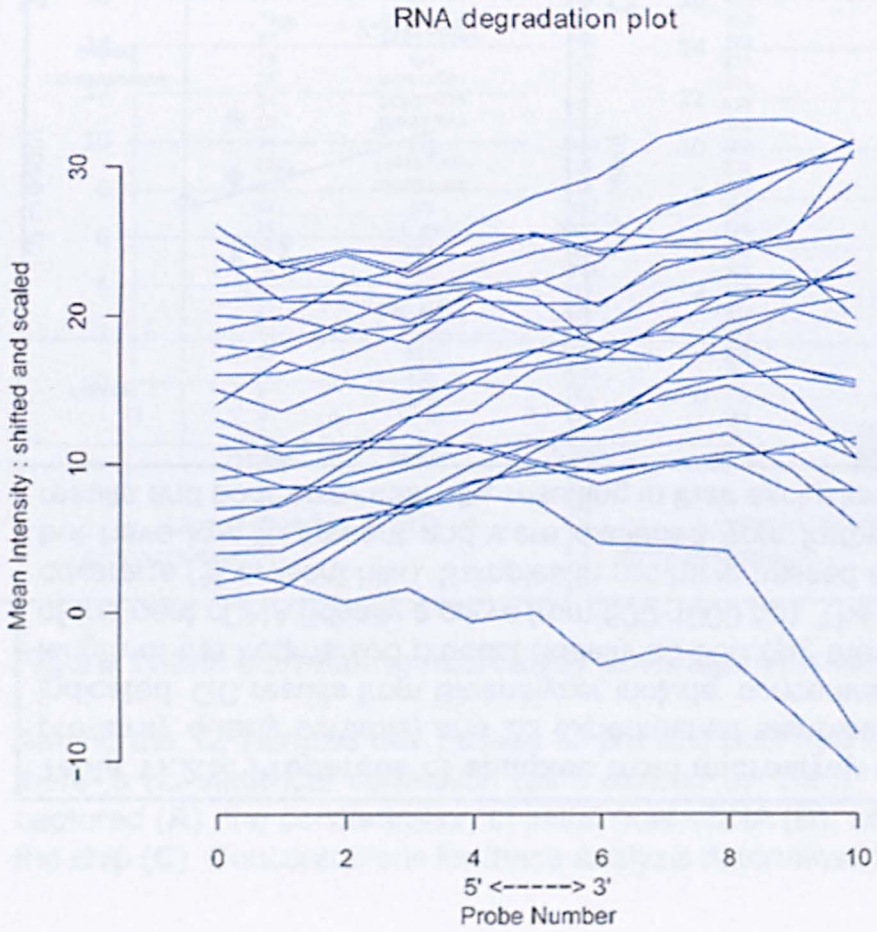

Figure 11.2.4: RNA degradation analysis of the single cell transcriptome samples

RNA degradation plots indicate the vast majority of the samples had little difference in the mean intensity of the 5' versus 3' probes in the microarrays, which should imply there is little RNA degradation among the samples; furthermore, the cDNA was long enough to not be too biased toward the 3' probes. The validity of using RNA degradation plots as a quality control for single-cell transcriptome analyses has not been raised previously in the literature.

Table 11.2.5: Properties of samples from microarray analyses. Properties of the 5 control (samples which failed pre-array quality controls) and 26 experimental samples. Cell ID and region from which the cell was captured are indicated. QC results from Bioanalyzer include: concentrations of 1 µL of neat and fragmented cDNAs, as well as the length of the fragmented product (ideally 25-500 bp), the intensity of the fragmented product, and the characteristics of the neat cDNA (ideally a curve from 500-1000 bp). The intensity on the arrays is also indicated, as well as the array coverage (% present hits). Samples in red have passed all pre and post-array QC; samples in blue have passed QC but have low % present and were excluded from further analyses; arrays in green had questionable Bioanalyzer results and poor array intensity, resulting in their exclusion from further analyses.

	Cell ID	Region	[neat]	[frag]	ug hybed	Array Coverage	Frag Length	neat cDNA	Intensity Frag	Array Intensity
Control	blank	--	--	--	--	1	--	--	--	--
	8	C_Ph	331	64	2.6	2.1	<30	peak at 30	2	ok
	8	C_Ph	547	10	0.4	2.6	<20	curve at 30	--	ok
	14	FM	1237	389	15.6	1.2	500	peak/curve at 500	20	ok
	31	PCF	1158	141	5.6	2.4	500	peak at 500	20	ok
Experimental Cohort	80	C_Ph	826	500	20	8.9	25-500	peak at 500	20	Good
	31	NC Vasc	855	236	9.4	10.6	25-500	curve at 500	20	Good
	39	PCF	833	190	7.6	4.9	25-500	curve at 500	15	Good
	45	PCF	1117	227	9.1	5.7	25-500	curve at 500	20	ok
	48	PCF	653	225	9	5.8	25-500	curve at 500	15	Good
	74	C_Ph	1312	238	9.5	2.2	25-500	curve at 500	20	ok
	88	FM	1371	398	15.9	3.1	25-500	curve >500	25	Good
	4	Meso Vasc	879	284	11.4	9.7	25-500	curve >500	30	Good
	11	Meso Vasc	972	308	12.3	11	25-500	curve at 500	20	ok
	14	FM	1399	305	12.2	2.5	25-500	curve >500	20	Good
	19	Meninges	1295	236	9.4	7.5	25-500	curve >500	25	Good
	24	PCF Loose	863	229	9.2	8.5	25-500	curve at 500	15	Good
	27	Meninges	956	244	9.8	14.9	25-500	curve at 500	20	Good
	18	FM	809	111	4.4	4	25-500	peak at 1000	20	Good
	31	PCF Loose	665	157	6.3	3	25-500	peak at 1000	25	Good
	33	PCF Loose	582	130	5.2	2.5	25-500	peak at 1000	20	Good
	87	FM	622	132	5.3	8.6	25-500	odd curve >1000	20	Good
	51	BA	373	141	5.6	1.7	25-500	curve >500	2	Poor
	58	BA	505	137	5.5	1.8	25-500	peak at 500	20	Poor
	66	BA	650	107	4.3	1.8	25-500	peak at 500	15	Poor
	45	Meso Vasc	1871	182	7.3	2	25-500	peak at 500	10	Poor
	46	Meso Vasc	1252	9	0.4	3.3	25-500	peak <500	3	Poor
	28	NC Vasc	1495	20	0.8	5	25-500	peak <500	3	Poor
	30	NC Vasc	1356	32	1.3	2	25-500	peak <500	6	Poor
	20	Meninges	1458	16	0.6	3.8	25-500	peak <500	2	Poor
	24	Meninges	1414	20	0.8	4.6	25-500	peak <500	3	Poor

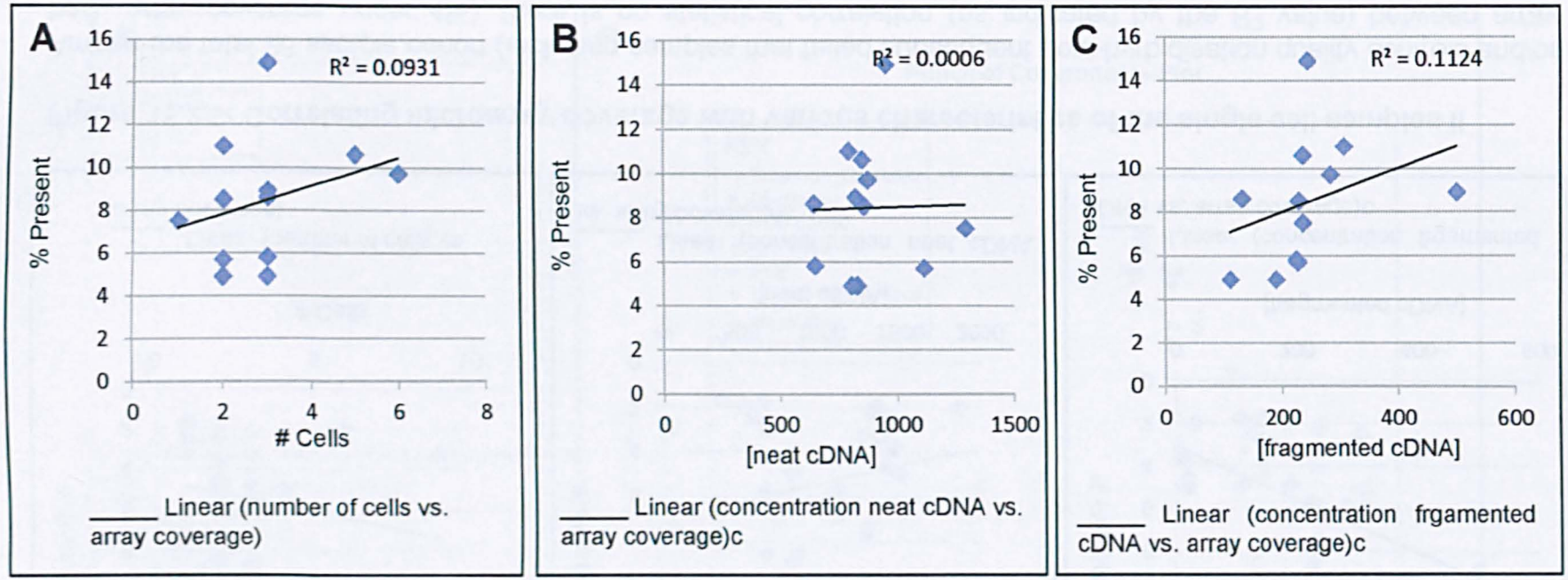

Figure 11.2.5: Correlating microarray coverage with various characteristics of the single cell samples

Among the 12 samples that passed all pre and post-hybridisation quality controls, and had over 4% array coverage, there is no statistical correlation (as indicated by the R^2 value) between array coverage and the number of cells captured (**A**), the concentration of initial neat cDNA (**B**), nor the concentration of the fragmented cDNA hybridised to the chip (**C**). Concentrations for these analysis determined by Bioanalyzer results.

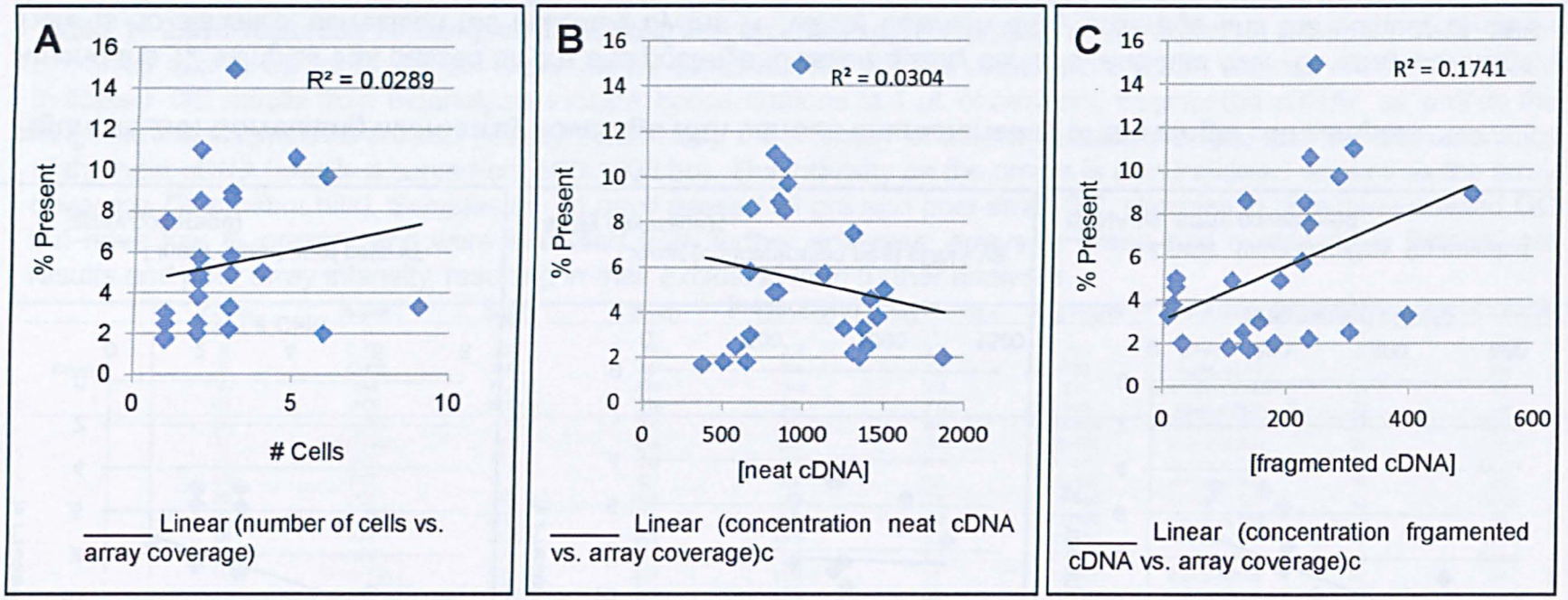

Figure 11.2.6: Correlating microarray coverage with various characteristics of the single cell samples II

Among the total 26 sample cohort (including samples that failed subsequent post-hyrbidisation quality controls and/or had array coverage under 4%), there is no statistical correlation (as indicated by the R^2 value) between array coverage and the number of cells captured (**A**), the concentration of initial neat cDNA (**B**), nor the concentration of the fragmented cDNA hybridised to the chip (**C**). Concentrations for these analysis determined by Bioanalyzer results.

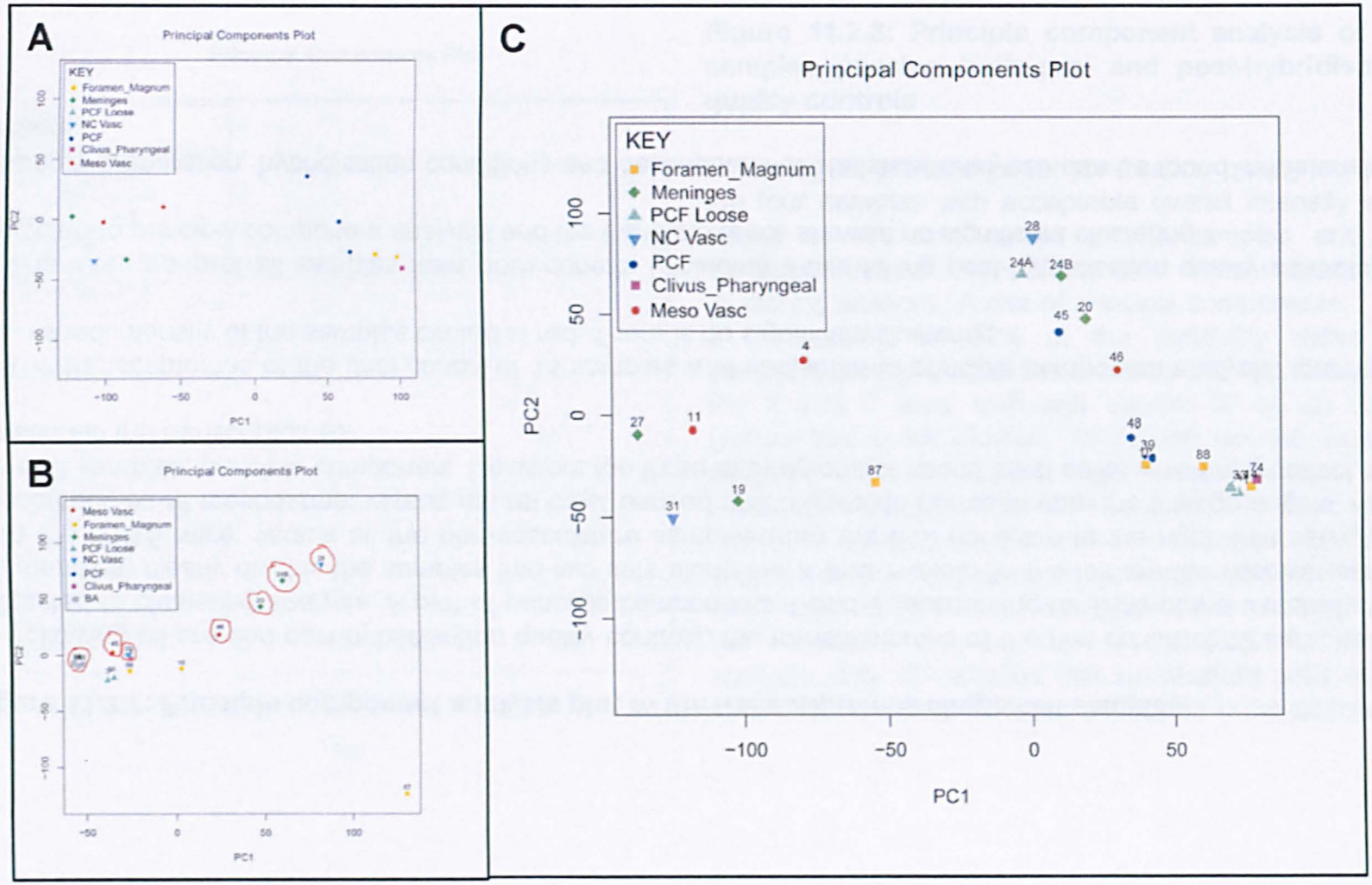
A
Principal Components Plot
KEY
Foramen_Magnum
Meninges
PCF Loose
NC Vasc
PCF
Clivus_Pharyngeal
Meso Vasc
PC1
PC2
B
Principal Components Plot
Meso Vasc
Foramen_Magnum
Meninges
PCF Loose
NC Vasc
PCF
Clivus_Pharyngeal
BA
PC1
PC2
C
Principal Components Plot
KEY
Foramen_Magnum
Meninges
PCF Loose
NC Vasc
PCF
Clivus_Pharyngeal
Meso Vasc
PC1
PC2

Figure 11.2.7: Principle component analysis plot of the transcriptomes single cell samples

A. Following all pre and post-hybridisation quality controls, the transcriptomes of the first cohort of 12 samples were subjected to clustering analysis. A plot of principle components 1 and 2 (accounting for 99% of the variability within the samples) clearly divides the samples into two sets along the X and Y axes. To the left are the vascular samples from the E18.5 mice; versus all the non-vasculature samples from the E13 mice are to the right. Interestingly, the transcritpomes of mesodermal versus neural crest derived vasculature do not segregate the lineage origins. Among the E13 samples, principle component 1 clusters the three sub-regions of neural crest cells, which may reflect region variation in the transcriptomes.

B. The transcriptomes of the final cohort of 14 samples was subjected to principle component analysis, ignoring the diminished intensity of the samples circled in red. There is no significant clustering.

C. The total group of all samples from both cohorts (including those failing post-hybridisation quality controls) was subjected to principle component analysis and the transcriptomes showed no significant clustering.

* Sample preparation, hybridisation conditions and descriptions of statistical analyses can be found in Materials and Methods.

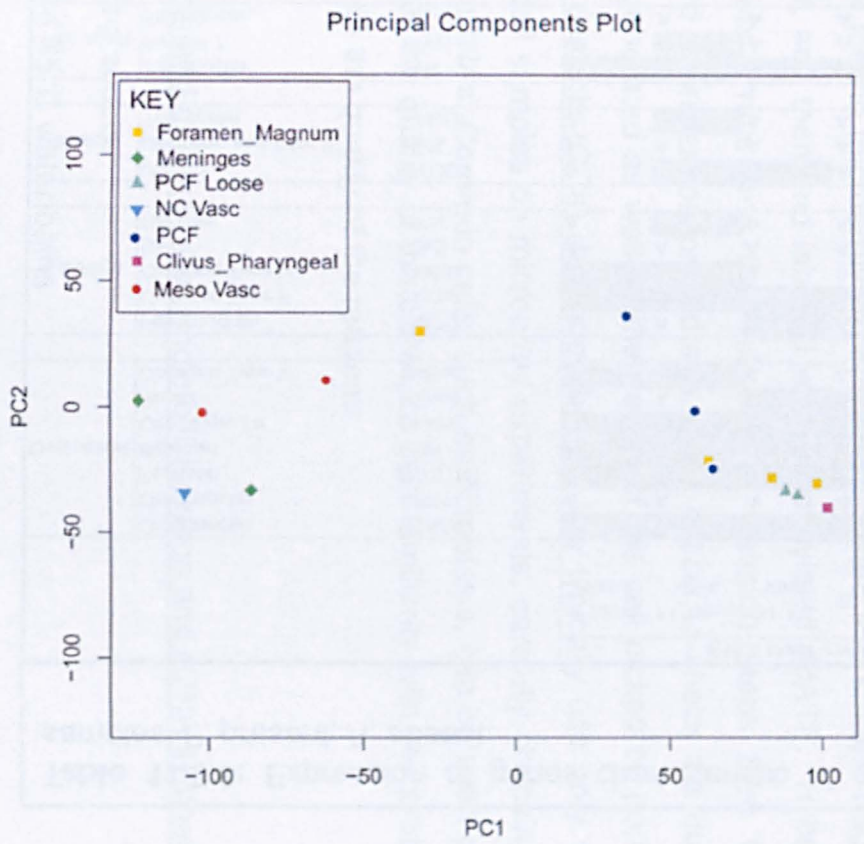

Figure 11.2.8: Principle component analysis of the samples passing both pre- and post-hybridisation quality controls

Following all pre and post-hybridisation quality controls, the four samples with acceptable overall intensity were added to the first cohort of 12 samples and the transcriptomes of the 16 samples were subjected to clustering analysis. A plot of principle components 1 and 2 (accounting for 99% of the variability within the samples) clearly divides the samples into two sets along the X and Y axes, with only sample 87 as an outlier (yellow box in left cluster). To the left are the vascular samples from the E18.5 mice; versus all the non-vasculature samples (bar #87) from the E13 mice are to the right. Notably, the samples to the bottom right most corner, comprising samples from 3 sub-regions of neural crest cells, have the lowest overall array coverage and this clustering may be due to that fact. For further analysis, only 12 sampled that successfully pass all QC and have %present > 4% were included in the analysis.

Table 11.2.6: Expression of genes characteristic of certain lineages within the final experimental cohort of 12 samples. P, present; A, absent.

			E18.5 *Wnt1*-cre x XZ-DR					E13 *Wnt1*-cre x ROSA26LacZ						
			4_Meso Vasc	11_Meso Vasc	31_NC Vasc	19_Meninges	27_Meninges	39_PCF	45_PCF	48_PCF	24_Loose PCF Mes	87_ForMag	18_ForMag	80 _Cli/Ph
Osteoblast	Osteonectin	SPARC	P	P	P	P	P	A	P	P	P	P	A	P
	Osteopontin	SPP1	A	A	A	A	A	A	A	A	A	A	A	A
	Periostin	POSTN	P	P	P	P	P	A	A	A	P	P	A	P
	Biglycan	BGN	P	P	P	P	P	A	M	P	M	P	A	A
	Coll I Type 2a	Col2a1	P	P	P	P	P	A	P	P	A	A	A	A
	Runx2	Runx2	A	A	P	P	P	A	A	A	A	P	A	M
	Collagen Type V	Col5a2	P	P	A	A	P	A	P	A	P	P	P	M
Cartilage	Fibromodulin	FMOD	A	A	P	A	P	P	A	A	P	P	A	A
	Collagen Type II	Col2a1	P	P	P	P	P	A	P	P	A	A	A	A
	Collagen Type IX	Col9a1	P	P	A	A	P	P	P	A	P	A	A	P
	Sox9	Sox9	A	A	A	A	A	A	P	P	P	A	A	
	Decorin	DCN	A	P	A	A	A	A	A	A	P	A	A	A
Muscle	Myosin	MYOD1	A	M	P	A	A	A	M	P	A	A	A	A
	Myogenic regulator 5	Myf5	A	A	A	A	A	A	A	A	A	A	A	A
	Transgelin	TAGLN	A	P	A	A	A	A	A	A	A	A	A	A
Fibroblast	Fibronectin	FN1	P	P	P	P	P	M	A	A	P	P	A	A
	Fibrillin 1	FBN1	A	P	A	A	P	A	P	A	A	A	A	A
	Fibroglycan	SDC2	A	A	A	A	P	A	P	M	A	A	A	A
Vascular	factor	VEGF	A	A	A	A	A	P	A	A	A	A	A	A
	Endothelial differentiation-related factor 1	EDF1	P	P	P	A	P	P	P	A	A	A	A	P
	LDL Receptor	LRP.../LDLR	A	M	P	A	P	A	P	A	A	A	P	A
	actin	ACTA1	P	P	P	P	P	A	P	A	A	A	A	P
	Tropomyosin alpha-1 chain	TMP1	P	P	P	P	P	A	P	A	A	A	A	P
	Matrix metalloproteinase 2	MMP2	P	M	P	A	P	A	P	A	P	P	A	A

11.2.7 SINGLE CELL MICROARRAY PROTOCOL: FROM SAMPLE PREPARATION TO MICROARRAY HYBRIDISATION

The following protocol was used to perform Affymetrix microarray analysis of single cell cDNAs. The generation of single cell cDNA is modified from Tiejen *et al.* 2003, itself a modification (Dulac and Axel 1995). Single cells are obtained by laser capture microdissection. Several micrograms of amplified cDNA are then synthesized by lysing the cell, reverse transcribing the total cellular RNA after oligodT priming, polyA tailing the 5' cDNA end, and finally amplifying the cell cDNA with a unique polyT primer. The reverse transcription is performed in limiting conditions of nucleotides and time in order to generate cDNA of uniform size (between ~500 bp and 1 kb), which are then more likely to be uniformly amplified. This allows the amplified cDNA to reflect an accurate representation of the various cell RNAs. This cDNA synthesis can be done on single cells, groups of cells, as well as very small amounts of RNA purified from several hundred cells by the RNAzol procedure. The single cell cDNA is usually re-amplified to provide enough material for the microarray experiment, digested into smaller fragments with DNAseI, and then end labelled with a biotinylated ddATP. Hybridization to Affymetrix arrays and the subsequent washing steps then follows the standard hybridization procedures. It is *critical* to check the quality of the cDNA generated as well as the nature of the cell picked by performing the quality controls (QCs) described herein. We typically use only 10% of our single cell samples on microarray experiments, carefully choosing only high quality cDNAs. Common cells, such as fibroblasts, can be used as a pilot to check for the quality of the cDNA, to gain familiarity with the protocol and to control for the quality of the reagents.

Reagents and materials (for single cell isolation and cDNA synthesis)

Dissecting scope

37°C and 65°C water baths

Perkin Elmer DNA thermal cyler

Multiwell PCR Machine

Arcturus PixCell II LCM

Agilent Bioanalyzer

NanoDrop Spectrophotometer

- AL1 primer: ATT GGA TCC AGG CCG CTC TGG ACA AAA TAT GAA (T)24 (0.2 µmol scale) MWGEurofins/Operon
- Amplitaq 5000, with 10X buffer, Applied Biosystems 5U/ul #N8080-156
- AMV reverse transcriptase 100U, 15 U/µl, Fisher UK
- Arcturus Capsure LCM caps
- Autoclaved thin walled reaction tubes, Applied Biosystems #N8010611
- BSA molecular grade 20 mg/ml, Roche #711454
- dNTP set, 100 mM each Roche #1277049
- H2O, RNAse, DNAse free, Cell & Mol Tech #TMS006C
- Mineral oil, molecular biology grade Sigma #M5904
- MMLV reverse transcriptase + buffer 5X, 40,000U, 200U/ul Fisher UK #BPE3208-5
- Nonidet P40 (NP40), 500 mL USB #19628
- Oligo dT24 (0.2 µmol scale) MWGEurofins/Operon
- Qia-quick PCR purification kit, Qiagen #28704
- RNAse inhibitor, 2500 units, Applied Biosystems #0032005.357
- Terminal transferase buffer 5X, Invitrogen #16314-015
- Terminal transferase, 8000 U, 400 U/µl Roche #3333566
- Triton X100, RNAse and DNAse free Sigma #T8787

I. Isolation of Single Cells

-- Embryonic day E9.5 & E10.5 wild-type mice, E13 *Wnt1*-Cre$^{+/-}$ x ROSA26LacZ$^{-/-}$ transgenic and E18.5 *Wnt1*-Cre$^{+/-}$ x XZ-DR$^{-/-}$ transgenic mice were dissected and embedded without fixation in Tissue-Tek OCT

compound, cryosectioned into 7-10 µm thick parasagittal sections, placed on permafrost coated glass slides (non-charged), and frozen immediately on dry ice before storage at -80°C.

The slides are taken through the following dehydration series immediately from the –80°C freezer; make sure all staining jars (coplin jars or disposable mailing jars) are thoroughly cleaned to be DNAse/RNAse free prior to staining:

Wild-type & ROSA26LacZ		XZ-DR	
70% EtOH	2 minutes	70% EtOH + 5:1000 DAPI	2 min
H2O	5 sec	95% EtOH	10 sec
Mayer's Hematoxylin	2 minutes	95% EtOH	30 sec
H2O	5 sec	100% EtOH	1 minute
Bluing Reagent	1 minute	100% EtOH	1 minute
70% EtOH	10 sec	Xylene*	5 min
95% EtOH	10 sec	Xylene*	5 min
Eosin Y	20 sec	air dry	2 min
95% EtOH	30 sec		
95% EtOH	30 sec		
100% EtOH	1 min		
100% EtOH	1 min		
Xylene*	5 minutes		
Xylene*	5 minutes		
air dry	2 minutes		

* Xylene kept in coplin jars in hood as Xylene dissolves plastic.

– Single cells were dissected using a PixCell II Laser Capture Microdissection microscope, as described by the manufacturer. The single cells were captured into Arcturus Capsure caps, using minimal power and duration to reduce spot size to capture single cells.

– Using a very clean (RNAse free: Wipe clean with RNAse Away or other appropriate solution. Keeping these tools under UV-light prior to use can also minimize contamination.) micro-scalpel or microdissection needle, the single cells were removed from the Capsure caps under a dissection microscope. This is done by cutting the plastic cap around each single cell with the micro-needle.

-- Using the micro-needle to lift the sample, place the dissected single cell into the bottom of a thin-walled PCR tube. Samples then stored at –80°C until the lysis step.

-- Prepare the single cell lysis buffer; for 25 reactions mix on ice:

MMLV buffer 5X (the "1st strand buffer")	25 µL
NP40 5%	0.625 µL
PrimeRNase inhibitor(= 60 U)	2 µL
stock primer mix	2.5 µL
dH2O	9 5µL

Stock primer mix (aliquot and store at –20°C)

100 mM dATP, dCTP, dGTP, dTTP solutions (12.5mM final)	10 µL each
50 OD/ml pd(T)24* [0.05OD/µL]	10 µL
H2O	30 µL

-- Aliquot 4 µl of this buffer into a thin-walled PCR reaction tube (Perkin Elmer) for each sample (Important: don't forget a zero control tube with no cell in it).

--Spin immediately for 30 seconds, to make sure the cell is indeed in the lysis buffer. Keep the collected cells on ice. Proceed to Part II.

II cDNA Synthesis and Amplification

--Lyse the cells by transferring the PCR tubes containing lysis buffer mix and cells from ice to a 65°C water bath for 2 min.

-- Keep several minutes at room temperature to allow the oligo-dT to anneal to the RNA.

-- Put back on ice. Spin 2 min at 4°C.

-- Prepare the 1:6 AMV:MMLV reverse transcriptase master mix; for 25 reactions mix on ice:

MMLV-reverse transcriptase (50 U/cell)	6.25 µL
AMV-reverse transcriptase (0.625 U/cell)	1.05 µL

– Add 0.3 µL of the reverse transcriptase mix to the cell mix and incubate for exactly 20 min at 37°C (no longer).

– Inactivate 10 min at 65°C.

– Put back on ice. Spin 2 min at 4°C.

– On ice, add 10U terminal tranferase (0.3 µL) to 4.5 µl 2X tailing buffer and add to cells:

stock 2X tailing buffer:

5X terminal transferase buffer (Invitrogen)	800 µL
100 mM dATP	30 µL
H2O	1.17 mL

– Incubate at 37°C for 15 min.

– Inactivate at 65°C for 10 min.

– Put back on ice. Spin 2 min at 4°C.

– Add 90 µl of ice cold PCR buffer (keep all reagents and PCR mix on ice to avoid primer dimer formation):

10X PCR buffer II	10 µL
MgCl2 25 mM	10 µL
BSA 25mg/mL	1 µL
each 100mM dNTP	1 µL
5% Triton (250 µl Trition + 4.75 mL dH2O)	1 µL
AL1 primer	5 µg
H20	to total vol 90 µL
AmpliTaq	2 µL
1or 2 drops of mineral oil	

(Note: If using thermocycler with heated lid, mineral oil is not necessary)

– Hot start PCR reaction on a Perkin Elmer DNA Thermal Cycler [holds up to 48 samples] (We have also used the Perkin Elmer geneamp PCR system 2400). Perform 25 cycles:

94°C for 1 min
42°C for 2 min
72°C for 6 min with a 10 sec extension time added each cycle

– When these 25 cycles have finished, add 1 µl of AmpliTaq directly in each tube (see a cloud when Taq is added).

– Perform 25 more cycles with the same program, except do not add the extension time, end with 4°C Hold.

– Once completed, keep on ice/store at –20°C.

IIa. QUALITY CONTROL:

1. Run a 5 µL aliquot of each sample on a 1.5% agarose gel and confirm there is a thick band of cDNA at the bottom and a faint smear or corners of the band, ideally reaching 0.4-1.2 kB. There may be a smear in the zero control due to minor bacterial contaminants in the enzyme solution.

– The best samples from Part II are used to proceed to Part III.

III. Re-Amplification of Single Cell cDNA

Re-amplify the single cell samples to generate large amounts of single cell cDNA.

- Per reaction, make up the following solution on ice:

Ultrapure H2O	80 µL
10X PCR buffer II	10 µL
10X MgCl2	10 µL
100 mM dATP	0.2 µL
100 mM dCTP	0.2 µL
100 mM dGTP	0.2 µL
100 mM dTTP	0.2 µL
AmpliTaq	1 µL
AL-1 primer	5µg

Each cell gets five reactions, so if three cells are to be re-amplified, make 16 reactions worth (3 cells x 5 + blank DNA control = 16).

– Add 100 µL to a negative control tube.

– Add 100 µl to each tube for each single cell reaction, then add 2 µl of single cell cDNA .

– Add mineral oil to each tube (if using PCR machine without heated top).

– On the PCR machine, run the following for 30 cycles:

94°C	1 min 30s
42°C	2 min
72°C	3 min
followed by 72°C	20 min
4°C	until ready to process

– PCR purify using Qiagen PCR purification kit. Each column can hold 10 µg of cDNA, so 2 reactions can be purified/column. Elute each column in 30 µL, generating ~20 µg of each single cell reaction in 60 µL total volume.

– Use a spectrophotometer to measure the concentration of cDNA. Following this procedure, we typically get between 20-50 µg of single cell cDNA.

IIIa. QUALITY CONTROL

1. Run a 5-10 µL aliquot of each sample on a 1.5% agarose gel and confirm there is a thick smear of cDNA reaching >500 bp in length. There may be a faint smear in the zero control due to minor bacterial contaminants in the enzyme solution.

2. Confirm the presence of the transgene, or highly expressed housekeeping genes (such as GAPDH) with PCR. Primers must correspond to 3' most end of the genes as the cDNA generated are mostly <1 kB.

3. Test the quality of the cDNA using quantitative PCR for GAPDH. Run each sample in triplicate and also run a re-amplified sample from single cell cDNA that has previously successfully generated good microarray results; compare

the results to an RT-negative control, the standard curves generated from cDNA of known concentration (such as from a cell line), and each other. qPCR should be used to discriminate between the quality of the individual reamplificates and not for quantification.

4. Run a 1 µL aliquot of each single cell re-amplified cDNA on Agilent Bioanalyzer to confirm concentration, cDNA length, and quality. Neat cDNA should generate a long curve. Compare the results of "good" and "bad" samples from previous QC to become familiar with the results expected from high and low quality samples (and the zero control). ** No cDNA should be hybridized to microarrays unless they pass Bioanalyzer QC!

– Based on these control experiments, it is possible to find a number of high quality samples that can be used for a microarray experiment in Part V

V. Labeling of Single Cell cDNA and Microarray Hybridization

Additional materials and reagents:

One Phor-All Buffer, Amersham, but no longer available #27-0901-02

RNAse free DNAse, RQ1, Promega 1000 U, #M6101

Biotin-N6 ddATP, Perkin Elmer #NEL508

Terminal Transferase, 500 U, Invitrogen #10533-016

(Note: all volumes are scaled up 1.5X to avoid evaporation problems. This ensures enough volume for multiple hybridizations with the same sample to standard Affymetrix Genechips.)

– In an eppendorf tube, mix the following reaction for each single cell cDNA to be analyzed:

20 µg* of re-amplified, purified single cell cDNA	x µL
10X One-Phor-All buffer	6 µL
0.7 U RQ1 DNAse	0.75 µL

Eluate buffer (Tris from Qiagen kit)	up to 60 µL
Total rxn:	60 µl

* note: standard Affy protocol will only use 2/3 of reaction for hybridization, therefore using 20 µg of cDNA will mean 15 µg is hybridized. Less cDNA can be used, Affymetrix recommends no less than 7-10 µg.

– Incubate the samples at 37°C for 13 minutes (sharp).

– Heat Inactivate the DNAse at 99°C for 15 minutes (ALWAYS cap the samples). Spin briefly in microfuge.

– Remove 1 µL aliquot of sample for Bioanalyzer quality control.

– Using the entire 60 µl sample of fragmented DNA, add:

Biotin-N6_ddATP (1.0 mM)	1.5 µL
Terminal Transferase (15 U/µl; Invitrogen)	1.25µL

– Incubate at 37°C for 1.5 hours.

– Heat inactivate reaction at 65°C for 15 minutes. Put on ice for 5 minutes.

**At this point, protocol essentially merges with the standard Affymetrix protocol for preparing samples for microarrays.

Va. QUALITY CONTROL

1. Run the 1 µL aliqot of fragmented cDNA on an Agilent Bioanalyzer to confirm the cDNA has been successfully fragmented. Over fragmented samples will be less than 25-bp length and under-fragmented samples will still be around 500 bp in length. After fragmentation the concentration is reduced, but should still be >250 ng/µL; the fragmented cDNA appears as a peak, not a curve. ** No cDNA should be hybridized to microarrays unless they pass Bioanalyzer QC!

– Based on these control experiments, it is possible to find a number of high quality samples that can be hybridised to microarrays

12. Bibliography

Abzhanov, A., Rodda, S. J., McMahon, A. P. and Tabin, C. J. (2007). Regulation of skeletogenic differentiation in cranial dermal bone. *Development* **134**(17): 3133-3144.

Abzhanov, A., Tzahor, E., Lassar, A. B. and Tabin, C. J. (2003). Dissimilar regulation of cell differentiation in mesencephalic (cranial) and sacral (trunk) neural crest cells in vitro. *Development* **130**(19): 4567-4579.

Ahlberg, P. E. and Koentges, G. (2006). Homologies and cell populations: a response to Sanchez-Villagra and Maier. *Evol Dev* **8**(2): 116-118.

Akech, J., Wixted, J. J., Bedard, K., van der Deen, M., Hussain, S., Guise, T. A., van Wijnen, A. J., Stein, J. L., Languino, L. R., Altieri, D. C., Pratap, J., Keller, E., Stein, G. S. and Lian, J. B. (2010). Runx2 association with progression of prostate cancer in patients: mechanisms mediating bone osteolysis and osteoblastic metastatic lesions. *Oncogene* **29**(6): 811-821.

Anderson, H. C., Harmey, D., Camacho, N. P., Garimella, R., Sipe, J. B., Tague, S., Bi, X., Johnson, K., Terkeltaub, R. and Millan, J. L. (2005). Sustained osteomalacia of long bones despite major improvement in other hypophosphatasia-related mineral deficits in tissue nonspecific alkaline phosphatase/nucleotide pyrophosphatase phosphodiesterase 1 double-deficient mice. *Am J Pathol* **166**(6): 1711-1720.

Armstrong, V. J., Muzylak, M., Sunters, A., Zaman, G., Saxon, L. K., Price, J. S. and Lanyon, L. E. (2007). Wnt/beta-catenin signaling is a component of osteoblastic bone cell early responses to load-bearing and requires estrogen receptor alpha. *J Biol Chem* **282**(28): 20715-20727.

Armulik, A., Abramsson, A. and Betsholtz, C. (2005). Endothelial/pericyte interactions. *Circ Res* **97**(6): 512-523.

Aubin, J. E., Gupta, A., Zirngibl, R. and Rossant, J. (1995). Bone sialoprotein knockout mice have bone abnormalities. *Bone* **17**(6): 558.

Baderca, F., Lighezan, R., Dema, A., Alexa, A. and Raica, M. (2005). Angiogenesis in urothelial tumors of the upper urinary tract. *Rom J Morphol Embryol* **46**(4): 263-268.

Bala, Y., Farlay, D., Delmas, P. D., Meunier, P. J. and Boivin, G. (2010). Time sequence of secondary mineralization and microhardness in cortical and cancellous bone from ewes. *Bone* **46**(4): 1204-1212.

Bandyopadhyay, A., Kubilus, J. K., Crochiere, M. L., Linsenmayer, T. F. and Tabin, C. J. (2008). Identification of unique molecular subdomains in the perichondrium and periosteum and their role in regulating gene expression in the underlying chondrocytes. *Dev Biol* **321**(1): 162-174.

Barnes, G. L., Hebert, K. E., Kamal, M., Javed, A., Einhorn, T. A., Lian, J. B., Stein, G. S. and Gerstenfeld, L. C. (2004). Fidelity of Runx2 activity in breast cancer cells is required for the generation of metastases-associated osteolytic disease. *Cancer Res* **64**(13): 4506-4513.

Baumert, U., Golan, I., Redlich, M., Aknin, J. J. and Muessig, D. (2005). Cleidocranial dysplasia: molecular genetic analysis and phenotypic-based description of a Middle European patient group. *Am J Med Genet A* **139A**(2): 78-85.

Benjamin, M., Kumai, T., Milz, S., Boszczyk, B. M., Boszczyk, A. A. and Ralphs, J. R. (2002). The skeletal attachment of tendons--tendon "entheses". *Comp Biochem Physiol A Mol Integr Physiol* **133**(4): 931-945.

Bilezikian, J. P., Raisz, L. G. and Martin, T. J. (2008). *Principles of bone biology.* San Diego, Calif., Academic Press/Elsevier.

Birnbaum, K., Sindelar, R., Gartner, J. R. and Wirtz, D. C. (2001). Material properties of trabecular bone structures. *Surg Radiol Anat* **23**(6): 399-407.

Boskey, A. L. (1995). Osteopontin and related phosphorylated sialoproteins: effects on mineralization. *Ann N Y Acad Sci* **760**: 249-256.

Boskey, A. L., Maresca, M., Ullrich, W., Doty, S. B., Butler, W. T. and Prince, C. W. (1993). Osteopontin-hydroxyapatite interactions in vitro: inhibition of hydroxyapatite formation and growth in a gelatin-gel. *Bone Miner* **22**(2): 147-159.

Boukhechba, F., Balaguer, T., Michiels, J. F., Ackermann, K., Quincey, D., Bouler, J. M., Pyerin, W., Carle, G. F. and Rochet, N. (2009). Human primary osteocyte differentiation in a 3D culture system. *J Bone Miner Res* **24**(11): 1927-1935.

Buccione, R., Orth, J. D. and McNiven, M. A. (2004). Foot and mouth: podosomes, invadopodia and circular dorsal ruffles. *Nat Rev Mol Cell Biol* **5**(8): 647-657.

Buckwalter, J. A., Glimcher, M. J., Cooper, R. R. and Recker, R. (1995). Bone Biology. *The Journal of Bone & Joint Surgery* **77A**(8): 1276-1289.

Burton, C. J., Combe, C., Walls, J. and Harris, K. P. (1996). Fibronectin production by human tubular cells: the effect of apical protein. *Kidney Int* **50**(3): 760-767.

Calvi, L. M., Adams, G. B., Weibrecht, K. W., Weber, J. M., Olson, D. P., Knight, M. C., Martin, R. P., Schipani, E., Divieti, P., Bringhurst, F. R., Milner, L. A., Kronenberg, H. M. and Scadden, D. T. (2003). Osteoblastic cells regulate the haematopoietic stem cell niche. *Nature* **425**(6960): 841-846.

Case, N., Ma, M., Sen, B., Xie, Z., Gross, T. S. and Rubin, J. (2008). Beta-catenin levels influence rapid mechanical responses in osteoblasts. *J Biol Chem* **283**(43): 29196-29205.

Cepko, C. L., Ryder, E. F., Austin, C. P., Walsh, C. and Fekete, D. M. (1993). Lineage analysis using retrovirus vectors. *Methods Enzymol* **225**: 933-960.

Chen, Y., Whetstone, H. C., Youn, A., Nadesan, P., Chow, E. C., Lin, A. C. and Alman, B. A. (2007). Beta-catenin signaling pathway is crucial for bone morphogenetic protein 2 to induce new bone formation. *J Biol Chem* **282**(1): 526-533.

ChiariOne. Symptom List. from http://chiarione.org/symptoms.html.

Coben, S. E. (1998). The spheno-occipital synchondrosis: the missing link between the profession's concept of craniofacial growth and orthodontic treatment. *Am J Orthod Dentofacial Orthop* **114**(6): 709-712; discussion 713-704.

Cohen, M. M., Jr. (2006). The new bone biology: pathologic, molecular, and clinical correlates. *Am J Med Genet A* **140**(23): 2646-2706.

Colnot, C., Lu, C., Hu, D. and Helms, J. A. (2004). Distinguishing the contributions of the perichondrium, cartilage, and vascular endothelium to skeletal development. *Dev Biol* **269**(1): 55-69.

Coskun, S. and Hirschi, K. K. (2010). Establishment and regulation of the HSC niche: Roles of osteoblastic and vascular compartments. *Birth Defects Res C Embryo Today* **90**(4): 229-242.

Couly, G. F., Coltey, P. M. and Le Douarin, N. M. (1993). The triple origin of skull in higher vertebrates: a study in quail-chick chimeras. *Development* **117**(2): 409-429.

Crane, N. J., Popescu, V., Morris, M. D., Steenhuis, P. and Ignelzi, M. A., Jr. (2006). Raman spectroscopic evidence for octacalcium phosphate and other transient mineral species deposited during intramembranous mineralization. *Bone* **39**(3): 434-442.

Dabovic, B., Chen, Y., Colarossi, C., Obata, H., Zambuto, L., Perle, M. A. and Rifkin, D. B. (2002). Bone abnormalities in latent TGF-[beta] binding protein (Ltbp)-3-null mice indicate a role for Ltbp-3 in modulating TGF-[beta] bioavailability. *J Cell Biol* **156**(2): 227-232.

Dabovic, B., Chen, Y., Colarossi, C., Zambuto, L., Obata, H. and Rifkin, D. B. (2002). Bone defects in latent TGF-beta binding protein (Ltbp)-3 null mice; a role for Ltbp in TGF-beta presentation. *J Endocrinol* **175**(1): 129-141.

Dale, R. M., Sisson, B. E. and Topczewski, J. (2009). The emerging role of Wnt/PCP signaling in organ formation. *Zebrafish* **6**(1): 9-14.

Darken, R. S., Scola, A. M., Rakeman, A. S., Das, G., Mlodzik, M. and Wilson, P. A. (2002). The planar polarity gene strabismus regulates convergent extension movements in Xenopus. *EMBO J* **21**(5): 976-985.

Denis, C. V. (2002). Molecular and cellular biology of von Willebrand factor. *Int J Hematol* **75**(1): 3-8.

Donoghue, P. C. and Sansom, I. J. (2002). Origin and early evolution of vertebrate skeletonization. *Microsc Res Tech* **59**(5): 352-372.

Donoghue, P. C., Sansom, I. J. and Downs, J. P. (2006). Early evolution of vertebrate skeletal tissues and cellular interactions, and the canalization of skeletal development. *J Exp Zool B Mol Dev Evol* **306**(3): 278-294.

Dulac, C. and Axel, R. (1995). A novel family of genes encoding putative pheromone receptors in mammals. *Cell* **83**(2): 195-206.

Egeblad, M. and Werb, Z. (2002). New functions for the matrix metalloproteinases in cancer progression. *Nat Rev Cancer* **2**(3): 161-174.

el Ghouzzi, V., Le Merrer, M., Perrin-Schmitt, F., Lajeunie, E., Benit, P., Renier, D., Bourgeois, P., Bolcato-Bellemin, A. L., Munnich, A. and Bonaventure, J. (1997). Mutations of the TWIST gene in the Saethre-Chotzen syndrome. *Nat Genet* **15**(1): 42-46.

Esumi, S., Wu, S. X., Yanagawa, Y., Obata, K., Sugimoto, Y. and Tamamaki, N. (2008). Method for single-cell microarray analysis and application to gene-expression profiling of GABAergic neuron progenitors. *Neurosci Res* **60**(4): 439-451.

Etchevers, H. C., Vincent, C., Le Douarin, N. M. and Couly, G. F. (2001). The cephalic neural crest provides pericytes and smooth muscle cells to all blood vessels of the face and forebrain. *Development* **128**(7): 1059-1068.

Evans, D. J. and Noden, D. M. (2006). Spatial relations between avian craniofacial neural crest and paraxial mesoderm cells. *Dev Dyn* **235**(5): 1310-1325.

Fanarraga, M. L., Charite, J., Hage, W. J., De Graaff, W. and Deschamps, J. (1997). Hoxb-8 gain-of-function transgenic mice exhibit alterations in the peripheral nervous system. *J Neurosci Methods* **71**(1): 11-18.

Fanto, M. and McNeill, H. (2004). Planar polarity from flies to vertebrates. *J Cell Sci* **117**(Pt 4): 527-533.

Farrow, E. G., Davis, S. I., Ward, L. M., Summers, L. J., Bubbear, J. S., Keen, R., Stamp, T. C., Baker, L. R., Bonewald, L. F. and White, K. E.

(2009). Molecular analysis of DMP1 mutants causing autosomal recessive hypophosphatemic rickets. *Bone* **44**(2): 287-294.

Ferguson, C. A. and Graham, A. (2004). Redefining the head-trunk interface for the neural crest. *Dev Biol* **269**(1): 70-80.

Franz-Odendaal, T. A., Hall, B. K. and Witten, P. E. (2006). Buried alive: how osteoblasts become osteocytes. *Dev Dyn* **235**(1): 176-190.

Frazen, A., Hultenby, K., Reinholt, F. P., Onnerfjord, P. and Heinegard, D. (2008). Altered osteoclast development and function in osteopontin deficient mice. *Journal of Orthopaedic Research* **26**: 721-728.

Fujii, T., Iwane, A. H., Yanagida, T. and Namba, K. (2010). Direct visualization of secondary structures of F-actin by electron cryomicroscopy. *Nature* **467**(7316): 724-728.

Funato, N., Chapman, S. L., McKee, M. D., Funato, H., Morris, J. A., Shelton, J. M., Richardson, J. A. and Yanagisawa, H. (2009). Hand2 controls osteoblast differentiation in the branchial arch by inhibiting DNA binding of Runx2. *Development* **136**(4): 615-625.

Gajjeraman, S., Narayanan, K., Hao, J., Qin, C. and George, A. (2007). Matrix macromolecules in hard tissues control the nucleation and hierarchical assembly of hydroxyapatite. *J Biol Chem* **282**(2): 1193-1204.

Gans, C. (1988). Craniofacial growth, evolutionary questions. *Development* **103 Suppl**: 3-15.

Gans, C. (1989). Stages in the origin of vertebrates: analysis by means of scenarios. *Biol Rev Camb Philos Soc* **64**(3): 221-268.

Gans, C. and Northcutt, R. G. (1983). Neural crest and the origin of vertebrates: a new head. *Science* **220**(4594): 268-273.

Geissmann, F., Manz, M. G., Jung, S., Sieweke, M. H., Merad, M. and Ley, K. (2010). Development of monocytes, macrophages, and dendritic cells. *Science* **327**(5966): 656-661.

George, A. and Veis, A. (2008). Phosphorylated proteins and control over apatite nucleation, crystal growth, and inhibition. *Chem Rev* **108**(11): 4670-4693.

Giraud-Guille, M. M., Besseau, L., Chopin, C., Durand, P. and Herbage, D. (2000). Structural aspects of fish skin collagen which forms ordered arrays via liquid crystalline states. *Biomaterials* **21**(9): 899-906.

Giraud-Guille, M. M., Besseau, L. and Martin, R. (2003). Liquid crystalline assemblies of collagen in bone and in vitro systems. *J Biomech* **36**(10): 1571-1579.

Goldstein, M. E., Grant, P., House, S. B., Henken, D. B. and Gainer, H. (1996). Developmental regulation of two distinct neuronal phenotypes in rat dorsal root ganglia. *Neuroscience* **71**(1): 243-258.

Golub, E. E. (2009). Role of matrix vesicles in biomineralization. *Biochim Biophys Acta* **1790**(12): 1592-1598.

Gross, W. (1956). U¨ ber Crossopterygier und Dipnoer aus dem baltischen Oberdevon im Zusammenhang einer vergleichenden Untersuchung des Porenkanalsystems pala¨ozoischer Agnathen und Fische. *Kungl Svenska Vetenskap Hand* **5**: 1-140.

Hale, L. V., Ma, Y. F. and Santerre, R. F. (2000). Semi-quantitative fluorescence analysis of calcein binding as a measurement of in vitro mineralization. *Calcif Tissue Int* **67**(1): 80-84.

Hall, B. K. (2005). *Bones and cartilage : developmental and evolutionary skeletal biology*. Australia ; San Diego, Calif., Elsevier Academic Press.

Hall, B. K. and Miyake, T. (1992). The membranous skeleton: the role of cell condensations in vertebrate skeletogenesis. *Anat Embryol (Berl)* **186**(2): 107-124.

Hall, B. K. and Miyake, T. (2000). All for one and one for all: condensations and the initiation of skeletal development. *BioEssays* **22**(2): 138-147.

Halstead, L. B. and Sarjeant, W. A. S. (1995). *Vertebrate fossils and the evolution of scientific concepts : writings in tribute to Beverly Halstead*. Australia ; United States, Gordon and Breach.

Hanken, J. and Hall, B. K. (1993). *The Skull*. Chicago, University of Chicago Press.

Harada, H., Tagashira, S., Fujiwara, M., Ogawa, S., Katsumata, T., Yamaguchi, A., Komori, T. and Nakatsuka, M. (1999). Cbfa1 isoforms exert functional differences in osteoblast differentiation. *J Biol Chem* **274**(11): 6972-6978.

Hashimoto, Y., Yoshida, G., Toyoda, H. and Takaoka, K. (2007). Generation of tendon-to-bone interface "enthesis" with use of recombinant BMP-2 in a rabbit model. *J Orthop Res* **25**(11): 1415-1424.

Hava, D., Forster, U., Matsuda, M., Cui, S., Link, B. A., Eichhorst, J., Wiesner, B., Chitnis, A. and Abdelilah-Seyfried, S. (2009). Apical membrane maturation and cellular rosette formation during morphogenesis of the zebrafish lateral line. *J Cell Sci* **122**(Pt 5): 687-695.

He, F., Xiong, W., Yu, X., Espinoza-Lewis, R., Liu, C., Gu, S., Nishita, M., Suzuki, K., Yamada, G., Minami, Y. and Chen, Y. (2008). Wnt5a regulates directional cell migration and cell proliferation via Ror2-mediated

noncanonical pathway in mammalian palate development. *Development* **135**(23): 3871-3879.

Hems, T. and Tillmann, B. (2000). Tendon entheses of the human masticatory muscles. *Anat Embryol (Berl)* **202**(3): 201-208.

Hendershot, T. J., Liu, H., Clouthier, D. E., Shepherd, I. T., Coppola, E., Studer, M., Firulli, A. B., Pittman, D. L. and Howard, M. J. (2008). Conditional deletion of Hand2 reveals critical functions in neurogenesis and cell type-specific gene expression for development of neural crest-derived noradrenergic sympathetic ganglion neurons. *Dev Biol* **319**(2): 179-191.

Hessle, L., Johnson, K. A., Anderson, H. C., Narisawa, S., Sali, A., Goding, J. W., Terkeltaub, R. and Millan, J. L. (2002). Tissue-nonspecific alkaline phosphatase and plasma cell membrane glycoprotein-1 are central antagonistic regulators of bone mineralization. *Proc Natl Acad Sci U S A* **99**(14): 9445-9449.

Horiuchi, K., Amizuka, N., Takeshita, S., Takamatsu, H., Katsuura, M., Ozawa, H., Toyama, Y., Bonewald, L. F. and Kudo, A. (1999). Identification and characterization of a novel protein, periostin, with restricted expression to periosteum and periodontal ligament and increased expression by transforming growth factor beta. *J Bone Miner Res* **14**(7): 1239-1249.

Howard, T. D., Paznekas, W. A., Green, E. D., Chiang, L. C., Ma, N., Ortiz de Luna, R. I., Garcia Delgado, C., Gonzalez-Ramos, M., Kline, A. D. and Jabs, E. W. (1997). Mutations in TWIST, a basic helix-loop-helix transcription factor, in Saethre-Chotzen syndrome. *Nat Genet* **15**(1): 36-41.

Huang, L. F., Fukai, N., Selby, P. B., Olsen, B. R. and Mundlos, S. (1997). Mouse clavicular development: analysis of wild-type and cleidocranial dysplasia mutant mice. *Dev Dyn* **210**(1): 33-40.

Huang, R., Zhi, Q., Patel, K., Wilting, J. and Christ, B. (2000). Contribution of single somites to the skeleton and muscles of the occipital and cervical regions in avian embryos. *Anat Embryol (Berl)* **202**(5): 375-383.

Inada, M., Wang, Y., Byrne, M. H., Rahman, M. U., Miyaura, C., Lopez-Otin, C. and Krane, S. M. (2004). Critical roles for collagenase-3 (Mmp13) in development of growth plate cartilage and in endochondral ossification. *Proc Natl Acad Sci U S A* **101**(49): 17192-17197.

Jabs, E. W., Muller, U., Li, X., Ma, L., Luo, W., Haworth, I. S., Klisak, I., Sparkes, R., Warman, M. L., Mulliken, J. B. and et al. (1993). A mutation in the homeodomain of the human MSX2 gene in a family affected with autosomal dominant craniosynostosis. *Cell* **75**(3): 443-450.

Janvier, P. (2008). Early jawless vertebrates and cyclostome origins. *Zoolog Sci* **25**(10): 1045-1056.

Jeffery, N. and Spoor, F. (2004). Ossification and midline shape changes of the human fetal cranial base. *Am J Phys Anthropol* **123**(1): 78-90.

Jeffery, N. and Spoor, F. (2004). Prenatal growth and development of the modern human labyrinth. *J Anat* **204**(2): 71-92.

Jiang, X., Rowitch, D. H., Soriano, P., McMahon, A. P. and Sucov, H. M. (2000). Fate of the mammalian cardiac neural crest. *Development* **127**(8): 1607-1616.

Jimenez, M. J., Balbin, M., Lopez, J. M., Alvarez, J., Komori, T. and Lopez-Otin, C. (1999). Collagenase 3 is a target of Cbfa1, a transcription factor of the runt gene family involved in bone formation. *Mol Cell Biol* **19**(6): 4431-4442.

Jonason, J. H., Xiao, G., Zhang, M., Xing, L. and Chen, D. (2009). Post-translational Regulation of Runx2 in Bone and Cartilage. *J Dent Res* **88**(8): 693-703.

Kamme, F., Salunga, R., Yu, J., Tran, D. T., Zhu, J., Luo, L., Bittner, A., Guo, H. Q., Miller, N., Wan, J. and Erlander, M. (2003). Single-cell microarray analysis in hippocampus CA1: demonstration and validation of cellular heterogeneity. *J Neurosci* **23**(9): 3607-3615.

Kanczler, J. M. and Oreffo, R. O. (2008). Osteogenesis and angiogenesis: the potential for engineering bone. *Eur Cell Mater* **15**: 100-114.

Kardon, G. (1998). Muscle and tendon morphogenesis in the avian hind limb. *Development* **125**(20): 4019-4032.

Kardon, G., Harfe, B. D. and Tabin, C. J. (2003). A Tcf4-positive mesodermal population provides a prepattern for vertebrate limb muscle patterning. *Dev Cell* **5**(6): 937-944.

Karner, C., Wharton, K. A. and Carroll, T. J. (2006). Apical-basal polarity, Wnt signaling and vertebrate organogenesis. *Semin Cell Dev Biol* **17**(2): 214-222.

Karner, C., Wharton, K. A., Jr. and Carroll, T. J. (2006). Planar cell polarity and vertebrate organogenesis. *Semin Cell Dev Biol* **17**(2): 194-203.

Katoh, M. (2007). Comparative integromics on non-canonical WNT or planar cell polarity signaling molecules: transcriptional mechanism of PTK7 in colorectal cancer and that of SEMA6A in undifferentiated ES cells. *Int J Mol Med* **20**(3): 405-409.

Kawasaki, K. and Weiss, K. M. (2008). SCPP gene evolution and the dental mineralization continuum. *J Dent Res* **87**(6): 520-531.

Kessel, M. (1992). Respecification of vertebral identities by retinoic acid. *Development* **115**(2): 487-501.

Kihara, T., Oshima, A., Hirose, M. and Ohgushi, H. (2004). Three-dimensional visualization analysis of in vitro cultured bone fabricated by rat marrow mesenchymal stem cells. *Biochem Biophys Res Commun* **316**(3): 943-948.

Kikuchi, M., Ikoma, T., Itoh, S., Matsumoto, H. N., Koyama, Y., Takauda, K., Shinomiya, K. and Tanaka, J. (2004). Biomimetic synthesis of bone-like nanocomposites using the self-organization mechanism of hydroxyapatite and collagen. *Composites Science and Technology* **64**: 819-825.

Knecht, A. K. and Bronner-Fraser, M. (2002). Induction of the neural crest: a multigene process. *Nat Rev Genet* **3**(6): 453-461.

Kontges, G. and Lumsden, A. (1996). Rhombencephalic neural crest segmentation is preserved throughout craniofacial ontogeny. *Development* **122**(10): 3229-3242.

Koyanagi, I. and Houkin, K. (2010). Pathogenesis of syringomyelia associated with Chiari type 1 malformation: review of evidences and proposal of a new hypothesis. *Neurosurg Rev* **33**(3): 271-284; discussion 284-275.

Kramer, I., Halleux, C., Keller, H., Pegurri, M., Gooi, J. H., Weber, P. B., Feng, J. Q., Bonewald, L. F. and Kneissel, M. (2010). Osteocyte Wnt/beta-catenin signaling is required for normal bone homeostasis. *Mol Cell Biol* **30**(12): 3071-3085.

Labuda, R. (2010). An Overview of the Chiari Malformation. from http://www.conquerchiari.org/Chiari%20Overview%202010.pdf.

Lana-Elola, E., Rice, R., Grigoriadis, A. E. and Rice, D.P. (2007). Cell fate specification during calvarial bone and suture development. *Dev Bio* **311**: 335-346.

Laue, K., Janicke, M., Plaster, N., Sonntag, C. and Hammerschmidt, M. (2008). Restriction of retinoic acid activity by Cyp26b1 is required for proper timing and patterning of osteogenesis during zebrafish development. *Development* **135**(22): 3775-3787.

Le Douarin, N. and Kalcheim, C. (1999). *The neural crest.* Cambridge, UK ; New York, NY, USA, Cambridge University Press.

Le Douarin, N. M., Ziller, C. and Couly, G. F. (1993). Patterning of neural crest derivatives in the avian embryo: in vivo and in vitro studies. *Dev Biol* **159**(1): 24-49.

Le Guellec, D., Morvan-Dubois, G. and Sire, J. Y. (2004). Skin development in bony fish with particular emphasis on collagen deposition in the dermis of the zebrafish (Danio rerio). *Int J Dev Biol* **48**(2-3): 217-231.

Lee, R. M. K. W. (1989). *Blood vessel changes in hypertension : structure and function.* Boca Raton, Fla., CRC Press.

Lerner, U. H. (2006). Bone remodeling in post-menopausal osteoporosis. *J Dent Res* **85**(7): 584-595.

Li, Y. and Dudley, A. T. (2009). Noncanonical frizzled signaling regulates cell polarity of growth plate chondrocytes. *Development* **136**(7): 1083-1092.

Lieberman, D.E. and McCarthy, R.C. (1998) The ontogeny of cranial base angulation in humans and chimpanzees and its implications for reconstructing pharyngeal dimensions. *J Hum Evol* **36**(5): 487-517.

Lieberman, J. R. and Friedlaender, G. E. (2005). *Bone regeneration and repair : biology and clinical applications.* Totowa, N.J., Humana Press.

Liu, N., Barbosa, A. C., Chapman, S. L., Bezprozvannaya, S., Qi, X., Richardson, J. A., Yanagisawa, H. and Olson, E. N. (2009). DNA binding-dependent and -independent functions of the Hand2 transcription factor during mouse embryogenesis. *Development* **136**(6): 933-942.

Liu, X., Long, F., Peng, H., Aerni, S. J., Jiang, M., Sanchez-Blanco, A., Murray, J. I., Preston, E., Mericle, B., Batzoglou, S., Myers, E. W. and Kim, S. K. (2009). Analysis of cell fate from single-cell gene expression profiles in C. elegans. *Cell* **139**(3): 623-633.

Livesey, F. J., Furukawa, T., Steffen, M. A., Church, G. M. and Cepko, C. L. (2000). Microarray analysis of the transcriptional network controlled by the photoreceptor homeobox gene Crx. *Curr Biol* **10**(6): 301-310.

Lois, C., Hong, E. J., Pease, S., Brown, E. J. and Baltimore, D. (2002). Germline transmission and tissue-specific expression of transgenes delivered by lentiviral vectors. *Science* **295**(5556): 868-872.

Lomri, A., Lemonnier, J., Hott, M., de Parseval, N., Lajeunie, E., Munnich, A., Renier, D. and Marie, P. J. (1998). Increased calvaria cell differentiation and bone matrix formation induced by fibroblast growth factor receptor 2 mutations in Apert syndrome. *J Clin Invest* **101**(6): 1310-1317.

Loukas, M., Noordeh, N., Shoja, M. M., Pugh, J., Oakes, W. J. and Tubbs, R. S. (2008). Hans Chiari (1851-1916). *Childs Nerv Syst* **24**(3): 407-409.

Maderson, P. F. A. (1987). *Developmental and evolutionary aspects of the neural crest.* New York, Wiley.

Marcus, R., Feldman, D., Nelson, D. A. and Rosen, C. J., Eds. (2008). *Osteoporosis*. London, Elsevier.

Marin-Padilla, M. and Marin-Padilla, T. M. (1981). Morphogenesis of experimentally induced Arnold--Chiari malformation. *J Neurol Sci* **50**(1): 29-55.

Matsuoka, T., Ahlberg, P. E., Kessaris, N., Iannarelli, P., Dennehy, U., Richardson, W. D., McMahon, A. P. and Koentges, G. (2005). Neural crest origins of the neck and shoulder. *Nature* **436**(7049): 347-355.

Mesiwala, A. H., Shaffrey, C. I., Gruss, J. S. and Ellenbogen, R. G. (2001). Atypical hemifacial microsomia associated with Chiari I malformation and syrinx: further evidence indicating that chiari I malformation is a disorder of the paraaxial mesoderm. Case report and review of the literature. *J Neurosurg* **95**(6): 1034-1039.

Milhorat, T. H., Bolognese, P. A., Nishikawa, M., McDonnell, N. B. and Francomano, C. A. (2007). Syndrome of occipitoatlantoaxial hypermobility, cranial settling, and chiari malformation type I in patients with hereditary disorders of connective tissue. *J Neurosurg Spine* **7**(6): 601-609.

Milhorat, T. H., Chou, M. W., Trinidad, E. M., Kula, R. W., Mandell, M., Wolpert, C. and Speer, M. C. (1999). Chiari I malformation redefined: clinical and radiographic findings for 364 symptomatic patients. *Neurosurgery* **44**(5): 1005-1017.

Mirzadeh, Z., Merkle, F. T., Soriano-Navarro, M., Garcia-Verdugo, J. M. and Alvarez-Buylla, A. (2008). Neural stem cells confer unique pinwheel architecture to the ventricular surface in neurogenic regions of the adult brain. *Cell Stem Cell* **3**(3): 265-278.

Morriss-Kay, G. M. (2001). Derivation of the mammalian skull vault. *J Anat* **199**(Pt 1-2): 143-151.

Mountcastle, V. B. (1997). The columnar organization of the neocortex. *Brain* **120 (Pt 4)**: 701-722.

Mueller, D. M. and Oro, J. J. (2004). Prospective analysis of presenting symptoms among 265 patients with radiographic evidence of Chiari malformation type I with or without syringomyelia. *J Am Acad Nurse Pract* **16**(3): 134-138.

Muenke, M., Schell, U., Hehr, A., Robin, N. H., Losken, H. W., Schinzel, A., Pulleyn, L. J., Rutland, P., Reardon, W., Malcolm, S. and et al. (1994). A common mutation in the fibroblast growth factor receptor 1 gene in Pfeiffer syndrome. *Nat Genet* **8**(3): 269-274.

Mundlos, S., Engel, H., Michel-Behnke, I. and Zabel, B. (1990). Distribution of type I and type II collagen gene expression during the development of human long bones. *Bone* **11**(4): 275-279.

Mundlos, S., Otto, F., Mundlos, C., Mulliken, J. B., Aylsworth, A. S., Albright, S., Lindhout, D., Cole, W. G., Henn, W., Knoll, J. H., Owen, M. J., Mertelsmann, R., Zabel, B. U. and Olsen, B. R. (1997). Mutations involving the transcription factor CBFA1 cause cleidocranial dysplasia. *Cell* **89**(5): 773-779.

Myers, D. C., Sepich, D. S. and Solnica-Krezel, L. (2002). Bmp activity gradient regulates convergent extension during zebrafish gastrulation. *Dev Biol* **243**(1): 81-98.

Nagoshi, N., Shibata, S., Kubota, Y., Nakamura, M., Nagai, Y., Satoh, E., Morikawa, S., Okada, Y., Mabuchi, Y., Katoh, H., Okada, S., Fukuda, K., Suda, T., Matsuzaki, Y., Toyama, Y. and Okano, H. (2008). Ontogeny and multipotency of neural crest-derived stem cells in mouse bone marrow, dorsal root ganglia, and whisker pad. *Cell Stem Cell* **2**(4): 392-403.

Nakamura, H., Sato, G., Hirata, A. and Yamamoto, T. (2004). Immunolocalization of matrix metalloproteinase-13 on bone surface under osteoclasts in rat tibia. *Bone* **34**(1): 48-56.

Nijweidi, P. J., Feyen, E. H. B. and J.H.M., F. (1986). Cells of Bone: Proliferation, Differentiation, and Hormonal Regulation. *Physiological Reviews* **66**(4): 855-886.

Nilsson, S. K., Johnston, H. M., Whitty, G. A., Williams, B., Webb, R. J., Denhardt, D. T., Bertoncello, I., Bendall, L. J., Simmons, P. J. and Haylock, D. N. (2005). Osteopontin, a key component of the hematopoietic stem cell niche and regulator of primitive hematopoietic progenitor cells. *Blood* **106**(4): 1232-1239.

NINDS (2011). Chiari Malformation Fact Sheet. from http://www.ninds.nih.gov/disorders/chiari/detail_chiari.htm#157713087.

Nishiyama, T., McDonough, A. M., Bruns, R. R. and Burgeson, R. E. (1994). Type XII and XIV collagens mediate interactions between banded collagen fibers in vitro and may modulate extracellular matrix deformability. *J Biol Chem* **269**(45): 28193-28199.

Noden, D. M. (1983). The role of the neural crest in patterning of avian cranial skeletal, connective, and muscle tissues. *Dev Biol* **96**(1): 144-165.

Norris, R. A., Damon, B., Mironov, V., Kasyanov, V., Ramamurthi, A., Moreno-Rodriguez, R., Trusk, T., Potts, J. D., Goodwin, R. L., Davis, J., Hoffman, S., Wen, X., Sugi, Y., Kern, C. B., Mjaatvedt, C. H., Turner, D. K., Oka, T., Conway, S. J., Molkentin, J. D., Forgacs, G. and Markwald, R. R. (2007). Periostin regulates collagen fibrillogenesis and the

biomechanical properties of connective tissues. *J Cell Biochem* **101**(3): 695-711.

Northcutt, R. G. and Gans, C. (1983). The genesis of neural crest and epidermal placodes: a reinterpretation of vertebrate origins. *Q Rev Biol* **58**(1): 1-28.

Noudel, R., Jovenin, N., Eap, C., Scherpereel, B., Pierot, L. and Rousseaux, P. (2009). Incidence of basioccipital hypoplasia in Chiari malformation type I: comparative morphometric study of the posterior cranial fossa. Clinical article. *J Neurosurg* **111**(5): 1046-1052.

O'Brien, F. J., Taylor, D. and Lee, T. C. (2002). An improved labelling technique for monitoring microcrack growth in compact bone. *J Biomech* **35**(4): 523-526.

Oishi, I., Suzuki, H., Onishi, N., Takada, R., Kani, S., Ohkawara, B., Koshida, I., Suzuki, K., Yamada, G., Schwabe, G. C., Mundlos, S., Shibuya, H., Takada, S. and Minami, Y. (2003). The receptor tyrosine kinase Ror2 is involved in non-canonical Wnt5a/JNK signalling pathway. *Genes Cells* **8**(7): 645-654.

Olesen, J. (2006). *The headaches*. Philadelphia, Lippincott Williams & Wilkins.

Olsson, L., Falck, P., Lopez, K., Cobb, J. and Hanken, J. (2001). Cranial neural crest cells contribute to connective tissue in cranial muscles in the anuran amphibian, Bombina orientalis. *Dev Biol* **237**(2): 354-367.

Opperman, L.A. (2000). Cranial sutures as intramembranous bone growth sites. *Dev Dyn* **219**: 472-485.

Paic, F., Igwe, J.C., Nori, R., Kronenberg, M.S., Franceschetti, T., Harrington, P., Kuo, L., Dong-Guk, S., Rowe, D.W., Harris, S.E. and Kalajzik, I. (2009). Identification of differentially expressed genes between osteoblasts and osteocytes. *Bone* **45**: 682-692.

Pautke, C., Vogt, S., Tischer, T., Wexel, G., Deppe, H., Milz, S., Schieker, M. and Kolk, A. (2005). Polychrome labeling of bone with seven different fluorochromes: enhancing fluorochrome discrimination by spectral image analysis. *Bone* **37**(4): 441-445.

Pratap, J., Lian, J. B., Javed, A., Barnes, G. L., van Wijnen, A. J., Stein, J. L. and Stein, G. S. (2006). Regulatory roles of Runx2 in metastatic tumor and cancer cell interactions with bone. *Cancer Metastasis Rev* **25**(4): 589-600.

Price, J., Turner, D. and Cepko, C. (1987). Lineage analysis in the vertebrate nervous system by retrovirus-mediated gene transfer. *Proc Natl Acad Sci U S A* **84**(1): 156-160.

Rakic, P. (1972). Mode of cell migration to the superficial layers of fetal monkey neocortex. *J Comp Neurol* **145**(1): 61-83.

Rakic, P. (1988). Specification of cerebral cortical areas. *Science* **241**(4862): 170-176.
Rice, D. P., Ed. (2008). Craniofacial Sutures. Frontiers of Oral Biology. Basel, Karger.

Rinn, J. L., Bondre, C., Gladstone, H. B., Brown, P. O. and Chang, H. Y. (2006). Anatomic demarcation by positional variation in fibroblast gene expression programs. *PLoS Genet* **2**(7): e119.

Rinn, J. L., Wang, J. K., Allen, N., Brugmann, S. A., Mikels, A. J., Liu, H., Ridky, T. W., Stadler, H. S., Nusse, R., Helms, J. A. and Chang, H. Y. (2008). A dermal HOX transcriptional program regulates site-specific epidermal fate. *Genes Dev* **22**(3): 303-307.

Ruest, L. B., Dager, M., Yanagisawa, H., Charite, J., Hammer, R. E., Olson, E. N., Yanagisawa, M. and Clouthier, D. E. (2003). dHAND-Cre transgenic mice reveal specific potential functions of dHAND during craniofacial development. *Dev Biol* **257**(2): 263-277.

Schiavi, S. C. (2006). Bone talk. *Nat Genet* **38**(11): 1230-1231.

Schorpp, M., Jager, R., Schellander, K., Schenkel, J., Wagner, E. F., Weiher, H. and Angel, P. (1996). The human ubiquitin C promoter directs high ubiquitous expression of transgenes in mice. *Nucleic Acids Res* **24**(9): 1787-1788.

Seshi, B., Kumar, S. and King, D. (2003). Multilineage gene expression in human bone marrow stromal cells as evidenced by single-cell microarray analysis. *Blood Cells Mol Dis* **31**(2): 268-285.

Shapiro, F. (2008). Bone development and its relation to fracture repair. The role of mesenchymal osteoblasts and surface osteoblasts. *Eur Cell Mater* **15**: 53-76.

Sigma (2001) Matrix Metalloproteinases and their Inhibitors – Current Status and Future Challenges. Celltransmissions **17**, 3-11

Simmons, D. J., Teitelbaum, S. L. and Rosenberg, G. D. (1981). Altered metabolic rhythm of rabbit osteoblasts by tetracycline. *Metab Bone Dis Relat Res* **3**(1): 51-54.

Simmons, D. L., Walker, C., Power, C. and Pigott, R. (1990). Molecular cloning of CD31, a putative intercellular adhesion molecule closely related to carcinoembryonic antigen. *J Exp Med* **171**(6): 2147-2152.

Simons, M. and Mlodzik, M. (2008). Planar cell polarity signaling: from fly development to human disease. *Annu Rev Genet* **42**: 517-540.

Soriano, P. (1999). Generalized lacZ expression with the ROSA26 Cre reporter strain. *Nat Genet* **21**(1): 70-71.

Speer, M. C., George, T. M., Enterline, D. S., Franklin, A., Wolpert, C. M. and Milhorat, T. H. (2000). A genetic hypothesis for Chiari I malformation with or without syringomyelia. *Neurosurg Focus* **8**(3): E12.

Storer, R. J., Akerman, S. and Goadsby, P. J. (2001). GABA receptors modulate trigeminovascular nociceptive neurotransmission in the trigeminocervical complex. *Br J Pharmacol* **134**(4): 896-904.

Storer, R. J., Akerman, S. and Goadsby, P. J. (2003). Characterization of opioid receptors that modulate nociceptive neurotransmission in the trigeminocervical complex. *Br J Pharmacol* **138**(2): 317-324.

Strassman, A. M., Raymond, S. A. and Burstein, R. (1996). Sensitization of meningeal sensory neurons and the origin of headaches. *Nature* **384**(6609): 560-564.

Takeshita, S., Kikuno, R., Tezuka, K. and Amann, E. (1993). Osteoblast-specific factor 2: cloning of a putative bone adhesion protein with homology with the insect protein fasciclin I. *Biochem J* **294 (Pt 1)**: 271-278.

Tam, C. S. and Anderson, W. (1980). Tetracycline labeling of bone in vivo. *Calcif Tissue Int* **30**(2): 121-125.

Tartaglia, M., Valeri, S., Velardi, F., Di Rocco, C. and Battaglia, P. A. (1997). Trp290Cys mutation in exon IIIa of the fibroblast growth factor receptor 2 (FGFR2) gene is associated with Pfeiffer syndrome. *Hum Genet* **99**(5): 602-606.

Tietjen, I., Rihel, J. M., Cao, Y., Koentges, G., Zakhary, L. and Dulac, C. (2003). Single-cell transcriptional analysis of neuronal progenitors. *Neuron* **38**(2): 161-175.

Ting, M-C., Wu, N.L., Roybal, P.G., Sun, J., Liu, L., Yen, Y. and Maxson, R.E. Jr. (2009). *EphA4* as an effector of *Twist1* in the guidance of osteogenic precursor cells during clavarial bone growth in craniosynostosis. *Development* **136**(5): 855-864.

Trinh, L. A., Yelon, D. and Stainier, D. Y. (2005). Hand2 regulates epithelial formation during myocardial diferentiation. *Curr Biol* **15**(5): 441-446.

Truett, G. E., Heeger, P., Mynatt, R. L., Truett, A. A., Walker, J. A. and Warman, M. L. (2000). Preparation of PCR-quality mouse genomic DNA with hot sodium hydroxide and tris (HotSHOT). *Biotechniques* **29**(1): 52, 54.

Tu, X., Joeng, K. S., Nakayama, K. I., Nakayama, K., Rajagopal, J., Carroll, T. J., McMahon, A. P. and Long, F. (2007). Noncanonical Wnt signaling through G protein-linked PKCdelta activation promotes bone formation. *Dev Cell* **12**(1): 113-127.

Vaananen, H. K., Zhao, H., Mulari, M. and Halleen, J. M. (2000). The cell biology of osteoclast function. *J Cell Sci* **113 (Pt 3)**: 377-381.

Veis, A. (1981). *The chemistry and biology of mineralized connective tissues : proceedings of the First International Conference on the Chemistry and Biology of Mineralized Connective Tissues, held 3-7 May 1981 at the Northwestern University Dental School, Chicago, Illinois, U.S.A.* New York, Elsevier/North-Holland.

Vu, T. H., Shipley, J. M., Bergers, G., Berger, J. E., Helms, J. A., Hanahan, D., Shapiro, S. D., Senior, R. M. and Werb, Z. (1998). MMP-9/gelatinase B is a key regulator of growth plate angiogenesis and apoptosis of hypertrophic chondrocytes. *Cell* **93**(3): 411-422.

Walsh, C. and Cepko, C. L. (1992). Widespread dispersion of neuronal clones across functional regions of the cerebral cortex. *Science* **255**(5043): 434-440.

Walsh, C. and Cepko, C. L. (1993). Clonal dispersion in proliferative layers of developing cerebral cortex. *Nature* **362**(6421): 632-635.

Wang, J., Hamblet, N. S., Mark, S., Dickinson, M. E., Brinkman, B. C., Segil, N., Fraser, S. E., Chen, P., Wallingford, J. B. and Wynshaw-Boris, A. (2006). Dishevelled genes mediate a conserved mammalian PCP pathway to regulate convergent extension during neurulation. *Development* **133**(9): 1767-1778.

Wansleeben, C. and Meijlink, F. (2011). The planar cell polarity pathway in vertebrate development. *Dev Dyn* **240**(3): 616-626.

Weiner, S. (2006). Transient precursor strategy in mineral formation of bone. *Bone* **39**(3): 431-433.

Weiner, S. (2008). Biomineralization: a structural perspective. *J Struct Biol* **163**(3): 229-234.

Westendorf, J. J. (2006). Transcriptional co-repressors of Runx2. *J Cell Biochem* **98**(1): 54-64.

Whelan, M. C. and Senger, D. R. (2003). Collagen I initiates endothelial cell morphogenesis by inducing actin polymerization through suppression of cyclic AMP and protein kinase A. *J Biol Chem* **278**(1): 327-334.

Wilkie, A. O., Slaney, S. F., Oldridge, M., Poole, M. D., Ashworth, G. J., Hockley, A. D., Hayward, R. D., David, D. J., Pulleyn, L. J., Rutland, P.

and et al. (1995). Apert syndrome results from localized mutations of FGFR2 and is allelic with Crouzon syndrome. *Nat Genet* **9**(2): 165-172.

Witten, P. E. and Huysseune, A. (2009). A comparative view on mechanisms and functions of skeletal remodelling in teleost fish, with special emphasis on osteoclasts and their function. *Biol Rev Camb Philos Soc* **84**(2): 315-346.

Wu, J. and Mlodzik, M. (2009). A quest for the mechanism regulating global planar cell polarity of tissues. *Trends Cell Biol* **19**(7): 295-305.

Xiong, W., He, F., Morikawa, Y., Yu, X., Zhang, Z., Lan, Y., Jiang, R., Cserjesi, P. and Chen, Y. (2009). Hand2 is required in the epithelium for palatogenesis in mice. *Dev Biol* **330**(1): 131-141.

Yanagisawa, H., Clouthier, D. E., Richardson, J. A., Charite, J. and Olson, E. N. (2003). Targeted deletion of a branchial arch-specific enhancer reveals a role of dHAND in craniofacial development. *Development* **130**(6): 1069-1078.

Yin, T. and Li, L. (2006). The stem cell niches in bone. *J Clin Invest* **116**(5): 1195-1201.

Yoshida, T., Vivatbutsiri, P., Morriss-Kay, G., Saga, Y. and Iseki, S. (2008). Cell lineage in mammalian craniofacial mesenchyme. *Mech Dev* **125**(9-10): 797-808.

Zhang, X. and Koentges, G., Unpublished

Zhu, S., Barbe, M. F., Amin, N., Rani, S., Popoff, S. N., Safadi, F. F. and Litvin, J. (2008). Immunolocalization of Periostin-like factor and Periostin during embryogenesis. *J Histochem Cytochem* **56**(4): 329-345.